Retarder la transition vers la turbulence en imitant les feuilles de lotus

Francesco Picella

To cite this version:

Francesco Picella. Retarder la transition vers la turbulence en imitant les feuilles de lotus. Mécanique [physics]. Ecole nationale supérieure d'arts et métiers - ENSAM, 2019. Français. NNT : 2019ENAM0014 . tel-02191508

HAL Id: tel-02191508
https://pastel.hal.science/tel-02191508
Submitted on 23 Jul 2019

HAL is a multi-disciplinary open access archive for the deposit and dissemination of scientific research documents, whether they are published or not. The documents may come from teaching and research institutions in France or abroad, or from public or private research centers.

L'archive ouverte pluridisciplinaire **HAL**, est destinée au dépôt et à la diffusion de documents scientifiques de niveau recherche, publiés ou non, émanant des établissements d'enseignement et de recherche français ou étrangers, des laboratoires publics ou privés.

2019-ENAM-00XX

École doctorale n° 432 : Sciences des Métiers de l'Ingénieur

Doctorat ParisTech

THÈSE

pour obtenir le grade de docteur délivré par

l'École Nationale Supérieure d'Arts et Métiers

Spécialité “ Mécanique ”

présentée et soutenue publiquement par

Francesco PICELLA

le 17 avril 2018

Controlling Laminar-Turbulent process with Superhydrophobic surfaces

Influence of transition scenarios and surface modellings

Directeur de thèse : **Jean-Christophe ROBINET**
Co-encadrement de la thèse : **S. Cherubini**

Jury	
M. José-Eduardo WESFREID, Professeur, PMMH, ESPCI, Paris, France	Président
M. Alessandro BOTTARO, Professeur, DICCA, Università di Genova, Italie	Rapporteur
M. Franco AUTERI, Professeur associé HDR, AERO, Politecnico di Milano, Milano, Italie	Rapporteur
Mme Taraneh SAYADI, Chargé de recherche, Institut d'Alembert, UPMC, Paris, France	Examinateur
M. Olivier MARQUET, Senior Research Fellow, DAAA, ONERA, Meudon, France	Examinateur
M. Jean-Christophe ROBINET, Professeur, Dynfluid, Arts et Métiers, Paris, France	Examinateur
Mme Stefania CHERUBINI, Professeur Associé, DMMM, Politecnico di Bari, Italie	Examinateur

THÈSE

Arts et Métiers ParisTech - Centre de Paris
DynFluid - Laboratoire de dynamique des fluides - EA 92

Mémoire de thèse

pour obtenir le grade de

DOCTEUR

de

L'ÉCOLE NATIONALE SUPÉRIEURE D'ARTS ET MÉTIERS

Spécialité : Mécanique

présenté et soutenu

par

Francesco PICELLA

le 17 Avril 2019

Controlling laminar-turbulent transition with bio-mimetic superhydrophobic surfaces

Directeur de thèse : **M. Jean-Christophe Robinet**
Co-directrice de thèse : **Mme. Stefania Cherubini**

devant le jury composé de :

M. José-Eduardo Wesfreid,	Professeur, Pmmh, ESPCI, Paris, France	Président
M. Alessandro Bottaro,	Professeur, DICCA, Universitá di Genova, Genova, Italie	Rapporteur
M. Franco Auteri,	Professeur associé, AERO, Politecnico di Milano, Milano, Italie	Rapporteur
Mme Taraneh Sayadi,	Chargé de recherche, Institut d'Alembert, UPMC, Paris, France	Examinateur
M. Olivier Marquet,	Senior Research Fellow, DAAA, ONERA, Meudon, France	Examinateur
M. Jean-Christophe Robinet,	Professeur, DynFluid, Arts et Métiers ParisTech, Paris	Examinateur
Mme Stefania Cherubini,	Professeur associé, DMMM, Politecnico di Bari, Bari, Italie	Examinateur

DynFluid - Laboratoire de Dynamique des Fluides

Arts et Métiers ParisTech, centre de Paris

Arts et Métiers ParisTech (École Nationale Supérieure d'Arts et Métiers) est un Grand Établissement dépendant du Ministère de l'Enseignement Supérieur et de la Recherche, composé de huit centres :
AIX-EN-PROVENCE ANGERS BORDEAUX CHÂLONS-EN-CHAMPAGNE CLUNY LILLE METZ PARIS

'Essentially, all models are wrong,
but some are useful.'

G.E.P. Box (1919-2013)

Acknowledgements

From splashing water in the bathtub as a toddler, up to the obtention of a PhD in fluid mechanics, this process could not have taken place without the help of some special people I have had the chance to meet during my life. Here I would like to thank few of them.

First of all I would like to thank Prof.Jean-Christophe Robinet (Senior) and Prof.Stefania Cherubini, my supervisors and *’scientific parents’.* I am grateful to Senior, first for having accepted my application as Master student, then for introducing me to academic research and spending so much effort in stimulating my love for science. I am thankful to Prof.Cherubini for having taught me how to carry out scientific research, and for having supported my training with her *deux ex machina* fundings. Despite the geographical distance, she has always succeeded in following my progresses, guiding me during these three years with a little help of Skype, Overleaf and Ryanair.

I would like to express my gratitude Professor Franco Auteri and Professor Alessandro Bottaro, who accepted to proofread my manuscript as referees.

Thanks to Prof. Taraneh Sayadi and to Prof. Olivier Marquet for joining my Jury board, for their demanding questions, both during the dissertation as well as at the *pot.*

Thanks to Prof. Eduardo Wesfreid, for bringing an experimental perspective in reviewing my manuscript, and for playing the role of *président du jury.*

I would like to thank my *brothers-in-PhD*, Jean-Christophe Loiseau, Alessandro Bucci and Mirko Farano, for having shared with me their knowledge, trying to give me an answer to my question, especially to the ones that I had never dared to ask to anyone else.

Thanks to Prof. Paola Cinnella and Prof. Michele Napolitano, for giving me the opportunity to take part to of the Double Degree program with Politecnico di Bari.

Thanks to all the members of Dynfluid, my *extended family* at ENSAM in Paris, for their teaching about fluid mechanics while enduring the noise of my clicky keyboard.

Thanks to the ones that, together with Fluid Mechanics, shared with me their most diverse interests, such as Prof. Laurette Tuckerman’s reckless Contra-Dance, Prof. François Lusseyran’s flashy laser beams and Prof. Luc Pastur’s massive wind tunnels.

Special thanks to all the *expat* in MEASE and around Paris, for sharing with me their their geo-political toughts as well as their *pacco da giú* trying to fight homesickness.

Thanks to the *Cité-U family*, for the years and the encounters I have the chance to make, around Velo Volant and Jardin du Monde, as well as at fencing club and petit caveau.

Grazie alla mia famiglia italiana, per avermi dato valori ed incoraggiato negli studi.
Merci à ma belle famille, pour m’avoir accueilli entre eux comme un fils.
Merci à Laure, pour m’avoir dit ’oui’.

Contents

1 Introduction **1**
1.1 State of the art . . . 2
1.2 Controlling the laminar-turbulent transition process with superhydrophobic surfaces . . . 4
1.3 Triggering *uncontrolled* transition in channel flow numerical simulations . . . 6
1.4 Modelling superhydrophobic surfaces: influence of microstructure size and gas-water free-surface dynamics . . . 9
1.5 Organization of the manuscript . . . 12

2 Mathematical Framework **13**
2.0.1 The Navier-Stokes equations . . . 13
2.1 Instability Framework . . . 14
2.2 Linear Stability . . . 14
2.3 Non-normal operator . . . 16
2.3.1 Short time dynamics, optimal perturbations . . . 16
2.3.2 Response to harmonic forcing, optimal forcing . . . 17

3 Numerical Tools **19**
3.1 Introduction to the spectral elements code Nek5000 . . . 19
3.1.1 Spatial discretization: spectral elements . . . 19
3.1.2 Variational formulation and spatial discretization . . . 20
3.1.3 Time discretisation . . . 21
3.2 Boundary conditions . . . 22
3.2.1 Robin Boundary Condition . . . 22
3.2.2 Arbitrary Lagrangian-Eulerian Formulations and Free-Surface Flows . . . 23
3.2.3 Preliminary concepts . . . 23
3.2.4 ALE implementation within NEK5000 . . . 25
3.2.5 How ALE is used in NEK5000 . . . 26
3.3 Modal decomposition . . . 26
3.3.1 Global linear stability, time-stepping algorithm . . . 26
3.3.2 Local stability analysis . . . 27

4 Triggering Natural transition in numerical simulations **29**
4.1 Problem Statement and numerical methods . . . 29
4.1.1 Governing equations . . . 30

4.1.2 Building a volume forcing to enforce a prescribed energy spectrum . 32
4.1.3 Constraints on α, β, and ω 35
4.2 Algorithm testing: linear regime 36
4.2.1 Transient dynamics 38
4.2.2 Recovering the optimal dynamics 39
4.2.3 Spectrum analysis 40
4.3 Non-Linear Dynamics 41
4.3.1 Evolution of the turbulence intensity 41
4.3.2 Wavenumber decomposition 42
4.3.3 Transition energy thresholds 45
4.4 Turbulent state 46
4.4.1 Statistics and energy budget 48
4.4.2 Energy spectrum comparison 50
4.4.3 Automatic forcing amplitude control 52
4.5 Conclusions 53

5 Controlling transition with superhydrophobic surfaces **57**
5.1 Governing equations 57
5.1.1 Linear Stability Analysis (LSA) 58
5.1.2 Direct Numerical Simulations 60
5.2 Transition triggered by modal mechanisms 60
5.2.1 Supercritical case: TS waves 61
5.2.2 Subcritical case: K-type transition 61
5.3 Transition triggered by nonmodal mechanisms 71
5.3.1 Optimal perturbations 71
5.3.2 Uncontrolled transition 74
5.4 Summary and conclusions 76

6 Influence of SHS Modelling on K-type transition **79**
6.1 Problem formulation 80
6.1.1 Modelling Underwater SuperHydrophobic Surfaces 80
6.1.2 Simulation parameters 82
6.2 Influence of Surface Modelling onto Linear Stability 84
6.3 K-type transition 88
6.3.1 Coherent structures and preliminary qualitative observations 90
6.3.2 Fourier harmonics 94
6.3.3 Vorticity dynamics 95
6.3.4 Generation of coherent structures 102
6.4 Summary and perspectives 104

7 Conclusions **107**
7.1 Overall Conclusions 107
7.2 Perspectives 108

A Derivation of Mean and Turbulent Kinetic Energy balance equations 111
A.1 MKE derivation 111
A.2 TKE derivation 113

B Numerical validation of chapter 5 115

C Fully turbulent channel flow over superhydrophobic substrates: influence of surface modellings 117

D Validation of DNS over deformable free-surfaces modelled with ALE approach 119

E Nek5000 subroutines for Robin boundary condition 121

List of Figures

1.1 (a) Scanning electron micrograph depicting a drop of liquid mercury onto the epidermal surface of a *colocasia esculenta*, demonstrating the Lotus-Effect. Bar = $50\mu m$, from Barthlott and Neinhuis (1997). (b) Sketch of a water drop onto a textured surface. Contact angles of $\theta \approx\geq 120$ denotes superhydorphobic surfaces (Rothstein, 2010). An example of natural superhydrophobic surface is depicted in figure 7.1 2

1.2 Sketch of a channel flow with submerged SuperHydrophobic Surfaces, depicting the length-scales gap between the overlying laminar-turbulent *macroscopic* flow (H) and the near-wall, capillary driven *microscopic* free-surface dynamics (L) 6

1.3 Sketch of a transitional flow over a flat plate. Depending onto the intensity of perturbations in the external free-stream, measured with the quantity Tu which is introduced in chapter 4, path to transition can follow different routes. (a) Sketch of low-intensity, K-type like transition scenario, with the characteristic succession of TS-waves, λ and hairpin vortices, widely discussed in chapters 5 and 6. (b) Representation of transition triggered by uncontrolled, higher intensity perturbation, typically identified by transient energy growth and the onset of streamwise velocity modulation (streaks), introduced in chapter 4. 7

1.4 Sketch depicting K-type transition occurring over a superhydrophobic surface. Snapshots represents a DNS where both spatial heterogeneity and free-surface dynamics have been taken into account. The typical succession of TS-like waves ($t = 28$), λ ($t = 135$) and hairpin vortices ($t = 150$) up to the breakdown to turbulence ($t = 200$), identified as isosurfaces of the λ_2 criterion, is somehow influenced by the dynamics of the moving interface, shifted sideways for sake of visualization. Re_τ, introduced in chapter 5, measure the friction within the channel, and indicates the onset of turbulence. For more details the reader is referred to chapter 6. 11

4.1 Some typical optimal forcings/responses for Plane Poiseuille Flow (PPF) with $\alpha = 1, \beta = 0.25, Re = 2000$, for various forcing frequencies ω: $\omega = \alpha U/3$ (upper frames), $\omega = \alpha 2\alpha U/3$ (middle frames), and $\omega = \alpha U$ (bottom frames), triggering A-modes (viscous T-S modes), S-modes (critical layer modes) and P-modes (inviscid modes), respectively. From left to right the boxes represents the optimal forcing $\tilde{\boldsymbol{f}}^{opt}$, the optimal response $\tilde{\boldsymbol{u}}^{opt}$, the resolvent norm $R(\omega)$ highlighted as a circle, and the eigenspectrum λ_i^{eig} of $\boldsymbol{L}$. The forcing and response vectors are built as a linear composition of the system's eigenvectors following equation 4.9, whose weights are proportional to the sizes the markers. 32

4.2 Sketch depicting the **F-type** forcing method detailed in algorithm 1, aiming to build a forcing which ensures a velocity perturbation field reaching Tu^{linear}. 35

4.3 Orr-Sommerfeld spectra of plane Poiseuille flow for $Re = 5000, \beta = 0$ and different values of α provided in the legend. The spectra widens as the streamwise wavenumber is increased. This physically means that shorter streamwise wavelengths can be linked to higher forcing frequencies. For this computation we have used a pseudo-spectral Chebyshev collocation method with numerical resolution of 256 points in the y direction. 37

4.4 Graphical summary of section 4.1.3. Diamonds and circles represent the spatial and temporal wavenumbers taken into account for building up the synthetic volume forcing. 37

4.5 Time evolution of turbulent intensity extracted from a linearised DNS forced by the F-type method with $Tu^{linear} = 0.01$, $\boldsymbol{u}(\boldsymbol{x}, t = 0) = \boldsymbol{0}$, and for different N_ω and $N_{\alpha,\beta} = 4$ as indicated in the legend. The prescribed turbulence intensity Tu^{linear} is attained after a finite *rising time*, when the transient behaviour has left place to an asymptotic regime. 39

4.6 Same as in figure 4.5, but with $\boldsymbol{u}(\boldsymbol{x}, t = 0) = \boldsymbol{u}_{opt}$. Differently from figure 4.5, the flow immediately settles to the asymptotic regime, without any rising time. 39

4.7 Energy spectra of the forcing (blue solid line) and associated response obtained by DNS (purple solid line) and by the resolvent analysis (dashed line) with $N_{\alpha,\beta} = 1$, $(\alpha = 1.12, \beta = 0.0)$, $N_\omega = 8$, and $[\omega_{min}, \omega_{max}] \approx [0.747, 1.120]$. 40

4.8 Energy spectra extracted from several DNS using different values of N_ω. The dashed line represents the target energy spectra prescribed for constructing the F-type forcing. 40

4.9 Energy spectra extracted from a fully developed turbulent channel flow $Re_\tau = 210$, used as target energy spectra for constructing a F-type forcing. The method, that for this test has been constrained to be deployed within a forcing range $[\omega_{min}, \omega_{max}] = [1/3, 2]$ for sake of visualisation, can accurately mimic the signature of a turbulent flow, as well as the FST for the flow over a flat plate. Here we have used $N_\omega = 64$ and $N_{\alpha,\beta} = 4$. 41

4.10 Time evolution of Tu measured in different nonlinear DNS where the F-type forcing has been imposed at different target energies Tu^{linear} indicated in the legend. 42

4.11 Uncontrolled transition scenario obtained with the F-type method. Boxes a), b), c) and d) depict the isosurfaces of the streamwise component of the forcing (top), the streamwise velocity perturbation u (middle) as well as the isosurfaces of the λ_2 criterion to visualise the onset of coherent vortical structures. The snapshots are extracted from a DNS of a 3D transitional channel flow with $Tu^{linear} = 0.5\%, N_\omega = 64, N_{\alpha,\beta} = 4$, for $t = 25, 75, 130, 215$, respectively; the lower plot represents the friction Reynolds number Re_τ (see equation (4.29)), which indicates whether transition has taken place. Only the lower half of the channel is displayed for sake of clarity. 43

4.12 Energy density of selected Fourier components (i_α, i_β) for different values of Tu^{linear}. Subframe (a) is a phase portrait representing the evolution of the first two streamwise-invariant modes generated by the non-linear interactions, usually referred as *streaks* (Schmid and Henningson, 2001), for different values of Tu^{linear}. Subframes (b,c,d) show the emergence of the streaky modes from the forced background noise. Depending on the forcing energy levels, several flow behaviours are observed, from laminar to turbulent (see figure 4.10). 44

4.13 Energy density of selected Fourier modes (i_α, i_β) for a DNS with initial condition composed by random Stokes modes (N-type transition) as computed by Reddy et al. (1998) (left frame) and for the F-type forcing method (right frame) both for $Re = 5000$. The energy of the initial perturbation for the N-type transition is $||\boldsymbol{u}(t=0)||_E \approx 2e^{-4}$. The forcing intensity for the F-type method has been set so that the induced velocity field attains the same energy value. Even though the velocity fields induced by the F-type method are initially devoid of $\alpha = 0$ modes, these modes rapidly grow in amplitude overtaking the other ones, as also observed in the N-type transition 45

4.14 Time evolution of Tu during the initial phases of transition for the F-type method and for white noise perturbations. $Tu^{linear} = 0.05\%$ is used for the F-type method, while the initial random noise has been scaled in order to reach $Tu(t=0) = 0.05\%$ as well. The Tu growth in the initial phase is almost linear for the F-type method. 45

4.15 Time evolution of Re_τ for the standard K-type transition scenario (Schlatter et al., 2009) (dashed line) and the F-type forcing method for several forcing levels (continuous lines coloured by the imposed Tu^{linear} value). 46

4.16 Threshold energy densities for triggering transition using the synthetic forcing method proposed here (F-type) and for several transition scenarios (Reddy et al., 1998) where different velocity fields are used as initial condition, namely Tollmien-Schlichting waves (TS), random noise (N), streamwise vortices (SV) and oblique waves (OW). 47

4.17 Threshold energy densities for triggering transition of the imposed forcing as well as the resulting velocity perturbations, $||\boldsymbol{f}||_E$ and $||\boldsymbol{u}||_E$, whose amplitude is scaled by the resolvent norm R. The slope of the $||\boldsymbol{u}||_E$ and $||\boldsymbol{f}||_E$ lines differs since the resolvent norm R increases with Re 47

4.18 Comparison of mean flow and Reynolds stresses extracted by fully turbulent DNS for a classical K-type (Schlatter et al., 2004) transition scenario as well as the F-type forcing method. 49

4.19 Sketch of the global energy balance in a channel flow. Arrow widths are proportional to the corresponding values, except F_p that is scaled by a factor of 1000 for the sake of visualization and exists only if a volume forcing is used. Energy is initially pumped into the flow via the $U_b\tau_w$ term. One part is dissipated by the mean flow (D_u), the rest is transferred to the fluctuations via the production term of the turbulent kinetic energy P_{uv}, which eventually coincides with the turbulent dissipation ϵ. The F-type method creates an additional sink-source energy F_p, but its effect turns out to be negligible. . . 49

4.20 Turbulent Kinetic Energy Decomposition plots. Labels are defined in A. . . 50

4.21 Comparison of the streamwise velocity one-dimensional turbulent energy spectra E_{uu} for $\Re_\tau = 210$ at $y = 0$ (midplane) for the K-type, F-type, and F-type with Controlled Forcing Amplitude (F-CFA) method, as discussed in section 4.4.3, as well as for the MKM benchmark literature case at $Re_\tau = 180$ from Moser et al. (1999). The spectrum recovered with the F-type method slightly deviates from the expected result, as a result of the presence of the volume forcing. This behaviour can be avoided by simply switching the forcing off as explained in section 4.4.3, resulting in the F-type with Controlled Forcing Amplitude case. The slight misalignment between the spectra obtained from the present computations (K-type, F-type and F-CFA) and the reference case is due to the fact that the former are computed for $Re_\tau = 210$, while the latter for $Re_\tau = 180$. 51

4.22 Re_τ time signals and spectra for K-type (blue line), F-type (light blue line) and F-type with interrupted forcing (F-CFA, green line) methods. Spurious energy peaks in the F-type method occur within the same range of the forcing used to trigger transition, as indicated by the vertical lines in the right frame. If the forcing is turned off (for $t > 500$ as indicated by the vertical line in the left frame), these spurious energy peaks disappear. K-type related data are shifted by a factor of 5000 for sake of readability. 51

4.23 Transition in a channel flow at $Re = 5000$ using F-type method with Controlled Forcing Amplitude (F-CFA). The forcing amplitude Δ_F continuously decreases as the friction Reynolds number increases, finally reaching a zero value when Re_τ attains the turbulent plateau. 53

4.24 Uncontrolled transition scenario, obtained with the F-type with Controlled Forcing Amplitude method. Boxes a), b), c) and d) depict the isosurfaces of the streamwise component of the forcing (top) and response (bottom) within the 3D transitional channel flow, for $t = 110, 140, 150, 180$, respectively; the lower plot represents the turbulent intensity Tu as well as the automatic forcing amplitude control intensity Δ_F in time. It can be clearly seen that, when turbulent conditions are attained, the forcing shuts off automatically. In this computation $Tu^{linear} = 0.5\%, N_\omega = 64, N_{\alpha,\beta} = 4$. Hairpin-like structures can be visualised in the λ_2-criterion surfaces during the late stages of transition, see b) and c). Only the lower half of the channel is displayed for sake of clarity. 54

4.25 Controlled amplitude F-type transition method for a *low* Reynolds number, $Re = 1250$. The forcing intensity is the lowest one for which a transitional behaviour can be observed: $Tu^{linear} = 0.7\%$. Forcing is activated intermittently to keep a turbulent state. 55

5.1 Sketch of a channel flow with submerged SuperHydrophobic Surfaces, depicting the near-wall, capillary driven *microscopic* free-surface dynamics as well as its modelling using a slip condition with slip length L_s. 58

5.2 Linear stability and transient growth analyses for different values of L_s: neutral curve for linear stability for $\beta = 0$ (a) and optimal energy gain in the $\alpha - \beta$ plane for $Re = 1000$ (b), both in perfect match with Min and Kim (2005). The slip length strongly affects the time asymptotic behaviour, while being ineffective in controlling finite-time dynamics, as shown by the unmodified contours of the optimal transient energy growth. Contours in subplot (b) are related to the same values of L_s reported in subplot (a). The values of the isocontours in subplot (b), from outer to inner, correspond to $G^{Opt}_{max} = [110, 120, 130, \ldots, 180, 190, 200]$. 60

5.3 Influence of SHS on the supercritical transition path at $Re = 10000$. Simulations have been initialised with the most unstable eigenvector of $\boldsymbol{L}$, with initial perturbation kinetic energy density equal to $E(t) = 10^{-5}$, for different slip lengths L_s. Dashed lines represent the exponential energy growth predicted by the linear theory, for both considered slip lengths. 62

5.4 Time evolution of the instantaneous wall shear normalised by its laminar value in a standard K-type transition scenario as in equation (5.9). Referring to the no-slip case ($L_s = 0.0$), with SHS transition to turbulence can be retarded ($L_s = 0.01$) or even avoided ($L_s = 0.02$). The symbols L^V_s are validations with respect to the case 3 from Min and Kim (2005). 63

5.5 Time evolution of the friction Reynolds number Re_τ, for the modified K-type transition scenario (equation (5.10)) and different slip lengths. Differently from the case in figure 5.4 transition occurs even for $L_s = 0.02$. 64

5.6 Overview of the K-type transition over superhydrophobic surfaces with different slip lengths. For each slip length, snapshots extracted at different times are placed one next to the other in order to provide an overall view of transition. The time values are reported on the black lines separating the snapshots. The iso-surfaces show the λ_2 criterion, coloured by its distance from the wall, and the iso-contours represent the streamwise velocity measured at the lower wall, shifted in the spanwise direction for visualisation issues. Only the lower channel half is showed for the sake of visualisation. . 66

5.7 Time evolution of the energy associated to (1,0), (1,1) and (0,2) Fourier modes during K-type transition for different values of L_s. While the 2D and 3D TS waves, respectively identified by modes (1,0) and (1,1) evolve in a similar way in all cases, for the $L_s = 0.02$ case streaks ((0,2) modes) dominate the flow evolution for a large time range, leading to a consistent delay in transition. 67

5.8 Streamwise and spanwise vorticity averaged along the homogeneous directions $x - z$, $\langle\omega_x\rangle, \langle\omega_z\rangle$ in subplots x.a and x.b, respectively. Subplots x.c show the time evolution of the friction Reynolds number Re_τ, coloured by the spanwise deformation amplitude A_s. Plots are arranged in columns according to the L_s to which they belong. 68

5.9 First row: contours of the streamwise velocity disturbances averaged onto the $x - z$ plane ($\langle u\rangle$). Second row: contours of the uv product measuring Q2 and Q4 events averaged onto wall-parallel planes ($\langle uv\rangle$). Third row: time evolution of the spanwise amplitude deformation A_s, coloured by the friction coefficient C_f. Each column is associated to a given slip length, $L_s = 0.00, 0.01, 0.02$ from left to right. 69

5.10 Upper row: contours of the logarithm of the probability density function of the wall-normal and streamwise velocity disturbances in a $u - v$ plane ($w = 0$) averaged in the wall-parallel planes in the region $0 < y < 1$. Values of the logarithm of the PDF have been normalized with respect to the total number of points of the computational domain. Bottom row: profiles of the positive/negative (u^+/u^-) streamwise velocity disturbances, averaged on the $x - z$ planes. For each computed L_s, arranged in columns, we plot the data at time T so that the $Re_\tau(T) = 1.1 \cdot Re_\tau(t = 0)$, at the beginning of the non-linear phase. 70

5.11 Wall-normal integral of the averaged spanwise and streamwise components of vorticity for different slip lengths. A scaled time $t^* = t/t(Re_\tau = 1.1 \cdot Re_\tau(t = 0))$ has been used for the sake of visualization. 72

5.12 Isosurfaces of λ_2 (red, on the left) and ω_z, ω_x (blue, green, on the right) during K-type transition over a no-slip ($L_s = 0.00$) wall at different times indicated in the plot: $\lambda_2 = -0.001, \omega_z = 2.0$ for $t = 90$; $\lambda_2 = -0.02, \omega_x = 0.8, \omega_z = 3.0$ for the other snapshots. Isosurfaces are coloured with their wall-normal location (darker is closer to the wall). Straight lines highlights the exponential growth of ω_x, indicating the vorticity stretching phase (Malm et al., 2011). 72

5.13 Isosurfaces of $\lambda_2 = -0.001$ (red, on the left) and $\omega_z = 1.475, \omega_x = 1.0$ (blue, green, on the right) during K-type transition over a no-slip wall for $T = 90$ and increasing slip. Whilst spanwise vortices arising from the weakly non-linear interaction of TS waves phase appear to remain substantially unchanged, ω_z is strongly reduced by the introduction of a slip length. . . 73

5.14 Integrals of the spanwise vorticity equation (5.17) terms, for $t = 40$ and different slip lengths L_s. Terms $(A_z, T_{zx}, T_{zy}, S_{zz})$ have been scaled by a factor of $(10^{-2}, 10^{-1}, 10^{-3}, 10^{-3})$, respectively, for the sake of visualization. 73

5.15 (a) Time evolution of the kinetic energy density of the velocity perturbation during laminar-turbulent transitions triggered by linear optimal perturbations, for a no-slip wall ($L_s = 0.00$) and for two prescribed values of the initial energy, $E(t = 0) = 10^{-6}$ and $E(t = 0) = 10^{-5}$ (thick solid lines coloured by the value of A_s). The dashed lines indicate the energy growth as predicted by the linear theory for the two imposed initial energy levels. (b) Isocontours of the streamwise velocity perturbation in a $z - y$ plane for the case with $E(t = 0) = 10^{-6}$ at $t = 150$ showing the highly deformed nonlinearly saturated streaks. (c) Isocontours of the streamwise velocity perturbation in a $z - y$ plane for the case with $E(t = 0) = 10^{-5}$ at $t = 380$. In both (b) and (c) cases, the velocity field is invariant in the streamwise direction, therefore any x-normal plane will provide the same data. 75

5.16 Influence of SHS on subcritical transition at $Re = 5000$ triggered by linear optimal perturbations. Both subfigures represent the same dataset. In a) the energy gain evolution is represented to highlight the initial linear phases, whereas in b) the energy is plotted, for two initial energy levels and two slip lengths indicated in the legend. The dashed lines indicate the energy growth as predicted by the linear theory for the two imposed initial energy levels. . 75

5.17 Streamwise velocity perturbation measured at $T = 150$ in a DNS initialized with the optimal perturbation having initial energy $E(t) = 10^{-5}$ for two slip lengths. The non-linear streaks observed in the no-slip case ($L_s = 0.0$, subplot 5.15.c) match those developing onto a slippery surface with $L_s = 0.02$. 76

5.18 Time evolution of the friction Reynolds number Re_τ and of the energy of three selected Fourier modes for channel flow with different slip lengths undergoing F-type transition. The process is completely unaffected by the increase in slip length L_s. 77

5.19 Overview of F-type transition over superhydrophobic surfaces. As in figure 5.6 snapshots depict the isosurfaces of the λ_2 criterion and streamwise velocity at the wall for different values of the slip length L_s. This *uncontrolled* scenario, characterised by the onset of streaky velocity perturbations occurring in the flow bulk, appears to be completely unaffected by the introduction of a slippery boundary. 78

6.1 Sketch of a channel flow with Superhydrophobic Surfaces, depicting the length-scales gap between the overlying laminar-turbulent *macroscopic* flow (H) and the near-wall, capillary driven *microscopic* free-surface dynamics (L) 80

6.2 Equivalent boundary conditions for modelling the influence of Underwater SuperHydrophobic surfaces. 82

6.3 (a) Eigenspectra of the linearized Navier-Stokes operator for a channel flow enclosed with superhydrophobic surfaces at $Re = 5000$. Using a spatially homogeneous slip length for modelling SHS allows for the use of a 1D local approach, where $\alpha = 1.0, \beta = 0.0$. Employing a spatially heterogeneous slip/no-slip one (SNS) requires for the use of a Global framework. (b) Norm of the streamwise component associated to the most unstable eigenvalue represented in (a). Despite the radically different framework employed and surface modelling employed, we recover in both case the same eigenmode, which represent the Tollmien-Schlichting wave equivalent for superhydrophobic surfaces. Mode obtained using SNS modelling has been averaged in wall-parallel directions so to make the comparison with the HSL case easier. 86

6.4 (a) Streamwise velocity isocontours of the leading unstable mode computed for SNS superhydrophobic surfaces using the global stability analysis framework, on top of the streamwise velocity at the boundary. It appears clear that the lenghtscale associated to the spatial heterogeneity L is much smaller than the one of TS waves. Spatial heterogeneity does not interact with overlying structures, despite the closeness of TS waves to the wall. (b) Evolution of the leading unstable modes, computed for HSL and SNS modelled hydrophobic surfaces, together with the 3D base flow deformation U_d introduced in 6.12. Looking at the maximum and minimum mode amplitude at the wall for SNS we can immediately recognise the influence of the heterogeneous boundary condition slip (shear free, $\partial U/\partial y = 0$ and no slip $U = 0$). On the other hand spatial heterogeneity rapidly fades out further from the wall, as indicated by the U_d profile. 3D modes are coloured by their normalised distance from the wall $|y|$ in (a), while $A(y)$ represents the streamwise velocity component for each quantity plotted in (b). 87

6.5 Trace of the evolution of wall-normal velocity in a fixed point of the domain, measured during DNS. A, B, C lines represents computations performed for DNS onto HSL, SNS and MVB modelled surfaces respectively, but all of them initialized adding on top of their respective base flows the TS 2D wave computed from the 1D local framework using HSL approach. After a short initial transient, in all three cases we recover the dynamics predicted from the linear stability framework. 88

6.6 Temporal evolution of the friction Reynolds number Re_τ, measured during laminar turbulent K-type triggered transition over no slip (PPF) walls, as well as onto spatially homogeneous (HSL), spatially heterogeneous (SNS) and deformable (MVB) modelled superhydrophobic surfaces. While Re_τ measured during the laminar and turbulent regimes is the same for the three models, the transition process is strongly affected by the different SHS modelling 90

6.7 Overview of K-type triggered laminar-turbulent transition over smooth, no slip wall (PPF), as well as variously modelled superhydrophobic surfaces (HSL, SNS, MVB). For each configuration, snapshots extracted at different times are placed one next to the other in order to provide an overall view of transition. The time values are reported on the black lines separating the snapshots. The iso-surfaces show the λ_2 criterion (Jeong and Hussain, 1995), coloured by its distance from the wall, and the iso-contours represent the streamwise velocity measured at the lower wall, shifted in the spanwise direction for visualisation issues. Only the lower channel half is showed for the sake of visualisation. 92

6.8 Evolution of streamwise velocity U and wall-normal velocity V at the boundary, as well as interface deformation η, measured during K-type triggered transition over MVB modelled underwater superhydrophobic surfaces. The onset of coherent structures during transition leaves a characteristic footprint on the interface, producing wall-normal velocities at the wall that are synchronised with the overlying dynamics. This behaviour is kept until the late stages of transition ($t = 140$), while the interface dynamics during the turbulent regime qualitatively resembles the one found by Seo et al. (2017) for SHS having the same texture size. On top of textured microposts $U = V = 0$, leaving a characteristic pattern onto the presented slices. 93

6.9 Time evolution of the energy associated to (1,0), (1,1) and (0,2) Fourier modes during K-type transition over no-slip (PPF) and SHS surfaces (HSL, SNS, MVB). The initial linear and weakly non-linear stages of transition do not seem to be affected by the introduction of superhydrophobic surfaces. Besides a temporal shift, the late stages of transition appears to be qualitatively identical, suggesting that following the energy evolution mode by mode is not suitable to study the fully non-linear stages of the transition process. 94

6.10 (a,c,e) Selected Snapshots from figure 6.7 depicting the coherent structures and the underlying interface dynamics occurring onto MVB modelled surfaces during transition. (b,d,f) Power spectral density of the Fourier harmonics of the wall-normal velocity at the deformable interface. Long wavelengths $(k_x, k_z) = (1, 0)$ are associated to the deformation produced by the overlying coherent structures, while short ones $(k_x, k_z) = (28, 28)$ to the characteristic size of the textured superhydrophobic surface L. Their ratio is high enough so that they do not interfere with each other during transition ($t = 130, 145$). When fully developed turbulent state is achieved the PSD spectra becomes much noisier (f), but one can still recognise the wavelengths accounting for the highest intensities. 96

6.11 Streamwise and spanwise vorticity averaged along the homogeneous directions $x - z$, $\langle \omega_x \rangle, \langle \omega_z \rangle$ in subplots x.a and x.b, respectively. Subplots x.c show the time evolution of the friction Reynolds number Re_τ, coloured by the spanwise deformation amplitude A_s. Plots are arranged in columns according to the surface modelling to which they belong. SNS results matches the observations made for HSL modelled superhydrophobic surfaces, and are reported in chapter 5. 97

6.12 Wall normal integral of the averaged spanwise component of vorticity. Notice the early plateau obtained in the benchmark PPF case, representing the saturation of TS-like spanwise vortices and their development into characteristic Λ vortices (Malm et al., 2011) 99

6.13 Integrals of the spanwise vorticity equation (5.16) terms, for $t = 40$ and different surface modellings. Each term has been normalised with respect to the SNSs counterpart, so to enhance their variation. 99

6.14 Wall normal integral of the averaged streamwise component of vorticity. Notice the exponential growth obtained in the benchmark PPF case, marking the development of characteristic Λ vortices (Malm et al., 2011) 100

6.15 Streamwise component of vorticity close to the wall for $t = 40$, averaged along the wall-parallel directions. High vorticity intensities measured for SNS and MVB cases are due to the presence of tiny vortices at the wall, generated by the slip/no-slip discontinuity used to spatially discretize the surface texture. These peaks rapidly fades out far from the wall, and do not affect the dynamics of the bulk flow. The streamwise velocity profile of a TS wave is reported as a reference of the typical wall-normal distance for the overlying structures occurring during transition. TS profile has been rescaled so that its maximum is 0.01, so to facilitate the comparison with ω_x profiles. 101

6.16 First row: contours of the streamwise velocity disturbances averaged onto the x-z plane ($\langle U \rangle$). Second row: contours of the $U'V'$ product measuring Q2 and Q4 events averaged onto wall-parallel planes ($\langle U'V' \rangle$). Third row: time evolution of the spanwise amplitude deformation A_s, coloured by the friction coefficient C_f. Each column is associated to a given surface modelling. Results for SNS matches the ones for HSL, which are reported in chapter 5 102

6.17 Sketch based on data from PPF simulation at $t = 108$. -0.02 isosurfaces of the λ_2-criterion, depicting a Λ-vortex, characterised by ω_x vorticity, just after the formation of a primary hairpin arch, indicated with ω_z, and right before the development of a secondary arch. Dash-dotted line represent the rotation axis of the coherent structure, curved arrows its rotational sense, and $Q4, Q2$ annotations the key areas for sweep-ejection events. Notice how the hairpin legs, formerly Λ-vortices, produce an outward transport of mass 103

6.18 Sketch based on data from MVB simulation at $t = 108$. -0.02 isosurfaces of the λ_2 criterion on top of the deformable U-SHS surface. Upward interface displacement is related to strong ejections (Q_2), producing ω_z vortices similar to the ones of hairpin-heads but without their typical legs. Streamwise vortices (not streaks) are measured on top of negative deformations of the MVB modelled surface. These latter, to which is associated most of the sweeping events (Q_4), have a rotation sense that is opposite to the one of the hairpin-like legs. Rotation axis are qualitatively indicated with a dash-dotted line. 104

7.1 The author posing with a Lotus Flower plant. Notice the water drop onto the large leaf. Silvery areas that can be seen in transparence are due to light reflection on the gas-water interface. 110

B.1 (a) Mean velocity profiles compared with the ones for $Re_\tau = 180$ (Min and Kim, 2004). The discrepancy derives from the fact that our turbulent states arise from transition made at a constant flow rate. (b) Same mean velocity profiles as in a), now compared with shifted-turbulent boundary layer model (Fukagata et al., 2006), for the different obtained Re_τ. 116

B.2 Reynolds stresses in wall scaling for different L_s. From top to bottom $\langle uu \rangle^{1/2}/u_\tau$, $\langle ww \rangle^{1/2}/u_\tau$, $\langle vv \rangle^{1/2}/u_\tau$, $\langle uv \rangle/u_\tau^2$. Open circles represents the values computed for $L_s = 0.0$ (no-slip wall) by Schlatter (2005) at $Re_\tau \approx 210$. 116

C.1 (a) Mean velocity profiles for statistically converged turbulen flows. Standard no-slip condition provides $Re_\tau = 210$, and is compared with Min and Kim (2004). Provided that flow is kept constant during all transitional simulations, slippery SHS provides a lower friction, resulting in $Re_\tau \approx 190$. For this reason we compare our profiles with the ones obtained using the S-TBL model C.1. (b) Reynolds stresses in wall scaling for different surfaces. From top to bottom $\langle U'U' \rangle$, $\langle W'W' \rangle$, $\langle V'V' \rangle$ and $\langle U'V' \rangle$. 118

D.1 Evolution in time of the interface location, for a watertable flow configuration. Solid lines represents the reference solution obtained using the 1D local framework as well as dashed lines represents the numerical results obtained with the DNS having ALE modelled gas-liquid free interfaces. (a) Interface location in time in the range ($t = 0 - 0.2$), from blue to yellow. (b) Trace of the peak point of the wall-normal velocity, normalised by its initial intensity. 120

List of Tables

4.1 Lower and upper bounds for the spatial (left) and temporal (right) wavenumbers of the optimal forcing fields used for constructing the desired volume forcing. 36

6.1 Simulation parameters. Superhydrophobic surfaces capable of withstanding wetting transition while supporting a turbulent flow requires for $L^+ \approx 20$, therefore the spatial discretization arising from heterogeneous models (SNS, MVB) overwhelms the one needed to accurately compute the turbulent state over a smooth, spatially homogeneous (PPF, HSL) surfaces, as shown by Seo and Mani (2016). 84

Chapter 1

Introduction

3 OUT OF THE 4 STATES OF MATTER KNOWN ARE FLUIDS: liquids, gases and plasmas are ubiquitous, and their motion is studied by a branch of Physics called Fluid Dynamics. Pioneer of modern fluid-dynamics, Osborne Reynolds in 1883 has been amongst the first to focus onto the different regimes a flow can pursue, and most importantly, he identified the key physical parameters involved in the *transition* process from one state to another. His experimental apparatus consisted of straight pipes immersed in a water-tank. Using a trumpet mouthpiece he managed to provide an undisturbed inlet to the tubes, while injecting a streak of highly coloured water so to track the flow evolution. He found that when velocities were sufficiently low, the injected streak of colour extended in a steady straight line. This is one of the key feature of laminar flows, where the motion of each fluid particle follows well predictable, streamlined, layered paths (Latin *lamina*: layer). Increasing the flow velocity he noticed that the coloured streaks tended to become unsteady, oscillating and suddenly breaking-up, causing the colour to mix with surrounding water, filling all the tube. Employing the intermittent light of an electric spark he remarked that, despite appearing homogeneous, this stage was instead characterised by a disordered, chaotic motion, with the coexistence of swirly and fluctuating eddies. What he witnessed was the *transition* process leading to a fully developed *turbulent* flow, which he attributed to an imbalance between viscous and inertial forces. He introduced what is now known as the Reynolds number Re which, accounting for this ratio, characterises the behaviour a flow.

While laminar flows are generally associated to slow, viscosity dominated dynamics, turbulent ones are those most commonly found in almost all technical applications. Flow around an aircraft wing or a sail, or that inside an engine or an oil duct, ocean waves onto a shore or the stream within a windfarm, are all characterized by a turbulent motion, which has the important drawback of a drag increase with respect to laminar conditions. Drag is the resistance to motion experienced by a fluid flowing on a surface, generated by the difference in velocity between the solid object and the fluid. The larger the drag, the larger the forces (and the costs) to keep the fluid and the body in relative motion.

Drag reduction in wall bounded flows has been pursued in the last decades through the introduction of many passive and active flow control means. Focusing on passive flow control, many researchers have taken inspiration from Nature to engineer bio-mimetic surfaces allowing to reduce friction at the wall.

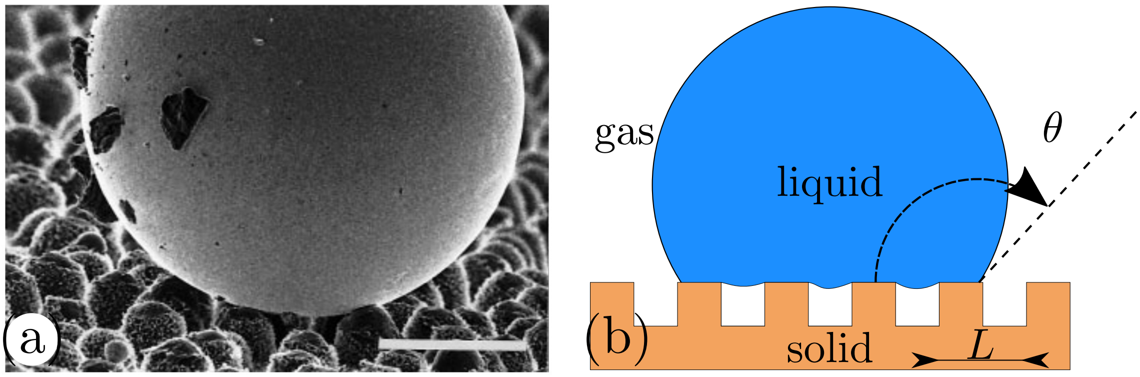

Figure 1.1 – (a) Scanning electron micrograph depicting a drop of liquid mercury onto the epidermal surface of a *colocasia esculenta*, demonstrating the Lotus-Effect. Bar $= 50\mu m$, from Barthlott and Neinhuis (1997). (b) Sketch of a water drop onto a textured surface. Contact angles of $\theta \approx\geq 120$ denotes superhydorphobic surfaces (Rothstein, 2010). An example of natural superhydrophobic surface is depicted in figure 7.1

.

1.1 State of the art

Taking inspiration from the Nelumbo nucifera, the *Lotus* flower, researchers have recently started to engineer highly water repellent solid substrates, called SuperHydrophobic Surfaces (SHS) (Barthlott et al., 2017). The nanostructure of the Lotus leaves is composed of a hierarchical structure which, trapping air underneath falling water droplets owing to capillary forces, reduces the wetting by limiting direct contact of the liquid with the solid substrate, see sketch in figure 1.1.

The renewed self-cleaning property of Lotus leaves, where water droplets rolls at the slightest incline (Schellenberger et al., 2016) collecting all solid impurities (Barthlott and Neinhuis, 1997), is due to the low air to water viscosity ratio ($\mu_{air}/\mu_{water} \approx 2\%$). SuperHydrophobic Surfaces engineered on the basis of Lotus leaves are capable of trapping gas pockets within the micro-roughnesses on their surfaces by means of capillary forces when submerged by a liquid. When the flow conditions allow to maintain this *non-wetted* (Cassie and Baxter, 1944) state, the overlying liquid flow is only partially in contact with the solid substrate as well as partially sustained by the underlying mattress of trapped gas bubbles (plastron) with the overall effect of lubricating the overlying liquid flow. In recent years, a number of experimental works have studied the effect of superhydrophobic surfaces on wall-bounded flows, starting from laminar microchannels (Ou et al., 2004; Byun et al., 2008; Schäffel et al., 2016) towards fully turbulent channel and boundary layer flows (Daniello et al., 2009; Zhang et al., 2016; Rosenberg et al., 2016; Gose et al., 2018).

Ou et al. (2004) have been amongst the first to experimentally demonstrate the potential of submerged superhydrophobic surfaces for reducing drag in laminar flows. Through μPIV measurements they have found resulting slip velocities greater than 60% of the average velocity measured at the wall, as well as a parabolic velocity profile, confirming the previous analytical results obtained by Philip (1972), the first to theoretically study this kind of flows. Starting from this seminal work, a number of successive experimental works have provided an increasingly better understanding of the influence of submerged superhydrophobic surfaces in laminar flows. At first focusing on their capacity in providing some sort of slip (Truesdell et al., 2006; Tsai et al., 2009; Lee and Kim, 2009) in channel and Taylor-Couette flows, researchers have addressed their attention to SHS's capability of retaining their lubricating features (Byun et al., 2008; Lee and Kim, 2011; Xu et al., 2014; Xiang et al., 2017), they have studied their liquid-lubricant dynamics (Schellenberger et al., 2016; Liu et al., 2016) and even measured the flow field within the nano sculptures characterising them (Schäffel et al., 2016). At the same time, numerous analytical and numerical studies have been carried out. Ybert et al. (2007) have proposed scaling laws so that complex textured superhydrophobic surfaces could be modelled as a single spatially homogeneous partial slip, considered a major result for researchers working both in laminar and turbulent flows (Seo et al., 2015), as indicated in the following. In fact, studies onto wetting stability (Emami et al., 2013) and drag reduction (Davies et al., 2006; Haase et al., 2016; Li et al., 2017; Alinovi and Bottaro, 2018) in the laminar regime report a drag reduction up to 40%, depending on the amount of slip a superhydroprobic surface can provide. This quantity has been found to scale approximately linearly with the texture size up to the point where capillary forces are capable of robustly retain the lubricating gas layer (Lee et al., 2016). These encouraging findings have promoted the interest of using such gas-lubricated surfaces so to reduce drag also in fully turbulent flows. Gogte et al. (2005) have been the first to the author knowledge to report turbulent drag reduction using superhydrophobic surfaces. They managed to obtain a 18% drag reduction onto an hydrofoil coated with randomly dispersed superhydrophobic coating. In the following years researchers have been capable to further decrease drag (Henoch et al., 2006; Daniello et al., 2009; Jung and Bhushan, 2009), up to the latest work of Gose et al. (2018) who attained a 90% drag reduction. Altering the behaviour of the turbulence inner scale (Ling et al., 2016; Rowin et al., 2017, 2018), superhydrophobic surfaces have demonstrated their potential in reducing turbulent drag in a number of flow configurations, spanning from channel flows (Daniello et al., 2009), boundary layers (Gose et al., 2018) up to the Taylor-Couette flow (Srinivasan et al., 2015). Numerical simulations of turbulent flows over superhydrophobic surfaces as well have extensively increased in accuracy, thereby enabling to provide a better understanding of the key physical mechanisms involved in the drag reduction observed in experiments. Min and Kim (2004) have been amongst the first to study the behaviour of a flow in a channel enclosed with superhydrophobic surfaces, again modelled as a spatially homogeneous partial slip boundary condition (Navier, 1823; Ybert et al., 2007) so to reduce the numerical cost of each simulation. For a constant flow rate mass, they showed that streamwise slip can reduce skin-friction, whereas spanwise slip can increase drag, altering the mean velocity profiles. A model for skin friction of turbulent flows over SHS has been first presented by Fukagata et al. (2006), then successively improved by Busse and Sandham (2012) and Seo and Mani (2016) so to take into account more complex surface patterns. Only more recently Seo and Mani (2016) and Fairhall and García-Mayoral (2018) have proven the accuracy of spatially homogeneous modellings to predict the performance of SHSs. In fact these latter studies rely on the a priori assumption that the scales of the overlying turbulent flows are large compared to the size of the rough surface texture (Bechert and Bartenwerfer, 1989). In other words, this modelling is reliable only in the 'vanishingly small' textures (Fairhall et al., 2018), therefore providing only a limited amount of slip. In fact while increasing texture size would provides larger slips, their characteristic length could match the one of the overlying turbulent structures, invalidating the previous assumption and requiring for the explicit resolution of the SHS rough texture (Martell et al., 2010; Park et al., 2013; Rastegari and Akhavan, 2015; Seo et al., 2015). Even if these spatially refined simulations account for the size of the surface roughness, the dynamics of the gas-water free-interface is generally neglected. Only more recently Seo et al. (2017) carried out a comprehensive study taking into account its influence. They observed the onset of flow-induced capillary waves and provided a new criterion to determine the robustness of air-water interfaces, therefore enabling an accurate design of superhydrophobic surfaces capable of withstanding wetting transition while providing drag reduction. In fact numerous experiments have shown that the larger the surface texture, the higher the possibility for the gas layer depletion to occur, producing an increase in drag up to 90% (Gose et al., 2018). This behaviour is due to the *wetting* transition, and while mastering this phenomenon is crucial for real world application, multiphase-fully-resolved turbulent simulations capable of capturing the triple-point dynamics have still not been reported in literature.

Regarding the influence of superhydrophobic surfaces in controlling the laminar-turbulent transition process, only few studies are available up to date, the majority of which focusing onto its initial linear stages. The first linear stability analysis of a channel flow with superhydrophobic walls modelled with a spatially homogeneous Robin boundary condition have been reported by Min and Kim (2005), who found that introducing slip stabilises the Tollmien-Schlichting waves. This effect was attributed to the shear reduction, and similar results have been found accounting for anisotropic surfaces (Pralits et al., 2017; Alinovi, 2018). In 2D, local stability analysis have been carried out by Donati (2015); Yu et al. (2016) onto streamwise homogeneous configurations. A global stability analysis has been carried out for the flow over a bluff body by Auteri et al. (2016), who have attributed the flow stabilisation to a shear reduction.

The study by Min and Kim (2005) represents to the authors knowledge the only work showing the influence of superhydrophobic surfaces in controlling the whole laminar-turbulent process. They have shown that transition delayed further for increasing slip lengths but apart from this promising result, no details on the transition process has been provided in that pioneering 4 pages letter. The aim of the present thesis is to extend the work of Min and Kim (2005), trying to shed some light onto the physical mechanism involved in this transition delay, by means of both qualitative and quantitative observations. The effectiveness of SHS in delaying the onset of turbulence is tested for various transition scenarios. The influence of the different characteristic features of superhydrophpbic surfaces is explored using increasingly accurate modelling where, relaxing a priori assumptions, we take into account for additional physical features.

1.2 Controlling the laminar-turbulent transition process with superhydrophobic surfaces

Tackling this problem with numerical tools requires some modelling; since the viscosity of a gas is usually negligible comparing to that of a liquid, and conjecturing that the gas-liquid surface will remain constantly flat, it is generally agreed that this surface can be modelled by a flat wall characterised by alternating no-slip and shear-free zones, as discussed, to cite a few, by Ybert et al. (2007); Martell et al. (2009); Jelly et al. (2014); Rastegari and Akhavan (2015).

Even though such approximations allow for the use of the single phase, incompressible Navier-Stokes equations, accurate simulations remains computationally demanding (Seo and Mani, 2016). In fact, to study these configurations one has to solve both the *macroscopic* laminar-turbulent *bulk* flow having the scale of the channel half-height H, as well as the *microscopic* dynamics at the scale of the texture roughnesses, L, as depicted in the sketch of figure 1.2, where x, y, z represent the streamwise, wall-normal and spanwise directions respectively. Whilst for laminar flows in microchannels at low Reynolds number the H/L ratio is of order ≈ 10 (Byun et al., 2008), it can easily reach ≈ 1000 when a fully developed turbulent flow at large Reynolds number is considered (Daniello et al., 2009; Zhang et al., 2016; Rowin et al., 2017), considerably increasing the computational cost of the problem.

For both laminar (Tretheway and Meinhart, 2002; Choi et al., 2003; Ou et al., 2004) and turbulent flows (Daniello et al., 2009; Seo and Mani, 2016; Rosenberg et al., 2016) it has been found that these alternating, spatially heterogeneous slip/no-slip boundary condition patterns can be effectively modelled via an equivalent spatially homogeneous Robin boundary condition:

$$u_s = L_s \frac{\partial u}{\partial n}, \text{ and } w_s = L_s \frac{\partial w}{\partial n} \tag{1.1}$$

where $[u_s, w_s]$ and $\partial[u, w]/\partial n$ are the slip velocity and the shear rate at the wall, while L_s denotes the slip length, as sketched in figure 5.1. While a number of studies take into account anisotropic patterns (Min and Kim, 2004; Aghdam and Ricco, 2016; Pralits et al., 2017), the simplest approach is that of considering surfaces that are statistically homogeneous in all wall-parallel directions, therefore allowing for the use of a single isotropic slip length L_s which, together with a standard non permeable assumption ($v = 0$) will constitute the framework of a part of the present work. This approach, similar to that recently proposed by Zampogna et al. (2019) for rough walls, allows for a huge reduction of the computational cost of a Direct Numerical Simulation (DNS) of channel flow: Seo and Mani (2016) have recently shown that a DNS using heterogeneous slip/no-slip boundary conditions would need a 12 times more refined computational grid compared to an equivalent computation using a homogeneous slip boundary condition. Recent Direct Numerical Simulations of turbulent flows over spatially heterogeneous boundary conditions, resolved up to the scale of the texture roughness (Seo and Mani, 2016) have confirmed the trend found in experiments for both laminar (Ou et al., 2004; Choi et al., 2003) and turbulent regimes (Daniello et al., 2009; Zhang et al., 2015, 2016), as well as the theoretical predictions by Fukagata et al. (2006); Seo and Mani (2018). Given the texture geometry, in most flow conditions the slip length L_s is linearly dependent on the texture characteristic size L. Since L_s scales (mostly) linearly with L (Rastegari and Akhavan, 2015), one would be tempted to increase the texture size to obtain higher drag reduction. However, for roughness of very large characteristic size, the high shear and pressure fluctuations will induce gas bubble depletion, resulting in a *wetted* (Wenzel, 1936) state, resulting in an overall increase of the drag (Zhang et al., 2016; Gose et al., 2018; Seo et al., 2017), despite the large value of the slip length theoretically expected.

While the influence of superhydrophobic surfaces as a mean of passive flow control has been extensively studied in laminar and turbulent regimes, to the authors knowledge only one study has by now focused on the impact of SHS onto the transition process. Using homogeneous slip boundary conditions, Min and Kim (2005) investigated the effect of the imposed slip length on a specific transition path, the K-type scenario (Zang and Krist, 1989). They showed that in this particular case transition can be delayed by using a slippery boundary condition, but they did not explain how and why this effect is achieved nor they investigate which physical mechanism is inhibited or damped by the presence of a superhydrophobic surface. This point is particularly interesting and worth to be investigated since it can potentially provide the key for avoiding transition in specific flow conditions, leading to a considerable drop of the drag. Moreover, since the laminar-turbulent transition path is strongly dependent on the initial disturbances affecting the flow, it still remains to be investigated in which flow conditions transition delay, and the consequent drag reduction, can be actually achieved.

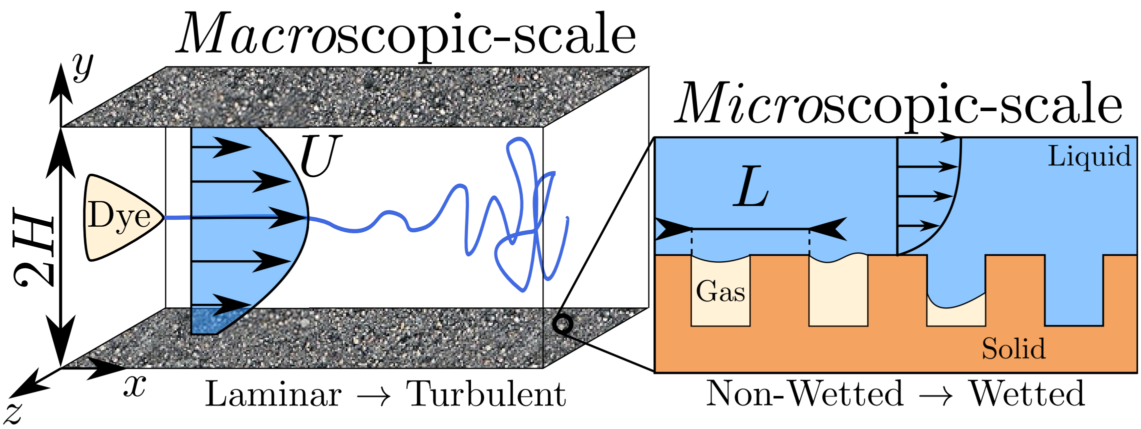

Figure 1.2 – Sketch of a channel flow with submerged SuperHydrophobic Surfaces, depicting the length-scales gap between the overlying laminar-turbulent *macroscopic* flow (H) and the near-wall, capillary driven *microscopic* free-surface dynamics (L)

In this framework, chapter 5 focuses on how SHSs affect the laminar to turbulent process in a channel flow for a number of different transition scenarios. Direct Numerical Simulations with homogeneous slip conditions are used in order to make a direct validation with the available literature results (Min and Kim, 2005) as well as for keeping the computational cost sufficiently low (Zang and Krist, 1989). Standard transition scenarios (K-type, optimal) have been considered, as well as uncontrolled transition, whose modelling has been the object of one of the chapters of this work.

1.3 Triggering *uncontrolled* transition in channel flow numerical simulations

While procedures for triggering controlled transitions in numerical simulations of a temporal channel flow has been introduced already in the eighties (Zang and Krist, 1989), at the present day a theoretical-numerical framework to properly trigger *uncontrolled* transition as a consequence of the flow receptivity to external noise is still missing. This is not the case of semi-open configurations such as the boundary layer for which, noisy velocity perturbations can be easily added at the *free-stream* so to trigger receptivity of the underlying boundary layer, thus resulting in different transition scenarios depending onto the intensity of these external disturbances (Brandt et al., 2004a), as depicted in figure 1.3.

Differently from boundary layers, channel flows are not characterized by any freestream region, where a statistically homogeneous flow in the wall-normal direction can be retrieved. Therefore, uncontrolled transition is often triggered by using noisy velocity perturbations, although producing an initial non-physical transient behaviour, which can be detrimental when studying laminar-turbulent transition. Many techniques have been already developed to ensure a fully turbulent state when solving numerically the Navier-Stokes equations (Wu, 2017), such as the recycling inflow (Lund et al., 1998), the synthetic eddy (Jarrin et al., 2006) or the random Fourier method (Kraichnan, 1970). These approaches rely on ad-hoc inlet boundary conditions which are maintained during the course of the simulation, affecting the flow up to considerable distances downstream of it before reaching a fully turbulent regime. For this reason, these techniques are ill-suited for studying laminar-turbulent transition, since the footprints of these inlet conditions strongly affect the transition process. Differently from fully-developed turbulent flows which are charac-

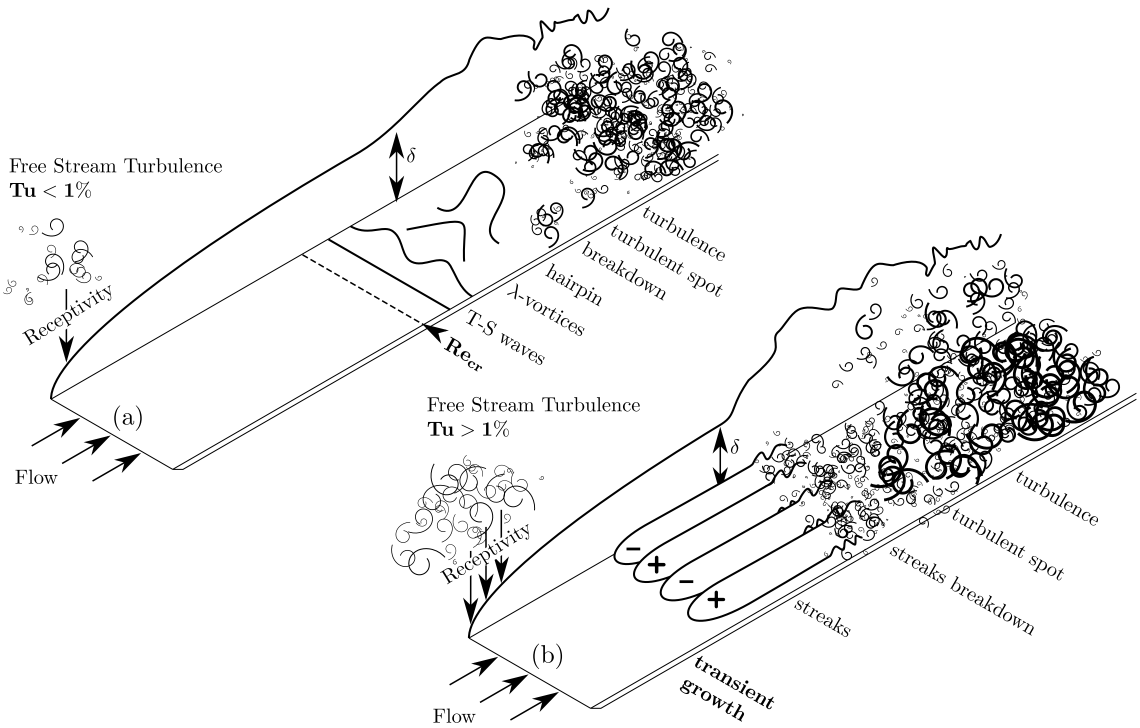

Figure 1.3 – Sketch of a transitional flow over a flat plate. Depending onto the intensity of perturbations in the external free-stream, measured with the quantity Tu which is introduced in chapter 4, path to transition can follow different routes. (a) Sketch of low-intensity, K-type like transition scenario, with the characteristic succession of TS-waves, λ and hairpin vortices, widely discussed in chapters 5 and 6. (b) Representation of transition triggered by uncontrolled, higher intensity perturbation, typically identified by transient energy growth and the onset of streamwise velocity modulation (streaks), introduced in chapter 4.

terized by time-decorrelated properties (Pope, 2000), the main features of transitional flows are strictly dependent on initial and boundary conditions, each imposed condition leading to a specific *transition path* which relies on different physical mechanisms (Kachanov, 1994b). For this reason, transition scenarios are classified depending on the nature of the initial and boundary conditions from which they stem: deterministic transition scenarios, that usually occur under *controlled* (laboratory) conditions, and stochastic ones, typical of *uncontrolled* configurations. The first class of transition paths is based on mechanisms that are well understood on a theoretical basis (Schlichting and Gersten, 2017) including notably the *K-type*, *H-type* (Sayadi et al., 2013b), Oblique Waves (OW) (Berlin et al., 1994), and Streamwise Vortices (SV) (Hoepffner et al., 2005) scenarios, to cite a few. Being mostly based on linear mechanisms at least in their early phases, they are quite easy to reproduce numerically although difficult to observe experimentally due to the low level of background noise requested (Klebanoff et al., 1962b). On the other hand, when noise levels are sufficiently high, transition can occur *bypassing* some phases of linear growth of the disturbances, leading more rapidly to breakdown as a consequence of non-linear effects. This second class of transition paths, despite currently occurring in experiments in uncontrolled environments (Kendall, 1998; Matsubara and Alfredsson, 2001), is challenging to reproduce numerically. For boundary-layer flows, the Free-Stream Turbulence (FST) typically occurring in experiments can be reproduced numerically by ad-hoc inlet boundary conditions using a numerical method introduced by Brandt et al. (2004b); Jacobs and Durbin (2001b). This method, which has been specifically designed for wall-bounded open flows (namely, the flow over a flat plate), relies on the idea of injecting at the inlet of the numerical domain a velocity perturbation which accurately models the main features of free-stream turbulence, such as spectrum, turbulence intensity, and integral length scale. Due to the receptivity of the boundary layer, this disturbance will trigger transition downstream of the inlet, similarly to what happens in an experimental setup in the presence of grids. Numerically, this *synthetic FST* is constructed as a weighted sum of eigenmodes of the continuous branch of the Orr-Sommerfeld and Squire operator (Jacobs and Durbin, 2001b), with wavenumbers and associated amplitudes suitably chosen to satisfy a prescribed energy spectrum (Brandt et al., 2004b) in the homogeneous area outside the boundary layer. Using these methods, uncontrolled transition to turbulence in boundary-layer flows has been extensively studied (Elder, 1960; Wu et al., 2014; Lee and Zaki, 2015) and compared to controlled scenarios (Klebanoff, 1955; Berlin et al., 1999; Sayadi et al., 2013b; Berlin et al., 1999; Schlatter et al., 2009), producing a rich body of literature (Morkovin, 1994; Kachanov, 1994b). On the other hand, in wall-bounded parallel flows such as the channel flow, although controlled transition has been long studied (Zang and Krist, 1989; Sandham and Kleiser, 1992b; Lee and Zaki, 2017) (also due to the relatively low computational cost as compared to spatially evolving flows (Kleiser and Zang, 1991)), a little body of literature is available to the authors knowledge regarding uncontrolled transition. In fact, the presence of streamwise-periodic boundary conditions and the lack of a *free-stream* prevent the use of synthetic FST to induce uncontrolled transition in numerical experiments, which in most cases is triggered using noisy velocity fields built as a random superposition of Stokes modes (Reddy et al., 1998). However, despite being less studied, uncontrolled transition is far more common than controlled one, especially considering the fact that it usually occurs in subcritical conditions, namely for values of the Reynolds number lower than the critical linear one. Thus, new methods for numerically triggering this type of transition are worth to be introduced in the literature.

Towards this aim, we propose a new method to trigger turbulence in a streamwise-periodic shear flow using a synthetic forcing appropriately constructed on the basis of an optimal forcing analysis, so to mimick the *uncontrolled* transition scenario. We present and discuss this method in chapter 4, where we design a method for triggering transition in a channel flow via response to a suitably constructed noisy perturbation mimicking those typically observed in uncontrolled transition. Due to the streamwise periodicity of the flow, this perturbation cannot be injected at the domain inlet, but it should be introduced in the Navier-Stokes equations as a forcing, in the same way as it is done for plasma actuators (Mullenix et al., 2013). In many recent works (Klein et al., 2017; Schmidt and Breuer, 2017), volume forcing is used to trigger turbulence in numerical simulations. Differently from these works, the method we propose is not specifically designed to efficiently obtain a turbulent state, but to induce uncontrolled transition in closed wall-bounded flows through receptivity of the flow to external disturbances, as it would occur in an experimental facility. In other words, the method proposed here intends to provide a numerical tool to trigger in a physically accurate way transition to turbulence, at the same time avoiding to impose a continuous forcing to sustain a constant turbulence level, as it usually occurs in unbounded flows (Klein et al., 2017).

In order to construct a perturbation able to trigger a large-amplitude response in the flow as a consequence of receptivity, we have chosen to use as a basis a set of harmonic disturbances that maximise (within a linear framework) the flow response for different given frequencies (Schmid and Henningson, 2001; Schmid, 2007). The usefulness of the optimal response to harmonic forcing, mediated by the resolvent operator, for constructing simple models reproducing key statistical and structural descriptions of wall turbulence, has been proven by many recent works (see Moarref et al. (2014); Sharma et al. (2017) among others). The synthetic noisy volume forcing is then constructed as a linear composition of these *optimal* volume forcings issued from resolvent analysis, suitably weighted in order to respect a chosen energy spectrum.

1.4 Modelling superhydrophobic surfaces: influence of microstructure size and gas-water free-surface dynamics

Under certain conditions SHS can retain gas bubbles trapped within their roughness even when fully submerged in water (Cassie and Baxter, 1944), offering a form of passive control in hydrodynamic flow (Lee and Kim, 2011). In fact, unlike active control methods (Ceccio, 2010), SHS have already proven the potential of reducing drag in a number of applications by providing lubricating air layer (plastron) without the need of any external energy output (Daniello et al., 2009; Castagna et al., 2018), acting as a slippery boundary and reducing skin friction for the overlying hydrodynamic flow (Rothstein, 2010).

Barrier to the real world application of SHS is the depletion of the lubricating gas layer. Whilst on one hand one would be tempted to attain higher slip by increasing the texture size, as theoretically predicted both in laminar (Ybert et al., 2007) and turbulent (Seo and Mani, 2016) flows, air-water interfaces becomes less stable, and the *wetting* transition would be more likely to occur. Following the depletion of the gas bubbles, the liquid fills the roughness elements (Wenzel, 1936), transforming the SHS into a wetted, drag-increasing rough surface (Zhang et al., 2016; Ling et al., 2016; Gose et al., 2018). It is nowadays well known that a number of different causes could affect the plastron stability in laminar flows (Wexler et al., 2015; Patankar, 2016), but only recently Seo et al. (2015, 2017) have quantified physical mechanism involved in the failure of a SHS supporting fully developed turbulent flows. The "boundary map for stable superhydroprobic surface design" proposed by Seo et al. (2017) suggests that with the maximum texture size (L_c^+) for *wetting-stable* gas-infused surface, drag reduction in a realistic superhydrophobic surface would be approximately less than 30%. This prediction is consistent with the latest experimental observations (Bidkar et al., 2014; Park et al., 2014; Zhang et al., 2015, 2016; Ling et al., 2016; Gose et al., 2018), therefore providing a reliable threshold for realistic use of SHSs in turbulent flows. As a consequence, the typical size of a *wetting stable* SHS roughness is $\mathcal{O} \approx 100$ smaller than the characteristic length of the overlying turbulent flow (Seo et al., 2017). In these conditions the slippery wall does not modify the overlying turbulence dynamics (Fairhall et al., 2018), and the mechanism for drag reduction is akin to the one observed for the flow over riblets (Luchini et al., 1991).

Accurate numerical simulation of the wetting transition, characterised amongst the others by the gas-liquid-solid contact line dynamics, surface tension and liquid-gas diffusion, is an extremely complex task per se, requiring for sophisticated and computationally demanding methods such as free-energy simulations (Lisi et al., 2017), but which are still not adapted for the simulation of high Reynolds number regimes.

Owing to the major impacts in understanding the physical mechanisms involved in designing passive drag control methods, researchers have come up with a number of models in order to study underwater superhydrophobic surfaces, trying to retain most of the physical mechanisms while reducing the computational cost. Here we shortly introduce the most common ones, in decreasing order of complexity.

The first is based onto the assumption that, in order to provide some form of drag reduction, the lubricating plastron layer must be retained within the surface sculptures, hence that the air-water interfaces are securely pinned to the roughness edges (Steinberger et al., 2007; Seo et al., 2015), therefore unconditionally wetting-stable. But even simulating both the multi-scale//multi-phase physics of such flows is still computationally challenging, and the latest available works are limited to the laminar regime (Li et al., 2017; Alinovi and Bottaro, 2018).

To reach the turbulent regime, Seo et al. (2017) have modelled the superhydrophobic surfaces as periodic textures of patterned slip and no-slip boundary conditions on the overlying flow. The gas-liquid interface dynamics is taken into account via a linearised Young-Laplace equation, solved coupled with the overlying turbulent flow. By replacing the air-water surface with an equivalent hyperelastic compliant (Gad-El-Hak et al., 1984; Luhar et al., 2015) yet slippery membrane, Seo et al. (2017) confirmed that the interface fluctuations are very small compared to the overlying flow scales (Martell et al., 2010), and that the free-surface deformation does not alter the mean nor the fluctuations of velocity profiles in turbulent statistics.

This result can be considered, in our opinion, as an *a posteriori* validation of a second modelling, in which gas-liquid interface are assumed to be flat, where the superhydrophobic surface is modelled as an alternation of no-slip–shear-free patterned patches (Martell et al., 2010; Park et al., 2013; Jelly et al., 2014; Rastegari and Akhavan, 2015; Seo et al., 2015, 2017; Fairhall et al., 2018), greatly reducing the complexity and the cost of numerical simulations (Seo et al., 2017).

The third and last approach consist of using a macroscopic, spatially homogeneous Navier (Robin) slip (Navier, 1823) boundary condition

$$u_s = L_s \frac{\partial u}{\partial n}, \tag{1.2}$$

to effectively model the flow over a rough superhydrophobic surface (Zampogna et al., 2019). Here the average velocity on the boundary u_s, called slip velocity, is linked to the mean wall shear by a single constant, the slip length L_s. Seo and Mani (2016) have proven that in the limit of small roughness size the single slip length model provides the same mean and fluctuations that would be measured by using a spatially accurate heterogeneous slip–no-slip boundaries.

Many recent studies have shown the equivalency of these methods in modelling the influence of a SHS drag-reducing wall, both in laminar (Davis and Lauga, 2010; Li et al., 2017) and in turbulent regimes, as long as some key physical constraints are satisfied (Seo and Mani, 2016; Seo et al., 2017). However, while being crucial for any real world application, the in-between laminar-turbulent transitional regime remains at the present day mostly unexplored, except for a single work by Min and Kim (2005).

In chapter 6, we investigate the influence of different SHS modelling onto the benchmark K-type laminar-turbulent transition process (Klebanoff et al., 1962a; Sandham and Kleiser, 1992a; Kachanov, 1994a; Sayadi et al., 2013a) by means of global linear stability analysis and time resolved direct numerical simulations (DNS). We have considered SHS made out of a regular pattern of square posts because of their relevance in studying arbitrary disposed, sprayed-like coatings (Seo and Mani, 2018), and at the same time to dispose of a quantitative comparison of our simulations in the turbulent regime (Seo and Mani, 2016; Seo et al., 2017). Moreover, being spatially isotropic, SHS made out of square post will simplify the modelling process, both when using spatially homogeneous (Min and Kim,

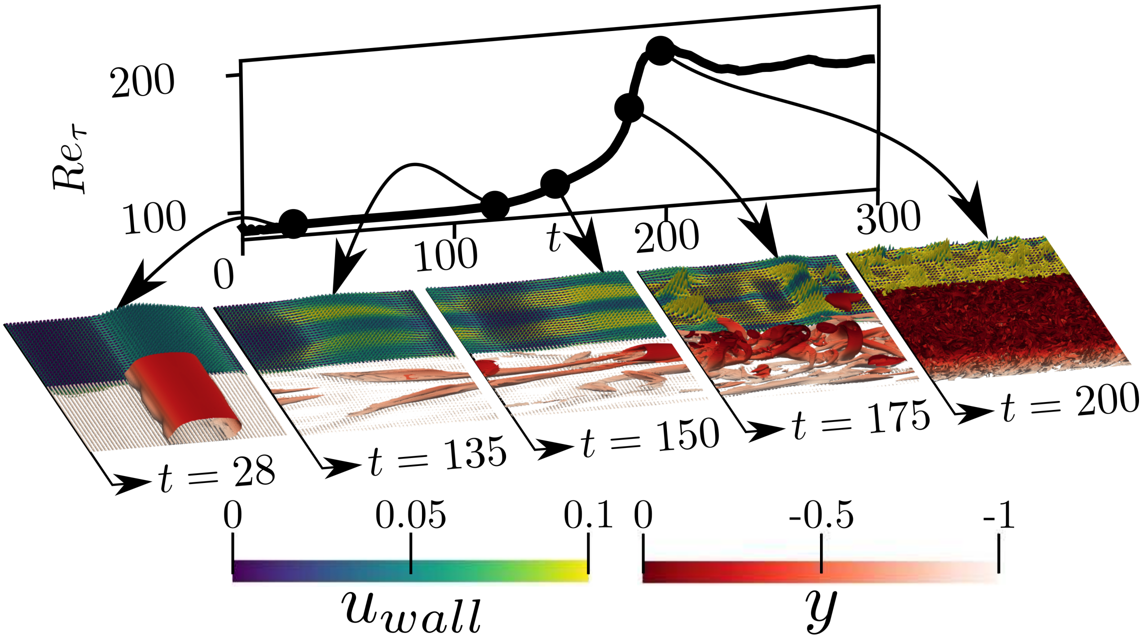

Figure 1.4 – Sketch depicting K-type transition occurring over a superhydrophobic surface. Snapshots represents a DNS where both spatial heterogeneity and free-surface dynamics have been taken into account. The typical succession of TS-like waves ($t = 28$), λ ($t = 135$) and hairpin vortices ($t = 150$) up to the breakdown to turbulence ($t = 200$), identified as isosurfaces of the λ_2 criterion, is somehow influenced by the dynamics of the moving interface, shifted sideways for sake of visualization. Re_τ, introduced in chapter 5, measure the friction within the channel, and indicates the onset of turbulence. For more details the reader is referred to chapter 6.

2004) or heterogeneous equivalent boundary conditions (Seo et al., 2017). Roughness size of the SHS has been selected based on the design principles proposed by Seo et al. (2017), thus small enough to ensure wetting stability while providing the highest possible slip. In chapter 5 we have extended the work of Min and Kim (2005) showing how superhydrophobic walls modelled via a simple Homogeneous Slip Length (HSL) could differently affect transition in a channel flow, depending onto the specific transition scenario one wishes to control. In fact, while being totally ineffective in delaying uncontrolled transitions, dominated by streamwise velocity modulations (streaks)(Jacobs and Durbin, 2001a; Brandt et al., 2003), SHS have proven to be a viable method to delay or even inhibit the onset of turbulence in scenarios characterised by the presence of near-wall structures, such as the K-type transition (Nishioka et al., 1975; Kleiser and Zang, 1991; Schlatter et al., 2006). Reducing the wall shear, the slippery boundary interferes with the development of the coherent structures usually occurring during this specific transition scenario, altering the vortex stretching-tilting processes that produces Λ and hairpin vortices (Malm et al., 2011; Sayadi et al., 2013a). Depending on its performance, namely on the slip it could provide, we showed how SHS inhibits the sweep-ejection process, therefore drastically retarding or even avoiding the breakdown to turbulence.

Objective of chapter 6 is to determine whether more physically accurate models, including spatially heterogeneity as well as the free-surface dynamics, would affect laminar-turbulent transition with respect to the predictions made using a simple equivalent Navier boundary condition. Our aim is to verify the robustness of different SHS modellings in transitional flows, as it has been proven to be the case in both laminar (Ou et al., 2004) and turbulent(Seo and Mani, 2016; Seo et al., 2017) regimes. On the one hand our investigation proves that the size of SHS roughness capable of sustaining wetting transition is so small that it does not interact with the overlying coherent structures occurring during transition, and that the slip provided by these gas-impregnated surfaces can effectively retard the process. On the other we demonstrate that considering the air-water interface deformation introduces a non-zero wall normal velocity on the wall which, despite being small, promotes the ejection mechanism which eventually advances transition. Figure 1.4 depicts the main features observed during K-type triggered transition occurring over superhydrophobic surfaces, such as the deformation of the gas-liquid free-surfaces and its interaction with the overlying coherent structures characterising the process.

To sum up, this thesis addresses the following three main questions:

- How is the laminar-turbulent transition process affected by the use of superhydrophobic surfaces as a mean of passive control?
- Does it depend on the specific transition scenario occurring?
- What are the key physical features to take into account for an accurate modelling of superhydrophobic surfaces in transitional flows?

The objective of this thesis is to give some answers to these questions.

1.5 Organization of the manuscript

In Chapter 2 we introduce the key mathematical notions on which the present work is based, while in Chapter 3 we provide the numerical framework used to carry out our analysis. In chapter 5 we show how superhydrophobic surfaces, modelled as a single spatially homogeneous slip length, can affect the laminar-turbulent transition process. We show that the effectiveness of slippery surfaces in delaying the occurrence of turbulence relies on their capacity to interact with the physical mechanism characteristic of each transition scenario. In Chapter 4 we present a method to trigger *uncontrolled* transition in numerical simulations of a temporal channel flow. Using this purpose-built technique, we show that while being highly effective in controlling deterministic K-type process, superhydrophobic surfaces are ineffective in delaying natural transition. Finally, in chapter 6 we study how including other physical features in the modelling of superhydrophobic surfaces can change our previous findings. Finally, general conclusions and perspectives are provided in chapter 7.

Chapter 2

Mathematical Framework

In this section we introduce the basic concepts for the study of fluid mechanics, along with some of the tools we employ for the analysis of the laminar-to-turbulent transitional regime. We present the notions from the linear stability framework, such as the concepts of base flow, the time asymptotic behaviour of infinitesimal perturbations, the spatial homogeneity and the difference between local and global stability. Also we introduce the concepts of short time dynamics and response to a harmonic forcing.

2.0.1 The Navier-Stokes equations

The Navier-Stokes equations, named after Claude-Louis Navier and George Gabriel Stokes, describe the motion of viscous fluids. They are based on the assumption that the conservation of momentum, arising from Newton's second law applied to the fluid motion, is balanced by *stresses* in the fluid system. If these latter depend linearly on the sum of diffusing viscous term, proportional to the gradient of velocity, and pressure, the fluid is defined as *Newtonian.* When effects such as temperature, fluid velocity with respect to the speed of sound, and the scales of the motion compared to the free patch of atoms are large, most gases and liquids can be considered as incompressible. Under these assumptions the Navier-Stokes equations read as:

$$\frac{\partial \boldsymbol{U}}{\partial t} = -(\boldsymbol{U} \cdot \nabla)\boldsymbol{U} - \nabla P + \frac{1}{Re}\nabla^2 \boldsymbol{U} + \boldsymbol{f} \tag{2.1}$$

$$\nabla \cdot \boldsymbol{U} = 0, \tag{2.2}$$

where $\boldsymbol{U}(\boldsymbol{x}, t)$ and $P(\boldsymbol{x}, t)$ are the velocity and pressure field and Re is the dimensionless Reynolds number characterising the flow, representing the ratio between the inertial and viscous forces occurring within the flow. The first equation is the conservation of momentum while the second one represents the incompressibility constraint. Whilst this set of partial differential equations is well defined mathematically when boundary and initial conditions are defined, the presence of the non-linear term $(\boldsymbol{U} \cdot \nabla)\boldsymbol{U})$ in the momentum conservation has restrained the analytical resolution of these equations to a few configurations. This is still nowadays an open problem; approximate mumerical solution can be obtained discretizing equations (2.1) and (2.2) in space and in time, representing the research field of Computational Fluid Dynamics (CFD). The *numerical* framework employed in this thesis is described in chapter 3.

2.1 Instability Framework

First step to study the departure of an initially laminar flow up to a fully turbulent regime, is to investigate the evolution of perturbations on top of an unperturbed state. If the perturbation decays in time/space, it is said to be stable, while if its amplitude grows asymptotically it is labelled as unstable. These notions, borrowed from the dynamical system framework, are essential for posing the physical and mathematical problems in the following. In general, time-evolving systems such as those governed by equations (2.1) and (2.2) can be written as

$$\frac{\partial \boldsymbol{Q}}{\partial t} = \boldsymbol{\mathcal{F}}(\boldsymbol{Q}), \tag{2.3}$$

where $\boldsymbol{Q} = (\boldsymbol{u}, p)^T$ and $\boldsymbol{\mathcal{F}}$ is a non-linear operator. The state variables can be expressed as:

$$\boldsymbol{Q}(\boldsymbol{x}, t) = \boldsymbol{Q}_b(\boldsymbol{x}) + \boldsymbol{q}(\boldsymbol{x}, t), \tag{2.4}$$

which is to say that $\boldsymbol{Q}$ is sum of a (steady) *base* state $\boldsymbol{Q}_b(\boldsymbol{x})$ plus a time evolving perturbation $\boldsymbol{q}(\boldsymbol{x}, t)$. Substituting (2.4) in (2.3) we obtain:

$$\begin{cases} \dfrac{\partial \boldsymbol{Q}_b}{\partial t} = \mathcal{F}(\boldsymbol{Q}_b) = 0 \\ \dfrac{\partial (\boldsymbol{Q}_b + \boldsymbol{q})}{\partial t} = \mathcal{F}(\boldsymbol{Q}_b + q) \end{cases} \tag{2.5}$$

where the base solution is provided and the perturbation represents the unknown of the problem. At this point the definition of *stability* itself is not unique. Let us assume a system such as that in equation (2.5), evolving on a domain $\mathcal{V}$ and closed with a convenient set of boundary and initial conditions. The norm of the perturbation can be expressed as:

$$||\boldsymbol{Q} - \boldsymbol{Q}_b||(t) = \left[\int_{\mathcal{V}} (\boldsymbol{Q} - \boldsymbol{Q}_b)^2 d\mathcal{V} \right]^{\frac{1}{2}}. \tag{2.6}$$

The base state $\boldsymbol{Q}_b$ is said to be:

- **Lyapunov stable** if: $\forall \epsilon > 0, \exists \delta(\epsilon) > 0$ such that if$||\boldsymbol{Q}(\boldsymbol{x}, 0) - \boldsymbol{Q}_b(\boldsymbol{x}, 0)|| < \delta$ then $||\boldsymbol{Q}(\boldsymbol{x}, t) - \boldsymbol{Q}_b(\boldsymbol{x}, t)|| < \epsilon, \forall t \geq 0$
- **Asymptotically stable** if it is Lyapunov stable and $\lim_{t\to\infty} ||\boldsymbol{Q}(\boldsymbol{x}, t) - \boldsymbol{Q}_b(\boldsymbol{x}, t)|| = 0$
- **Globally unconditionally stable** if it is asymptotically stable $\forall \; ||\boldsymbol{Q}(\boldsymbol{x}, 0) - \boldsymbol{Q}_b(\boldsymbol{x}, 0)|| \Rightarrow \lim_{t\to\infty} ||\boldsymbol{Q}(\boldsymbol{x}, t) - \boldsymbol{Q}_b(\boldsymbol{x}, t)|| = 0$

A base state is conditionally stable when finite amplitude perturbations depart from it asymptotically. On the other hand, focusing onto the evolution of infinitesimal perturbations we are allowed to linearise the governing equations, which represents the fundamental idea behind the linear stability theory framework.

The key physical mechanism involved in the linear instability of wall-bounded shear flows as well as in the first stages of the laminar-turbulent transition process of have been studied during the last century relying onto the linearized framework (Schmid and Henningson, 2001). The present work aims at extending these findings indicating how the linear stability of shear flows is modified if bounded with slippery superhydrophobic surfaces.

2.2 Linear Stability

In the linear stability framework, a base flow Q_b is said to be stable if all perturbations $\boldsymbol{q}$ decay in time/space. To study the evolution of such perturbations, we inject equation

(2.4) in equation (2.3), and linearising around the base state we obtain the general form:

$$\begin{cases} \boldsymbol{B}\dfrac{\partial \boldsymbol{q}}{\partial t} = \boldsymbol{J}\boldsymbol{q} \\ \boldsymbol{q}(\boldsymbol{x}, t=0) = \boldsymbol{q}_0 \\ \boldsymbol{\mathcal{L}}\boldsymbol{q}(\boldsymbol{x}_0, t) = 0 \in \partial\mathcal{D} \end{cases} \tag{2.7}$$

where $\boldsymbol{B}$ is a mass matrix Schmid and Henningson (2001), $\boldsymbol{J}$ is the Jacobian operator, $\boldsymbol{q}_0$ the initial and $\boldsymbol{\mathcal{L}}\boldsymbol{q}(\boldsymbol{x}_0, t)$ the boundary conditions of the problem. Being system (2.7) autonomous in time, we can assume solutions in the form:

$$\boldsymbol{q}(\boldsymbol{x}, t) = \frac{1}{2\pi}\int_{L_\lambda} \hat{\boldsymbol{q}}(\boldsymbol{x}) e^{\lambda t} d\lambda + c.c. \tag{2.8}$$

where $\hat{\boldsymbol{q}}$ is the Fourier-Laplace transform of $\boldsymbol{q}$, *c.c.* denotes the complex conjugation and $\lambda = \sigma + i\omega$ is the complex frequency of the normal mode considered, integrated onto the L_λ path in the complex plane. Injecting (2.8) in (2.7) we obtain the eigenvalue (λ) and eigenvector ($\hat{\boldsymbol{q}}$) problem:

$$\lambda \boldsymbol{B}\hat{\boldsymbol{q}} = \boldsymbol{J}\hat{\boldsymbol{q}}, \tag{2.9}$$

representing the temporal stability of the system itself. To each eigenvector $\hat{\boldsymbol{q}}_i$ is associated an eigenvalue, where $\text{Re}(\lambda_i) = \omega_i$, describes the evolution of its amplitude in time, while oscillating at a frequency $\text{Im}(\lambda_i) = \sigma_i$. If at least one $\sigma_i > 0$, the system is said to be asymptotically unstable, whereas if $\sigma_i < 0 \; \forall i$, it is considered as asymptotically stable. This constitutes the concepts of the linear **Global** stability analysis framework, where no assumption is made on the base state and perturbation spatial distribution, therefore the fully three-dimensional base flow reads $\boldsymbol{U}_b(\boldsymbol{x}) = (U_b(\boldsymbol{x}), V_b(\boldsymbol{x}), W_b(\boldsymbol{x}))^T$. Thus, equation (2.9) can be written as:

$$\begin{cases} \lambda\hat{u} = -U_b\dfrac{\partial \hat{u}}{\partial x} - V_b\dfrac{\partial \hat{u}}{\partial y} - W_b\dfrac{\partial \hat{u}}{\partial z} - \hat{u}\dfrac{\partial U_b}{\partial x} - \hat{v}\dfrac{\partial U_b}{\partial y} - \hat{w}\dfrac{\partial U_b}{\partial z} - \dfrac{\partial \hat{p}}{\partial x} + \dfrac{1}{Re}\Delta\hat{u} \\ \lambda\hat{v} = -U_b\dfrac{\partial \hat{v}}{\partial x} - V_b\dfrac{\partial \hat{v}}{\partial y} - W_b\dfrac{\partial \hat{v}}{\partial z} - \hat{u}\dfrac{\partial V_b}{\partial x} - \hat{v}\dfrac{\partial V_b}{\partial y} - \hat{w}\dfrac{\partial V_b}{\partial z} - \dfrac{\partial \hat{p}}{\partial y} + \dfrac{1}{Re}\Delta\hat{v} \\ \lambda\hat{w} = -U_b\dfrac{\partial \hat{w}}{\partial x} - V_b\dfrac{\partial \hat{w}}{\partial y} - W_b\dfrac{\partial \hat{w}}{\partial z} - \hat{u}\dfrac{\partial W_b}{\partial x} - \hat{v}\dfrac{\partial W_b}{\partial y} - \hat{w}\dfrac{\partial W_b}{\partial z} - \dfrac{\partial \hat{p}}{\partial z} + \dfrac{1}{Re}\Delta\hat{w} \\ \dfrac{\partial \hat{u}}{\partial x} + \dfrac{\partial \hat{v}}{\partial y} + \dfrac{\partial \hat{w}}{\partial z} = 0 \end{cases} \tag{2.10}$$

While being the most general framework available, tackling a global stability problem is still computationally challenging as we will show in chapter 3, and only in the last decades we have been able of obtaining reliable solutions of the eigenvalue problem for fully 3D flows (Loiseau et al., 2014).

On the other hand, taking advantage of spatial homogeneity of the base state, the linear stability of *parallel-flow* (i.e. whose base state has one or more spatially homogeneous directions, such as Couette and Poiseuille flows), have allowed in the past for the resolution of less computationally expensive approaches (Orszag, 1971). Assuming a base state, or base flow, in the form of $\boldsymbol{U}_b = (U_b(y), 0, 0)^T$, the linearised Navier-Stokes equations become homogeneous in the x and z directions, as well as in time. Further expanding the perturbations

$$\boldsymbol{q}(\boldsymbol{x}, t) = \frac{1}{(2\pi)^3}\int_{L_\lambda}\left[\int_{L_\beta}\left(\int_{L_\alpha}\hat{\boldsymbol{q}}(y, \alpha, \beta, \lambda) e^{i(\alpha x + \beta z) + \lambda t} d\alpha\right) d\beta\right] d\lambda + c.c., \tag{2.11}$$

where we have assumed the perturbations to have a sinusoidal form, characterised by a dispersion relation for the streamwise and spanwise wavenumbers, α and β, respectively. This normal modes expansion represents the building block of the **local** stability theory framework. Prescribing perturbations having a prescribed real wavevector $\boldsymbol{k} = \alpha\boldsymbol{x} + \beta\boldsymbol{z}$ is the idea behind the temporal stability analysis framework. Relying on the work of Squire (1933), (2.10) can be reduced to:

$$\begin{cases} \lambda\hat{u} = -\hat{v}\dfrac{\partial U_b}{\partial y} - i\alpha\hat{u}U_b - i\alpha\hat{p} + \dfrac{1}{Re}\left(\dfrac{\partial^2}{\partial y^2} - \alpha^2\right)\hat{u} \\ \lambda\hat{v} = -i\alpha\hat{u}U_b - i\alpha\dfrac{\partial\hat{p}}{\partial y} + \dfrac{1}{Re}\left(\dfrac{\partial^2}{\partial y^2} - \alpha^2\right)\hat{v} \\ i\alpha\hat{u} + \dfrac{\partial\hat{v}}{\partial y} = 0 \end{cases} \tag{2.12}$$

The advantage of this approach is that the eigenproblem (2.9) has now been massively reduced, from 3D to 1D, allowing for inexpensive numerical resolutions. Before concluding this section we would like to stress again that the key difference between global and local stability analysis relies onto the fact that in the latter the flow is homogeneous in one or two spatial directions (for instance, in the direction of mean flow advection for parallel flows). While the most direct consequence relies on the complexity of the base flow studied, one has to take special care about the implications on convective and absolute instability (Huerre and Monkewitz, 1990) too.

2.3 Non-normal operator

Following Squire's theorem (Squire, 1933), the most unstable mode of equation (2.12) is a 2D perturbation, having $\beta = 0$. Using this assumption Orszag (1971) has been the first to accurately determine the critical Reynolds number (Re_c) for a Plane Poiseuille Flow (PPF), namely the one for which at least one eigenvalue has a $\sigma_i > 0$. Whereas $Re_c \approx 5772$, it is well known that transition to turbulence can be observed for way lower values of the Reynolds number, $Re \approx 1000$ (Manneville, 2015). The same can be said about Couette flow, where transition is observed for $Re \approx 350$ (Lundbladh and Johansson, 1991), whilst being unconditionally stable from a linear point of view (Romanov, 1973). This behaviour is not only related to non-linear effects, but also to the non-normality of the $\boldsymbol{J}$ operator (Reddy and Henningson, 1993; Schmid, 2007), which allows a strong transient growth of initially small perturbations triggering non-linearity. Here we report some of the key results arising from the linear non-normal framework. The reader is referred to chapter 4 for more details.

2.3.1 Short time dynamics, optimal perturbations

Let us consider $\boldsymbol{A}$ operator to be the Jacobian operator in a divergence free space, therefore equation (2.7) yields:

$$\frac{\partial \boldsymbol{u}}{\partial t} = \boldsymbol{A}\boldsymbol{u}. \tag{2.13}$$

The evolution of a given velocity field, from time $t = 0$ to a target time T is therefore described by the relation:

$$\boldsymbol{u}_T = \boldsymbol{M}\boldsymbol{u}_0, \tag{2.14}$$

where $\boldsymbol{M}$ is the exponential propagator matrix $e^{\boldsymbol{A}T}$. Our goal is to find the perturbation $\boldsymbol{u}_0$ which maximises the quantity

$$G(T) = \max_{\boldsymbol{u}_0} \frac{E_T}{E_0}, \tag{2.15}$$

called *gain*, representing the ratio between energy increase from time 0 → T, where energy is defined as the inner product $E(t) = \langle \boldsymbol{u}_t, \boldsymbol{u}_t \rangle$. Ratio (2.15) can be recast in:

$$G(T) = \max_{\boldsymbol{u}_0} \frac{E_T}{E_0} = \max_{\boldsymbol{u}_0} \frac{\langle \boldsymbol{u}_T, \boldsymbol{u}_T \rangle}{\langle \boldsymbol{u}_0, \boldsymbol{u}_0 \rangle} = \max_{\boldsymbol{u}_0} \frac{\langle \boldsymbol{M}\boldsymbol{u}_0, \boldsymbol{M}\boldsymbol{u}_0 \rangle}{\langle \boldsymbol{u}_0, \boldsymbol{u}_0 \rangle} = \max_{\boldsymbol{u}_0} \frac{\langle \boldsymbol{M}^+\boldsymbol{M}\boldsymbol{u}_0, \boldsymbol{u}_0 \rangle}{\langle \boldsymbol{u}_0, \boldsymbol{u}_0 \rangle}, \tag{2.16}$$

where $\boldsymbol{M}^+$ is the adjoint operator of $\boldsymbol{M}$, equal to its conjugate transpose (Schmid, 2007). Finding the $\boldsymbol{u}_T$ maximising condition (2.15) consists of solving the *optimal perturbation* problem, and can be written as an eigenvalue problem, yielding:

$$\left(\boldsymbol{M}^+\boldsymbol{M} - \gamma\right) \boldsymbol{u}_0 = 0. \tag{2.17}$$

Matrix $\boldsymbol{M}^+\boldsymbol{M}$ is symmetric and defined positive and the optimal perturbation $\boldsymbol{u}_0$ turns out to be the eigenvector associated to the largest eigenvalue γ. Finally, perturbation $\boldsymbol{u}_T$ at time T is recovered using equation (2.14). Even if the system is linearly stable, yielding that all eigenvectors of $\boldsymbol{A}$ have negative growth rate and each eigenvector decays asymptotically, non-normal interaction of these latter can lead to transient energy growth, eventually producing non-linearities and transition to turbulence. We will cover this specific transition scenario in chapter 5.

2.3.2 Response to harmonic forcing, optimal forcing

Let us suppose our system 2.13 to be forced by a forcing term$\boldsymbol{f}$ leading

$$\frac{\partial \boldsymbol{u}}{\partial t} = \boldsymbol{A}\boldsymbol{u} + \boldsymbol{f}, \tag{2.18}$$

and that this forcing is harmonic in time, namely $\boldsymbol{f} = \hat{\boldsymbol{f}} e^{i\omega t} + c.c.$, with $\omega \in \mathbb{R}$. Its response $\boldsymbol{u}$ it short time dynamics is strictly related to the non-normality of the eigenmodes of $\boldsymbol{A}$ (Schmid, 2007). When system (2.13) is stable, and all eigenmodes of $\boldsymbol{A}$ are stable, its homogeneous solution goes asymptotically to zero, leaving only the particular solutions in the form

$$\boldsymbol{u} = \hat{\boldsymbol{u}} e^{i\omega t} + c.c. \tag{2.19}$$

Injecting (2.19) in (2.18) yields:

$$\hat{u} = \underbrace{(i\omega \boldsymbol{I} - \boldsymbol{A})^{-1}}_{\boldsymbol{R}} \hat{\boldsymbol{f}} \tag{2.20}$$

linking the harmonic forcing $\boldsymbol{f}$ (input) to the system's response $\boldsymbol{u}$ (output), at a fixed ω. Operator $\boldsymbol{R}$ is known as resolvent matrix. Following the same process described in the previous section, we can wonder which is the forcing able to maximize the response, namely $||\hat{\boldsymbol{u}}||^2/||\hat{\boldsymbol{f}}||^2$. Again we can rearrange the previous equation into an eigenvalue problem from which the *optimal forcing* can be obtained (Schmid, 2007). Further details about this optimal forcing analysis as well as its application for triggering transition in closed wall-bounded flows, are presented in chapter 4.

Chapter 3

Numerical Tools

3.1 Introduction to the spectral elements code Nek5000

In the mid-eighties Paul Fischer, Lee Ho, and Einar Rønquist (M.I.T) developed the incompressible fluid flow solver NEKTON, with technical input from A. Patera and Y. Maday. A commercial version was brought to market by Fluent, Inc, as NEKTON 2.0, in 1996. Paul Fischer branched off a research version of the code known as Nek5000. This code was recognized with the Gordon Bell prize for algorithmic quality and sustained parallel performance in 1999. Today, Fischer's code is released as an open source project covering a broad range of applications including thermal hydraulics of reactor cores, transition in vascular flows, ocean current modeling and combustion. More than two dozen research institutions and more than 100 users worldwide are using the code. Leading edge scalability has been demonstrated up to 262144 processors producing more than 170TFlops (Extreme Scaling Workshop 2010 Report)[1]. All the 3D simulations reported in this work have been carried out using NEK5000, a Spectral Element Method (SEM) (Patera, 1984) combining finite elements with spectral methods. The reader is referred to the books of Deville et al. (2002); Canuto et al. (2007). For sake of simplicity the notation used in this section is the same as the one in Deville et al. (2002).

3.1.1 Spatial discretization: spectral elements

In order to be solved numerically, linear and non-linear Navier-Stokes equations are spatially discretized using spectral elements method. These methods share many similarities with the finite elements, as such they are part of the family of approximation schemes based on the Galerkin method, therefore Navier-Stokes equations are solved in their *weak form.* Following the approach suggested by Loiseau et al. (2014), we will introduce the method by applying spectral elements spatial discretization to a simpler case, namely the 1D Burgers equation.

$$\begin{cases} \dfrac{\partial u}{\partial t} + u\dfrac{\partial u}{\partial x} = \nu\dfrac{\partial^2 u}{\partial x^2}, \\ u(t=0,x) = u^0, \\ u(t, x=\mp 1) = \pm 1, \end{cases} \tag{3.1}$$

Computational domain considered is $\Omega := \{x \in [-1,1]\}$. Equation (3.1) is subject to Dirichlet boundary condition (BC) at each end of the domain. Despite its simplicity this partial differential equation contains some of the key ingredients of the Navier-Stokes ones, namely the non-linearity, making it a suitable benchmark for numerical methods.

---

[1] `https://nek5000.mcs.anl.gov/index.php/Main_Page`

3.1.2 Variational formulation and spatial discretization

As mentioned before SEM share many similarities with the Galerkin method. In this framework partial differential equations are solved in their *weak form.* To this end we introduce a set of trial function $v(x)$ belonging to a Sobolov space $\mathcal{H}_0^N(\Omega)$ which, injected in (3.1), provides its weak counterpart:

$$\int_\Omega v\frac{\partial u}{\partial t}dx + \int_\Omega vu\frac{\partial u}{\partial x}dx = -\nu\int_\Omega \frac{\partial v}{\partial x}\frac{\partial u}{\partial x}dx \tag{3.2}$$

If the solution and the test function of the problem are approximated as

$$\begin{cases} u(x,t) = \sum_{i=0}^N \phi_i(x)u_i(t) \\ v(x) = \phi_j(x),\ 0 \leq j \leq N \end{cases} \tag{3.3}$$

it is possible to rewrite the variational problem in the form:

$$\left(\int_\Omega \phi_i\phi_j dx\right)\frac{du_i}{dt} + \left(\int_\Omega \phi_j\phi_i u_i\frac{d\phi_k}{dx}dx\right)u_k = -\left(\nu\int_\Omega \frac{d\phi_j}{dx}\frac{d\phi_i}{dx}dx\right)u_i \tag{3.4}$$

which can be further recast in matrix-vector form:

$$\mathcal{M}\frac{d}{dt}\boldsymbol{u} + \mathcal{C}(\boldsymbol{u})u + \mathcal{K}\boldsymbol{u} = 0 \tag{3.5}$$

with $u = (u_0, \ldots, u_N)^T$, $\mathcal{M}$ the mass matrix, $\mathcal{C}(\boldsymbol{u})$ the convective operator and $\mathcal{K}$ the stiffness matrix. Matrices components are given by:

$$\begin{cases} \mathcal{M}_{ij} = \int_\Omega \phi_i\phi_j dx, \\ \mathcal{C}_{ij}(\boldsymbol{u}) = \int_\Omega \phi_i\phi_j\frac{d\phi_i}{dx}dx, \\ \mathcal{K}_{ij} = \nabla\int_\Omega \frac{d\phi_j}{dx}\frac{d\phi_i}{dx}dx, \end{cases} \tag{3.6}$$

The derivation of the variational form of the Burgers equation is up to this point identical to the one used in standard Galerkin methods. The differences with SEM arise from the different choice of test and trial functions $\phi_i(x)$, namely the selection of the approximation space and basis. In fact while finite elements methods generally relies on uniform spacings, Legendre polynomials are used in SEM, since they can provide the best approximation in the H^N norm (Deville et al., 2002). The domain Ω is discretized into E hexaedral elements. Each one is defined as $\Omega^e := \{\boldsymbol{x}; \boldsymbol{x}_{e-1} < \boldsymbol{x} < \boldsymbol{x}_e\}, 1 \leq e \leq E$, and let $\hat{\Omega} := \{\xi; -1 \leq \xi \leq 1\}$ to be the reference element onto which each element Ω^e is mapped through an affine transformation. Assuming a three-dimensional flow, the discrete velocity in each element Ω^e mapped on the three-dimensional reference element $\hat{\Omega}^3$ can be written as:

$$\boldsymbol{u}\left(\boldsymbol{x}\left(\xi,\zeta,\eta\right)\right)|_{\Omega^e} = \sum_{i=0}^N\sum_{j=0}^N\sum_{k=0}^N \boldsymbol{u}_{i,j,k}^e h_{N,i}(\xi)h_{N,k}(\zeta)h_{N,k}(\eta) \quad (\xi,\zeta,\eta) \in \hat{\Omega} \tag{3.7}$$

where $h_{N,i}, h_{N,j}$ and $h_{N,k}$ are the one-dimensional Nth-order Lagrange interpolants based on the Legendre polynomials, $\boldsymbol{x}$ is a mapping function of the local geometry and $\boldsymbol{u}_{i,j,k}^e$

are the unknown nodal values in Ω^e(Deville et al., 2002). To avoid spurious pressure modes two different quadratures rules are used. Velocity is represented on a $N+1$ Gauss-Lobatto-Legendre (GLL) quadrature, while the pressure on the $N-1$ Gauss-Legendre (GL), resulting in the $\mathrm{P}_N - \mathrm{P}_{N-2}$ formulation. At this point discretizing Burgers equation equations using GLL quadrature rules yields:

$$\boldsymbol{M}\frac{d}{dt}\boldsymbol{u} + \boldsymbol{C}(\boldsymbol{u})\boldsymbol{u} + \boldsymbol{K}\boldsymbol{u} = 0 \tag{3.8}$$

where $\boldsymbol{M}, \boldsymbol{K}$ are the discretised mass matrix, containing the integration weights, and stiffness matrices representing the discrete Laplacian, while $\boldsymbol{C}(\boldsymbol{u})\boldsymbol{u}$ represents the non-linear advection operator evaluated using the convection form. Applying the same procedure to the dimensionless Navier-Stokes equations, using both GLL and GL quadratures, we obtain:

$$\begin{cases} \boldsymbol{M}\dfrac{d}{dt}\boldsymbol{u} = -\boldsymbol{C}(\boldsymbol{u})\boldsymbol{u} - \dfrac{1}{Re}\boldsymbol{K}\boldsymbol{u} + \boldsymbol{D}^T p + \boldsymbol{M}\boldsymbol{f} \\ -\boldsymbol{D}\boldsymbol{u} = 0 \end{cases} \tag{3.9}$$

In addition to the terms already present in equation (3.8), here we have introduced $\boldsymbol{D}$ and $\boldsymbol{D}^T$ representing the divergence and gradient operators. In all the different studies presented in this manuscript we have used a polynomial approximation of order 7, while the number of spectral elements in each direction as well as their spatial distribution has been tuned so to meet the typical requirements for the simulation of a turbulent channel flow, as indicated in the following chapters.

3.1.3 Time discretisation

In Nek5000, linear terms are solved by using stable implicit methods, while the non-symmetric non-linear $\boldsymbol{C}(\boldsymbol{u})\boldsymbol{u}$ term is treated explicitly so to avoid algorithmic difficulties. This results into a peculiar semi-implicit scheme BFD_k/EXT_k: the viscous terms are discretized implicitly using backward differentiation of order k, while the non-linear ones are treated explicitly by extrapolation of order k, where in general $k = 1, 2, 3$. For $k = 3$, the fully discretized Navier-Stokes equation written with the BFD_3/EXT_3 scheme reads as:

$$\begin{aligned} \left(\frac{11}{6\Delta t}\boldsymbol{M} + \boldsymbol{K}\right)\underline{\boldsymbol{u}}^{n+1} - D_i^T \underline{p}^{n+1} = \frac{\boldsymbol{M}}{\Delta t}\left(3\underline{\boldsymbol{u}}^n - \frac{3}{2}\underline{\boldsymbol{u}}^{n-1} + \frac{1}{3}\underline{\boldsymbol{u}}^{n-2}\right) \\ - \left(3\boldsymbol{C}\underline{\boldsymbol{u}}^n - 3\boldsymbol{C}\underline{\boldsymbol{u}}^{n-1} + \boldsymbol{C}\underline{\boldsymbol{u}}^{n-2}\right) + \boldsymbol{M}\underline{\boldsymbol{f}}^n \end{aligned} \tag{3.10}$$

$$-\boldsymbol{D}\underline{\boldsymbol{u}}^{n+1} \tag{3.11}$$

which is solving for the discrete variables $\underline{\boldsymbol{u}}^{n+1}$ and $\underline{p}^{n+1}$ at the time step $n+1$ with a third-order global accuracy (see equation (6.4.22) in Deville et al. (2002)). Equations (3.10) and (3.11) rearranged in matrix form yield:

$$\begin{pmatrix} \boldsymbol{H} & -\boldsymbol{D}^T \\ -\boldsymbol{D} & 0 \end{pmatrix}\begin{pmatrix} \underline{\boldsymbol{u}}^{n+1} \\ \delta\underline{p}^{n+1} \end{pmatrix} = \begin{pmatrix} \boldsymbol{M}\underline{\boldsymbol{f}}^{n+1} + \boldsymbol{D}^T\underline{p}^n \\ 0 \end{pmatrix} \tag{3.12}$$

where $\boldsymbol{D}^T\underline{p}^n$ have been added to both sides to avoid non-vanishing error for steady state solution, function of $\delta\underline{p}^{n+1} = \underline{p}^{n+1} - \underline{p}^n$, which goes to zero for a steady solution (Deville et al., 2002). This matrix problem can be solved using LU decomposition. In order to obtain a solution that is solenoidal, the matrix $\boldsymbol{Q}$ is used to project $\boldsymbol{u}$ on a divergence free space. Therefore the solution to such LU decomposition is a two-step procedure:

$$\begin{pmatrix} \boldsymbol{H} & 0 \\ -\boldsymbol{D} & -\boldsymbol{D}\boldsymbol{Q}^T \end{pmatrix} \begin{pmatrix} \underline{\boldsymbol{u}}^* \\ \delta \underline{p}^{n+1} \end{pmatrix} = \begin{pmatrix} \boldsymbol{M}\underline{\boldsymbol{f}}^{n+1} + \boldsymbol{D}^T \underline{p}^n \\ 0 \end{pmatrix} \tag{3.13}$$

and

$$\begin{pmatrix} \boldsymbol{I} & -\boldsymbol{Q}\boldsymbol{D}^T \\ 0 & \boldsymbol{I} \end{pmatrix} \begin{pmatrix} \underline{\boldsymbol{u}}^{n+1} \\ \delta \underline{p}^{n+1} \end{pmatrix} = \begin{pmatrix} \underline{\boldsymbol{u}}^* \delta \underline{p}^{n+1} \end{pmatrix} \tag{3.14}$$

where the *predicted* velocity field $\underline{\boldsymbol{u}}^*$ is then projected into a divergence-free space up to obtention of the solenoidal field $\underline{\boldsymbol{u}}^{n+1}$. The choice of matrix $\boldsymbol{Q}$ determines which projection method is used. In the present code, the matrix $\boldsymbol{Q}$ is set to be:

$$\boldsymbol{Q} = \boldsymbol{H}^{-1} \tag{3.15}$$

resulting into a Uzawa algorithm. Evaluation of the inverse of the Helmholtz operator $\boldsymbol{H}$ is computationally intense. To overcome this problem, instead of the exact Uzawa algorithm, the Blair-Perot formulation is implemented in NEK5000. The projection matrix then is $\boldsymbol{Q} = \gamma \boldsymbol{M}^{-1}/\Delta t$ (with $\gamma = 11\Delta t/6$ for the BDF_3/EXT_3 scheme). Since the mass matrix $\boldsymbol{M}$ is a diagonal, the computation of its inverse is straightforward. Using the Blair-Perot algorithm a non-zero splitting error is introduced, proportional to $\delta \underline{p}^{n+1}$. This requires for special care when choosing a suitable Δt for the time marching procedure. Extensive details can be found in Deville et al. (2002).

3.2 Boundary conditions

Spatial discretization has to take into account the boundary conditions to complete both the non-linear and linearised Navier-Stokes equations. Two types of boundary conditions are applicable to the fluid velocity in the standard Nek5000 distribution: essential (Dirichlet) and natural (Neumann). In our work we have chosen to use the nonstress formulation, therefore the boundary condition must be homogeneous on the entire fluid element. This will be one of the reasons why the simulation of the flow over superhydrophobic surfaces modelled as a spatial alternation of slip/no-slip patches requires a high number of spectral elements, as indicated in chapter 6.

3.2.1 Robin Boundary Condition

In this work we will present a method to model the presence of a superhydrophobic wall, based on the use of a Robin boundary condition for the wall-parallel velocities, namely:

$$\left(u + L_s^x \frac{\partial u}{\partial y} = 0, \quad w + L_s^z \frac{\partial w}{\partial y} = 0 \right)_{wall} \tag{3.16}$$

which, together with standard, no penetration in the wall normal direction

$$(v = 0)_{wall} \tag{3.17}$$

represents a flow bounded in the wall-normal direction by a slippery spatially homogeneous surface characterised by the scalar slip length $L_s^\bullet$, as introduced in chapter 5. Robin boundary condition for the velocity field is not originally implemented in NEK5000, and in the following we detail the procedure to include such condition. Taking cue from the Newton cooling boundary condition already implemented for the passive scalar within the subroutine BCNEUSC, Robin partial slip for the velocity field is implemented by refitting the $\boldsymbol{H}$ matrix involved in the resolution of the Helmholtz problem. According to equations (3.10) and (3.9), $\boldsymbol{H} = (b_0 \boldsymbol{M}/\Delta t + \boldsymbol{K})$, where $b_0 = 11/6$ for the BFD_3/EXT_3 scheme. Owing to the specific procedure used to ensure a divergence-free field, Helmholtz operator is kept splitted in Nek5000, so that $b_0 \boldsymbol{K}/\Delta t = \boldsymbol{H}_2$ and $-\boldsymbol{K} = \boldsymbol{H}_1$, and these matrices are formed with a call of the routine SETHLM.

Our approach to implement the Robin (ROB) boundary condition has been to tweak the symmetry (SYM) one. Symmetry condition to the velocity field for a $P_N - P_{N-2}$, no-stress formulation are imposed on top of the Helmholtz operator during the call of the subroutine PLAN3, which has been modified to accommodate for the modified $\boldsymbol{H}$.

$\boldsymbol{H}_1$ and $\boldsymbol{H}_2$ operators are formed within PLAN3 with a call to the subroutine SETHLM, after which our modification starts. At this point we compute the additional contribution due to the Robin boundary condition using a newly purpose-built routine. Subroutine BCNEUSC_MOD() is built upon the BCNEUSC one used for imposing the Newton cooling law. It is designed so to find all the boundary elements labelled as 'SYM', and to build a matrix containing the weights that has to be added on top of H2 so to ensure for the prescribed Robin boundary condition. Modified PLAN3 as well as BCNEUSC_MOD are reported in E.1 and E.2 respectively in appendix.

At this point the $\boldsymbol{H}_2$ contribution computed with BCNEUSC_MOD is added on top of the original component of the Helmholtz operator, and we resume to the native code operation.

This implementation is suitable for isotropic slip lengths, provided that the same modified H2 operator is used for both streamwise and spanwise velocity components, during the call to the OPHINV subroutine. For anisotropic slip lengths, it would have been necessary to build up different H2_X and H2_Z using a similar bcneusc_ROB subroutine, and modify the OPHINV so to take into account for the spatial anisotropy. A possible implementation within Nek5000 would require modifying subroutines OPHINV, and is indicated in E.3 and E.4 in the appendix. The advantage of having derived a Robin boundary condition from the SYM one is that the non penetration Dirichlet at the wall is automatically imposed, overwriting the results obtained during the CALL HMHOLTZ('VELY') obtained from the call to OPHINV subroutine. The implementation presented here relies on the fact that wall normal direction is always y. Some further development would be needed in order to extend it to surfaces with any orientation.

3.2.2 Arbitrary Lagrangian-Eulerian Formulations and Free-Surface Flows

In the present work we have studied the influence of different conditions aiming at modelling superhydrophobic surfaces withstanding laminar-turbulent transition in wall bounded flows. Characteristic feature of such surfaces is the presence of gas-liquid interface. In the present work Arbitrary Lagrangian-Eulerian (ALE) implementation has been used so to take into account the interface dynamics, as shown in chapter 6.

3.2.3 Preliminary concepts

In general solid mechanics problems are based on a Lagrangian formulation, while fluid mechanics ones uses an Eulerian approach. In the case of free-surface flows or fluid-structure interaction problems, neither of these two approaches are suitable to describe the ongoing physics due their intrinsic limitations.

In fact in the Eulerian formulation the domain definition is generally fixed. If not, a proper application of the boundary conditions requires for some form of interpolation of the geometry and the condition itself. On the other hand the reference system is attached to material points of the continuous medium when a Lagrangian formulation is employed, which is to say, the domain elements deform with the material. Arbitrary Lagrangian-Eulerian formulations aims at combining these two paradigms, taking the most desirable features from each of them. The idea is that the reference system is not defined a priori, but instead is an unknown of the problem, as well as for the fluid velocity field itself. Here we follow the approach described by Ho (1989), and reported by Deville et al. (2002). First we define as $\boldsymbol{w}(\boldsymbol{x},t)$ the mesh velocity field, which in general is different from the fluid velocity $\boldsymbol{u}(\boldsymbol{x},t)$. $\delta/\delta t$ denotes the time derivative of a fictious particle moving with the mesh at velocity $\boldsymbol{w}(\boldsymbol{x},t)$, and is called ALE derivative. From the definition of material derivative $D\bullet/Dt = \partial\bullet/\partial t + \boldsymbol{u}\cdot\nabla\bullet$, the evolution of a function f becomes:

$$\frac{\delta f}{\delta t} = \frac{\partial f}{\partial t} + \boldsymbol{w}\cdot\nabla f. \tag{3.18}$$

Three configurations are possible:

- — $\boldsymbol{w} = 0$, the mesh is fixed and we recover the Eulerian formulation;
- — $\boldsymbol{w} = \boldsymbol{u}$, the mesh moves as the continuum field, resulting into a Lagrangian Formulation;
- — $\boldsymbol{w} \neq \boldsymbol{u} \neq 0$, and time derivative (3.18) takes into account this variation.

In the following we recall some of the key ingredients of this method, referring the reader to Deville et al. (2002) for further details. Equilibrium of forces acting on a fluid reads as:

$$\frac{d}{dt}\int_{\Omega(t)} \rho\boldsymbol{u}dV = \int_{\partial\Omega(t)} \boldsymbol{t}dS + \int_{\Omega(t)} \rho\boldsymbol{f}dV \tag{3.19}$$

where $\boldsymbol{t}$ accounts for contact forces on the continuum surface (dS) and $\boldsymbol{f}$ for the body forces of the volume (dV), provided a domain $\Omega(t)$. According to Cauchy principle, stress vector $\boldsymbol{t}$ depends on the oriented normal $\boldsymbol{n}$ to the domain $\partial\Omega(t)$ at a given position $\boldsymbol{x}$, yielding:

$$\boldsymbol{t}(\boldsymbol{n}) = \boldsymbol{\sigma}\cdot\boldsymbol{n} \tag{3.20}$$

where in this chapter $\boldsymbol{\sigma}$ denotes the stress tensor, so that $t_i = \sigma_{ij}n_i$ using Einstein notation. Let's study the dynamics at the interface of two fluids, such as water ($\bullet_w$) and air ($\bullet_a$). Equilibrium of forces at the free interface is written as:

$$\boldsymbol{t}_w + \boldsymbol{t}_a = 0, \tag{3.21}$$

which, provided that $\boldsymbol{n}_{water} = -\boldsymbol{n}_{air}$, results in:

$$\boldsymbol{\sigma}_w\boldsymbol{n}_w = \boldsymbol{\sigma}_a\boldsymbol{n}_a. \tag{3.22}$$

We recall that for a Newtonian fluid the frame-indifferent stress tensor reads as

$$\boldsymbol{\sigma} = [-p + \lambda\, Tr\,(\boldsymbol{d})]\,\boldsymbol{I} + 2\mu\boldsymbol{d} \tag{3.23}$$

where λ is the second viscosity, μ the dynamic viscosity and d is the rate-of-deformation tensor, defined as:

$$\boldsymbol{d} = \frac{1}{2}\left[\nabla\boldsymbol{u} + (\nabla\boldsymbol{u})^T\right] \tag{3.24}$$

Considering that the air/water viscosity ratio is ($\mu_{water}/\mu_{air} \approx \mathcal{O}(1000)$), the gas is treated as inviscid, then the interface condition is:

$$(-p_w \boldsymbol{I} + 2\mu \boldsymbol{d}_w)\boldsymbol{n} = -p_a \boldsymbol{n} \tag{3.25}$$

Projecting the latter equation onto the normal $\boldsymbol{n}$ and tangent vector $\boldsymbol{\tau}$ to the free-surface yields:

$$-p_w + 2\mu(\boldsymbol{d}_w \boldsymbol{n}) \cdot \boldsymbol{n} = -p_a, \tag{3.26}$$

$$2\mu(\boldsymbol{d}_w \boldsymbol{n}) \cdot \boldsymbol{\tau}_w = 0. \tag{3.27}$$

For capillary tension dominated phenomena, a generalisation of Laplace law gives:

$$-p_w + 2\mu(\boldsymbol{d}_w \boldsymbol{n}) \cdot \boldsymbol{n} = -p_a - \gamma \left(\frac{1}{R_1} + \frac{1}{R_2} \right) \tag{3.28}$$

where γ denotes the surface tension coefficient and $1/R_1, 1/R_2$ the principal curvatures of the free-surface, thus $(1/R_1 + 1/R_2)$ is double the mean curvature of the surface. The key parameter accounting for the ratio between inertia and surface tension forces is the dimensionless Weber number:

$$We = \frac{\rho U^2 L}{\gamma} \tag{3.29}$$

3.2.4 ALE implementation within NEK5000

Here, we provide a brief description of the procedure developed by Ho (1989) so to implement ALE in within the SEM code NEK5000, employed in the present work so to take into account for the free-surface dynamics characteristic of underwater superhydrophobic surfaces. Being the free-surface a material surface, the resulting kinematic condition for the normal velocity reads as

$$\boldsymbol{w} \cdot \boldsymbol{n} = \boldsymbol{u} \cdot \boldsymbol{n} \tag{3.30}$$

and

$$\boldsymbol{w} \cdot \boldsymbol{\tau} = 0 \tag{3.31}$$

is imposed so to minimize the mesh deformation, while on solid boundaries $\boldsymbol{w} = 0$.

The approach proposed by Ho (1989) is to compute the mesh velocity by solving an elliptic problem of the form:

$$\mathcal{E}\boldsymbol{w} = 0, \tag{3.32}$$

The operator $\mathcal{E}$ comes from an elasticity problem, namely the steady linear equilibrium problem given by

$$\nabla \cdot \left(\boldsymbol{\sigma}^D + p\boldsymbol{I} \right) + \rho \boldsymbol{f} = 0 \tag{3.33}$$

where:

— $p = (3\lambda + 2\mu)\nabla \cdot \boldsymbol{a}$;

— $\boldsymbol{\sigma}^D = 2\mu\varepsilon$;

— $\mu = E/\left[2(1+\nu)\right]$, $\lambda = E\nu/\left[(1+\nu)(1-2\nu)\right]$ are the Lamé coefficients written using Young's modulus E and the Poisson coefficient is set to $\nu = 0.499$ so to obtain an incompressible elastic continuum;

— the deformation tensor $\boldsymbol{\varepsilon} = \frac{1}{2}\left[\nabla \boldsymbol{a} + (\nabla \boldsymbol{a})^T\right]$ written with reference to the mesh displacement vector $\boldsymbol{a}$.

Once the mesh velocity is obtained, its movement is obtained by integrating the equation

$$\frac{d\boldsymbol{x}}{dt} = \boldsymbol{w} \tag{3.34}$$

where $\boldsymbol{x}$ is the location of the mesh points. Assuming the wall tangent displacement of superhydrophobic surfaces is negligible (see chapter 6), during this work we will track only wall-normal location of the grid in time, which is stored within the YM1 field.

3.2.5 How ALE is used in NEK5000

ALE free-surface formulation employed in this thesis is based on the free-surface channel flow example[2], located within the FS_2 folder along with other examples provided with the code. Natively implemented 'MS ' free-surfaces boundary condition is used, where the surface tension is provided within the USRDAT2 subroutine, called once at the beginning of the code execution. This approach follows the one used by NEK5000 developers team to study free-surface dynamics, as reported in EXAMPLES/FS_2 case.

3.3 Modal decomposition

3.3.1 Global linear stability, time-stepping algorithm

Computing the eigenproblem (2.9) arising from a *global* framework in 3D such as the one presented in equation (2.10) using standard algorithms would require huge numerical resources, and most of the cases are just out of reach. As a consequence, a time-stepping approach can be used (Bagheri et al., 2009). Here we have employed the algorithmic implementation of Loiseau et al. (2014) within Nek5000. The dynamics of an infinitesimal perturbation around the base flow is governed by the first equation of (2.7), which we rewrite here:

$$\frac{\partial \boldsymbol{u}}{\partial t} = \boldsymbol{A}\boldsymbol{u} \tag{3.35}$$

where $\boldsymbol{A}$ is the Jacobian projected onto a divergence free space. Time integration of the latter formulation reads as $\boldsymbol{M} = e^{\boldsymbol{A}\delta T}$, which is the exponential propagator, whose related eigenvalue problem becomes:

$$\mu\hat{\boldsymbol{u}} = \boldsymbol{M}\hat{\boldsymbol{u}}. \tag{3.36}$$

The norm of the largest eigenvalue dictates the asymptotic behaviour of the system, since if $||\mu|| > 1$ the perturbation grows and vice versa, provided that $\boldsymbol{u}(\delta t) = e^{\boldsymbol{A}\delta t}\boldsymbol{u}_0 = \boldsymbol{M}\boldsymbol{u}_0$. While $\boldsymbol{M}$ can not be computed explicitly, its action can be approximated by time-marching the linearised Navier-Stokes equations from $t = 0$ to $t = \Delta T$, allowing for the use of Arnoldi-based iterative eigenvalue solvers. Finally, eigenpairs of the exponential propagator $(\mu, \hat{\boldsymbol{u}}$ are linked to those of the Jacobian $\boldsymbol{J}$ by:

$$\lambda = \frac{log(\mu)}{\Delta T}, \quad and \quad \boldsymbol{B}\hat{\boldsymbol{q}} = \hat{\boldsymbol{u}}. \tag{3.37}$$

Key of time-stepping approach is to project the $n \times n$ $\boldsymbol{M}$ operator into a smaller $m \times m$ space, where n is the number of degrees of freedom of the 3D global problem (namely the number of gridpoints times the number of variables) and $m << n$ to enable for standard eigenproblem solution. Let us consider a $n \times m$ operator $\boldsymbol{V}_m$ composed of m orthonormalized vectors of size $n \times 1$. Each m-th column of this matrix is a snapshot taken at time

---

[2] `https://github.com/Nek5000/NekExamples/tree/master/fs_2`

$t = (m-1)\cdot \delta t$ from the linearised Navier-Stokes solver, successively orthonormalised using a Gram-Schmidt process (see Loiseau et al. (2014) for more details). $\boldsymbol{V}\boldsymbol{V}^T \approx \boldsymbol{I}$, where $\boldsymbol{I}$ is the $n \times n$ identity matrix, therefore:

$$\boldsymbol{M} = \boldsymbol{V}\boldsymbol{V}^T\boldsymbol{M}\boldsymbol{V}\boldsymbol{V}^T = \boldsymbol{V}\boldsymbol{H}\boldsymbol{V}^T, \tag{3.38}$$

where $\boldsymbol{H}$ is the $m \times m$ *Hessenberg* matrix. In section 6 we compute the leading global eigenmodes of a channel flow enclosed with spatially heterogeneously modelled superhydrophobic surfaces using exactly this *Arnoldi algorithm* (Loiseau et al., 2014).

3.3.2 Local stability analysis

In chapter 5 and 6 modelling superhydrophobic surfaces with a spatially homogeneous slip length allows for the use of the local stability analysis framework, introduced in (2.12). A 1D local, spectral collocation method based on Chebyshev polynomials (Schmid and Henningson, 2001) has been implemented in Octave language. A primitive formulation is used and slippery surfaces are considered through a Robin boundary condition. In this framework problem (2.12) is spatially discretized onto a 1D vector $\boldsymbol{y} = [-1, \ldots, +1]$ of size $N \times 1$, with N the number of gridpoints. $N \times N$ matrices $\boldsymbol{D}_y\boldsymbol{D}_{yy}$ arise from the spectral collocation method (Hoepffner et al., 2019), and $\boldsymbol{D}_y\boldsymbol{u}$ indicates the derivative in the wall normal direction of the quantity $\boldsymbol{u}$. Owing to the mode expansion (2.11), spatial derivatives in streamwise and spanwise direction are $\boldsymbol{D}_x = i\alpha\boldsymbol{I}, \boldsymbol{D}_z = i\beta\boldsymbol{I}$, with $\boldsymbol{I}$ the $N \times N$ identity matrix and α, β the streamwise and spanwise wavenumbers, respectively. Eigenproblem (2.12) then assumes the form:

$$\lambda \underbrace{\begin{bmatrix} \boldsymbol{I} & \boldsymbol{0} & \boldsymbol{0} & \boldsymbol{0} \\ \boldsymbol{0} & \boldsymbol{I} & \boldsymbol{0} & \boldsymbol{0} \\ \boldsymbol{0} & \boldsymbol{0} & \boldsymbol{I} & \boldsymbol{0} \\ \boldsymbol{0} & \boldsymbol{0} & \boldsymbol{0} & \boldsymbol{0} \end{bmatrix}}_{\boldsymbol{B}} \underbrace{\begin{Bmatrix} \boldsymbol{u} \\ \boldsymbol{v} \\ \boldsymbol{w} \\ \boldsymbol{p} \end{Bmatrix}}_{\hat{\boldsymbol{q}}} = \underbrace{\begin{bmatrix} \boldsymbol{S} & -\boldsymbol{U}_y & \boldsymbol{0} & -\boldsymbol{D}_x \\ \boldsymbol{0} & \boldsymbol{S} & \boldsymbol{0} & -\boldsymbol{D}_y \\ \boldsymbol{0} & \boldsymbol{0} & \boldsymbol{S} & -\boldsymbol{D}_y \\ \boldsymbol{D}_x & \boldsymbol{D}_y & \boldsymbol{D}_z & \boldsymbol{0} \end{bmatrix}}_{\boldsymbol{A}} \hat{\boldsymbol{q}} \tag{3.39}$$

where $\boldsymbol{0}$ indicates a zeros $N \times N$ matrix, $\boldsymbol{U} = \boldsymbol{I}\boldsymbol{u}_b$, $\boldsymbol{U}_y = \boldsymbol{D}_y\boldsymbol{U}$ with $\boldsymbol{u}_b$ the vector containing the base flow U_b, and $\boldsymbol{S} = -\boldsymbol{U}\boldsymbol{D}_x + 1/Re(-\alpha^2\boldsymbol{I} + \boldsymbol{D}_{yy} - \beta^2\boldsymbol{I})$. Robin boundary conditions at the u, w components, as well as $v = 0$ at the walls, are imposed by replacing the rows within the previous matrix problem representing their values at the boundary:

$$\begin{aligned} \boldsymbol{A}(1+0\cdot N,\ldots) &= -\boldsymbol{Y}(1+0\cdot N,\ldots) + L_s \cdot \boldsymbol{T}(1+0\cdot N,\ldots) \\ \boldsymbol{A}(1+1\cdot N,\ldots) &= +\boldsymbol{Y}(1+1\cdot N,\ldots) \\ \boldsymbol{A}(1+2\cdot N,\ldots) &= +\boldsymbol{Y}(1+2\cdot N,\ldots) + L_s \cdot \boldsymbol{T}(1+2\cdot N,\ldots) \\ \boldsymbol{A}(N+0\cdot N,\ldots) &= -\boldsymbol{Y}(N+0\cdot N,\ldots) - L_s \cdot \boldsymbol{T}(N+0\cdot N,\ldots) \\ \boldsymbol{A}(N+1\cdot N,\ldots) &= +\boldsymbol{Y}(N+1\cdot N,\ldots) \\ \boldsymbol{A}(N+2\cdot N,\ldots) &= +\boldsymbol{Y}(N+2\cdot N,\ldots) + L_s \cdot \boldsymbol{T}(N+2\cdot N,\ldots) \end{aligned}$$

and

$$\begin{aligned} \boldsymbol{B}(1+0\cdot N,\ldots) &= 0 \\ \boldsymbol{B}(1+1\cdot N,\ldots) &= 0 \\ \boldsymbol{B}(1+2\cdot N,\ldots) &= 0 \\ \boldsymbol{B}(N+0\cdot N,\ldots) &= 0 \\ \boldsymbol{B}(N+1\cdot N,\ldots) &= 0 \\ \boldsymbol{B}(N+2\cdot N,\ldots) &= 0 \end{aligned}$$

provided that $\boldsymbol{Y}, \boldsymbol{T}$ are the block diagonal matrices built the $\boldsymbol{I}$ and $\boldsymbol{D}_y$ of size $4 \cdot N \times 4 \cdot N$, and that L_s is the slip length, introduced in equation (3.16). Eigenvalues and eigenvectors are computed calling the function EIG(A,B), using a QZ algorithm, while the results are numerically converged for $N = 100$.

Chapter 4

Triggering Natural transition in numerical simulations

Research on laminar-turbulent transition of wall-bounded parallel flows has usually focused on controlled scenarios where transition is triggered by perturbations having simple shapes and spectra. These disturbances strongly differ from the environmental noise usually present in experimental setups or industrial applications, where uncontrolled transition is usually observed. In this chapter a new method is proposed to trigger uncontrolled transition to turbulence in wall-bounded parallel flows exploiting the receptivity of the flow to a volume forcing (Picella et al., 2019).

Using some concepts provided by linear stability and sensitivity analysis, such as the *resolvent*, we propose a method for constructing a volume forcing capable of inducing stochastic velocity perturbations with a prescribed energy level, eventually leading to laminar-turbulent transition as a response of the system to external noise.

The method has been tested in a channel flow configuration, using direct numerical simulations of the fully nonlinear Navier-Stokes equations in the presence of the volume forcing constructed on the basis of *optimal* forcing functions. Subcritical transition to turbulence induced by the prescribed forcing has been investigated and compared to other transition scenarios, where deterministic perturbations are imposed for obtaining a turbulent flow. Finally, the fully developed turbulent flows induced by the proposed method has been analysed, showing that low-order statistics and energy balance equations are practically unaffected by the continuous synthetic forcing.

In section 4.1 we set the problem framework and we outline the method for triggering turbulence in a streamwise-periodic wall-bounded flow by using a synthetic noisy volume forcing. In section 4.2 we test the method in a linearised framework to verify the consistency of all the assumptions previously made. In section 4.3 we provide a detailed description of the non-linear dynamics observed when transition is triggered using the method proposed here, with particular focus on the physical mechanisms as compared to classical transition scenarios. In section 4.4 we verify that the subsequent fully turbulent state is independent of the transition scenario from which it is generated. Finally, relevant conclusions are drawn in section 4.5.

4.1 Problem Statement and numerical methods

The aim of this Chapter is to provide a new method for triggering *uncontrolled* transition in an incompressible wall-bounded streamwise-periodic flow such as a channel flow.

This configuration has proven to be particularly suitable for numerical investigations of turbulent shear flows. In fact, being the problem homogeneous in the directions parallel to the wall, turbulent channel flows can be accurately simulated in relatively small domains (Jiménez and Moin, 1991) using periodic boundary conditions in both streamwise and spanwise directions (Kim et al., 1987). The latter configuration, known as *temporal channel flow* (Zang and Krist, 1989), is chosen as framework due to its physical relevance, its large presence in the literature as well as to the low computational cost of numerical simulations in this setup as compared to spatially-evolving configurations such as the boundary-layer flow (Kleiser and Zang, 1991; Schlatter et al., 2004).

In this part of the thesis, differently from several works already present in the literature, we are not interested in controlled transition scenarios, such as for instance the K-type one (Sandham and Kleiser, 1992b; Lee and Zaki, 2017), but instead on investigating how transition arises as a response of the fluid system to external noise similar to that occurring in uncontrolled experimental conditions (Sano and Tamai, 2016). Thus, in the present Chapter we will set up a numerical method to study how transition arises as a response of the flow to a synthetic noisy volume forcing. The latter, solution of the equations governing the fluid system, will be constructed using an ad hoc procedure relying on some concepts of linear stability and sensitivity analysis such as the resolvent analysis (Schmid and Henningson, 2001).

4.1.1 Governing equations

The dynamics of the incompressible flow of a Newtonian fluid are governed by the Navier-Stokes equations

$$\frac{\partial \boldsymbol{U}}{\partial t} = -(\boldsymbol{U}\cdot\nabla)\boldsymbol{U} - \nabla P + \frac{1}{Re}\nabla^2\boldsymbol{U} + \boldsymbol{f} \tag{4.1}$$

$$\nabla\cdot\boldsymbol{U} = 0, \tag{4.2}$$

where $\boldsymbol{U} = (U(\boldsymbol{x},t), V(\boldsymbol{x},t), W(\boldsymbol{x},t))^T$ is the velocity field, $P(\boldsymbol{x},t)$ is the pressure and $\boldsymbol{f}$ the forcing field. The Reynolds number is defined as $Re = UH/\nu$, where U is the centerline velocity, H is half the height of the channel and ν the kinematic viscosity of the fluid. The reference frame $\boldsymbol{x} = (x,y,z)^T$ is chosen such that x is the streamwise, y the wall-normal and z the spanwise directions.

Steady solutions $\boldsymbol{Q}_b(\boldsymbol{x}) = (\boldsymbol{U}_b, P_b)^T$ of the Navier-Stokes equations are known as *base flows* or *fixed points* of the system. Under the assumption of small-amplitude disturbances, we decompose the flow field as a sum of the base flow and a perturbation such as $\boldsymbol{Q}(\boldsymbol{x},t) = \boldsymbol{Q}_b(\boldsymbol{x}) + \boldsymbol{q}(\boldsymbol{x},t)$, that is to say $(\boldsymbol{U}(\boldsymbol{x},t), P(\boldsymbol{x},t))^T = (\boldsymbol{U}_b(\boldsymbol{x}), P_b(\boldsymbol{x}))^T + (\boldsymbol{u}(\boldsymbol{x},t), p(\boldsymbol{x},t))^T$. Linearising the governing equations around the base flow we obtain the linearized Navier-Stokes equations for the perturbation field, which can be compactly written as:

$$\frac{\partial \boldsymbol{u}}{\partial t} = \boldsymbol{L}\boldsymbol{u} + \boldsymbol{f} \tag{4.3}$$

once projected onto a divergence-free vector space. Being this system autonomous in time and being the base flow periodic in both streamwise and spanwise directions one can apply a Fourier transform to any field $\boldsymbol{q}$ so that $\boldsymbol{q}(\boldsymbol{x},t) = \tilde{\boldsymbol{q}}(y)\exp[i(\alpha x + \beta z) + \lambda t] + c.c$, where the last term stands for *complex conjugate*, α and β are the streamwise and spanwise wavenumbers and λ is the temporal one. In general $\alpha, \beta, \lambda, \tilde{\boldsymbol{u}} \in \mathbb{C}$.

When $\boldsymbol{f} = 0$, the behaviour of a generic solenoidal velocity perturbation $\boldsymbol{u}$ is linked to the eigenpairs of $\boldsymbol{L}$ $(\lambda^{eig}, \tilde{\boldsymbol{u}}^{eig})$ (Orszag, 1971), since it can be written as $\boldsymbol{u}(\boldsymbol{x},t) =$

$\sum_l \kappa_l \tilde{\boldsymbol{u}}(y)_l^{eig} e^{i(\alpha x+\beta z)+\lambda_l^{eig} t}$, where κ_l is a scalar weight. For a given couple $\alpha, \beta \in \mathbb{R}$ (condition that will be held throughout the whole work), the *temporal* behaviour of each eigenvector of the linearised operator $\boldsymbol{L}$ is then described by its associated eigenvalue $\lambda_i^{eig} = \sigma_i^{eig} + i\omega_i^{eig}$, where σ_i^{eig} represents its asymptotic growth/decay and ω_i^{eig} its oscillation wavenumber.

We now assume the linearised system (4.3) to be forced, with a forcing harmonic in time, namely

$$\boldsymbol{f}(\boldsymbol{x}, t) = \tilde{\boldsymbol{f}}(y) e^{i\omega t} e^{i(\alpha x+\beta z)} + c.c. \tag{4.4}$$

and that the system is stable, namely that all the eigenvalues of $\boldsymbol{L}$ have growth rate $\sigma_i^{eig} < 0, \forall i$. Thanks to the linearity of the governing equations the Linear Time Invariant (LTI) system in equation (4.3) simplifies to

$$\tilde{\boldsymbol{u}} = (i\omega \boldsymbol{I} - \boldsymbol{L})^{-1} \tilde{\boldsymbol{f}}, \tag{4.5}$$

where $(i\omega \boldsymbol{I} - \boldsymbol{L})^{-1}$, called the *resolvent* of L, represents a mapping between the harmonic input and the corresponding output for a given $[\alpha, \beta, \omega, Re]$ set and $\boldsymbol{I}$ stands for the identity operator. Under such forcing input the resulting response of the system will oscillate at the same frequency ω, in particular:

$$\boldsymbol{u}(\boldsymbol{x}, t) = \tilde{\boldsymbol{u}}(y) e^{i(\alpha x+\beta z)} e^{i\omega t}, \tag{4.6}$$

which is a monochromatic wave oscillating in time and space with wavenumbers (ω, α, β). The kinetic energy density of this response for a given $[\alpha, \beta, \omega, Re]$ set is defined as:

$$||\tilde{\boldsymbol{u}}(y, \alpha, \beta, \omega)||_E^2 = \frac{1}{2V} \int_V \boldsymbol{u}^H \boldsymbol{u}(\boldsymbol{x}, t) d\boldsymbol{V} \bigg|_{\alpha,\beta,\omega} = E(\boldsymbol{u}(\boldsymbol{x}, t))|_{\alpha,\beta,\omega}, \tag{4.7}$$

where V is the volume of the computational domain and $\boldsymbol{u}^H$ is the transconjugate of $\boldsymbol{u}$. Among all the possible $(\boldsymbol{f}, \boldsymbol{u})$ couples, let us focus on the one which maximizes the ratio of the output energy with respect to the input one, namely:

$$R(\alpha, \beta, \omega) = \frac{||\tilde{\boldsymbol{u}}^{opt}||_E^2}{||\tilde{\boldsymbol{f}}^{opt}||_E^2} = \max_{\tilde{\boldsymbol{f}}} \frac{||\tilde{\boldsymbol{u}}||_E^2}{||\tilde{\boldsymbol{f}}||_E^2} = ||(i\omega \boldsymbol{I} - \boldsymbol{L})^{-1}||_E^2, \tag{4.8}$$

where $\tilde{\boldsymbol{f}}^{opt}, \tilde{\boldsymbol{u}}^{opt}$ are defined as *optimal* forcing and response, again evaluated for a given $[\alpha, \beta, \omega, Re]$ set and R is the resolvent norm. The optimal forcing and the associated response $(\tilde{\boldsymbol{f}}^{opt}, \tilde{\boldsymbol{u}}^{opt})$ can be built using a linear combination of the eigenvectors of $\boldsymbol{L}$:

$$\tilde{\boldsymbol{f}}^{opt}(y, \alpha, \beta, \omega, Re) = \sum_{k=1}^{K} \bigcirc_k \tilde{\boldsymbol{f}}_k^{eig}(y, \alpha, \beta, \omega, Re) \tag{4.9}$$

$$\tilde{\boldsymbol{u}}^{opt}(y, \alpha, \beta, \omega, Re) = \sum_{k=1}^{K} \square_k \tilde{\boldsymbol{u}}_k^{eig}(y, \alpha, \beta, \omega, Re), \tag{4.10}$$

whose scalar weights $(\bigcirc_k, \square_k)$ are retrieved by means of a singular value decomposition of the resolvent norm (Schmid and Henningson, 2001; Schmid, 2007). An application of the resolvent norm theory to the case of plane Poiseuille flow is depicted in figure 4.1. In the reminder of this section we drop the Re dependency for the sake of readability.

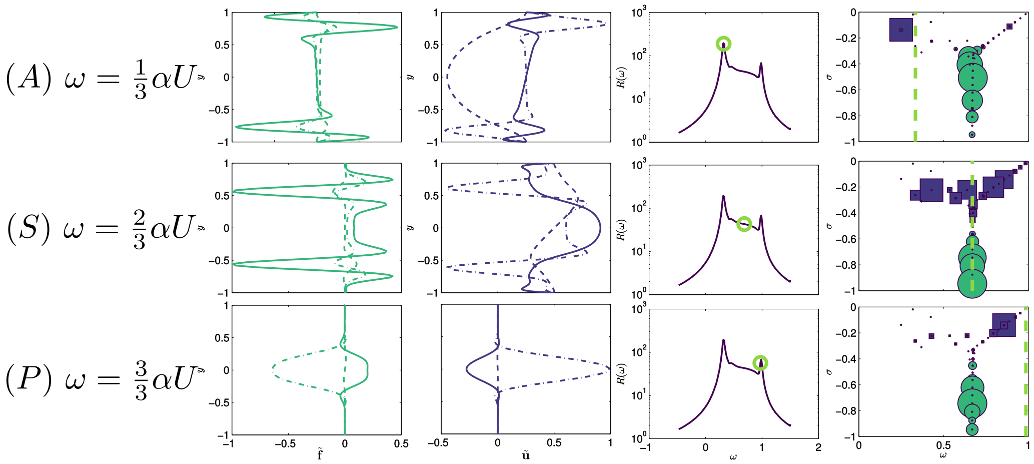

Figure 4.1 – Some typical optimal forcings/responses for Plane Poiseuille Flow (PPF) with $\alpha = 1, \beta = 0.25, Re = 2000$, for various forcing frequencies ω: $\omega = \alpha U/3$ (upper frames), $\omega = \alpha 2\alpha U/3$ (middle frames), and $\omega = \alpha U$ (bottom frames), triggering A-modes (viscous T-S modes), S-modes (critical layer modes) and P-modes (inviscid modes), respectively. From left to right the boxes represents the optimal forcing $\tilde{\boldsymbol{f}}^{opt}$, the optimal response $\tilde{\boldsymbol{u}}^{opt}$, the resolvent norm $R(\omega)$ highlighted as a circle, and the eigenspectrum λ_i^{eig} of $\boldsymbol{L}$. The forcing and response vectors are built as a linear composition of the system's eigenvectors following equation 4.9, whose weights are proportional to the sizes the markers.

4.1.2 Building a volume forcing to enforce a prescribed energy spectrum

Our aim is to construct a velocity perturbation attaining a target value of the turbulence intensity, $Tu = \sqrt{\boldsymbol{U}_{rms}^2/3}$, which, within the linear framework, is equivalent to

$$Tu^{linear} = \sqrt{\boldsymbol{u}^2/3} \equiv \sqrt{\frac{2}{3}E^{linear}}, \tag{4.11}$$

where $\boldsymbol{u}$ is the linear response to a given volume forcing.

Similarly to what is done in equation (4.9), we decompose the desired velocity perturbation field as a linear combination of a discrete set of *optimal responses* $\tilde{\boldsymbol{u}}^{opt}$, each one solution of equations (4.1) and (4.8). The associated *optimal* forcing fields are then used as a basis to construct the synthetic volume forcing able to induce the desired perturbation field via receptivity mechanisms. Optimal forcings are here chosen as a basis not only because they provide a straightforward force-velocity relation, but also because they are able to induce the given energy level Tu^{linear} with the lowest possible forcing intensity (within a linearized framework). The optimal forcing and response fields are computed using a simple 1D code solving equation (4.8) for different values of the wavenumbers $[\alpha, \beta, \omega]$, conveniently chosen to discretize the prescribed energy spectrum.

For the sake of simplicity, in the following we will assume a flat energy spectrum, whose energy is evenly distributed within a frequency range $[\omega_{min}, \omega_{max}]$, although the following procedure can be easily extended to more complex energy spectra (see section 4.2.3). The prescribed continuous energy spectrum is discretized into N_ω modes $\tilde{\boldsymbol{u}}_i$, each one associated to a specific frequency ω_i, so that:

$$\omega_i = \frac{(\omega_{max} - \omega_{min})\,(i-1)}{N_\omega} + \omega_{min} \tag{4.12}$$

and

$$\boldsymbol{u}(\boldsymbol{x},t) = \sum_{i=1}^{N_\omega} \check{\boldsymbol{u}}(\boldsymbol{x},\omega_i) e^{i\omega_i t}, \quad E\left(\check{\boldsymbol{u}}(\boldsymbol{x},\omega_i)\right) = \frac{E^{linear}}{N_\omega} \tag{4.13}$$

where the left side of equation (4.13) coincides with the Discrete Fourier Transform (DFT) of $\boldsymbol{u}(\boldsymbol{x},t)$, $\check{\boldsymbol{u}}(\boldsymbol{x},\omega_i)$ being a discrete subset of DFT modes associated to its respective discrete set of forcing frequencies:

$$\boxed{\omega} = [\omega_{min}, \ldots, \omega_i, \ldots, \omega_{max}]\,. \tag{4.14}$$

We further decompose the velocity field associated to a given frequency $\check{\boldsymbol{u}}(\boldsymbol{x},\omega_i)$ into $N_{\alpha,\beta}$ discrete modes for each *allowed* (α,β) spatial wavenumber. The physical reasons of this restriction will be explained in detail in section 4.1.3. Thus, the resolvent norm analysis will provide a discrete set of modes associated to $N_{\alpha,\beta}$ spatial wavenumbers:

$$\boxed{\alpha,\beta}(\omega_i) = \left[(\alpha,\beta)_i^1, \ldots, (\alpha,\beta)_i^j, \ldots, (\alpha,\beta)_i^{N_{\alpha,\beta}}\right], \tag{4.15}$$

each one compatible with a corresponding single frequency ω_i. Similarly to equation (4.13), we can further decompose the velocity field as follows:

$$\check{\boldsymbol{u}}(\boldsymbol{x},\omega_i) = \sum_{j=1}^{N_{\alpha,\beta}} \tilde{\boldsymbol{u}}(y,\alpha_i^j,\beta_i^j,\omega_i) e^{i(\alpha_i^j x + \beta_i^j z)}, \quad ||\tilde{\boldsymbol{u}}(y,\alpha_i^j,\beta_i^j,\omega_i)||_E^2 = \frac{E^{linear}}{N_\omega N_{\alpha,\beta}} \tag{4.16}$$

where each $\tilde{\boldsymbol{u}}(y,\alpha_i^j,\beta_i^j,\omega_i)$ has the same kinetic energy for the simple test case considered here. The couples (α_i^j,β_i^j) are suitably chosen to span a large number of wavelengths in order to increase the isotropy of the perturbation, similarly to FST methods (Jacobs and Durbin, 2001b; Brandt et al., 2004b).

Replacing the generic $\tilde{\boldsymbol{u}}$ with $\tilde{\boldsymbol{u}}^{opt}$ in equation (4.16) results in:

$$\check{\boldsymbol{u}}(\boldsymbol{x},\omega_i) = \sum_{j=1}^{N_{\alpha,\beta}} \tilde{\boldsymbol{u}}^{opt}(y,\alpha_i^j,\beta_i^j,\omega_i) e^{i(\alpha_i^j x + \beta_i^j z)}, \; ||\tilde{\boldsymbol{u}}^{opt}(y,\alpha_i^j,\beta_i^j,\omega_i)||_E^2 = \frac{E^{linear}}{N_\omega N_{\alpha,\beta}}. \tag{4.17}$$

The same procedure is then applied to the discrete set of forcing fields associated to the chosen optimal responses, obtaining:

$$\check{\boldsymbol{f}}(\boldsymbol{x},\omega_i) = \sum_{j=1}^{N_{\alpha,\beta}} A_i^j \tilde{\boldsymbol{f}}^{opt}(y,\alpha_i^j,\beta_i^j,\omega_i) e^{i(\alpha_i^j x + \beta_i^j z)} e^{i(\phi_x x + \phi_z z)}, \tag{4.18}$$

where each optimal forcing $\tilde{\boldsymbol{f}}^{opt}$ is multiplied by the scalar A_i^j to ensure a prescribed weight and shifted in space by a random phase ϕ_x, ϕ_z to increase homogeneity (Brandt et al., 2004b). The weights A_i^j are assigned in order to fulfill the prescribed energy spectrum; in particular, combining equations (4.8) and (4.17) one obtains:

$$\frac{E^{linear}}{N_\omega N_{\alpha,\beta}} = A_i^j ||\tilde{\boldsymbol{u}}^{opt}(y,\alpha_i^j,\beta_i^j,\omega_i)||_E^2 = A_i^j R(y,\alpha_i^j,\beta_i^j,\omega_i) ||\tilde{\boldsymbol{f}}^{opt}(y,\alpha_i^j,\beta_i^j,\omega_i)||_E^2, \tag{4.19}$$

which is then rearranged to provide the value of A_i^j for each forcing $\tilde{\boldsymbol{f}}^{opt}$:

$$A_i^j = \frac{E^{linear}}{N_\omega N_{\alpha,\beta} R(\alpha_i^j,\beta_i^j,\omega_i)} \tag{4.20}$$

.

The obtained discrete set of N_ω forcing fields reads:

$$\boxed{\check{\boldsymbol{f}}}(\omega_i) = \left[\check{\boldsymbol{f}}(\boldsymbol{x}, \omega_{min}), \ldots, \check{\boldsymbol{f}}(\boldsymbol{x}, \omega_i), \ldots, \check{\boldsymbol{f}}(\boldsymbol{x}, \omega_{max})\right]. \tag{4.21}$$

where each forcing is associated to a given frequency ω_i. The real volume forcing to be injected in equations (4.1) in order to obtain the requested response by time marching can be expressed as:

$$\boldsymbol{f}(\boldsymbol{x}, t) = \sum_{i=1}^{N_\omega} \check{\boldsymbol{f}}(\boldsymbol{x}, \omega_i) e^{i\omega_i t} = \sum_{i=1}^{N_\omega} \left[\Re(\check{\boldsymbol{f}}(\boldsymbol{x}, \omega_i)) cos(\omega_i t) - \Im(\check{\boldsymbol{f}}(\boldsymbol{x}, \omega_i)) sin(\omega_i t)\right] \tag{4.22}$$

Within a linearized framework, the obtained response reaching the prescribed energy level Tu^{linear} has the form:

$$\boldsymbol{u}(\boldsymbol{x}, t) = \sum_{i=1}^{N_\omega} \check{\boldsymbol{u}}(\boldsymbol{x}, \omega_i) e^{i\omega_i t} = \sum_{i=1}^{N_\omega} \left[\Re(\check{\boldsymbol{u}}(\boldsymbol{x}, \omega_i)) cos(\omega_i t) - \Im(\check{\boldsymbol{u}}(\boldsymbol{x}, \omega_i)) sin(\omega_i t)\right]. \tag{4.23}$$

The whole procedure, to which we will refer to as F-TYPE forcing method, is summarized in algorithm 1 and in figure 4.2.

```
Physical Parameters   : $L_x, L_z, Re$
Target                : $Tu^{linear}$
Numerical Parameters: $N_{\alpha,\beta}, N_\omega$
Result: $\boxed{\omega}(i), \boxed{\check{\boldsymbol{f}}}(i), \boldsymbol{u}(\boldsymbol{x}, t=0)$
$E^{linear} \leftarrow$ eq. (4.11);
$\boxed{\omega}(i), \boxed{\alpha,\beta}(i,j) \leftarrow$ AlphaBetaOmegaCompute($L_x, L_z, N_{\alpha,\beta}, N_\omega$);
$\boldsymbol{u} = 0$;
for $i \leftarrow 1$ to $N_\omega$ do
    $\omega_i = \boxed{\omega}(i)$;
    $\check{\boldsymbol{f}}(i) = 0$;
    for $j \leftarrow 1$ to $N_{\alpha,\beta}$ do
        $\alpha_i^j, \beta_i^j \leftarrow \boxed{\alpha,\beta}(i,j)$;
        $\tilde{\boldsymbol{u}}^{opt}, \tilde{\boldsymbol{f}}^{opt}, R(i,j) \leftarrow$ OptimalCompute($\alpha_i^j, \beta_i^j, \omega_i, Re$);
        $A_i^j \leftarrow$ eq. (4.20);
        $\check{\boldsymbol{f}}(i) = \check{\boldsymbol{f}}(i) + A_i^j R \tilde{\boldsymbol{f}} e^{i(\alpha_i^j x + i\beta_i^j)}$;
        $\check{\boldsymbol{u}}(i) = \check{\boldsymbol{u}}(i) + A_i^j \tilde{\boldsymbol{u}} e^{i(\alpha_i^j x + i\beta_i^j)}$;
    end
    $\boldsymbol{u} = \boldsymbol{u} + \Re(\check{\boldsymbol{u}}(i))$;
end
```

Algorithm 1: F-TYPE forcing method. The `AlphaBetaOmegaCompute` algorithm, detailed in algorithm (2) in section 4.1.3, provides the discrete ω_i and α_i^j, β_i^j sets for a given configuration, while the `OptimalCompute` function computes the 1D optimal forcing fields solving equation (4.8), as shown in (Schmid and Henningson, 2001). The whole method is sketched in figure 4.2.

From a practical point of view, we first compute the set of N_ω forcing fields $\check{\boldsymbol{f}}(\boldsymbol{x}, t)$ in the frequency domain as a preprocessing, prescribing only the discrete set of $N_{\alpha,\beta}$ and

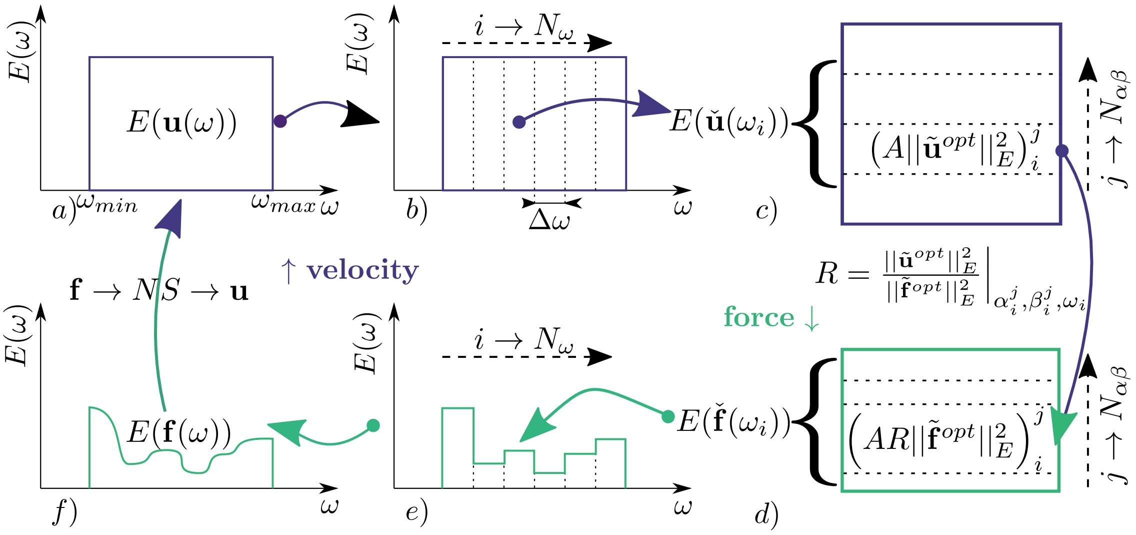
$E(\omega)$
$E(\mathbf{u}(\omega))$
a) ω_{min}
ω_{max} ω
$E(\omega)$
$i \to N_\omega$
b)
$\Delta\omega$
ω
$E(\check{\mathbf{u}}(\omega_i))$
$(A\|\tilde{\mathbf{u}}^{opt}\|_E^2)_i^j$
c)
$j \to N_{\alpha\beta}$
↑ velocity
$\mathbf{f} \to NS \to \mathbf{u}$
$R = \frac{\|\tilde{\mathbf{u}}^{opt}\|_E^2}{\|\tilde{\mathbf{f}}^{opt}\|_E^2}\Big|_{\alpha_i^j,\beta_i^j,\omega_i}$
force ↓
$E(\omega)$
$E(\mathbf{f}(\omega))$
f)
ω
$E(\omega)$
$i \to N_\omega$
e)
ω
$E(\check{\mathbf{f}}(\omega_i))$
$\left(AR\|\tilde{\mathbf{f}}^{opt}\|_E^2\right)_i^j$
d)
$j \to N_{\alpha\beta}$

Figure 4.2 – Sketch depicting the **F-type** forcing method detailed in algorithm 1, aiming to build a forcing which ensures a velocity perturbation field reaching Tu^{linear}.

N_ω wavenumbers. Then, we compute $\boldsymbol{f}$ at each timestep by means of equation (4.22) and feed it to the direct numerical simulation. It is noteworthy that, while the whole energy is equally distributed on the optimal response fields composing the desired velocity perturbation as imposed in equation (4.13), each optimal forcing can be associated to a different energy level, since the resolvent norm acting as input-output transfer function has a different value for each wavenumber/frequency. As a consequence, the energy spectrum of the forcing field will not be flat in ω.

4.1.3 Constraints on α, β, and ω

As mentioned in the previous subsection, the optimal forcing fields used to construct the desired synthetic volume forcing for triggering uncontrolled transition, are function of α, β, ω. These parameters cannot be assigned freely, being linked to each other due to some physical reasons detailed below. The first reason is based on simple geometrical considerations: being the numerical setup periodic in both streamwise and spanwise directions, only a finite number of wavelengths are allowed within the assigned domain. Beyond the trivial 0^{th} mode, the lowest possible wavelengths are therefore determined by the size of the computational domain L_x, L_z through the relations $\alpha_{box} = 2\pi/L_x, \beta_{box} = 2\pi/L_z$. Integer multiples of these wavenumbers can be also retrieved, up to the maximum wavenumber allowed due to spatial discretization. Using the Nyquist-Shannon sampling theorem (Jerri, 1977), one obtains $\alpha_{max} \approx 2\pi/(8\Delta x)$, ($\beta_{max} \approx 2\pi/(8\Delta z)$, providing the following discrete set of geometrically compatible wavelengths:

$$\boxed{\alpha}_{geom} = [0, \alpha_{box}, 2\alpha_{box}, \ldots, \alpha_{max}], \quad \boxed{\beta}_{geom} = [0, \beta_{box}, 2\beta_{box}, \ldots, \beta_{max}] \tag{4.24}$$

where $\Delta x, \Delta z$ indicate the characteristic grid size in the streamwise and spanwise directions, respectively. Concerning the wavenumber $\alpha = 0$, although being geometrically allowed within the domain, it would result in a deformation of the one dimensional base flow, changing the physical nature of the problem. Thus, the allowed wavenumber set is reduced to:

$$\boxed{\alpha} = [\alpha_{box}, 2 \cdot \alpha_{box}, \dots, \alpha_{max}] \tag{4.25}$$

$$\boxed{\beta} = [0,\ \beta_{box}, 2 \cdot \beta_{box}, \dots, \beta_{max}\ ] \tag{4.26}$$

The same can be said about the $\omega = 0$ temporal mode, which would result in an unphysical constant forcing. The forcing frequencies will thus lie in the range $[\omega_{min}, \omega_{max}]$, where the values of $\omega_{min}, \omega_{max}$ can be easily chosen due to the following physical considerations. In figure 4.1 one can notice how the wall normal distribution of the modes changes depending on the assigned value of ω: different forcing frequencies result in different sensitivity mechanisms, which can be retrieved in the spectrum in the form of viscous Tollmien-Schlichting, critical layer, and inviscid modes (from upper to bottom frames). Similarly to FST method in semi-bounded domains (Brandt et al., 2004b; Jacobs and Durbin, 2001b) where only *free-stream* modes are excited, in the current setup only inviscid modes will be used, whereas the viscous Tollmien-Schlichting waves, also referred to as *A-modes* (Schmid and Henningson, 2001), are discarded. Towards this aim, the forcing frequencies associated to a particular spatial wavenumber are constrained within the range:

$$\text{range}(\omega(\alpha)) = \left\{ \frac{2}{3}\alpha, \alpha \right\} U \tag{4.27}$$

where a generalisation of Taylor's hypothesis $\omega = \alpha U$ is used, $2/3U$ corresponding to the mean velocity of the flow. In this way, for a given α_i, all the viscous A-modes are discarded, leaving only inviscid (P and S) modes to construct the desired volume forcing. Moreover, as depicted in figure 4.3, one can observe that a given ω range is associated to each α. Thus, the ω range results from $\boxed{\alpha}$, as reported in equation (4.27). Table 4.1 summarises the lower and upper bounds of the spatial and temporal wavenumbers of the optimal forcing fields used for constructing the desired volume forcing. It is noteworthy to remark that, while $\boxed{\alpha}$ depends on the specific forcing frequency ω_i, $\boxed{\beta}$ is only dependent on the domain discretization.

α_{min}	α_{max}	β_{min}	β_{max}	ω_{min}	ω_{max}
$\frac{2\pi}{L_x}$	$\frac{2\pi}{8\Delta x}$	0	$\frac{2\pi}{8\Delta x}$	$\frac{2}{3}\alpha_{min}$	α_{max}

Table 4.1 – Lower and upper bounds for the spatial (left) and temporal (right) wavenumbers of the optimal forcing fields used for constructing the desired volume forcing.

This feature can result in a discontinuous spectrum for low forcing frequencies, depending on the domain sizes L_x, L_z.

A sketch of the allowed spatial and temporal wavenumbers is provided in figure 4.4, and the numerical procedure to choose them is summarised in algorithm 2.

.

4.2 Algorithm testing: linear regime

In the following we test and tune our method by running forced direct numerical simulations of equations (4.3). The Navier-Stokes equations are solved using the incompressible flow solver NEK5000 (Fischer et al., 2008) which is based on the spectral element method (SEM). A $\mathbb{P}_N - \mathbb{P}_{N-2}$ formulation has been used: the velocity field is discretised using N^{th} degree Lagrange interpolants, defined on the Gauss-Legendre-Lobatto quadrature points, as

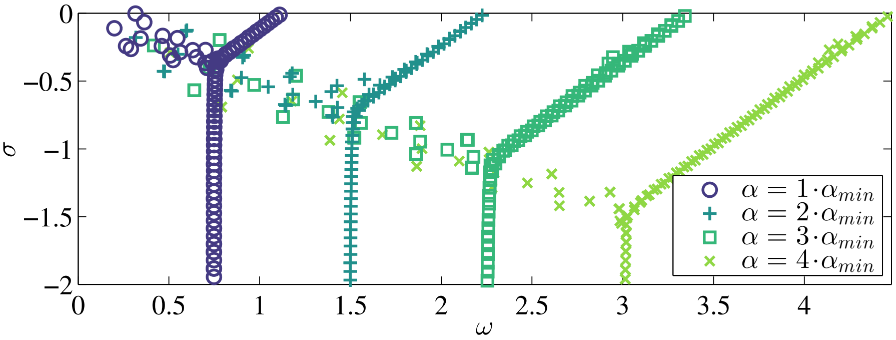

Figure 4.3 – Orr-Sommerfeld spectra of plane Poiseuille flow for $Re = 5000, \beta = 0$ and different values of α provided in the legend. The spectra widens as the streamwise wavenumber is increased. This physically means that shorter streamwise wavelengths can be linked to higher forcing frequencies. For this computation we have used a pseudo-spectral Chebyshev collocation method with numerical resolution of 256 points in the y direction.

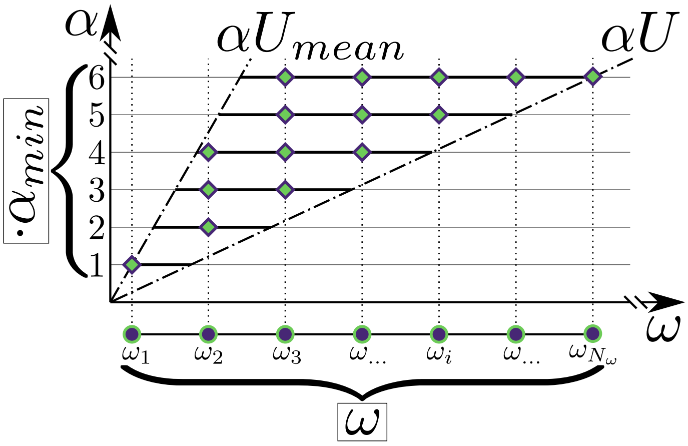

Figure 4.4 – Graphical summary of section 4.1.3. Diamonds and circles represent the spatial and temporal wavenumbers taken into account for building up the synthetic volume forcing.

basis and trial functions, while the pressure field is discretised using Lagrange interpolants of degree $N-2$ defined on the Gauss-Legendre quadrature points. Finally, the time integration is performed using the BDF3/EXT3 scheme: integration of the viscous terms relies on the backward differentiation (BDF3), while the convective terms are integrated explicitly using a third order accurate extrapolation (EXT3), both with a third-order accuracy. We wish to compare our forcing method with some *benchmark*, deterministic transition scenario, namely the K-type transition (Schlatter et al., 2004). Therefore we set our computational box dimensions as $[L_x, L_y, L_z] = [2\pi/1.12, 2, 2\pi/2.10]$, as well as the numerical resolution to $N_x \times N_y \times N_z = 128 \times 128 \times 128$ gridpoints on a $16 \times 16 \times 16$ spectral element grid with spectral order equal to 8. We have verified that the chosen parameters of the numerical discretization are sufficient to accurately reproduce the dynamics of perturbations in a channel flow (Sandham and Kleiser, 1992b; Zang and Krist, 1989). The Reynolds number is set to a subcritical value, namely $Re = 5000$; this value is kept constant in all the numerical simulations discussed in this work. As already mentioned, periodicity is enforced in the streamwise and spanwise directions while a Dirichlet boundary condition is imposed at wall normal boundaries.

```
Physical Parameters   : $L_x, L_z$
Numerical Parameters: $N_{\alpha,\beta}, N_\omega$
Result: $\boxed{\omega}(i), \boxed{\alpha,\beta}(i,j)$
$\alpha_{box} = \frac{2\pi}{L_x}, \alpha_{max} = \frac{2\pi}{8\Delta x}, \beta_{box} = \frac{2\pi}{L_z}, \beta_{max} = \frac{2\pi}{8\Delta z}$;
$\boxed{\alpha} = [\alpha_{box}, \ldots, \alpha_{max}], \boxed{\beta} = [0, \beta_{box}, \ldots, \beta_{max}]$ from eq. (4.25);
$N_\alpha$ =length($\boxed{\alpha}$), $N_\beta$ =length($\boxed{\beta}$);
$\omega_{min} = \frac{2}{3}\alpha_{min}, \omega_{max} = min\,\{\alpha_{max}, \beta_{max}\}$, from table (4.1);
$\boxed{\alpha,\beta}_{tot}$ =combinations($\boxed{\alpha}$, $\boxed{\beta}$);
for $i \leftarrow 1$ to $N_\omega$ do
    $\boxed{\omega}(i) = \omega_i = \frac{(\omega_{max}-\omega_{min})\cdot(i-1)}{N_\omega} + \omega_{min}$ from eq. (4.13);
    $\boxed{\alpha,\beta}_{tot}^{shuffled}$ =shuffle($\boxed{\alpha,\beta}_{tot}$);
    $j = 0, k = 1, \omega_{test} = \boxed{\omega}(i)$;
    while ($j \leq N_{\alpha,\beta}$ or $k \leq N_\alpha N_\beta$) do
        $(\alpha_{test}, \beta_{test}) = \boxed{\alpha,\beta}_{tot}^{shuffled}(k)$;
        if ($\omega_{test} \geq \frac{2}{3}\alpha_{test}$ and $\omega_{test} \leq \alpha_{test}$) then
            $\boxed{\alpha,\beta}(i,j) = (\alpha_{test}, \beta_{test})$;
            $j = j + 1$;
        end
        $k = k + 1$;;
    end
end
```

Algorithm 2: `AlphaBetaOmegaCompute` algorithm, which summarises the constraints on α, β for each discrete forcing frequency ω as detailed in section4.1.3. Function `length`() computes the number of elements of an input discrete list $\boxed{x}$; function `combinations`() provides all their possible combinations; and function `shuffle`() randomly redistribute the elements of the list.

4.2.1 Transient dynamics

In this section we test whether the $F-type$ forcing method is capable of delivering a velocity perturbation (within a linear approximation) attaining the target Tu^{linear}. The initial condition is set to $\boldsymbol{u}(\boldsymbol{x}, t = 0) = \boldsymbol{0}$, and the synthetic volume forcing constructed using equation (4.22) is injected into equation (4.3). In figure 4.5 one can observe the time evolution of the perturbation energy, which increases from zero up to the prescribed target value, regardless of the number of frequencies used to discretize the energy spectrum, N_ω. The asymptotic behaviour, related to the particular solution, is attained as long as the homogeneous solution is damped out, see equation (4.6), for a time $t \to \infty$. To characterize the transient behaviour we define the *Rising Time* (RT) so that:

$$\left| \frac{Tu(RT) - Tu^{linear}}{Tu^{linear}} \right| \leq \epsilon, \tag{4.28}$$

where ϵ is arbitrarily small; in the present work $\epsilon = 10^{-3}$. As shown in figure 4.5, RT increases as long as N_ω increases, being approximately proportional to the fundamental frequency of the whole forcing signal. It is worth noting that, while for $N_\omega = 1$ we have $RT \propto 2\pi/\omega$, when increasing N_ω the rising time rapidly becomes inconveniently long (de Cheveigné and Kawahara, 2002). In order to remove this transient behaviour we set as

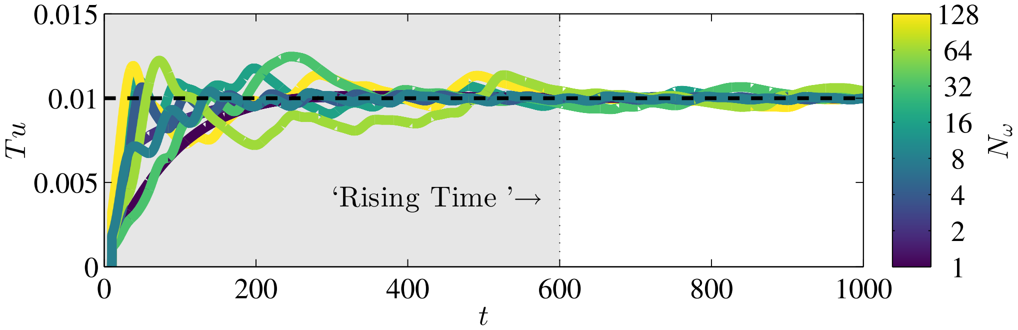

Figure 4.5 – Time evolution of turbulent intensity extracted from a linearised DNS forced by the F-type method with $Tu^{linear} = 0.01$, $\boldsymbol{u}(\boldsymbol{x}, t = 0) = \boldsymbol{0}$, and for different N_ω and $N_{\alpha,\beta} = 4$ as indicated in the legend. The prescribed turbulence intensity Tu^{linear} is attained after a finite *rising time*, when the transient behaviour has left place to an asymptotic regime.

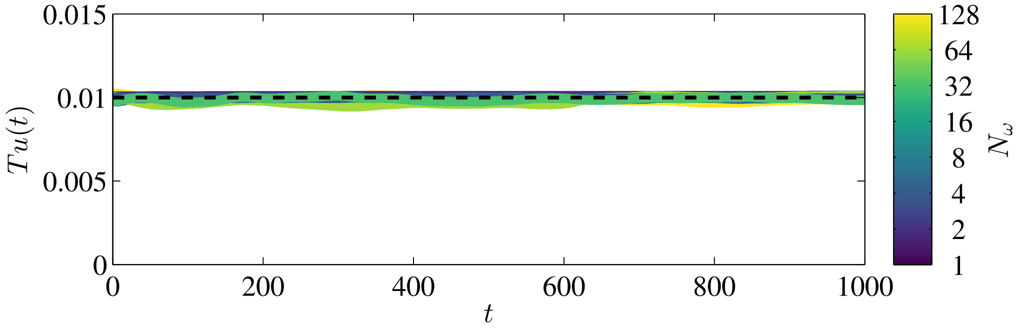

Figure 4.6 – Same as in figure 4.5, but with $\boldsymbol{u}(\boldsymbol{x}, t = 0) = \boldsymbol{u}_{opt}$. Differently from figure 4.5, the flow immediately settles to the asymptotic regime, without any rising time.

initial condition the velocity perturbation resulting from equation (4.8) for the previously constructed synthetic forcing, imposing both $\boldsymbol{u}$ and $\boldsymbol{f}$ with the associated time phases predicted by the resolvent analysis. In this way, we are able to cancel out the rising time, as shown in figure 4.6, attaining the desired Tu^{linear} already at $t = 0$. From now onward all our simulations are initialised as shown in this section.

4.2.2 Recovering the optimal dynamics

To further test our numerical setup we verify whether our fully 3D simulation is able to recover the 1D behaviour predicted by the optimal forcing analysis. Thus, we construct a forcing whose energy is concentrated on only one given couple of spatial wavenumbers, namely $\alpha = 1.12, \beta = 0.0$ ($N_{\alpha,\beta} = 1$), and 8 temporal frequencies ($N_\omega = 8$). The energy spectrum of the input signal (squares), as well as that of the output perturbation as provided by the numerical simulation (circles) and by the resolvent analysis (diamonds) are depicted in figure 4.7. The system energy response $||\boldsymbol{u}||_E^2$ matches the theoretical one $R(\omega)||\boldsymbol{f}||_E^2$ within the forcing range $[\omega_{min}, \omega_{max}]$. Conversely, for higher frequencies the energy level predicted by the resolvent analysis is well below the threshold observable with our DNS code, which is affected by numerical noise. One can also notice the large energy gap between $||\boldsymbol{u}||_E^2$ and $||\boldsymbol{f}||_E^2$: this is due to the *optimal* shape of the forcing for each given frequency, providing high values of the resolvent norm R. Thus, the F-type forcing method provides, within a linearized framework, the lowest possible input forcing amplitude for a given target output energy.

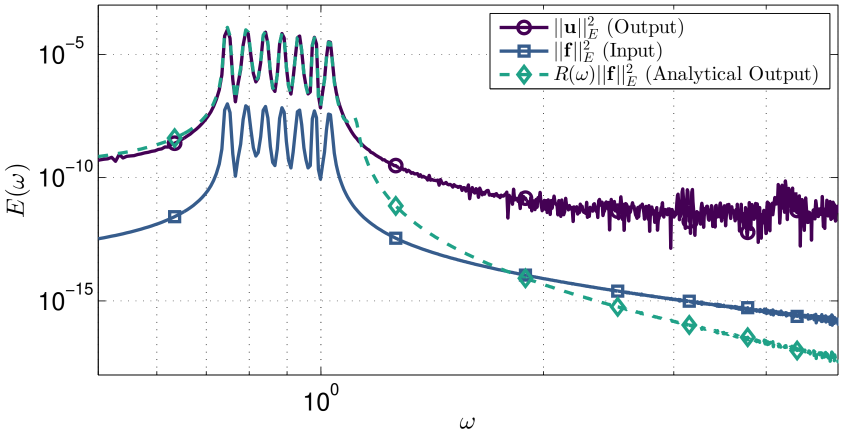

Figure 4.7 – Energy spectra of the forcing (blue solid line) and associated response obtained by DNS (purple solid line) and by the resolvent analysis (dashed line) with $N_{\alpha,\beta} = 1$, $(\alpha = 1.12, \beta = 0.0)$, $N_\omega = 8$, and $[\omega_{min}, \omega_{max}] \approx [0.747, 1.120]$.

4.2.3 Spectrum analysis

In this subsection we investigate the influence of N_ω on the energy spectrum recovered through DNS with F-type forcing.

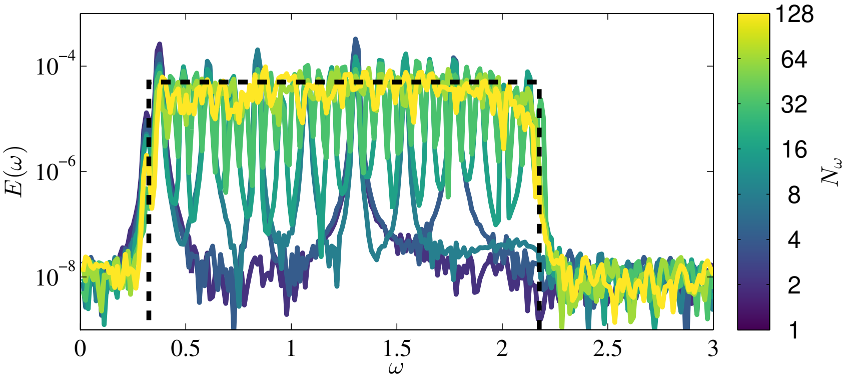

Figure 4.8 – Energy spectra extracted from several DNS using different values of N_ω. The dashed line represents the target energy spectra prescribed for constructing the F-type forcing.

In figure 4.8 one can observe that the shape of the spectra deeply changes with N_ω, becoming less spiky when this parameter is increased. Moreover, the area below the curve $E(\omega)$ must be the same for all the simulations, being Tu^{linear} constant. This results in a flattening of the energy spectra for $N_\omega \to \infty$. In particular, it appears that the energy spectra become almost independent from N_ω when more than 64 forcing modes are used. Thus, we set $N_{\alpha,\beta} = 4, N_\omega = 64$ throughout the reminder of the present work.

As a further validation of the method, we have imposed a different target energy spectrum, namely that extracted from DNS of a fully turbulent channel flow. First, we have recovered the turbulent energy spectrum at $Re_\tau = 210$ (see purple line in figure 4.9), resulting from turbulent transition starting from the laminar flow at $Re = 5000$. Then, we

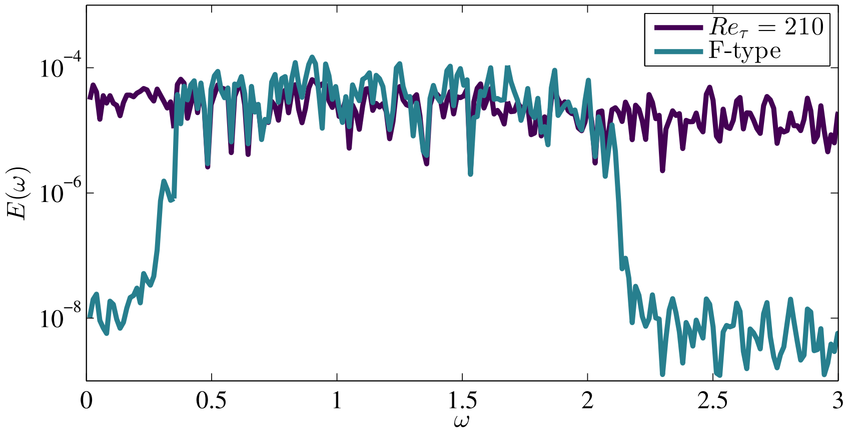

Figure 4.9 – Energy spectra extracted from a fully developed turbulent channel flow $Re_\tau = 210$, used as target energy spectra for constructing a F-type forcing. The method, that for this test has been constrained to be deployed within a forcing range $[\omega_{min}, \omega_{max}] = [1/3, 2]$ for sake of visualisation, can accurately mimic the signature of a turbulent flow, as well as the FST for the flow over a flat plate. Here we have used $N_\omega = 64$ and $N_{\alpha,\beta} = 4$.

have set it as a target spectrum in a further computation where the F-type volume forcing is imposed, in order to show that our method is capable of reproducing a stochastic volume forcing with any given spectrum. This is clearly demonstrated by the light blue curve, which follows closely the purple one representing the prescribed turbulent spectrum, within the selected frequency range. Please notice that the energy associated to each frequency recovered in a fully turbulent channel flow remains close to the mean value independently of the frequency, justifying our initial choice to use a flat energy spectrum. In fact, a flat energy spectrum would be recovered by ensemble-averaging several realisations of the turbulent flow in the same conditions.

4.3 Non-Linear Dynamics

In the previous section we have shown how the $F-type$ forcing method is capable of providing, within the linear framework, a synthetic *noisy* velocity perturbation with prescribed Tu^{linear}. However, it is still to be verified whether the provided method is capable of triggering transition for a given target energy level, eventually leading to sustained turbulence. Aiming at a qualitative and quantitative comparison of our non-linear results with the literature, we set Re and the domain size $L_x = 2\pi/\alpha\, L_z = 2\pi/\beta$, with $\alpha = 1.12, \beta = 2.10$ in order to match the well known $K-type$ channel-flow transition case investigated in Nishioka et al. (1975); Sandham and Kleiser (1992b), that is commonly used as benchmark in numerous numerical studies of turbulent transition (Schlatter et al., 2004; Lee and Zaki, 2017; Zhao et al., 2014, 2016). From now onward we will show results derived from Direct Numerical Simulation of the fully non-linear Navier–Stokes equations, all computed for $N_\omega = 64, N_{\alpha,\beta} = 4$, using the procedure summarised in algorithm 1, using the same Re and numerical discretisation applied in section 4.2.

4.3.1 Evolution of the turbulence intensity

Once the domain size and the parameters N_ω and $N_{\alpha,\beta}$ have been selected, the only physical control parameter that remains to be set is the intensity of the energy perturbation field generated by the forcing perturbation, which coincides with Tu^{linear} in the linear regime. Figure 4.10 shows the evolution of Tu measured in 6 direct numerical simulations (solid lines) forced using the *F-type* method with different target energy levels Tu^{linear}. For low levels of Tu^{linear}, the system response to the forcing matches the linear prediction as expected (Tu^{linear} remains equal to the imposed level $Tu = 10^{-4}$), as shown by the bottom line designated as *linear*. Increasing Tu^{linear} we observe that the perturbation energy slowly increases starting from the imposed level Tu^{linear}, reaching asymptotic saturation. This phenomenon is due to the fact that the prescribed forcing energy level is high enough to trigger non-linear effects, even if the flow still remains in the laminar regime. Further increasing Tu^{linear} one can observe, after an initial slow increase of Tu due to the previously mentioned *nonlinear laminar phase*, a sharp jump in Tu due to laminar-turbulent transition. Thus, the transition threshold for an initial Tu^{linear} sits between the two lines designated as *laminar* and *turbulent*, for the prescribed value of the Reynolds number. Increasing the energy of the forcing beyond the transition level one can observe that the *nonlinear laminar phase* shrinks in time, leading to transition in lower simulation time. It is worth to notice that, regardless of the initial energy level, the final Tu for the statistically converged turbulent cases remains the same. The transition scenario obtained for the case with $Tu^{linear} = 0.5\%$ (corresponding to the yellow line in figure 4.10) is depicted in figure 4.11. The streamwise component of the forcing (top) and of the resulting response (middle) as well as the response λ_2 surfaces (bottom) are provided at $t = 25, 75, 130, 215$ along with the Re_τ curve (see equation 4.29) allowing to identify the different stages of transition. At first, the velocity perturbations resulting from the receptivity of the flow to the volume forcing are localized in the flow bulk (see box (a) of the figure). This bulk noise then penetrates close to the wall through receptivity triggering elongated streamwise velocity perturbations (box (b)). A fully non-linear transitional phase is reached when these streaky structures become unstable generating vortices on their top and flanks, among which some hairpin-like vortices can be recognized in box (c). Finally, after breakdown to turbulence, the flow becomes statistically homogeneous in both spanwise and streamwise direction (see box (d)).

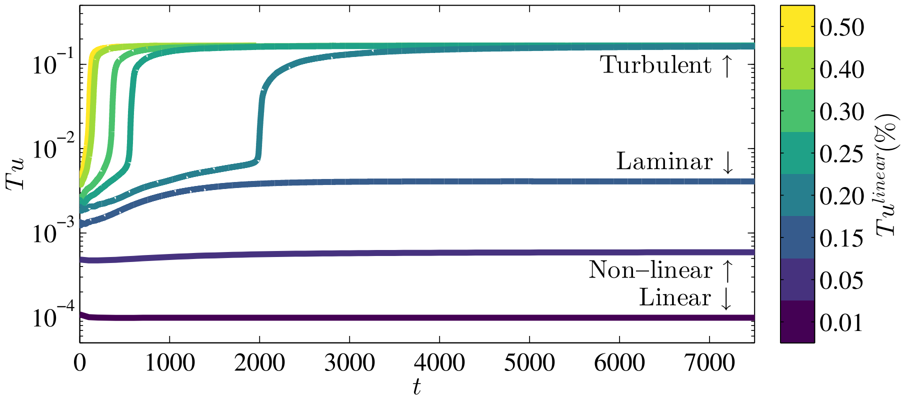

Figure 4.10 – Time evolution of Tu measured in different nonlinear DNS where the F-type forcing has been imposed at different target energies Tu^{linear} indicated in the legend.

4.3.2 Wavenumber decomposition

A powerful tool to study and unveil the mechanisms occurring in the first stages of transition is to analyse the mode-by-mode energy evolution, performing a spatial Fourier

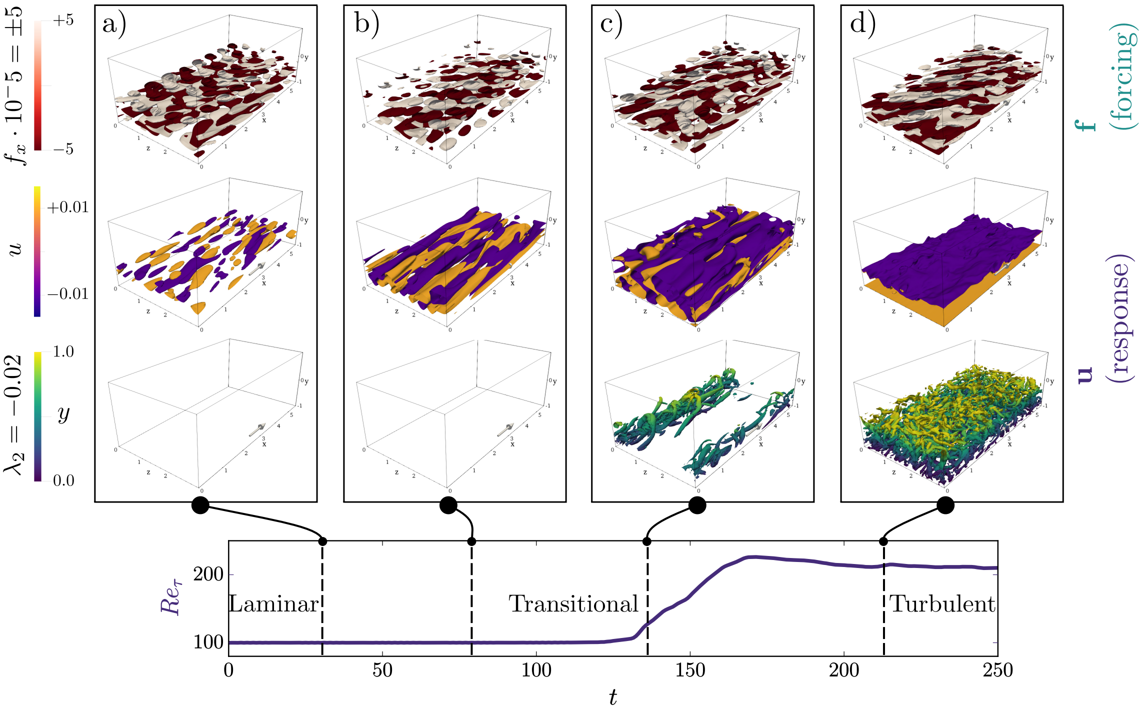

Figure 4.11 – Uncontrolled transition scenario obtained with the F-type method. Boxes a), b), c) and d) depict the isosurfaces of the streamwise component of the forcing (top), the streamwise velocity perturbation u (middle) as well as the isosurfaces of the λ_2 criterion to visualise the onset of coherent vortical structures. The snapshots are extracted from a DNS of a 3D transitional channel flow with $Tu^{linear} = 0.5\%, N_\omega = 64, N_{\alpha,\beta} = 4$, for $t = 25, 75, 130, 215$, respectively; the lower plot represents the friction Reynolds number Re_τ (see equation (4.29)), which indicates whether transition has taken place. Only the lower half of the channel is displayed for sake of clarity.

decomposition of the flow field at each timestep (Zang and Krist, 1989; Reddy et al., 1998). The results of this procedure are shown in figure 4.12, where the different spatial modes are identified by the couple of integers (i_α, i_β) indicating the i^{th} multiples of the fundamental wavenumbers $2\pi/L_x$, $2\pi/L_z$ (see also (Reddy et al., 1998)).

For high enough Tu levels, streamwise invariant *streaky* structures (identified by modes $(0, i_\beta)$ rapidly appear and grow in amplitude, despite not being injected in the flow via the synthetic forcing/response, for the reasons discussed in section 4.1.3. This is probably due to the fact that the *optimal* perturbation (Schmid, 2007) for shear flows has the form of a pair of streamwise streaks; thus, this kind of streamwise-invariant structure is also the most likely to occur when the laminar flow is perturbed, as discussed by Luchini (2000). For low values of Tu^{linear} (frame 4.12b) the streaky modes are characterized by an amplitude comparable with that of the other modes, and of the linear forcing itself. Increasing the value of Tu^{linear} (frame 4.12c) we observe a strong increase of their amplitude leading to nonlinear saturation, despite the flow remaining laminar, as discussed before. For the largest value of Tu^{linear} (frame 4.12d) secondary instability of the streaks is triggered after nonlinear saturation, leading to turbulence. A similar behaviour has been observed by Reddy et al. (1998) when triggering transition by using noise (constructed as a sum of random Stokes modes) as initial condition in a temporal channel flow, as provided in figure 4.13 (left frame). Comparing these literature results with those obtained by the

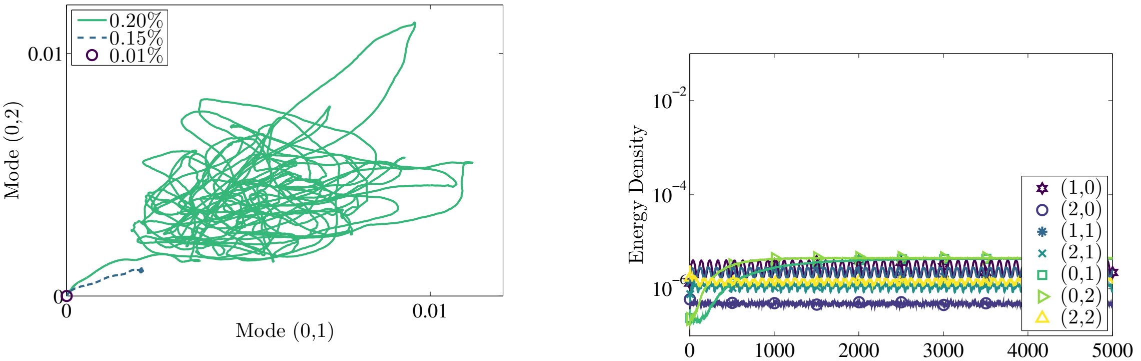

(a) Phase portrait for different Tu^{linear}. Amplitude of the first two streamwise invariant Fourier components.

(b) Time evolution of the energy density of different Fourier modes for $Tu^{linear} = 0.01\%$

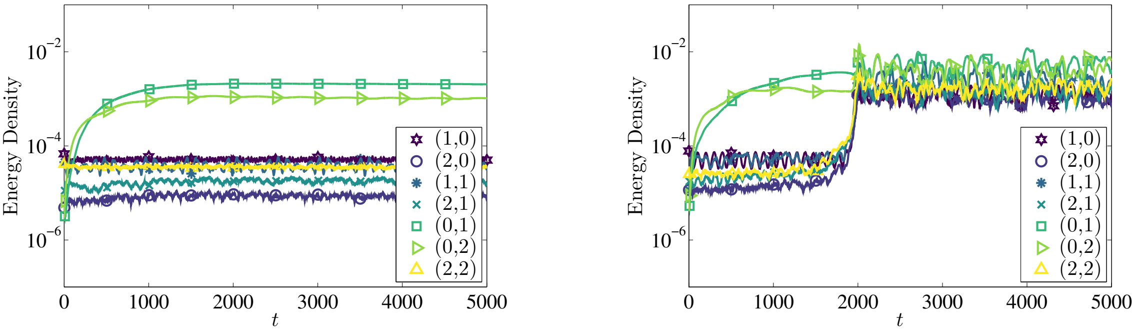

(c) Time evolution of the energy density of different Fourier modes for $Tu^{linear} = 0.15\%$

(d) Time evolution of the energy density of different Fourier modes for $Tu^{linear} = 0.20\%$

Figure 4.12 – Energy density of selected Fourier components (i_α, i_β) for different values of Tu^{linear}. Subframe (a) is a phase portrait representing the evolution of the first two streamwise-invariant modes generated by the non-linear interactions, usually referred as *streaks* (Schmid and Henningson, 2001), for different values of Tu^{linear}. Subframes (b,c,d) show the emergence of the streaky modes from the forced background noise. Depending on the forcing energy levels, several flow behaviours are observed, from laminar to turbulent (see figure 4.10).

F-type forcing method for high Tu^{linear} values (right frame), one can observe that the time evolution of the energy density of the Fourier components is similar, although some discrepancies can be found. For instance, at the very beginning of the F-type transition process, modes $(1, 0)$, $(1, 1)$, and $(0, 1)$ strongly increase their energy due to the high receptivity of the flow to the imposed forcing. Whereas, when random Stokes modes are used, an initial decrease of these modes energy is observed, followed by an energy increase of the streaky modes only. This notable difference in the initial phases of transition can be better visualized in figure 4.14, showing the early time evolution of Tu in both cases. When the flow is fed with random noise, a non-physical initial transient is observed, where Tu initially decreases while the disturbance is adapting itself to the underlying Navier-Stokes equations, then steeply increases again, saturates, and begin to substantially grow (mostly due to non-linearity) only at $t \approx 60$. Whereas, when the F-type method is used, Tu increases algebraically already at the very beginning of the simulation, since the flow receptivity is exploited optimally to trigger energy growth. This allows to induce transition with lower amplitude perturbations as compared to random noise.

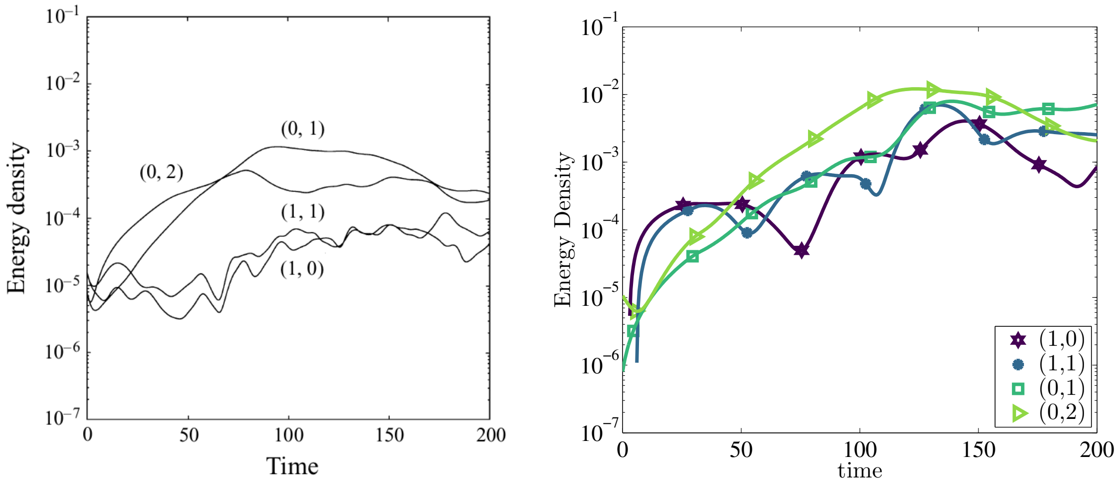

Figure 4.13 – Energy density of selected Fourier modes (i_α, i_β) for a DNS with initial condition composed by random Stokes modes (N-type transition) as computed by Reddy et al. (1998) (left frame) and for the F-type forcing method (right frame) both for $Re = 5000$. The energy of the initial perturbation for the N-type transition is $||\boldsymbol{u}(t = 0)||_E \approx 2e^{-4}$. The forcing intensity for the F-type method has been set so that the induced velocity field attains the same energy value. Even though the velocity fields induced by the F-type method are initially devoid of $\alpha = 0$ modes, these modes rapidly grow in amplitude overtaking the other ones, as also observed in the N-type transition

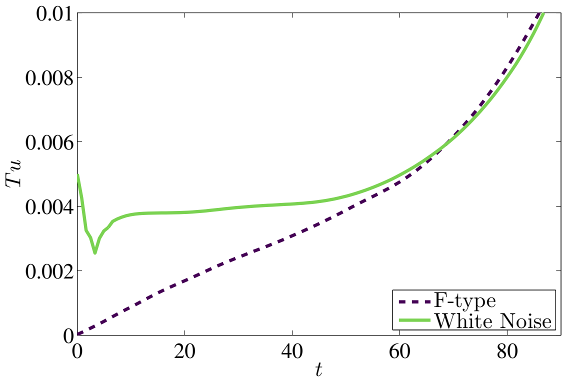

Figure 4.14 – Time evolution of Tu during the initial phases of transition for the F-type method and for white noise perturbations. $Tu^{linear} = 0.05\%$ is used for the F-type method, while the initial random noise has been scaled in order to reach $Tu(t = 0) = 0.05\%$ as well. The Tu growth in the initial phase is almost linear for the F-type method.

4.3.3 Transition energy thresholds

As the transition location in a spatially-evolving flow is strongly influenced by the intensity of the incoming perturbed flow (Schlatter et al., 2004), in a streamwise periodic flow the transition time is directly affected by the chosen Tu^{linear}. To identify transition to turbulence we measure the Reynolds number based on the friction velocity:

$$Re_\tau = \sqrt{Re \left| \frac{\partial \langle u \rangle}{\partial y} \right|_{wall}}, \tag{4.29}$$

where $\langle\cdot\rangle$ represents the spatial average in the two homogeneous directions at a given time. The time evolution of Re_τ for several values of Tu^{linear} is shown in figure 4.15 by the continuous lines, compared to the standard K-type transition scenario (Schlatter et al., 2009) (dashed line). Comparing figure 4.10 with 4.15 one can observe that Re_τ strongly overtakes the initial laminar value only when turbulence is attained, confirming that its value can be used to detect when transition has taken place. Thus, figure 4.15 shows that the transition time decreases monotonically with the forcing energy Tu^{linear}, similarly to the transition position in boundary layer flows (Brandt et al., 2004b). Therefore, it appears that using the F-type forcing method one can easily control the transition time changing the control parameter Tu^{linear}.

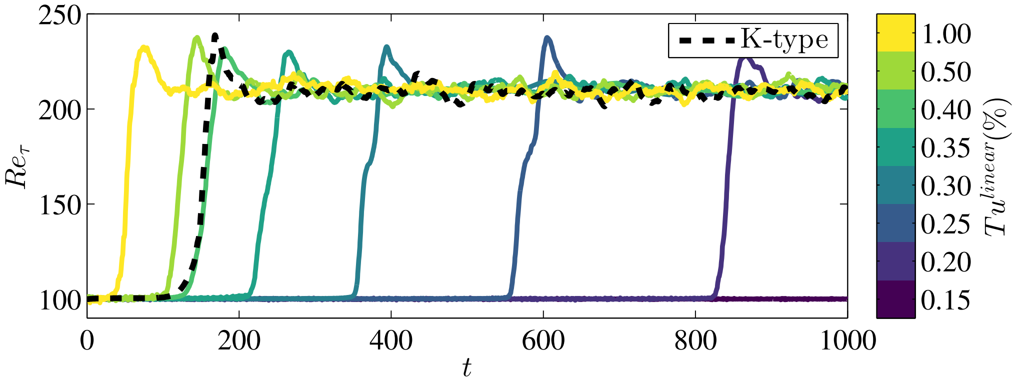

Figure 4.15 – Time evolution of Re_τ for the standard K-type transition scenario (Schlatter et al., 2009) (dashed line) and the F-type forcing method for several forcing levels (continuous lines coloured by the imposed Tu^{linear} value).

It is also worth to investigate the threshold energy able to trigger turbulence using the F-type method, as compared to other transition scenarios. The threshold energy density for different transition scenarios in channel flow is provided in figure 4.16 for different values of Re. Following Reddy et al. (1998), we consider that transition has taken place when $Re_\tau(t)$ overtakes the value $1.01 Re_\tau(laminar)$. As one can observe in figure 4.16, the threshold energy density of the velocity perturbation field induced by the F-type forcing is comparable to that needed for triggering turbulence by using random perturbations (N-type scenario). However, there is a crucial difference between the F-type method and the N-type scenario. Figure 4.17 provides the velocity perturbation energy $||\boldsymbol{u}||_E = \frac{1}{2V}\int_V \boldsymbol{u}^2(\boldsymbol{x},t)d\boldsymbol{V}$ and its corresponding forcing norm $||\boldsymbol{f}||_E = \frac{1}{2V}\int_V \boldsymbol{f}^2(\boldsymbol{x},t)d\boldsymbol{V}$. Since the flow is excited by a weighted sum of optimal forcings, the highest possible gain between the forcing itself and the induced velocity field is attained (Schmid, 2007). The curves in the figure show that the volume forcing energy injected within the flow is two to three orders of magnitude lower than the energy of the noisy velocity perturbation inducing transition. Thus, the F-type forcing method triggers transition to turbulence relying on a low-amplitude noisy volume forcing, without prescribing unrealistic initial perturbations linked to specific transition mechanisms (such as streamwise rolls, oblique waves, etc.) like the classical scenarios proposed in the literature.

4.4 Turbulent state

In this section, the statistically converged turbulent state induced by the F-type forcing method with $Tu^{linear} = 0.5\%$ is analysed, in comparison with that of the standard K-type

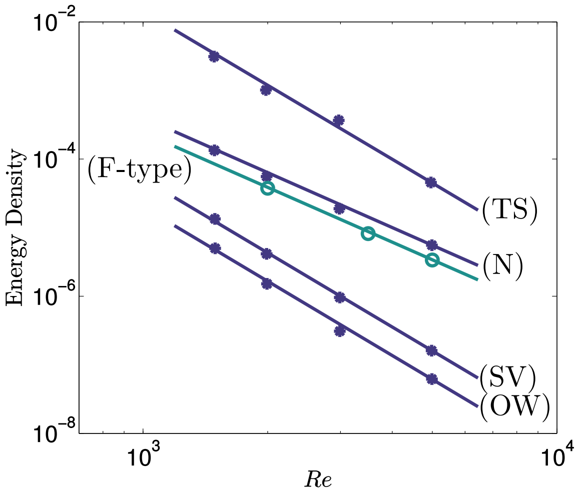

Figure 4.16 – Threshold energy densities for triggering transition using the synthetic forcing method proposed here (F-type) and for several transition scenarios (Reddy et al., 1998) where different velocity fields are used as initial condition, namely Tollmien-Schlichting waves (TS), random noise (N), streamwise vortices (SV) and oblique waves (OW).

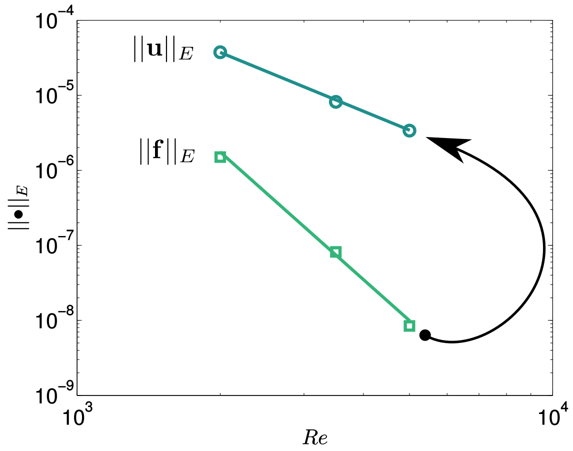

Figure 4.17 – Threshold energy densities for triggering transition of the imposed forcing as well as the resulting velocity perturbations, $||\boldsymbol{f}||_E$ and $||\boldsymbol{u}||_E$, whose amplitude is scaled by the resolvent norm R. The slope of the $||\boldsymbol{u}||_E$ and $||\boldsymbol{f}||_E$ lines differs since the resolvent norm R increases with Re

transition method (Schlatter et al., 2004). The fundamental wavenumbers $\alpha = 1.12, \beta = 2.10$ are chosen, the dimensions of the numerical domain being $2\pi/\alpha \times 2 \times 2\pi/\beta$, discretized on a $N_x \times N_y \times N_z = 192^3$ grid. Schlatter et al. (2004), starting with Reynolds number $Re = (UH)/\nu = 5000$ measured at the centerline, and keeping a constant flow rate throughout the whole simulation, reached a friction Reynolds number $Re_\tau \approx 208$ is defined using the friction velocity

$$u_\tau = \sqrt{\frac{\tau_{wall}}{\rho}} \tag{4.30}$$

with local shear stress at the wall given by:

$$\tau_{wall} = \mu \left| \frac{\partial \langle u \rangle}{\partial y} \right|_{wall}. \tag{4.31}$$

Using this value of the friction Reynolds number the chosen domain size and the grid resolution can be expressed in wall units as:

$$[L_x^+, L_y, L_z^+] = [\approx 1165, 2, \approx 435] \tag{4.32}$$

$$[\Delta x^+|_{mean}, \Delta y^+|_{wall}/\Delta y^+|_{centre}, \Delta z^+|_{mean}] = [7.3, 0.040/4.1, 3.9]$$

where the superscript $^+$ indicates adimensionalisation with respect to wall units, with

$$u_\tau = Re_\tau / Re_{centerline}^{laminar} \approx 0.0417$$

and $l^+ = 1/Re_\tau \approx 0.00481$. Thus, the selected computational domain is much larger than the minimal flow unit (Jiménez and Moin, 1991) and the grid size is sufficiently small to accurately describe a turbulent flow (Schlatter et al., 2004). The time averages presented in this chapter are based on a period of $T = 500$ time units starting 500 time units after transition takes place.

Following Ricco et al. (2012), the average of the three-dimensional, time dependent field $f(x, y, z, t)$ in the homogeneous directions x and z reads:

$$\overline{f}(y,t) = \frac{1}{L_x L_z} \int_0^{L_x} \int_0^{L_z} f(x,y,z,t)\; dx\; dz. \tag{4.33}$$

The velocity field can be thus decomposed as

$$\mathbf{u} = \{\overline{U}(y,t), 0, 0\} + \{u', v', w'\} \tag{4.34}$$

as well as the forcing field

$$\mathbf{f} = \{\overline{F}(y,t), \overline{G}(y,t), \overline{H}(y,t)\} + \{f', g', h'\}. \tag{4.35}$$

It is important to note that in the F-type forcing method the spatial average of the forcing is strictly zero ($\{\overline{F}, \overline{G}, \overline{H}\} \equiv \{0,0,0\}$), being constructed by a linear composition of Fourier modes in the homogeneous directions. Assuming f to be statistically steady over N periods of length T, we can define the phase average of $\overline{f}(y,t)$ as $\hat{f}(y,\tau)$, that can be written as:

$$\hat{f}(y,\tau) = \frac{1}{N} \sum_{n=0}^{N-1} \overline{f}(y, nT + \tau). \tag{4.36}$$

The space-time average over a period T is:

$$\langle f \rangle(y) = \frac{1}{T} \int_0^T \hat{f}(y,t)\; dt \tag{4.37}$$

and the global quantity $[f]_g$ is obtained integrating $\langle f \rangle(y)$ in the wall-normal direction:

$$[f]_g = \int_0^h \langle f \rangle(y)\; dy. \tag{4.38}$$

4.4.1 Statistics and energy budget

Figures 4.18a and 4.18b show the zero-th and first order statistics of fully turbulent DNS where transition has been triggered following different transition paths. As expected, the results of the different simulations are indistinguishable.

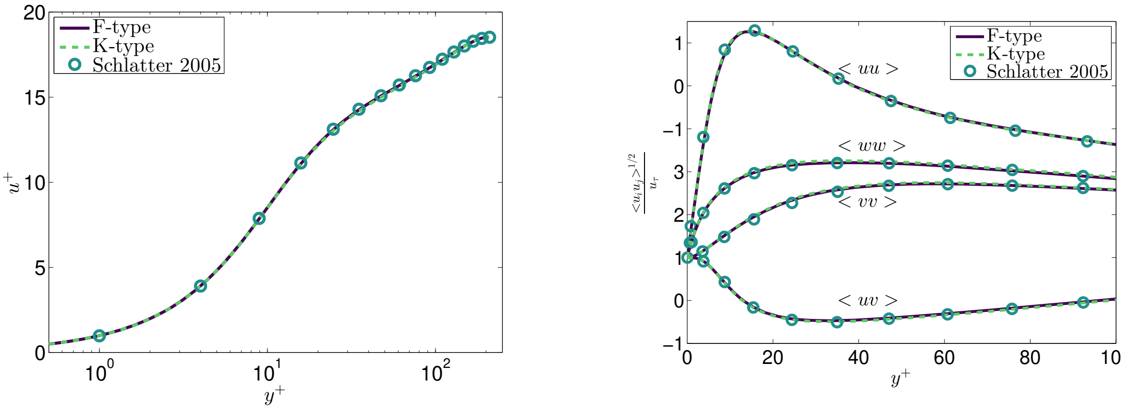

(a) Mean Velocity profiles $u^+ = \langle u \rangle / u_\tau$

(b) Reynolds stresses

Figure 4.18 – Comparison of mean flow and Reynolds stresses extracted by fully turbulent DNS for a classical K-type (Schlatter et al., 2004) transition scenario as well as the F-type forcing method.

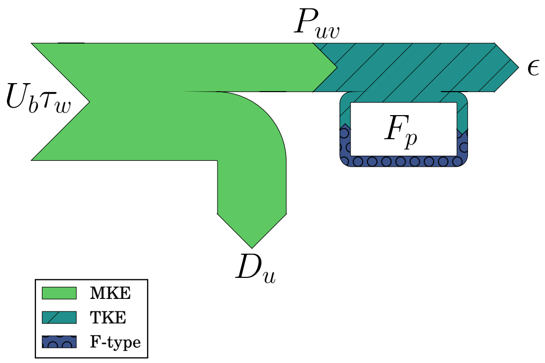

Figure 4.19 – Sketch of the global energy balance in a channel flow. Arrow widths are proportional to the corresponding values, except F_p that is scaled by a factor of 1000 for the sake of visualization and exists only if a volume forcing is used. Energy is initially pumped into the flow via the $U_b \tau_w$ term. One part is dissipated by the mean flow (D_u), the rest is transferred to the fluctuations via the production term of the turbulent kinetic energy P_{uv}, which eventually coincides with the turbulent dissipation ϵ. The F-type method creates an additional sink-source energy F_p, but its effect turns out to be negligible.

In order to determine whether the F-type forcing method affects in some way the energy balance within the turbulent flow, we analyse the transport equations of the Mean and Turbulent Kinetic Energy (MKE and TKE), identifying the terms associated with the volume forcing. The transport equations of the MKE and TKE are detailed in appendinx A, where it is also shown that the volume forcing affects the TKE equation, only. A sketch of the energy budget in a statistically turbulent channel flow is provided in figure 4.19. In a fully turbulent channel flow, since both MKE and TKE are statistically zero, the energy pumped by the pressure gradient is transferred by the production term to the flow oscillations and dissipated by the mean flow as well as by the turbulent fluctuations. This standard scenario (Pope, 2000) is altered by the F-type volume forcing due to the introduction of an energy term linked to the forcing itself, F_p, whose form and derivation is detailed in appendix A. In order to determine the amount of energy produced or dissipated by the volume forcing, we compute the time evolution of the different terms of the Kinetic Energy Budget (KEB), as in equation (A.14) in a statistically converged turbulent flow arising from different transition scenarios. The different terms are plotted in figure 4.20a, where one can observe that the term F_p associated to the forcing in equations (A.15) is three to four order of magnitudes smaller than the other production or dissipation terms. Thus, this term can be considered negligible in the energy balance account. In fact, in figure 4.20a one cannot distinguish between the energy terms of the turbulent states obtained by the K-type and F-type methods, although in the latter the volume forcing remains active throughout the simulations. Figure 4.20b provides a phase portrait describing the laminar–turbulent transition paths for the K-type and F-type methods. The time evolution of the production term P_{uv} and the turbulent dissipation ϵ is very similar for both transition scenarios. Moreover, when the final turbulent state is reached, the energy budget terms perfectly match.

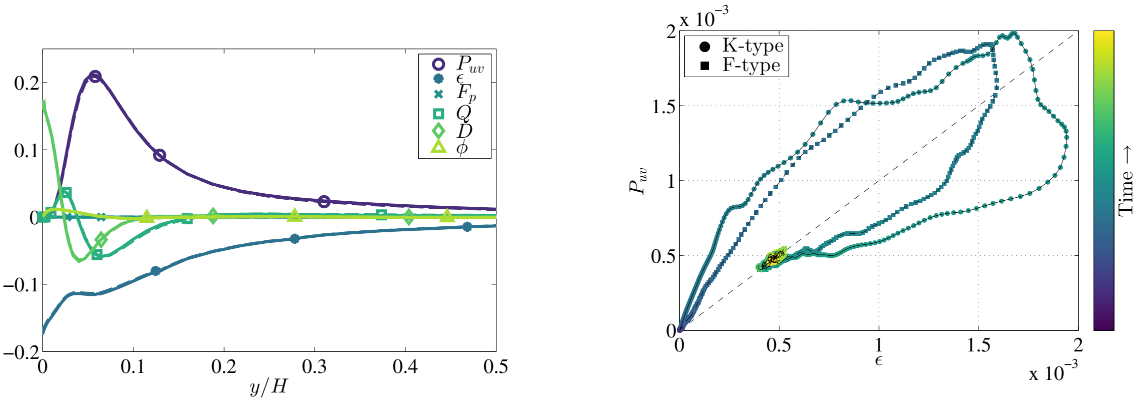

(a) Kinetic energy budget (A.14) for turbulent states triggered via K-type (solid line) and F-type (dashed line) transition methods.

(b) Comparison of the time evolution of production (P_{uv}) and turbulent dissipation (ϵ) terms during laminar-turbulent transition triggered with K-type and F-type methods.

Figure 4.20 – Turbulent Kinetic Energy Decomposition plots. Labels are defined in A.

4.4.2 Energy spectrum comparison

To further analyse the turbulent flow we plot in figure 4.21 the one-dimensional energy spectra for the turbulent states triggered via the K-type and F-type transition, compared to the benchmark data extracted from Moser et al. (1999). The energy density associated with large wavenumbers is several order of magnitudes lower than that at low wavenumbers, confirming that the grid resolution is adequate for accurately describing a turbulent state. However, one can observe that, for low wavenumbers, the energy spectrum does not perfectly match the benchmark values when the F-type forcing method is used. In order to find a possible reason for this weak discrepancy we analyse the time variation of the friction Reynolds number, provided in figure 4.22. Comparing in figure 4.22a the Re_τ signals issued from the turbulent states obtained with the K-type and F-type methods, one can observe that the latter is characterised by higher frequency oscillations than the former. Performing a Fourier transform in the time range $500 \leq t \leq 1000$ and invoking Taylor's relation linking spatial and temporal frequencies, we have found that these high frequencies match with those imposed using the F-type volume forcing, as represented in

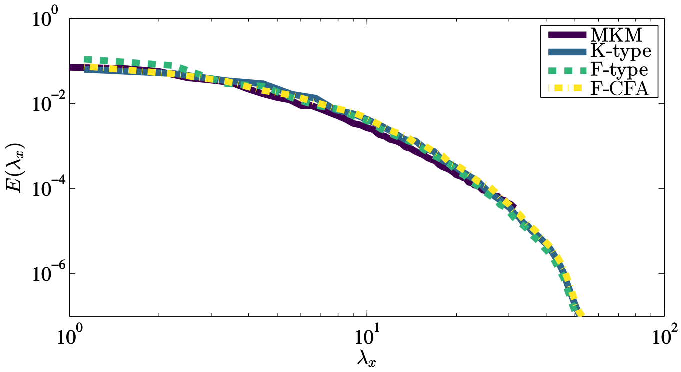

Figure 4.21 – Comparison of the streamwise velocity one-dimensional turbulent energy spectra E_{uu} for $\Re_\tau = 210$ at $y = 0$ (midplane) for the K-type, F-type, and F-type with Controlled Forcing Amplitude (F-CFA) method, as discussed in section 4.4.3, as well as for the MKM benchmark literature case at $Re_\tau = 180$ from Moser et al. (1999). The spectrum recovered with the F-type method slightly deviates from the expected result, as a result of the presence of the volume forcing. This behaviour can be avoided by simply switching the forcing off as explained in section 4.4.3, resulting in the F-type with Controlled Forcing Amplitude case. The slight misalignment between the spectra obtained from the present computations (K-type, F-type and F-CFA) and the reference case is due to the fact that the former are computed for $Re_\tau = 210$, while the latter for $Re_\tau = 180$.

figure 4.22b. To verify that the discrepancy of the spectra is indeed due to the imposed volume forcing, we suspend it once a fully turbulent state is obtained (for $t \geq 500$ in the considered case). In figure 4.22a the resulting Re_τ signal is provided. The high frequency oscillations rapidly decay when the forcing is interrupted, resulting in a spectrum devoid of spurious peaks, as shown in figure 4.22b. Finally, figure 4.21 shows that once turned off the forcing, the energy spectrum matches the benchmark one.

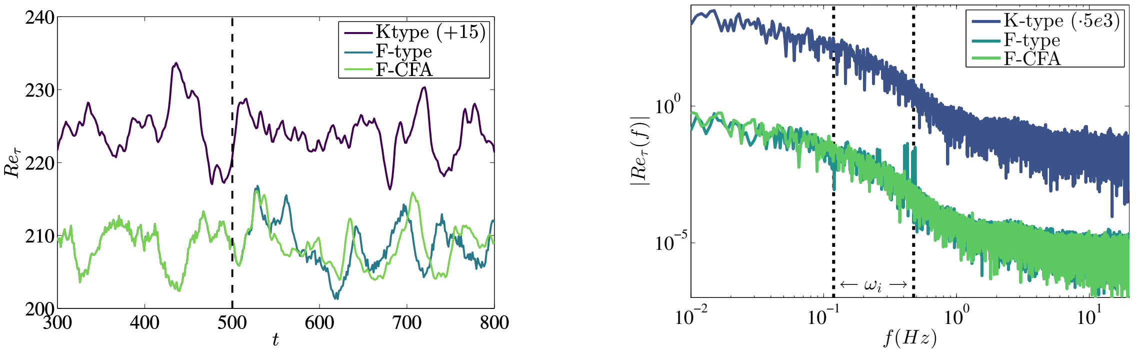

(a) $Re_\tau(t)$ signals. The vertical dashed line represents the time at which the forcing is interrupted.

(b) Re_τ spectra for the signals presented on the left frame; ω_i indicate the forcing frequency range for the F-type method.

Figure 4.22 – Re_τ time signals and spectra for K-type (blue line), F-type (light blue line) and F-type with interrupted forcing (F-CFA, green line) methods. Spurious energy peaks in the F-type method occur within the same range of the forcing used to trigger transition, as indicated by the vertical lines in the right frame. If the forcing is turned off (for $t > 500$ as indicated by the vertical line in the left frame), these spurious energy peaks disappear. K-type related data are shifted by a factor of 5000 for sake of readability.

4.4.3 Automatic forcing amplitude control

We have shown in the previous subsection that the volume forcing needs to be turned off once the turbulent state is attained in order to avoid spurious frequencies in the energy spectrum. However, the time to reach a fully turbulent state depends on a number of factors, namely: the Reynolds number Re, the initial velocity disturbances shape and intensity (for K-type like methods), the Tu^{linear} forcing intensity (for F-type method), to cite a few. For this reason, in this section we aim at constructing a function capable of automatically adjust the forcing intensity without any a priori knowledge of the final state.

Towards this aim, we define two functions:

$$A_{shift}(t) = \frac{Re_\tau^A(t) - Re_\tau(t)}{Re_\tau^A(t)} \tag{4.39}$$

and

$$B_{shift}(t) = \frac{Re_\tau^B - Re_\tau(t)}{Re_\tau^B} \tag{4.40}$$

$Re_\tau^A(t)$ being an exponential moving average (see Holt (2004)), computed at each iteration, it, as:

$$\left[Re_\tau^A\right]^{it} = \left[Re_\tau\right]^{it} + e^{(-dt\cdot T)} \cdot \left(\left[Re_\tau^A\right]^{it-1} - \left[Re_\tau\right]^{it}\right), \tag{4.41}$$

where the prescribed averaging window is $T = 100$, dt is the time difference between the it^{th} and the $(it-1)^{th}$ iterations. Whereas, Re_τ^B is a function of the laminar Reynolds number only, namely, $Re_\tau^B = \sqrt{2 \cdot Re}$. Functions (4.39) and (4.40) have been constructed in order to show an opposed behaviour in the laminar and in the turbulent regime. In the laminar regime, being $Re_\tau^A \approx Re_\tau^B$, we have $A_{shift}(t) \approx B_{shift}(t)$; whereas, in the turbulent one, the difference $Re_\tau^B - Re_\tau$ will be much larger than $Re_\tau^A - Re_\tau$, resulting in $A_{shift}(t) \ll B_{shift}(t)$. Thus, for detecting transition to turbulence one can define the following function:

$$\Delta_F = \left|\frac{A_{shift}}{B_{shift}}\right| \tag{4.42}$$

which is used to gradually damp the F-type forcing once transition is triggered. Towards this aim, the forcing field issuing from the F-type forcing method is premultiplied by Δ_F, which becomes equal to zero right after the flow reaches a self-sustained turbulent regime, as provided in figure 4.23. In the same figure one can observe the time evolution of Re_τ in the *Controlled Forcing Amplitude* (CFA) case, together with its space-time average, showing the establishment of a fully turbulent flow. In pictures 4.23 and 4.25, we report the average value $[Re_\tau^A]^{it}$ (referred to as $< Re_\tau(t) >$ for the sake of notation), which appears to clearly indicate when transition is taking place, attaining a plateau when turbulence is finally achieved.

The transition scenario observed using the controlled amplitude F-type forcing with $Tu^{linear} = 0.5\%$ is depicted in figure 4.24. The streamwise component of the forcing and the λ_2 surfaces of the associated response are provided at $t = 110, 140, 150, 180$. The stochastic forcing begins to fade away when the nonlinear phase of transition is attained. At $t = 140$, a few isolated hairpin-like structures can be clearly observed, which rapidly create secondary hairpin vortices as well as small scale vortical structures (see the λ_2 surfaces in the bottom plots). At $t = 180$ the turbulence intensity is saturating towards an asymptotic value, indicating that fully developed turbulence is almost attained. The forcing shuts off when Tu reaches its asymptotic value and turbulent conditions are attained.

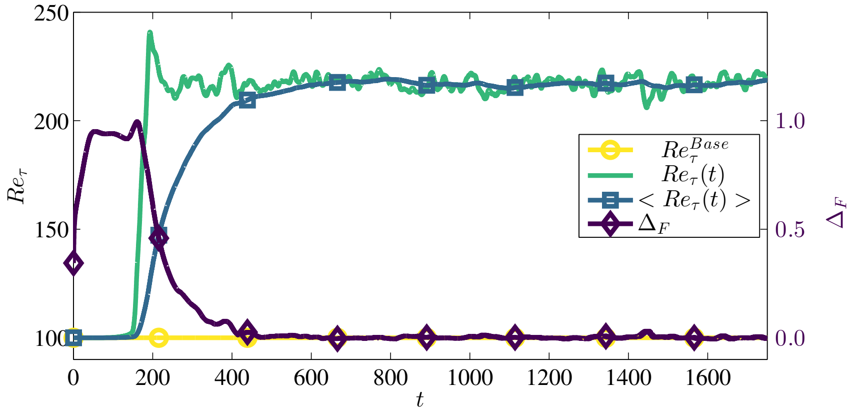

Figure 4.23 – Transition in a channel flow at $Re = 5000$ using F-type method with Controlled Forcing Amplitude (F-CFA). The forcing amplitude Δ_F continuously decreases as the friction Reynolds number increases, finally reaching a zero value when Re_τ attains the turbulent plateau.

We conclude this section by investigating whether the behaviour of the controlled amplitude parameter Δ_F is robust in a different flow setting. In fact, up to this point we have considered subcritical transition for $Re = 5000$, as depicted in figure 4.24, close to the threshold for linear stability (Schmid and Henningson, 2001), but considerably larger than the minimum Reynolds number at which transition to turbulence can be observed in a channel flow (Tsukahara et al., 2014), namely $Re \approx 1600$. For $Re < 1600$, turbulence is not self-sustained (Manneville, 2015); thus, an initial perturbation superposed to the base flow might induce transition for a finite time, but the flow will eventually relaminarize (Iida and Nagano, 1998). Applying the F-type forcing method with controlled amplitude in such case, for instance at $Re = 1250$, relaminarization is avoided since Δ_F never reaches zero, as shown in figure 4.25.

Whereas, by simply suspending the forcing beyond a threshold time, as done in figure 4.22a, relaminarization would have been attained. The controlled amplitude F-type forcing method is thus effective in inducing transition in the flow even at very low Reynolds numbers.

4.5 Conclusions

A new method is presented to build a continuous synthetic forcing capable of induce stochastic velocity perturbations with a prescribed energy level in wall-bounded parallel flows through receptivity mechanisms. The method is designed to provide a numerical framework for reproducing *uncontrolled* laminar-turbulent transition in wall-bounded parallel flows, characterised by high levels of external noise. Exploiting some concepts provided by linear stability and sensitivity analysis, such as the *resolvent norm*, we demonstrate that this method, which we refer to as F-type forcing method, is able to produce a stochastic velocity perturbation of prescribed energy level leading to turbulence. This goal is achieved by using a low-amplitude volume forcing composed of *optimal* forcing functions with different suitably chosen frequencies.

The method has been first tested in a linear framework using direct numerical simulations of the linearised Navier-Stokes equations, allowing a tuning of the numerical parameters. Then, direct numerical simulations of the fully nonlinear equations in the presence

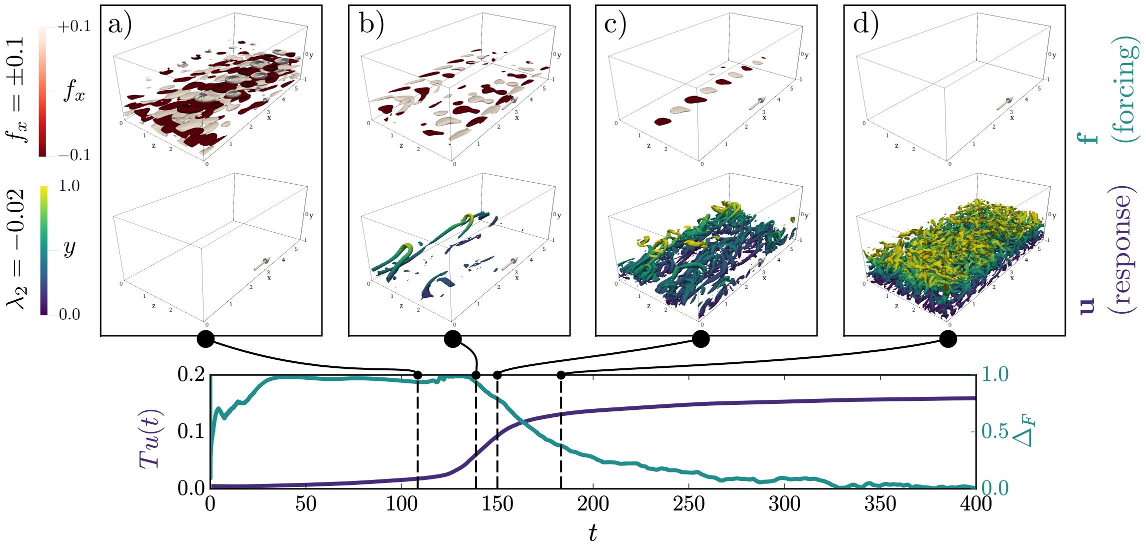

Figure 4.24 – Uncontrolled transition scenario, obtained with the F-type with Controlled Forcing Amplitude method. Boxes a), b), c) and d) depict the isosurfaces of the streamwise component of the forcing (top) and response (bottom) within the 3D transitional channel flow, for $t = 110, 140, 150, 180$, respectively; the lower plot represents the turbulent intensity Tu as well as the automatic forcing amplitude control intensity Δ_F in time. It can be clearly seen that, when turbulent conditions are attained, the forcing shuts off automatically. In this computation $Tu^{linear} = 0.5\%, N_\omega = 64, N_{\alpha,\beta} = 4$. Hairpin-like structures can be visualised in the λ_2-criterion surfaces during the late stages of transition, see b) and c). Only the lower half of the channel is displayed for sake of clarity.

of the F-type volume forcing have been performed to test the robustness of the method. Subcritical transition to turbulence induced by the prescribed forcing has been investigated and compared to other transition scenarios, where deterministic (and unrealistic) perturbations are imposed for obtaining a fully turbulent flow.

Finally, the fully developed turbulent flow induced by the F-type method has been investigated. Low-order statistics and energy balance equations are practically unaffected by the continuous synthetic forcing. However, in the energy spectra a slight discrepancy with respect to literature data is retrieved, that can be easily avoided by suspending the forcing once a fully turbulent regime is attained. Thus, the F-type forcing method is modified by adding a *controlled amplitude* parameter based on runtime measured quantities, able to automatically damp the continuous forcing once the turbulent state is attained. Finally, the robustness of the *controlled forcing amplitude* F-type method has been demonstrated, by verifying its effectiveness in sustaining a transitional state even at very low Reynolds number.

The F-type method introduced here has proven to be a useful tool for studying uncontrolled transition in wall-bounded, parallel flows, such as the channel flow considered here. The same technique can be used without any modification to study non-deterministic transition to turbulence in a number of other closed flow configuration, avoiding the use of unstable modes for constructing the initial condition (Schmid and Henningson, 2001; Tatsumi and Yoshimura, 1990), as for instance done for the duct flow in Biau and Bottaro (2009). The same volume forcing method could be also used in a spatially developing flow such as the boundary layer flow, by forcing a small part of the domain and letting the disturbance develop downstream. The F-type forcing method allows not only to

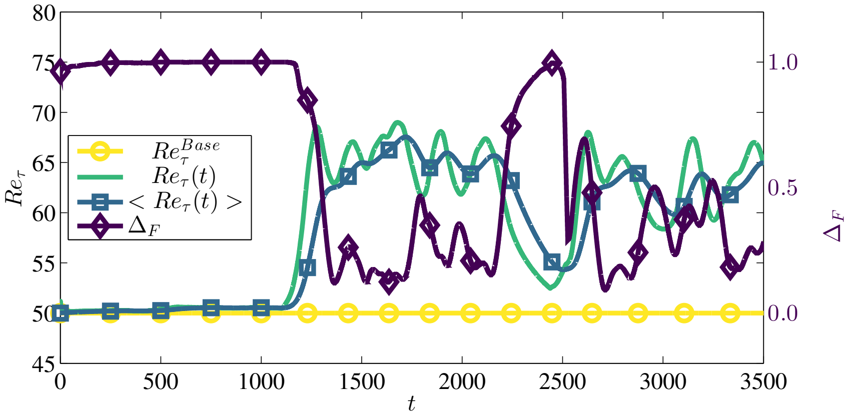

Figure 4.25 – Controlled amplitude F-type transition method for a *low* Reynolds number, $Re = 1250$. The forcing intensity is the lowest one for which a transitional behaviour can be observed: $Tu^{linear} = 0.7\%$. Forcing is activated intermittently to keep a turbulent state.

study uncontrolled transition in a wide range of closed, wall bounded shear flows, but also provides a numerical framework for better understanding the onset and propagation of turbulence at its edge, the dynamics of incipients turbulent fronts (Song et al., 2017), puffs and slugs (Barkley, 2016) in pipe flow, as well as the establishment of direct percolation in the Couette flow (Lemoult et al., 2016).

Chapter 5

Controlling transition with superhydrophobic surfaces

Superhydrophobic surfaces are capable of trapping gas pockets within the micro roughnesses on their surfaces when submerged in a liquid, with the overall effect of lubricating the flow on top of them. These bio-inspired surfaces have proven to be capable of dramatically reducing skin friction of the overlying flow in both laminar and turbulent regimes. However, their effect in transitional conditions, in which the flow evolution strongly depends on the initial conditions, has still not been deeply investigated. In this Chapter the influence of superhydrophobic surfaces on several scenarios of laminar-turbulent transition in channel flow is studied by means of direct numerical simulations. A single phase incompressible flow has been considered and the effect of the micro-structured superhydrophobic surfaces has been modelled imposing a slip condition with given slip length at both walls. The flow evolution from laminar, to transitional, to fully-developed turbulent flow has been followed starting from several different initial conditions. When modal disturbances issued from linear stability analyses are used for perturbing the laminar flow, as in supercritical conditions or in the classical K-type transition scenario, superhydrophobic surfaces are able to delay or even avoid the onset of turbulence, leading to a considerable drag reduction. Whereas, when transition is triggered by nonmodal mechanisms, as in the optimal or uncontrolled transition scenarios, which are currently observed in noisy environments, these surfaces are totally ineffective for controlling transition. Superhydrophobic surfaces can thus be considered effective for delaying transition only in low-noise environments, where transition is triggered mostly by modal mechanisms.

In this chapter the we will use the SHS acronym both for referring to superhydrophobic surfaces in general as well as to the spatially homogeneous slip approach that we will use to model them in this section.

5.1 Governing equations

The aim of the present study is to study how SHS at the walls of a plane channel affect flow stability and transition to turbulence in different flow conditions, allowing to delay or even avoid transition in some particular cases. . As previously discussed, when both the spanwise length of the grooves and the shear-free fraction are small enough with respect to the channel thickness so to ensure that the lubricating layer is retained within the surface microsculpture while sustaining a laminar-turbulent flow, namely withstanding wetting transition(Seo and Mani, 2016), the spatially heterogeneous solid and gas substrates can

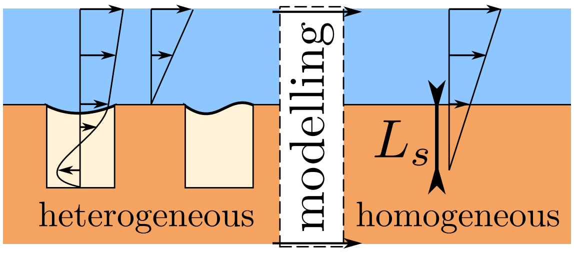

Figure 5.1 – Sketch of a channel flow with submerged SuperHydrophobic Surfaces, depicting the near-wall, capillary driven *microscopic* free-surface dynamics as well as its modelling using a slip condition with slip length L_s.

be modelled as a spatially homogeneous surface with a given slip length (see figure **??**

The dynamics of an incompressible Newtonian fluid flowing in a channel is governed by the Navier-Stokes equations:

$$\frac{\partial \boldsymbol{U}}{\partial t} = -(\boldsymbol{U} \cdot \nabla)\boldsymbol{U} - \nabla P + \frac{1}{Re}\nabla^2 \boldsymbol{U} \tag{5.1}$$

$$\nabla \cdot \boldsymbol{U} = 0, \tag{5.2}$$

where $\boldsymbol{U} = (U(\boldsymbol{x},t), V(\boldsymbol{x},t), W(\boldsymbol{x},t))^T$ is the velocity field and $P(\boldsymbol{x},t)$ is the pressure field. The Reynolds number is defined as $Re = U_r H/\nu$, where H is half the height of the channel and ν the kinematic viscosity of the fluid. Dimensionless time $t = H/U_r$ and reference velocity $U_r = 3U_a/2$ is based on its average over the entire domain $U_a = 1/2H \int U dxdydz$. The reference frame $\boldsymbol{x} = (x, y, z)^T$ is chosen so that x is the streamwise, y the wall-normal and z the spanwise directions. The presence of SHS is taken into account using an ad-hoc boundary condition at the wall, provided in equation (1.1).

Steady solutions $\boldsymbol{Q}_b(\boldsymbol{x}) = (\boldsymbol{U}_b, P_b)^T$ of the Navier-Stokes equations are known as *base flows* or *fixed points* of the system. Under the assumption of small-amplitude disturbances, we decompose the flow field as a sum of the base flow and a perturbation such as $\boldsymbol{Q}(\boldsymbol{x},t) = \boldsymbol{Q}_b(\boldsymbol{x}) + \varepsilon \boldsymbol{q}(\boldsymbol{x},t)$, with $\varepsilon \ll 1$, that is to say $(\boldsymbol{U}(\boldsymbol{x},t), P(\boldsymbol{x},t))^T = (\boldsymbol{U}_b(\boldsymbol{x}) P_b(\boldsymbol{x}))^T + \varepsilon(\boldsymbol{u}(\boldsymbol{x},t), p(\boldsymbol{x},t))^T$. In our framework, the base flow assumes the form $\boldsymbol{U}_b(\boldsymbol{x}) = (U_b(y), 0, 0)$, with

$$U_b(y) = (2L_s + 1 - y^2)/(3L_s + 1), \tag{5.3}$$

as found by Philip (1972). Despite $U(y = 0)$ value is usually employed for nondimensionalisation, the use of a slippery boundary condition modifies the velocity at the centerline. Again, this issue is overcome using U_r as reference velocity, enabling for a consistent definition of Re throughout all the present study. In order to trigger transition to turbulence starting from the laminar base flow, we will use perturbations constructed on the basis of modal and nonmodal linear stability analyses (see Min and Kim (2005) and Pralits et al. (2017)).

5.1.1 Linear Stability Analysis (LSA)

Linearising the governing equations around the base flow we obtain the linearized Navier-Stokes equations, which can be compactly written as:

$$\frac{\partial \boldsymbol{u}}{\partial t} = \boldsymbol{L}\boldsymbol{u} \tag{5.4}$$

once projected onto a divergence-free vector space. Being this system autonomous in time and being the base flow periodic in both streamwise and spanwise directions one can apply a Fourier-Laplace transform to any field $\boldsymbol{q}$ so that $\boldsymbol{q}(\boldsymbol{x},t) = \tilde{\boldsymbol{q}}(y)\exp[i(\alpha x + \beta z) + \lambda t] +$ *c.c*, where *c.c.* is the complex conjugate, α and β are the real streamwise and spanwise wavenumbers respectively, λ is the complex circular frequency and $\tilde{\boldsymbol{q}} \in \mathbb{C}^4$ is the associated eigenfunction.

In this framework, the behaviour of a generic solenoidal perturbation $\boldsymbol{u}$ is linked to the eigenpairs of $\boldsymbol{L}$: $\left\{\lambda^{eig}, \tilde{\boldsymbol{u}}^{eig}\right\}$ (Orszag, 1971), since it can be written as

$$\boldsymbol{u}(\boldsymbol{x},t) = \sum_{l} \kappa_l \tilde{\boldsymbol{u}}(y)_l^{eig} e^{i(\alpha x + \beta z) + \lambda_l^{eig} t}, \tag{5.5}$$

where κ_l is a scalar weight. For a given couple (α, β) the *temporal* behaviour of each eigenvector of the linearised operator $\boldsymbol{L}$ is then described by its associated eigenvalue $\lambda_i^{eig} = \sigma_i^{eig} + i\omega_i^{eig}$, where σ_i^{eig} represents its asymptotic growth/decay rate and ω_i^{eig} its circular frequency.

Solving the 1D local stability problem, which is to say seeking for the eigenvalues of $\boldsymbol{L}$ which govern the behaviour of small perturbations in the time-asymptotic limit, by means of a spectral code (Schmid and Henningson, 2001), we retrieve the same result found by Min and Kim (2005). The most unstable modes of the operator $\boldsymbol{L}$, i.e., the Tollmien-Schlichting (TS) waves, are strongly affected by the value of the slip length imposed at the wall. This is not surprising considering that TS waves are near-wall perturbations and that SHS reduces the velocity gradient near the wall. Figure 5.2(a) shows that, increasing the value of L_s the neutral curve moves towards higher values of Re, suggesting that SHS might delay transition to turbulence, at least in supercritical conditions (i.e., when the Reynolds number overtakes the critical value for linear instability).

In subcritical conditions, small-amplitude perturbations can transiently grow in time due to nonmodal mechanisms, linked to the nonnormality of the Navier-Stokes equations. To investigate how the nonmodal dynamics of small perturbations is affected by SHS in a finite-time framework, we seek for the 'optimal' perturbation at initial time, $\boldsymbol{u}_0^{Opt}(\boldsymbol{x})$, capable of inducing the maximum energy growth at a target time T (Butler and Farrell, 1992; Luchini, 2000). The energy gain to be optimized reads:

$$G(T) = \max_{\boldsymbol{u}_0} \frac{E(\boldsymbol{u}_T)}{E(\boldsymbol{u}_0)}, \tag{5.6}$$

where the integral energy in the computational domain V is defined as:

$$E(\boldsymbol{u}(t)) = \frac{1}{2L_xL_z} \int_V \boldsymbol{u}^T(t)\boldsymbol{u}(t)dV. \tag{5.7}$$

For obtaining the optimal energy gain $G^{opt}(T)$ and the corresponding initial and final optimal perturbations $\boldsymbol{u}_0^{Opt}(\boldsymbol{x})$, $\boldsymbol{u}_T^{Opt}(\boldsymbol{x})$ a singular value decomposition of the linearised governing equation (5.4) has been used, following the approach of Schmid and Brandt (2014). As shown in figure 5.2(b), a variation of L_s induces but a slight modification of the maximum energy gain and of the optimal perturbation shape, consisting of modulations in the spanwise direction of the streamwise velocity, i.e., streaks (Farrell, 1988). In fact, since these optimal structures essentially lie in the flow bulk far from the walls, they are much less affected by the surface boundary condition than the near-wall TS waves . The fact that velocity perturbations are slightly or strongly affected by SHS depending on their distance from the wall suggests that some specific transition scenarios can be better controlled than others by the introduction of SHS.

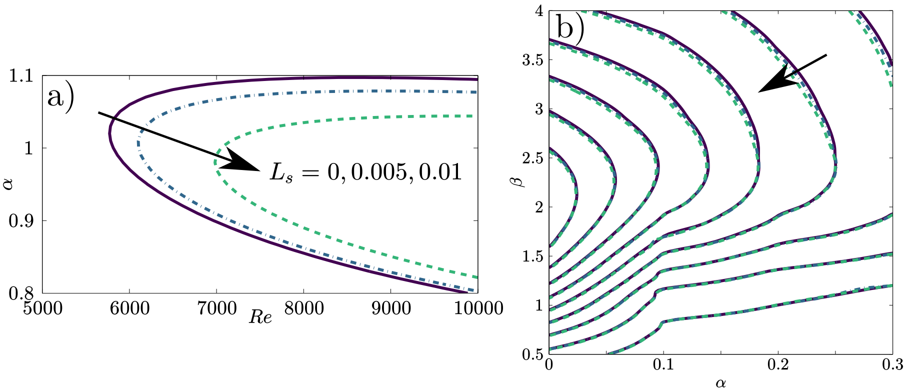

Figure 5.2 – Linear stability and transient growth analyses for different values of L_s: neutral curve for linear stability for $\beta = 0$ (a) and optimal energy gain in the $\alpha - \beta$ plane for $Re = 1000$ (b), both in perfect match with Min and Kim (2005). The slip length strongly affects the time asymptotic behaviour, while being ineffective in controlling finite-time dynamics, as shown by the unmodified contours of the optimal transient energy growth. Contours in subplot (b) are related to the same values of L_s reported in subplot (a). The values of the isocontours in subplot (b), from outer to inner, correspond to $G_{max}^{Opt} = [110, 120, 130, \ldots, 180, 190, 200]$.

5.1.2 Direct Numerical Simulations

In order to investigate the influence of SHS on laminar-turbulent transition, we superpose different perturbations built on the basis of the previously introduced modal and nonmodal stability analyses to the laminar base flow and follow their evolution using Direct Numerical Simulations (DNS). The flow in a streamwise-periodic channel with constant flow rate is simulated using the incompressible solver Nek5000 (Fischer et al., 2008), based on the spectral element method (SEM). The code, which has been modified to account for the Robin boundary condition (1.1), is based on a $\mathbb{P}_N - \mathbb{P}_{N-2}$ spatial discretisation and a BDF3/EXT3 spatial scheme. Throughout the present work, the domain size is set to $[L_x, L_y, L_z] = [2\pi/\alpha, 2H, 2\pi/\beta]$, where $\alpha = 1.12, \beta = 2.10$. In most computations the Reynolds number is set to $Re = 5000$, in order to match literature results about the K-type transition in channel flows (Zang and Krist, 1989). Using 24 spectral elements in each direction with polynomial order equal to 8, the resulting spatial resolution is $[N_x, N_y, N_z] = [192, 192, 192]$. Under these conditions and considering a no-slip wall, the resulting fully turbulent state is characterised by a friction Reynolds number $Re_\tau = 210$ (Schlatter et al., 2006) (albeit we will show that imposing a constant flow rate will result in a lower Re_τ for a turbulent flow over SHS). Therefore, the grid size expressed in friction units is small enough to accurately simulate a turbulent channel flow by DNS (Seo and Mani, 2018). In particular we have $\Delta x^+ \approx 6.2, \Delta z^+ \approx 3.0$, $\Delta y^+_{min} \approx 0.16$ at the wall and $\Delta y^+_{max} \approx 11.5$ at the centerline, which are lower than the values used by Min and Kim (2004, 2005).

5.2 Transition triggered by modal mechanisms

The aim of the present work is to explain how different scenarios of transition to turbulence are affected by a slip boundary condition with given slip length. First, we consider the case in which transition is triggered by modal stability mechanisms. Thus, following Zang and Krist (1989); Sandham and Kleiser (1992a); Schlatter et al. (2006), we use as initial conditions for the DNS a superposition of the laminar base flow plus a linear combination of eigenvectors of $\boldsymbol{L}$:

$$\boldsymbol{U}(\boldsymbol{x}, t=0) = \boldsymbol{U}_b(\boldsymbol{x}) + \sum_j \epsilon_j \tilde{\boldsymbol{u}}(y)_j^{eig} e^{i(\alpha x + \beta z) + \lambda_j^{eig} t}. \tag{5.8}$$

where ϵ_j is a given amplitude. In supercritical conditions, namely for $Re \geq Re_{critical} = 5772.22$ (Orszag, 1971), only one mode will be retained in the right hand side of the previous equation, namely the most unstable one. Conversely, in subcritical conditions (Zang and Krist, 1989), we will refer to the well-known K-type (or H-type) transition (Kachanov, 1994a), that can be obtained numerically by setting initial conditions similar to the experiments of Nishioka et al. (1975), where a sum of two-dimensional and oblique TS waves were used (Kleiser and Zang, 1991). In the literature, the effect of SHS on transition to turbulence have been studied for the K-type scenario only (see Min and Kim (2005)), but even for this case the physical mechanisms leading to transition delay have not been investigated yet.

5.2.1 Supercritical case: TS waves

For the chosen configuration, the most unstable eigenvalue of $\boldsymbol{L}$ is the two-dimensional TS wave with $\alpha = 1.00, \beta = 0.0$, which we will refer to as $\boldsymbol{u}_{TS_{2D}}$. We set $Re = 10000$ so that, according to the neutral curve shown in figure 5.2(a), the flow remains linearly unstable for a large range of slip lengths. We superpose the unstable mode to the base flow as $\boldsymbol{U}(\boldsymbol{x}, t=0) = \boldsymbol{U}_b(\boldsymbol{x}) + \epsilon \boldsymbol{u}_{TS_{2D}}(\boldsymbol{x})$ and study the flow evolution by DNS first for a no-slip wall and than for a SHS with a slip value compatible with the experiments of Gose et al. (2018), $L_s = 0.005$. The amplitude ϵ is set to $\approx 3 \cdot 10^{-3}$ to guarantee an initial linear phase of exponential growth before the onset of nonlinear effects, provided that $E(t=0) = 10^{-5}$.

In order to detect transition we track the evolution of the kinetic energy density of the velocity perturbation defined in equation (5.7). The result is plotted in figure 5.3 for $L_s = 0$ and $L_s = 0.005$. In both cases, after an initial phase characterised by exponential growth as predicted by the LSA, secondary instability sets in leading to a rapid increment of E towards saturation to a fully turbulent state. For both the considered values of L_s the onset of secondary instability is observed for $E \approx 5 \cdot 10^{-5}$, and the energy saturates towards the same value characterizing the turbulent regime. As predicted by LSA, in the presence of SHS the initial exponential phase is characterized by a lower growth rate, thus the threshold energy for secondary instability is reached in more time, leading to a time delay of the consequent transition to turbulence. For the chosen amplitude of the unstable mode, most of the transition time is spent during the initial exponential growth and the physical mechanisms leading to transition are essentially the same in both the considered cases. Therefore the transition time might be estimated using the e^N method (van Ingen, 2008) also for the SHS case.

5.2.2 Subcritical case: K-type transition

In this section we study in detail how the K-type transition scenario is influenced by a slippery wall at $Re = 5000$, pursuing the study made by Min and Kim (2005) in order to unveil the physical mechanisms leading to transition delay. This transition scenario is triggered setting as initial disturbances a sum of the 2D TS wave $\boldsymbol{u}_{TS_{2D}}$ and a sum of equal and opposite oblique 3D fundamental Tollmien-Schlichting waves $\boldsymbol{u}_{TS_{3D}}$. The initial

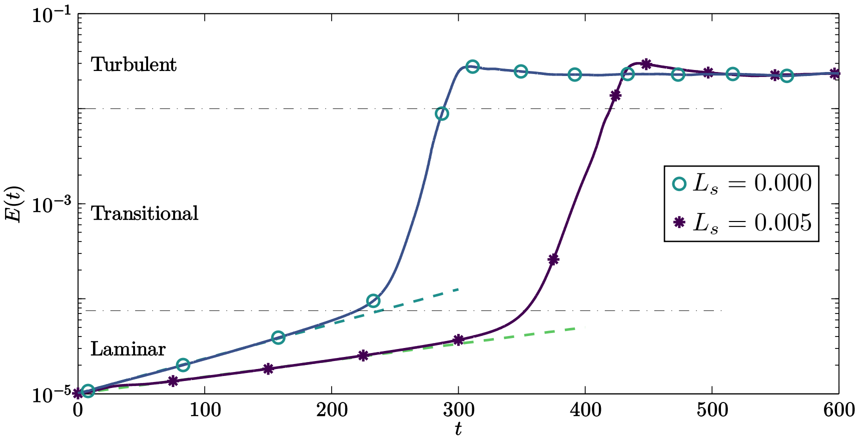

Figure 5.3 – Influence of SHS on the supercritical transition path at $Re = 10000$. Simulations have been initialised with the most unstable eigenvector of $\boldsymbol{L}$, with initial perturbation kinetic energy density equal to $E(t) = 10^{-5}$, for different slip lengths L_s. Dashed lines represent the exponential energy growth predicted by the linear theory, for both considered slip lengths.

condition for K-type transition then reads

$$\boldsymbol{U}(t=0) = \boldsymbol{U}_{BF} + 0.03\boldsymbol{u}_{TS_{2D}} + 0.001\boldsymbol{u}_{TS_{3D}}, \tag{5.9}$$

where the shape of the modes depends on the imposed value of L_s and their phase is set so that the maximum amplitude of the disturbances occurs at $z = L_z/2$ (Zang and Krist, 1989; Sandham and Kleiser, 1992a). For both waves, the maximum value of the streamwise velocity component is set to the desired amplitude and the other components are scaled accordingly. Figure 5.4 shows the temporal evolution of the instantaneous wall shear normalised by its laminar value for $L_s = 0.00, 0.01, 0.02$. The first two curves accurately reproduce those in figure 3(a) of the work by Min and Kim (2005) (where only $L_s = 0.00$ and $L_s = 0.01$ are considered), validating our numerical approach. The highest value of $L_s = 0.02$, already used by the same authors in a previous study (Min and Kim, 2004), would result from a SHS having a roughness texture period of $L^+ \approx 15$ in the turbulent regime (Seo and Mani, 2016). This value of L^+ is still sufficiently low to ensure the suitability of the spatially homogeneous numerical approach (Seo and Mani, 2016) and to avoid wetting transition (Zhang et al., 2016) and is comparable to values of the texture period in turbulent conditions reported in the literature, namely $L^+ \approx 0.5 - 10$ (Daniello et al., 2009; Woolford et al., 2009; Park et al., 2014; Rowin et al., 2018; Gose et al., 2018). While for $L_s = 0.01$ transition is only delayed in time (see also Min and Kim (2005)), for $L_s = 0.02$ it is completely avoided, although the wall shear increases to a value larger than the laminar one (but still much lower than the turbulent one). For investigating the physical mechanisms affecting transition in the presence of a slip length, we place ourselves in a threshold condition, slightly increasing the initial perturbations intensity of the case with $L_s = 0.02$ up to a value for which transition is triggered. This is achieved for a 10% increase of the perturbation amplitude, namely:

$$\boldsymbol{U}(t=0) = \boldsymbol{U}_{BF} + 1.10(0.001\boldsymbol{u}_{TS_{2D}} + 0.0003\boldsymbol{u}_{TS_{3D}}). \tag{5.10}$$

In the remainder of the chapter we will focus on this latter case (equation (5.10)), referring to it simply as K-type transition for the sake of simplicity, after having verified that initialising the simulation using equation (5.9) or (5.10) provides essentially the same results

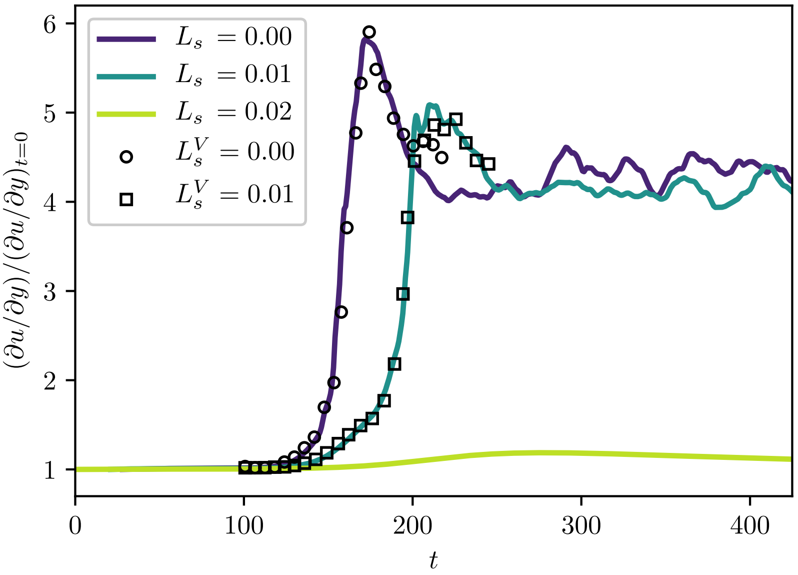

Figure 5.4 – Time evolution of the instantaneous wall shear normalised by its laminar value in a standard K-type transition scenario as in equation (5.9). Referring to the no-slip case ($L_s = 0.0$), with SHS transition to turbulence can be retarded ($L_s = 0.01$) or even avoided ($L_s = 0.02$). The symbols L_s^V are validations with respect to the case 3 from Min and Kim (2005).

for $L_s = [0.00, 0.01]$. For detecting whether transition has taken place, in figure 5.5 we provide the evolution of the friction Reynolds number, defined as:

$$Re_\tau = \sqrt{Re \left| \frac{\partial \langle U(\boldsymbol{x}, t)\rangle}{\partial y} \right|_{wall}}, \tag{5.11}$$

where $\langle \cdot \rangle$ represents the spatial average computed on the wall-parallel planes $x - z$ at a given time t and the laminar Reynolds number is set to the constant value $Re = 5000$ (Zang and Krist, 1989). Both the laminar ($t < 100$) and turbulent ($t > 500$) mean values of Re_τ change with L_s. The former can be easily derived injecting equation (5.3) within equation (5.11):

$$Re_\tau = \sqrt{Re \left| \frac{2y}{3L_s + 1} \right|_{wall}} = \sqrt{\frac{2Re}{(3L_s + 1)}}, \tag{5.12}$$

while the latter is reduced due to the reduced friction drag. This is a consequence of the fact that we have imposed a constant flow rate, therefore we cannot directly compare our results with other studies of turbulent flows over SHS where Re_τ is kept constant (Min and Kim, 2004; Seo and Mani, 2016).

Looking at the transitional phase, we observe that while Re_τ increases monotonically for $L_s = [0.00, 0.01]$, this is not the case for $L_s = 0.02$, where a transient growth of the skin friction is observed, followed by a saturation and a rapid increase towards the turbulent value. In the following sections we will analyse the coherent structures and associated Fourier modes arising in the different stages of transition with the aim of identifying the instability mechanisms inhibited by the presence of SHS.

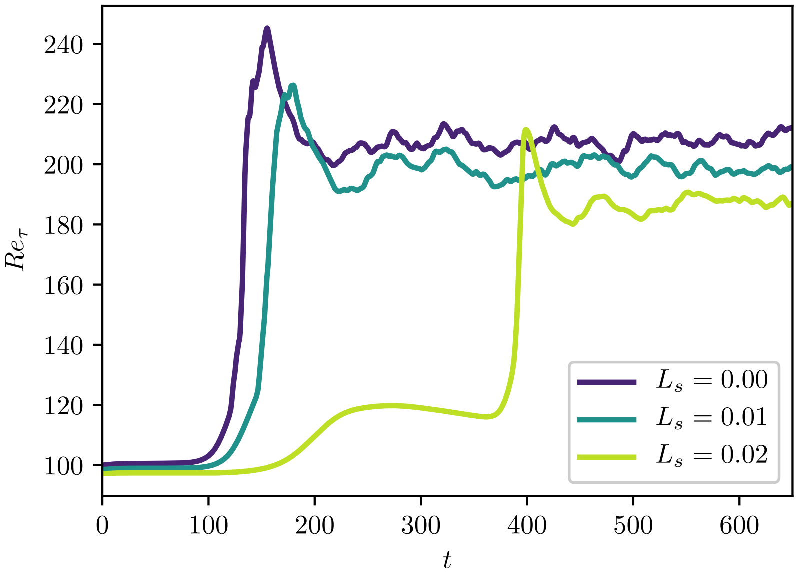

Figure 5.5 – Time evolution of the friction Reynolds number Re_τ, for the modified K-type transition scenario (equation (5.10)) and different slip lengths. Differently from the case in figure 5.4 transition occurs even for $L_s = 0.02$.

Coherent structures

Figure 5.6 provides snapshots of the flow structures observed during transition to turbulence for the three considered slip lengths. The snapshots are placed one next to the other in order to provide an overall view of the transition process; the time at which each snapshot has been extracted is reported in the figure. In figure 5.6(a) the standard K-type transition scenario is reported for comparison purpose. At first ($t \leq 80$) a saturation of the 2D TS wave is observed, followed by a symmetry breaking in the spanwise direction and a three-dimensionalization of the perturbation due to secondary instability ($t = 85$) (Gilbert and Kleiser, 1990). Then, the presence of strong shear layers promotes the formation of $\Lambda-$shaped vortices ($t = 103$). The roll up of the shear layer connects the downstream side of Λ vortices, forming the heads of characteristic hairpin vortices, whereas the legs formed in the upstream part of the $\Lambda-$vortices are stretched ($t = 113$) (Sandham and Kleiser, 1992a). The late stage of transition ($t = 125$) is characterised by the rapid formation of multiple hairpin heads as a succession of sweep-ejection events (Guo et al., 2010). Finally, at $t \geq 130$, breakdown to turbulence is observed.

Figure 5.6(b) depicts K-type transition over a SHS with $L_s = 0.01$. Transition appears to be qualitatively similar to the no-slip case in its early stages ($t < 100$). Notable differences arise in the late stages, where the $\Lambda-$ vortices weaken and stretch in the streamwise direction ($t = 125$). An inhomogeneous streamwise velocity distribution is also observed at the wall ($t = 120$). Hairpin vortices are created at a later time with respect to the no-slip case, showing smaller heads and legs that appear to originate right at the wall, leaving a clear footprint in the slip velocity ($t = 130$). Vortical structures such as Λ and hairpin vortices persist for a longer temporal range compared to the no-slip case ($t \approx 150$), while the final breakdown to turbulence appears to be qualitatively the same.

Increasing the slip length up to $L_s = 0.02$, as represented in figure 5.6(c), produces a drastic change in the transition path. First of all, the spanwise symmetry breaking of the

TS waves is considerably delayed in time ($t = 150$). Then, the development of Λ vortices appears to be inhibited by the slippery walls, leading to a saturation and subsequent slow decrease of the wall shear corresponding to the bump in the Re_τ time series at $t = 250$ shown in figure (5.5). At $t \approx 300$, due to flow receptivity (Luchini (2000)), the residual perturbations regroup in long, streamwise aligned velocity modulations (streaks), as suggested by the slip velocity distribution at the wall ($250 < t < 275$), whereas vortices appear almost completely damped. At $t \approx 365$, due to secondary instability of the streaks, new vortical structures arise in the flow, leading to the onset of bypass transition.

Fourier harmonics

With the aim of providing a more quantitative description of how K-type transition scenario is affected by the use of SHS, we track in time the amplitude of selected Fourier harmonics (Zang and Krist, 1989):

$$E_k(k_x, k_z) = \frac{1}{2E_0} \int_{-1}^{+1} |\hat{\boldsymbol{u}}_{k_x,k_z}(y,t)|^2 \, dy, \tag{5.13}$$

where $\hat{\boldsymbol{u}}_{k_x,k_z}(y,t)$ is a single component of the Fourier transform of the perturbation velocity field in the streamwise and spanwise direction with wavenumbers k_x, k_z, respectively, while E_0 is the kinetic energy of the laminar flow. Following the literature, the wavenumbers of the different Fourier modes will be indicated as multiples of the fundamental wavenumber, the couple (i_x, i_z) representing the i^{th} multiple of the fundamental streamwise and spanwise wavenumbers, $2\pi/L_x, 2\pi/L_z$, respectively. We recall that in this framework the presence of the TS waves $u_{TS_{2D}}, u_{TS_{3D}}$ is translated into spikes in the $(1, 0)$ and $(1, \pm 1)$ Fourier modes, respectively. The time evolution of the most energetic Fourier modes during the different phases of the K-type transition is provided in figure 5.7 for the considered values of the slip length. In all cases, despite energy is initially provided only to the $(1, 0)$ and $(1, \pm 1)$ modes, a streamwise invariant, subharmonic mode $(0, 2)$ is immediately generated, rapidly increasing in energy. This is a clear sign that, even if the mode initial amplitude is relatively small, non-linear interactions are already taking place, indicating that predictions based on linear amplification mechanisms are not sufficient for modelling the transition scenario (Min and Kim, 2005). For $L_s = 0.00$ and $L_s = 0.01$ the time evolution of the Fourier modes is substantially similar. On the other hand, for the $L_s = 0.02$ case we observe a decrease of the amplitude of the $(1, 0)$ mode and a much slower increase of $(1, 1)$ and $(0, 2)$ modes. At $t \approx 200$, the streamwise-dependent modes begin to decrease their energy whereas mode $(0, 2)$ saturates for a rather long time range. Thus, for $t > 200$ the flow is mostly characterised by streamwise-invariant velocity modulations, i.e., streaky structures.

Late stages of transition

In order to follow the development and eventual disruption of these streaky structures, in figure 5.8 we provide the time evolution of the streamwise and spanwise vorticity (ω_x, ω_z) within the channel section, as well as the friction Reynolds number (bottom) coloured by the amplitude of the spanwise modulation, which is defined as:

$$A_s(t) = [max_{y,z}(\boldsymbol{U}(\boldsymbol{x}, t) - \boldsymbol{U}_b(\boldsymbol{x}) - min_{y,z}(\boldsymbol{U}(\boldsymbol{x}, t) - \boldsymbol{U}_b(\boldsymbol{x}))] \tag{5.14}$$

as proposed by Andersson et al. (1999); Brandt et al. (2003). Monitoring these quantities in time allows to identify the hairpin legs and heads, characterised by high values of ω_x, ω_z, respectively (Zhou et al., 1999), as well as the onset of spanwise vortices, associated with

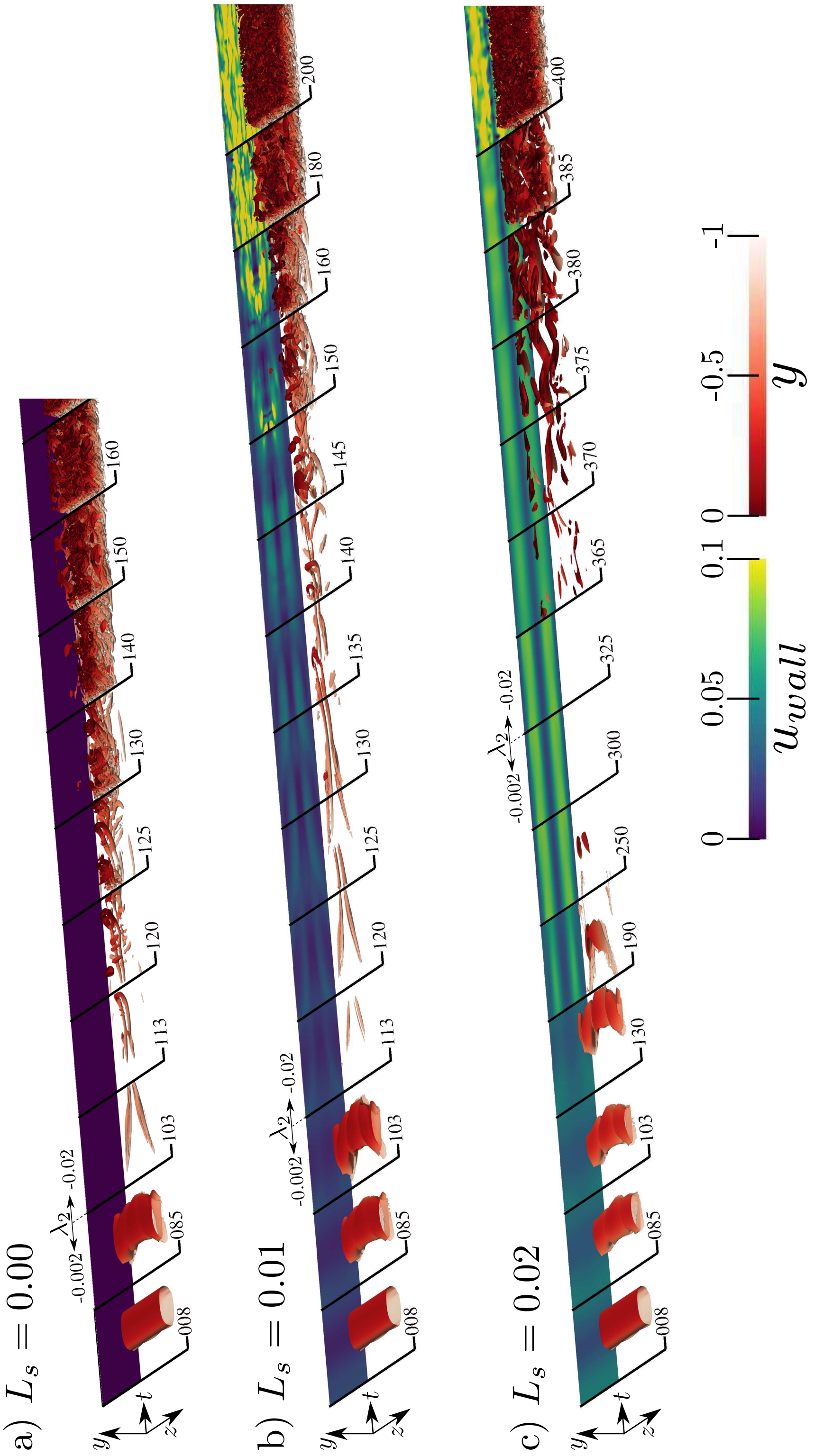
a) $L_s = 0.00$
b) $L_s = 0.01$
c) $L_s = 0.02$
y
t
z
λ_2
-0.002
-0.02
008
085
103
113
120
125
130
135
140
145
150
160
180
200
190
250
300
325
365
370
375
380
385
400
u_{wall}
0
0.05
0.1
y
0
-0.5
-1

Figure 5.6 – Overview of the K-type transition over superhydrophobic surfaces with different slip lengths. For each slip length, snapshots extracted at different times are placed one next to the other in order to provide an overall view of transition. The time values are reported on the black lines separating the snapshots. The iso-surfaces show the λ_2 criterion, coloured by its distance from the wall, and the iso-contours represent the streamwise velocity measured at the lower wall, shifted in the spanwise direction for visualisation issues. Only the lower channel half is showed for the sake of visualisation.

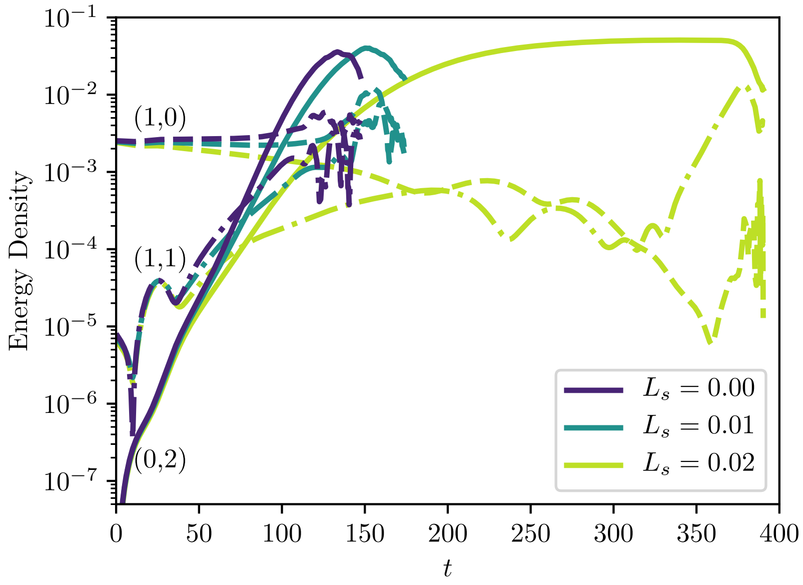

Figure 5.7 – Time evolution of the energy associated to (1,0), (1,1) and (0,2) Fourier modes during K-type transition for different values of L_s. While the 2D and 3D TS waves, respectively identified by modes (1,0) and (1,1) evolve in a similar way in all cases, for the $L_s = 0.02$ case streaks ((0,2) modes) dominate the flow evolution for a large time range, leading to a consistent delay in transition.

peaks of ω_z and A_s (Brandt et al., 2003). The time evolution of these three quantities is qualitatively and quantitatively similar for the $L_s = [0.00, 0.01]$ cases, as reported in the first two columns of figure 5.8. In both cases, the formation of Λ vortices (localized peak in ω_x for $t < 100$ in figures 5.8.0a and 5.8.1a) is followed by their evolution into hairpin vortices, as suggested by the ω_z spot at $t \approx 125$ indicating the rapid development of hairpin heads (see figures 5.8.0b and 5.8.1b). Although this ω_z peak is weaker for the $L_s = 0.01$ case, in both cases it is followed by a wall-normal spreading of both vorticity components together with a rapid increase of Re_τ, indicating the breakdown of hairpin vortices and consequent transition to turbulence (Sandham and Kleiser, 1992a). Figures 5.8.0c and 5.8.1c are also very similar, although for the slip case the transitional phase is longer and Re_τ is characterised by smaller values.

This process is radically modified for the largest slip length considered here, $L_s = 0.02$. Whilst the initial condition has been designed to promote the formation of Λ vortices (Sandham and Kleiser, 1992a), ω_x increases only transiently and then drops to very low values, as depicted in figure 5.8.2a. The reduced wall shear restrains the formation of Λ vortices, therefore inhibiting the consequent creation of hairpin vortices. Right after the disappearance of the ω_x transient peak, at $t \approx 200$, ω_z begins to increase, initially close to the wall and then migrating through the channel bulk up to $t \approx 400$ (see figure 5.8.2b). In this time range the friction Reynolds number Re_τ increases to a value larger than the laminar but lower than the turbulent mean one and the spanwise modulation amplitude saturates, as shown in figure 5.8.2c. In fact, in this phase streaky structures are created as a response of the flow to the residual perturbations present in the computational domain (Luchini (2000)). For $180 < t < 200$ the streaks linearly increase their amplitude (A_s) due to flow receptivity. Once A_s reaches a threshold amplitude nonlinear effects set

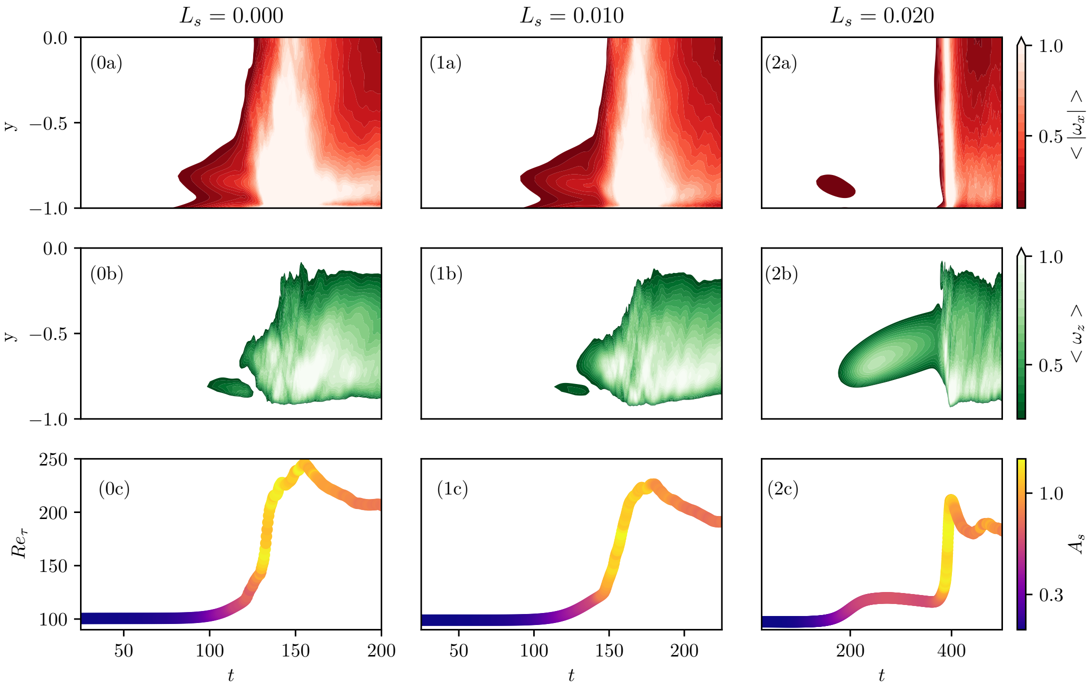

Figure 5.8 – Streamwise and spanwise vorticity averaged along the homogeneous directions $x-z$, $\langle \omega_x \rangle$, $\langle \omega_z \rangle$ in subplots x.a and x.b, respectively. Subplots x.c show the time evolution of the friction Reynolds number Re_τ, coloured by the spanwise deformation amplitude A_s. Plots are arranged in columns according to the L_s to which they belong.

in (according to (Brandt et al., 2004a), $A_s \approx 26\%$ of the free-stream velocity for sinuous instability), and lead to a saturation of both Re_τ and A_s, while the region of high amplitude ω_z departs from the wall. This indicates that the initial 'linear' streaks are deformed in the wall-normal direction due to nonlinear effects (Mao et al., 2017). Finally, at $t > 400$, abrupt secondary instability of these nonlinearly saturated flow occurs and breakdown to turbulence is finally reached.

The development of nonlinearly saturated streaks and the consequent creation of hairpin vortices can be further analysed by following the time evolution of the streamwise perturbation and of the uv product averaged in the wall-parallel planes as plotted in figure 5.9 together with the time variation of A_s coloured by the skin friction coefficient C_f. The first quantity, $\langle u \rangle$ allows to distinguish linear from nonlinear streak. In fact, linear high- and low- speed streaks are placed at the same wall-normal positions (Schmid and Henningson, 2001), thus spanwise averaging cancels out their contribution in the $\langle u \rangle$ term. When nonlinearity sets in, since low- (high-) speed streaks migrate upwards (downwards), the quantity $\langle u \rangle$ departs from zero. The second quantity, $\langle uv \rangle$, allows to identify the presence of sweep and ejection events, characterised by large values of $\langle uv \rangle$ with u and v anticorrelated in sign (belonging to the Q4 and Q2 quadrant of the $u-v$ plane, see Adrian (2007); Farano et al. (2015)). The presence of these events has been indicated in the figure using the Q4 and Q2 nomenclature respectively, as a reminder to the $\langle uv \rangle$ velocity quadrant to which they belong.

Comparing figure 5.9.0d .1d and .2d, one can see that, when L_s increases from 0 to 0.02, in the time range $t = [0, 120]$ the quantity $\langle u \rangle$ decreases to zero close to the wall, indicating that near-wall linear streaks almost disappear. In the same time range, sweeps

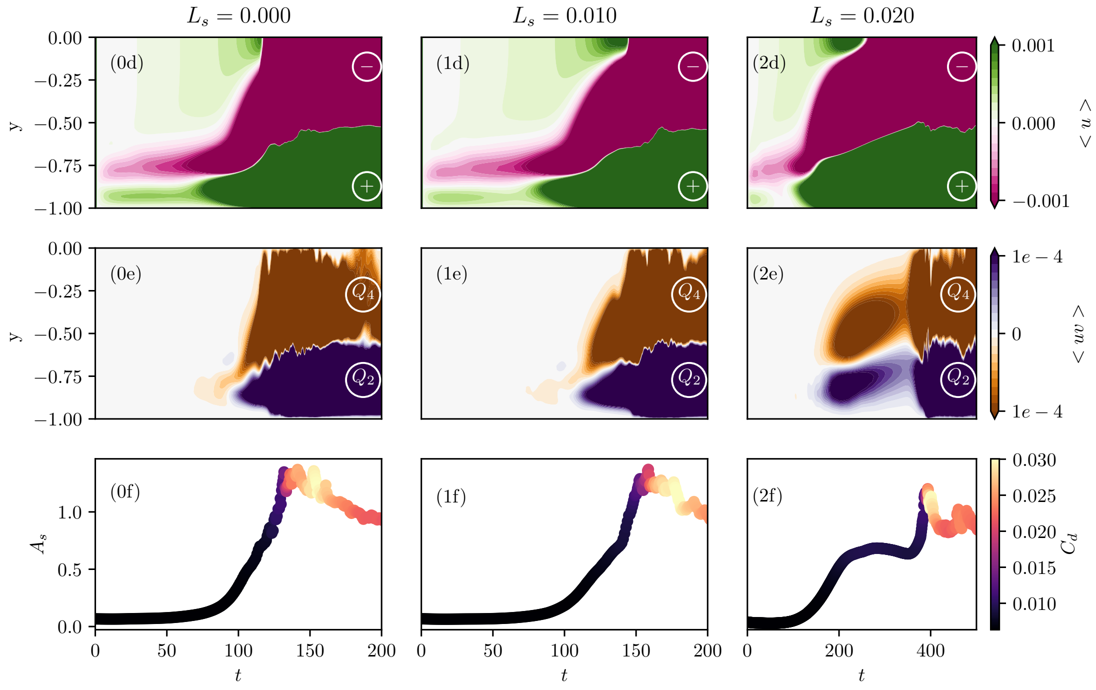

Figure 5.9 – First row: contours of the streamwise velocity disturbances averaged onto the $x - z$ plane ($\langle u \rangle$). Second row: contours of the uv product measuring Q2 and Q4 events averaged onto wall-parallel planes ($\langle uv \rangle$). Third row: time evolution of the spanwise amplitude deformation A_s, coloured by the friction coefficient C_f. Each column is associated to a given slip length, $L_s = 0.00, 0.01, 0.02$ from left to right.

and ejections are completely absent in the $L_s = 0.02$ case, whereas for $L_s = 0, 0.01$ they occur in the narrow $t = [75, 100]$ window (compare figures 5.9.0e, .1e and .2e). In this time range Q4 (Q2) events occur close to (far from) the wall, as typically observed in the presence of hairpin vortices. On the contrary, at $200 < t < 400$ for the $L_s = 0.02$ case, ejections are observed close to the wall whereas sweeps lay in the outer region (see figure 5.9.2e). This feature can be associated with the onset of nonlinearities saturating the streaks, where the lift-up of the low-speed streaks initially placed in the near-wall region induces Q2 events close to the wall and the downward motion of high-speed streaks produces Q4 events far from the wall. The same wall-normal arrangement of Q2 and Q4 events is observed in all the three cases in the turbulent regime, namely at $t > 150$ for $L_s = 0, 0.01$ and at $t > 400$ for $L_s = 0.02$ (as indicated by the rapid increase of C_f at these times), due to the presence of nonlinear streaks in the buffer and viscous layer in the fully turbulent flow (Jiménez, 2013).

The effect of the slip boundary condition on sweeps and ejections events in the nonlinear phase of the transition scenario can be further analysed inspecting the distribution of the $u - v$ probability density function averaged over the wall-parallel planes in the near-wall region ($0 < y < 1$), which is provided in the upper row of figure 5.10, together with the wall-normal distribution of the positive/negative streamwise velocity disturbances averaged onto the $x - z$ planes (u^+, u^-) provided in the lower row of figure 5.10, for different values of L_s. Sweep and ejection events are attenuated when the slip length is increased from $L_s = 0.0$ to $L_s = 0.01$ (compare figure 5.10.a with 5.10.b), whereas the u^+ and u^- velocity profiles in figures 5.10.d and 5.10.e, representing the wake of hairpin legs and heads respectively,

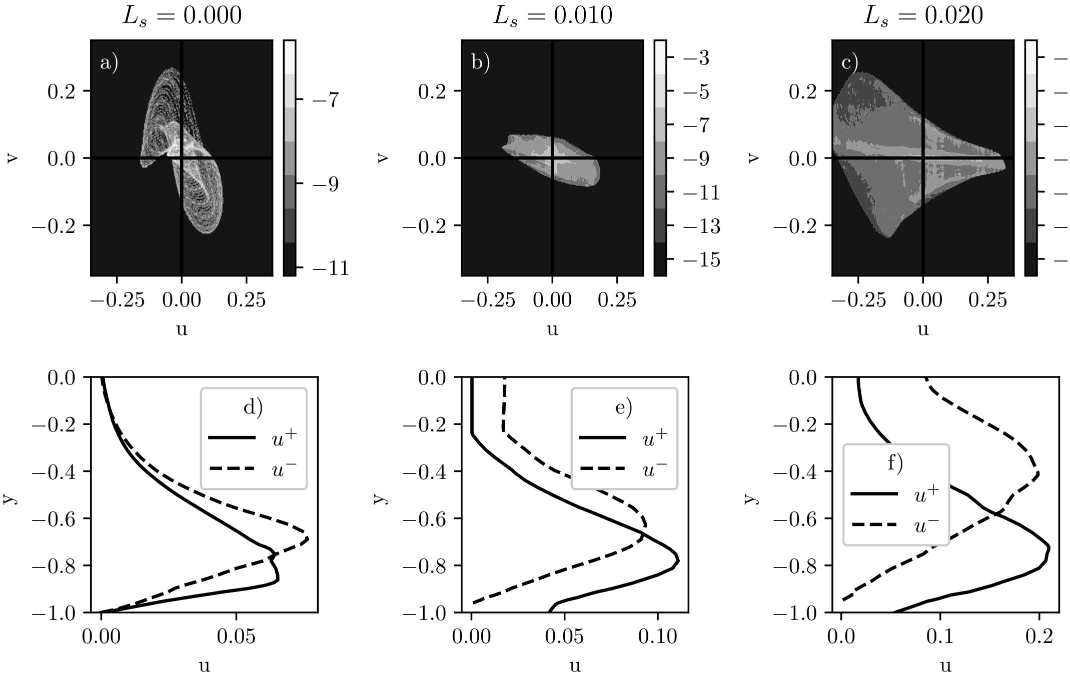

Figure 5.10 – Upper row: contours of the logarithm of the probability density function of the wall-normal and streamwise velocity disturbances in a $u-v$ plane ($w=0$) averaged in the wall-parallel planes in the region $0<y<1$. Values of the logarithm of the PDF have been normalized with respect to the total number of points of the computational domain. Bottom row: profiles of the positive/negative (u^+/u^-) streamwise velocity disturbances, averaged on the $x-z$ planes. For each computed L_s, arranged in columns, we plot the data at time T so that the $Re_\tau(T) = 1.1 \cdot Re_\tau(t=0)$, at the beginning of the non-linear phase.

remain qualitatively similar. In the case $L_s = 0.02$, Q4 events are strongly inhibited and the probability density function is mostly dominated by Q2-Q3 events (see figure 5.10.c), indicating that the flow is characterised by stronger low-speed streaks whose peak value moves upwards in the wall-normal direction (see figure 5.10.c, bottom), a further evidence of the development of non-linear streaks (Mao et al., 2017). Very similar $u-v$ distribution is found farther from the wall (not shown), confirming that the reduced shear succeeds in inhibiting Q4 events everywhere in the flow. These results clearly indicate that for a sufficiently large slip length ($L_s = 0.02$ in the present configuration) the SHS considerably alters the mechanisms leading to the creation of Λ and hairpin vortex, inhibiting Q4 events and consequent transition to turbulence. Depending on the initial amplitude of the imposed perturbations, K-type transition can be delayed or even completely avoided by the presence of SHS of sufficiently large slip length.

How slippery surfaces damp the growth of Λ vortices

We have shown that a slippery boundary is capable of delaying K-type transition by considerably modifying the coherent structures occurring in the process (Bake et al., 2002; Sayadi et al., 2013a). In particular, figure 5.6 clearly shows that introducing a slip length inhibits the development of hairpin vortices by strongly damping the growth of Λ vortices.

Since during K-type transition Λ vortices result from the vortex tilting of the spanwise vorticity associated with the initially imposed TS waves (Malm et al., 2011), we focus on the effect of the slippery walls on the streamwise and spanwise vorticity. Figure 5.11 provides the time evolution of the wall-normal averaged values of $\langle \omega_x \rangle$, $\langle \omega_z \rangle$ for the three considered slip lengths. For $L_s = 0.00$ we observe an initial increase of ω_z due to the presence of TS waves near the walls. After the spanwise vorticity has reached a plateau value, ω_x begins to increase exponentially due to vortex tilting (Malm et al., 2011), producing Λ vortices. The vortex tilting phase leading to the creation of Λ and subsequent hairpin vortices can be visualized in figure 5.12. Increasing L_s results in a reduction of ω_z right during the vortex tilting phase, with a consequent weaker growth of ω_x (see figure 5.13). This effect can be analysed by evaluating the different terms of the vorticity transport equation, which for an incompressible flow reads

$$\frac{D\boldsymbol{\omega}}{Dt} = (\boldsymbol{\omega} \cdot \nabla)\boldsymbol{u} + \frac{1}{Re}\nabla^2 \boldsymbol{\omega}, \tag{5.15}$$

where $\boldsymbol{\omega}$ is the three-dimensional vorticity vector field. Assuming the Re number to be large enough so that the diffusive term is small (Ye et al., 2018), the temporal evolution of the spanwise vorticity reduces to

$$\frac{D\omega_z}{Dt} \approx \underbrace{-\frac{\partial v}{\partial z}\frac{\partial w}{\partial x}}_{T_{zx}} \underbrace{+\frac{\partial u}{\partial z}\frac{\partial w}{\partial y}}_{T_{zy}} \underbrace{+\omega_z\frac{\partial w}{\partial z}}_{S_{zz}}, \tag{5.16}$$

where T_{zx}, T_{zy} and S_{zz} represent the vorticity tilting and stretching terms for the spanwise component, respectively. Further development of the latter relation provides the equation which describes the temporal evolution of the spanwise vorticity:

$$\frac{\partial \omega_z}{\partial t} \approx \underbrace{-\left(u\frac{\partial \omega_z}{\partial x} + v\frac{\partial \omega_z}{\partial y} + w\frac{\partial \omega_z}{\partial z} \right)}_{A_z} + T_{zx} + T_{zy} + S_{zz}. \tag{5.17}$$

The volume integral of each term of equation (5.17) is represented in figure 5.14 for different values of L_s at time $t = 40$. At this time, for $L_s = 0.00$, $\partial\omega_z/\partial t \approx 0$ results from a balance of all terms in equation (5.17) so that ω_z remains constant in time for a large time range. Introducing a slippery boundary the wall-normal gradients $\partial\left(\bullet\right)/\partial y$ (Min and Kim, 2004) are reduced, inducing a strong decrease of the vortex tilting term $T_{zy} = \partial u/\partial z \cdot \partial w/\partial y$. This results into a disequilibrium in equation (5.17) leading to a decrease of the spanwise vorticity and consequently of the vortex-tilting-induced streamwise one, inhibiting the growth of Λ vortices. Thus, introducing a slippery boundary mildly influences the evolution of the TS spanwise vortices, while strongly affects the subsequent onset of Λ vortices by reducing ω_z, as clearly shown in figure 5.13.

5.3 Transition triggered by nonmodal mechanisms

5.3.1 Optimal perturbations

In subcritical conditions in a noisy environment, streaky perturbation are usually observed prior to transition (Kendall, 1998; Saric et al., 2002; Manneville, 2015), since small-amplitude environmental perturbations project in time onto the largest singular value of the linearised Navier-Stokes operator $\boldsymbol{L}$ (Luchini, 2000), whose associated response corresponds

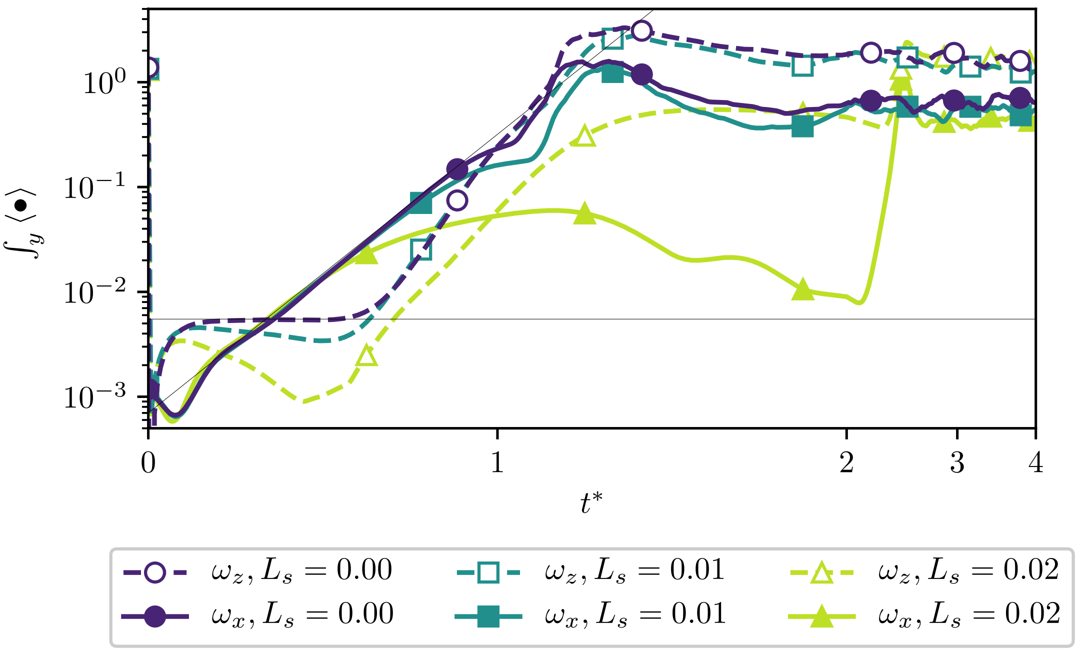

Figure 5.11 – Wall-normal integral of the averaged spanwise and streamwise components of vorticity for different slip lengths. A scaled time $t^* = t/t(Re_\tau = 1.1 \cdot Re_\tau(t=0))$ has been used for the sake of visualization.

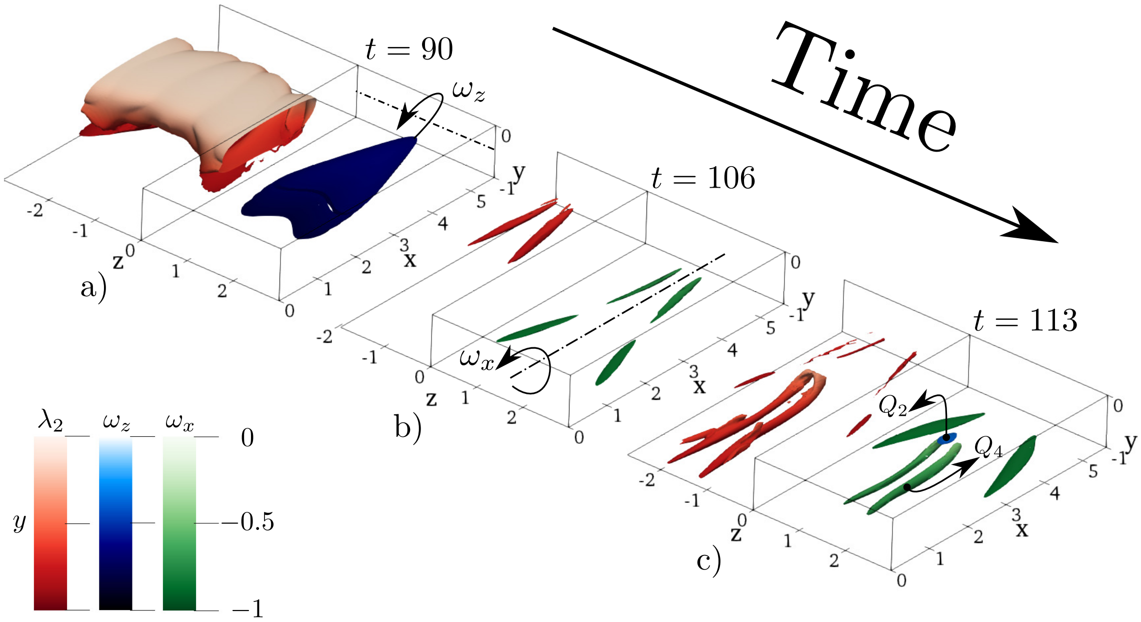

Figure 5.12 – Isosurfaces of λ_2 (red, on the left) and ω_z, ω_x (blue, green, on the right) during K-type transition over a no-slip ($L_s = 0.00$) wall at different times indicated in the plot: $\lambda_2 = -0.001, \omega_z = 2.0$ for $t = 90$; $\lambda_2 = -0.02, \omega_x = 0.8, \omega_z = 3.0$ for the other snapshots. Isosurfaces are coloured with their wall-normal location (darker is closer to the wall). Straight lines highlights the exponential growth of ω_x, indicating the vorticity stretching phase (Malm et al., 2011).

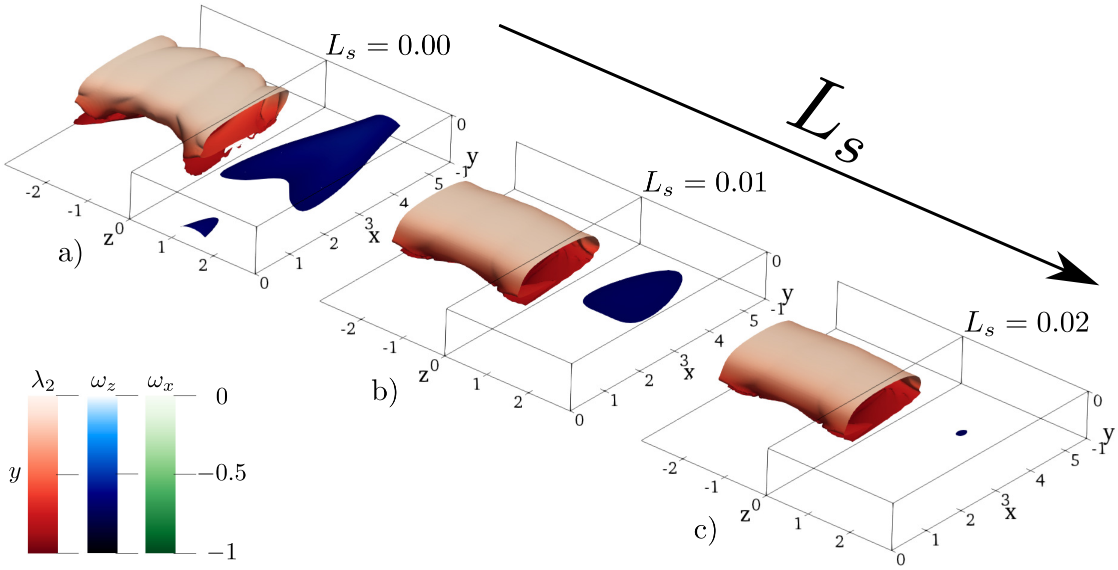

Figure 5.13 – Isosurfaces of $\lambda_2 = -0.001$ (red, on the left) and $\omega_z = 1.475, \omega_x = 1.0$ (blue, green, on the right) during K-type transition over a no-slip wall for $T = 90$ and increasing slip. Whilst spanwise vortices arising from the weakly non-linear interaction of TS waves phase appear to remain substantially unchanged, ω_z is strongly reduced by the introduction of a slip length.

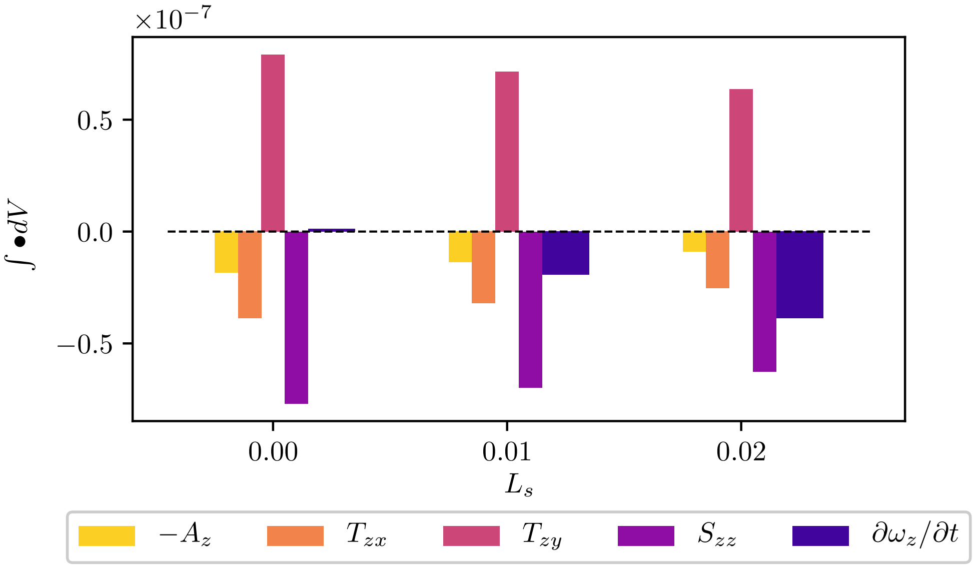

Figure 5.14 – Integrals of the spanwise vorticity equation (5.17) terms, for $t = 40$ and different slip lengths L_s. Terms $(A_z, T_{zx}, T_{zy}, S_{zz})$ have been scaled by a factor of $(10^{-2}, 10^{-1}, 10^{-3}, 10^{-3})$, respectively, for the sake of visualization.

to the optimal perturbation for the considered flow (Farrell, 1988). Optimal perturbations are able to induce, by means of non-normal yet linear interaction of eigenmodes of $\boldsymbol{L}$, the maximum possible transient energy growth in a finite time range (Schmid and Henningson, 2001). This energy growth allows the development of nonlinear interactions leading the flow to transition. To study the effect of the SHS on this optimal transition scenario, we impose as initial condition $\boldsymbol{U}(\boldsymbol{x}, t = 0) = \boldsymbol{U}_b(\boldsymbol{x}) + \epsilon \boldsymbol{u}_0^{Opt}(\boldsymbol{x})$, where $\epsilon \boldsymbol{u}_0^{Opt}(\boldsymbol{x})$ is the initial optimal perturbation computed in the chosen flow conditions and ϵ is a given amplitude, which has to be set sufficiently high for triggering nonlinear effects and consequently lead to transition (Reshotko, 2001). Being derived from linearised equations, the optimal perturbation can be freely scaled so to match an arbitrarily imposed energy level. If the initial perturbation energy is set to a very low value, the initial perturbation, composed of streamwise vortices, linearly evolves in time creating optimal streaks, which asymptotically fade away as predicted by the linear theory. Increasing the initial energy level to $E(0) = 10^{-6}$, as shown in figure 5.15 for the no-slip case, after an initial linear growth phase ($0 < t < 200$), the streaks saturate nonlinearly (see the inset at the bottom right) to an amplitude A_s. As soon as this amplitude overcomes a critical threshold (Brandt et al., 2003) secondary instabilities of the nonlinearly saturated optimal streaks set in ($t \approx 400$), immediately followed by breakdown to turbulence. Further increasing the initial energy to $E(0) = 10^{-5}$ leads to a more rapid departure from the linearly predicted energy growth curve due to the onset of non-linearities already at very small times, resulting in a different saturation energy threshold. Nonlinearly saturated streaks, strongly deformed with respect to the linear optimal solution as shown in the top right inset, are formed already at $t \approx 150$ and due to secondary instability, breakdown to turbulence is reached already at $t \approx 200$.

Introducing a slippery boundary does not modify this scenario, as depicted in figure 5.16. For the smallest considered energy level the growth rate curves for the cases $L_s = 0.00, 0.02$ are very close to each other, although a slightly larger energy gain is reached in the slippery case. The same effect is observed for the largest energy level considered here, where the case at $L_s = 0.02$ appears to follow more closely the linear evolution of $G(t)$ with respect to the no-slip one. This is probably due to the fact that in the no-slip case a slightly larger energy growth is predicted by the linear theory at small times (compare the solid with the dashed black lines in the left frame), resulting in a more rapid onset of nonlinear effects which translates in an earlier and more pronounced deviation from the linear energy growth curve. However, in both cases secondary instability is reached practically at the same time, since the energy level reached in the saturation phase (see the right frame of figure 5.16) and the shape of the nonlinearly saturated streaks (see figure 5.17) appear to be almost independent on the imposed slip length. The fact that, differently from the K-type one, the optimal transition scenario is virtually unaffected by the introduction of a slip length can be explained by the fact that the optimal perturbations are localised in the bulk of the channel, as opposed to TS waves which are placed close to the wall. Since SHS act by modifying the flow shear near the wall, it appears clear why optimal streaks are unaffected by this boundary modification even when non-linearities kicks-in, as depicted in figure 5.17.

5.3.2 Uncontrolled transition

In this section we aim at studying how *uncontrolled* transition, namely that naturally occurring in a noisy environment in subcritical conditions, is affected by the presence of superhydrophobic walls. Uncontrolled transition in a channel flow can be triggered using random noise, a random superposition of Stokes modes, or as proposed in 4, using an ad

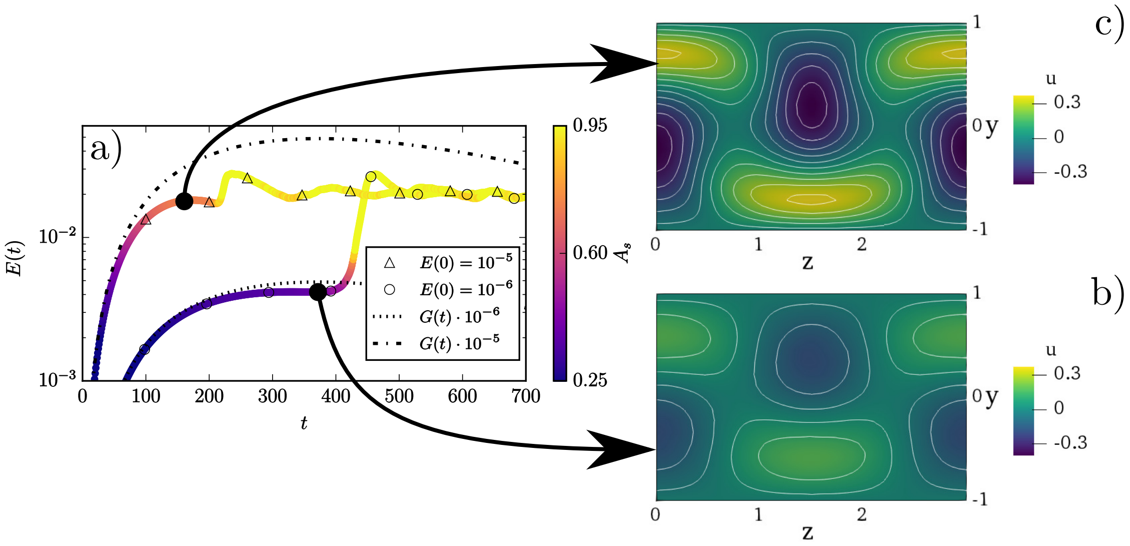

Figure 5.15 – (a) Time evolution of the kinetic energy density of the velocity perturbation during laminar-turbulent transitions triggered by linear optimal perturbations, for a no-slip wall ($L_s = 0.00$) and for two prescribed values of the initial energy, $E(t = 0) = 10^{-6}$ and $E(t = 0) = 10^{-5}$ (thick solid lines coloured by the value of A_s). The dashed lines indicate the energy growth as predicted by the linear theory for the two imposed initial energy levels. (b) Isocontours of the streamwise velocity perturbation in a $z - y$ plane for the case with $E(t = 0) = 10^{-6}$ at $t = 150$ showing the highly deformed nonlinearly saturated streaks. (c) Isocontours of the streamwise velocity perturbation in a $z - y$ plane for the case with $E(t = 0) = 10^{-5}$ at $t = 380$. In both (b) and (c) cases, the velocity field is invariant in the streamwise direction, therefore any x-normal plane will provide the same data.

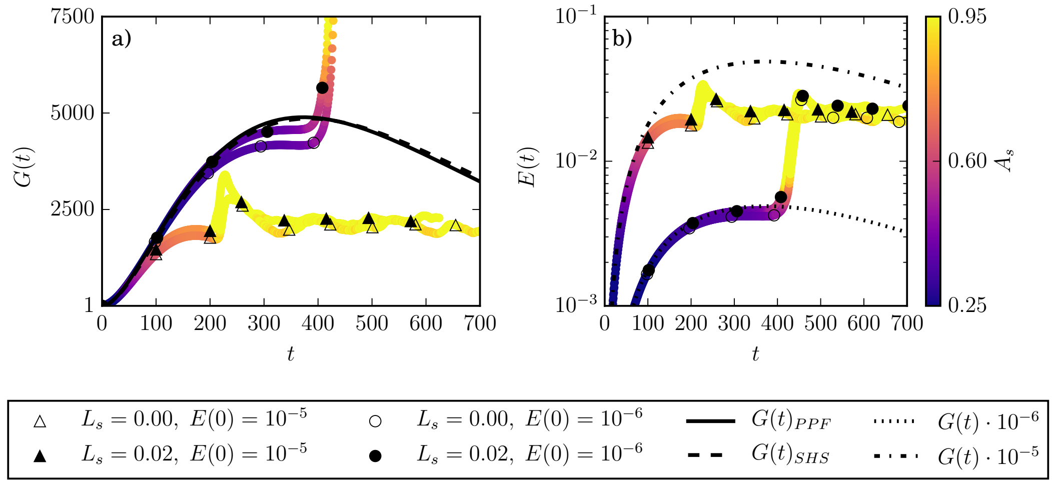

Figure 5.16 – Influence of SHS on subcritical transition at $Re = 5000$ triggered by linear optimal perturbations. Both subfigures represent the same dataset. In a) the energy gain evolution is represented to highlight the initial linear phases, whereas in b) the energy is plotted, for two initial energy levels and two slip lengths indicated in the legend. The dashed lines indicate the energy growth as predicted by the linear theory for the two imposed initial energy levels.

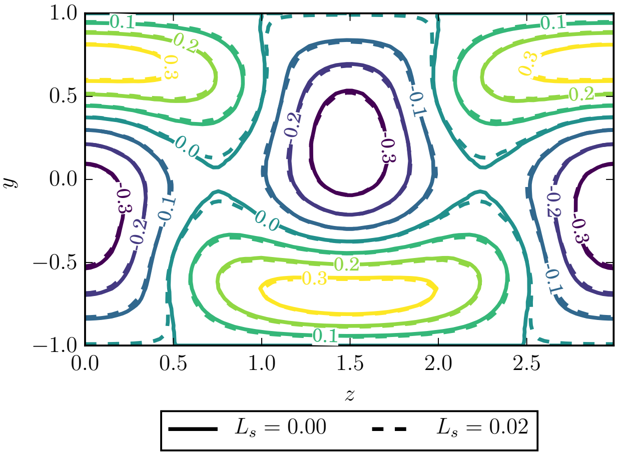

Figure 5.17 – Streamwise velocity perturbation measured at $T = 150$ in a DNS initialized with the optimal perturbation having initial energy $E(t) = 10^{-5}$ for two slip lengths. The non-linear streaks observed in the no-slip case ($L_s = 0.0$, subplot 5.15.c) match those developing onto a slippery surface with $L_s = 0.02$.

hoc volume forcing constructed by a superposition of optimal forcing functions. The latter technique, which we refer to as *F-type* transition, has been chosen here for studying the effect of SHS on laminar-turbulent uncontrolled transition. In figure 5.18 we show the impact of SHS on uncontrolled transition. Increasing L_s is totally ineffective in delaying the onset of turbulence, as shown by the evolution of the friction Reynolds number during F-type transition (figure 5.18.a). As explained in section 4 for the classical channel flow with no-slip walls, the imposed volume forcing acts similarly to a noisy environmental disturbance, promoting the development of streaks as a response of the flow to external disturbances (Schmid and Henningson, 2001; Jacobs and Durbin, 2001a; Brandt et al., 2004a). As previously shown in figure 5.16, streaks are mildly affected by a slippery boundary condition, being localised far from the walls. This is confirmed by figure 5.18.b, where the time evolution of the Fourier modes $(0, 1)$, $(1, 1)$ and $(0, 2)$ is provided, clearly showing the onset of streaks ($(0, 1)$) and $(0, 2)$ modes) from a noisy disturbance due to receptivity, their non-linear saturation as well as their final breakdown. Practically no difference can be noticed between the mode evolution for the considered three slip length. The time evolution of the coherent structures associated with uncontrolled transition is provided in Figure 5.19. The flow evolution appears very similar for the three slip lengths considered, except for the non-zero velocities measured at the wall in the SHS cases, which has practically no influence on the mechanisms leading to transition. Thus, we can conclude that uncontrolled transition cannot be effectively controlled by SHS, at least for the considered values of the slip length, since similarly to the optimal transition scenario, it mostly relies on the onset and instability of streamwise streaks, which are both intrinsically inviscid mechanisms not strongly affected by the presence of a slippery wall.

5.4 Summary and conclusions

In this chapter we investigate the influence of Superhydropbobic Surfaces (SHS) on different laminar-turbulent transition processes, in order to evaluate their effectiveness as

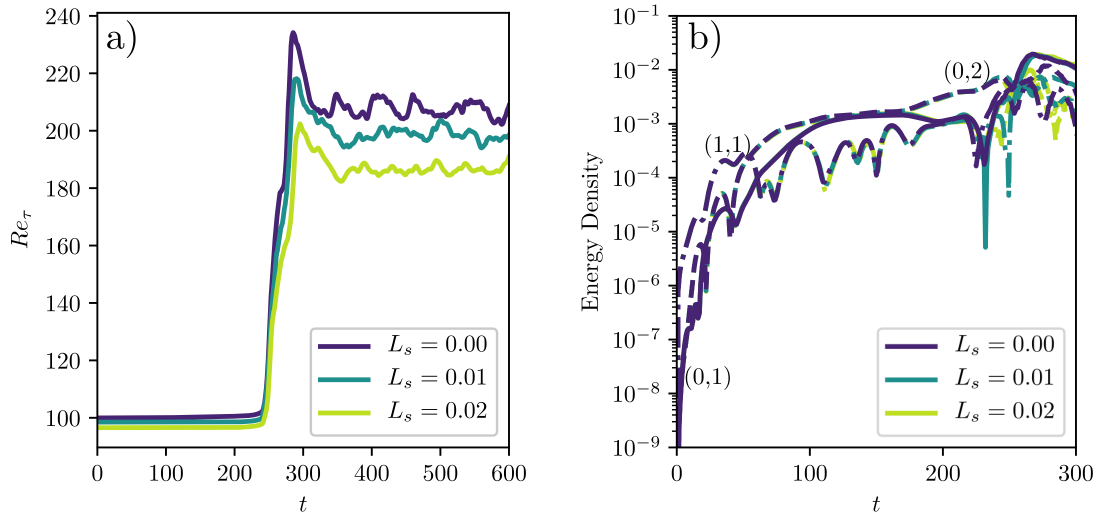

Figure 5.18 – Time evolution of the friction Reynolds number Re_τ and of the energy of three selected Fourier modes for channel flow with different slip lengths undergoing F-type transition. The process is completely unaffected by the increase in slip length L_s.

passive devices for flow control in transitional conditions. Following Min and Kim (2005), we have focused on the channel flow configuration where the superhydrophobic surfaces have been modelled by flat, spatially homogeneous and isotropic slippery boundaries. We have performed a wide range of DNSs showing that transition delay is not only dependent on the intrinsic slip length of a certain Superhydrophobic surface, but also strongly depends on the specific transition scenario one aims at controlling. Our investigation has revealed that a slippery wall can effectively control transition scenarios dominated by near-wall perturbations, i.e. Tollmien-Schlichting waves such as those naturally arising in the flow in supercritical conditions or those occurring during K-type transition in subcritical conditions. In this framework, superhydrophobic surfaces alter the development of Λ vortices, since the reduced wall normal velocity gradient inhibits their formation out of the initial Tollmien-Schlichting waves. In turn, this inhibits the formation of hairpin vortices altering the succession of sweep and ejection events, thus provoking relaminarization or a large delay in the transition time. On the other hand, our analyses indicates that superhydrophobic surfaces are ineffective in controlling transition initiated by linear optimal perturbations, or even uncontrolled transition, namely that occurring in noisy environments in subcritical conditions, where the seeds of transition (namely, streamwise vortices and streaks) are localised in the bulk of the flow, far from the bounding walls. Superhydrophobic surfaces can thus be considered effective in delaying or avoiding transition only in low-noise environments, where transition is triggered mostly by modal mechanisms, but not in noisy ones, where nonmodal mechanisms govern the transition scenario.

It remains to be verified whether a more accurate modelling of the superhydrophobic surface might lead to different results. The homogeneous slip condition can be replaced at first with a patterned slip/no-slip boundary condition on a flat wall to investigate the effects of this condition on laminar-turbulent transition. Eventually, also the dynamics of the deformable gas/liquid interfaces might be taken into account as already done by Seo and Mani (2018) for a turbulent channel flow. Increasing the model accuracy may result in further modifications of the transitional phase, and thus requires further investigation.

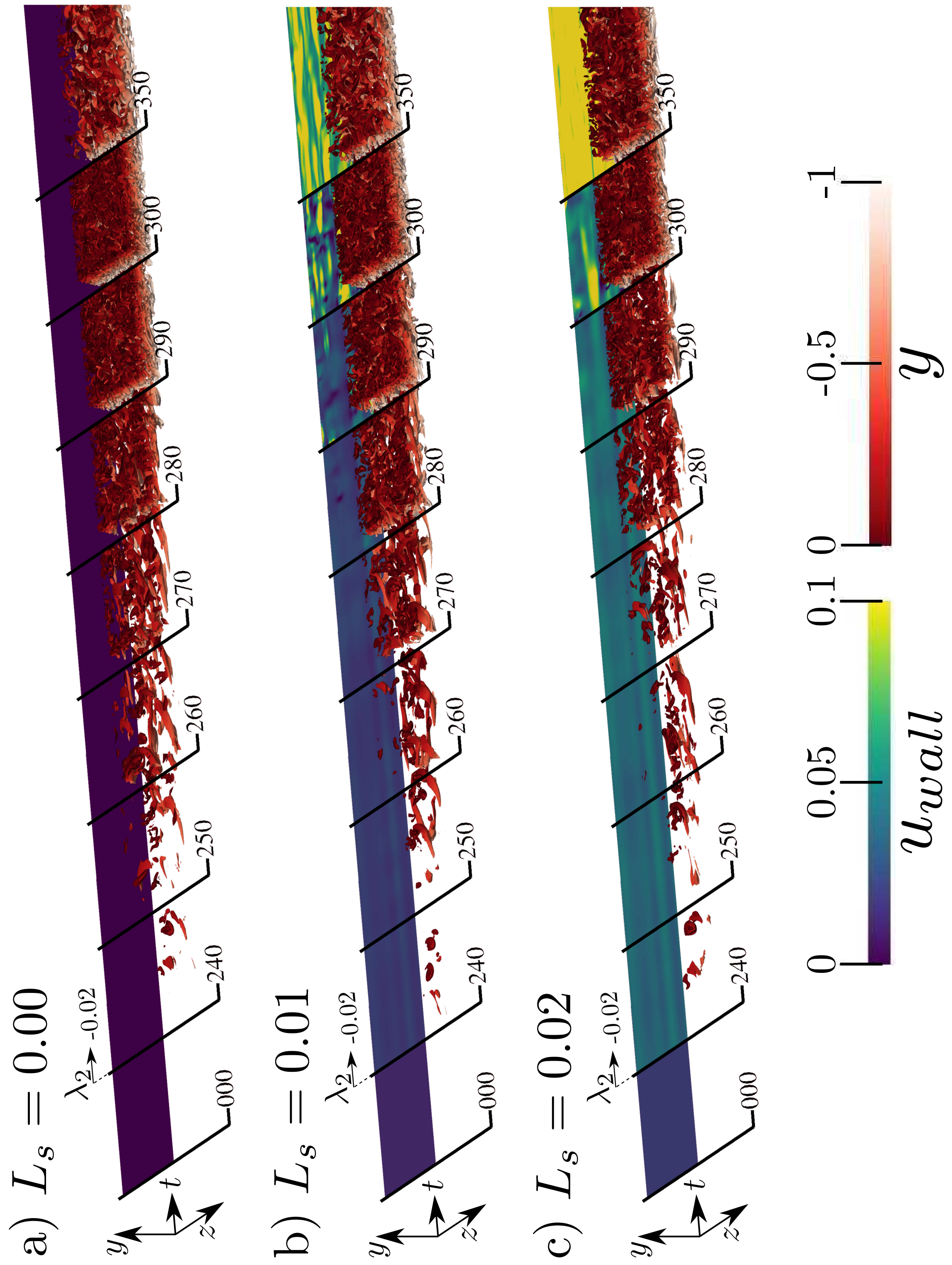
a) $L_s = 0.00$
b) $L_s = 0.01$
c) $L_s = 0.02$
λ_2 -0.02
000
240
250
260
270
280
290
300
350
t
y
z
0
0.05
0.1
u_{wall}
0
-0.5
-1
y

Figure 5.19 – Overview of F-type transition over superhydrophobic surfaces. As in figure 5.6 snapshots depict the isosurfaces of the λ_2 criterion and streamwise velocity at the wall for different values of the slip length L_s. This *uncontrolled* scenario, characterised by the onset of streaky velocity perturbations occurring in the flow bulk, appears to be completely unaffected by the introduction of a slippery boundary.

Chapter 6

Influence of SHS Modelling on K-type transition

Many passive control strategies have been recently proposed to reduce drag in wall bounded shear flows. Amongst them, underwater Superhydrophobic Surfaces (SHS) have proven to be capable of dramatically reduce the skin friction of a liquid current, providing a lubricating layer of gas bubbles, which is kept trapped within the surface nano-sculptures due to capillary forces. Under specific geometrical and thermodynamical conditions, such as the roughness size, wetting transition can be avoided, such textured surfaces can provide a slippery boundary, resulting in the so called Lotus effect. In this framework we propose to study, by means of numerical simulations, the influence of SHS on laminar-turbulent, K-type transition in a channel flow. The complete evolution from laminar, to transitional and fully developed turbulent flow is studied considering different surface modellings. First the SHS is considered to be flat, either with an alternation of slip–no-slip boundaries to discretise each roughness or through a spatially homogeneous equivalent slippery wall, showing that SHS can triple the transition time to turbulence by stretching hairpin's legs and inhibiting the sweep-ejection process. Then, the dynamics of each microscopic liquid-gas free-surface has been taken into account by means of a fully coupled fluid-structure solver. Whilst being extremely small compared to the streamwise component, the non-zero wall-normal velocity resulting from the interface deformation promotes ejection events, eventually advancing transition. This behaviour, undetected by global stability analysis, confirms that SHS can effectively control K-type transition scenario from its weakly nonlinear stages. The chapter is organised as follows. In section §6.1 we present the governing equations, as well as the method used to implement different modellings for taking into account the key physical features introduced by the use of underwater superhydrophobic surfaces and highlight the main characteristic lengths and dimensionless parameters for the problem. In section §6.2 we show how the behaviour of infinitesimal perturbations is influenced by differently modelled SHS by means of local and global stability analisys. Section §6.3 reports the DNS results of our simulations where we show that the laminar-turbulent transition process is strongly affected by the physical feature unlocked by each specific modelling. In particular we demonstrate that, while modelling each microtexture provides the same transition scenario as the one computed of spatially homogeneous slippery surfaces, taking into account the gas-liquid interface displacement produces wall-normal velocities at the boundary that strongly interacts with the overlying coherent structures characteristic of the transitional process. A final discussion and conclusions are given in section §6.4.

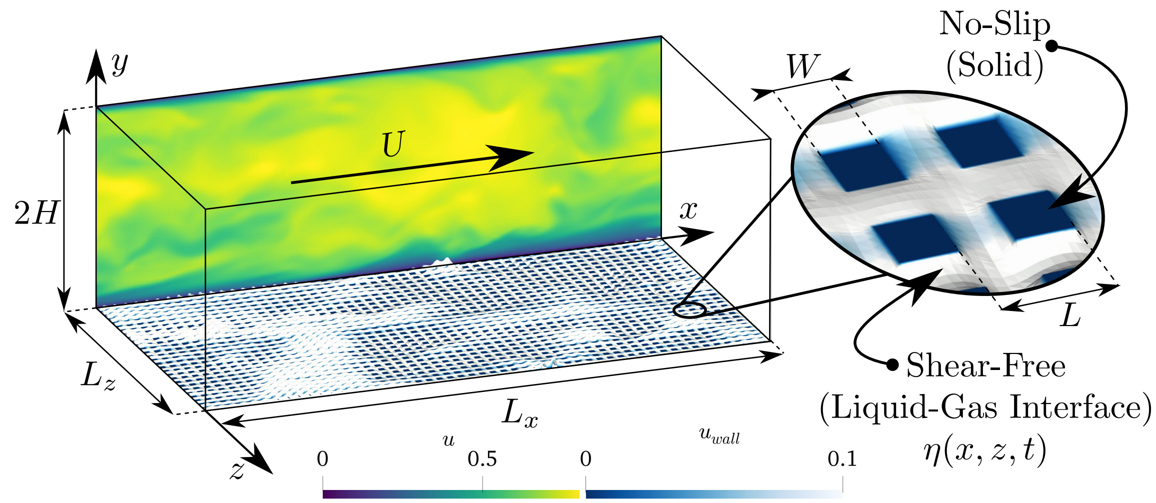

Figure 6.1 – Sketch of a channel flow with Superhydrophobic Surfaces, depicting the length-scales gap between the overlying laminar-turbulent *macroscopic* flow (H) and the near-wall, capillary driven *microscopic* free-surface dynamics (L)

6.1 Problem formulation

The channel flow configuration is chosen to study how laminar-turbulent transition could be controlled using superhydrophobic walls capable of entrapping a gas-lubricating layer. Assuming that air-water free-surfaces are kept pinned to the roughness surfaces, as sketched in figure 6.1, the influence of superhydrohobic surfaces can be modelled with an equivalent boundary condition for the overlying, incompressible Newtonian flow, governed by the Navier-Stokes equations

$$\frac{\partial \boldsymbol{U}}{\partial t} = -(\boldsymbol{U}\cdot\nabla)\boldsymbol{U} - \nabla P + \frac{1}{Re}\nabla^2\boldsymbol{U} + \boldsymbol{f} \tag{6.1}$$

$$\nabla\cdot\boldsymbol{U} = 0, \tag{6.2}$$

where $\boldsymbol{U} = (U(\boldsymbol{x},t), V(\boldsymbol{x},t), W(\boldsymbol{x},t))^T$ is the velocity field, $P(\boldsymbol{x},t)$ is the pressure and $\boldsymbol{f}$ the forcing field. The Reynolds number is defined as $Re = UH/\nu$, where U is the centerline velocity, H is half the height of the channel and ν the kinematic viscosity of the fluid. The reference frame $\boldsymbol{x} = (x,y,z)^T$ is chosen such that x is the streamwise, y the wall-normal and z the spanwise directions. The periodic roughness structure is made out of square post, and is characterised by its period L and width W as indicated in figures 6.1 and 6.2, while the free-surface interface is kept in place by capillary forces, characterised by the surface tension σ, dependent on the gas-liquid physical properties. The different boundary conditions aiming at modelling SHS have been implemented within Nek5000 (Fischer et al., 2008), a spectral element method flow solver. We have used streamwise periodic boundary conditions, as an alternative to the spatial framework for the numerical simulation of transitional flows (Gilbert and Kleiser, 1990). Reducing the computational size needed to observe transition, this approach enables the use of complex surface modellings such as the ones proposed in the present study, reducing considerably the computational cost.

6.1.1 Modelling Underwater SuperHydrophobic Surfaces

The first and simplest model consists of representing SHS using a spatially homogeneous Navier boundary condition on the surface, as introduced in equation (1.2). This approach, based on an homogeneization theory (Zampogna et al., 2019) and which we will refer to as spatially Homogeneous Slip Lenght (HSL), provides a computationally unexpensive method to describe the influence of gas-lubricated substrates. In fact simulations with HSL boundary conditions have proven to predict well the experimental results in both laminar (Rothstein, 2010) and turbulent regime (Seo and Mani, 2016), provided that the scalar slip length L_s is well evaluated (Seo et al., 2015). The choice of using SHS made out of square posts allows for the use of a single, constant slip length. This allows for an even more simplified model, in contrast with what would occur when dealing with anisotropic SHS patterns (Pralits et al., 2017) or considering shear-dependent slip length (Aghdam and Ricco, 2016).

The second approach used here aims at modelling each single microscopic gas-solid boundary with an equivalent Slip–No-Slip (SNS) boundary condition. The underlying assumption is that the free-surface remains perfectly flat while providing a shear-free boundary, a standard in the literature for DNS of turbulent flow supported by SHS (Martell et al., 2009; Park et al., 2014; Jelly et al., 2014; Lee et al., 2016). While the implementation of such method is straightforward, simulating texture sizes similar to the ones observed in experiments could require spatial discretization up to ten times more refined than using a simple spatially homogeneous boundary condition (i.e. cases P06 and HP06 in the work by Seo and Mani (2016)).

The third SHS model used here includes the dynamic influence of interface deformation on the overlying flow. Following the work of Seo et al. (2017), we consider an ideal free-shear boundary condition on the air-water interface (Schönecker et al., 2014), that neglects plastron viscosity, whilst ensuring a pinned interface(Steinberger et al., 2007; Teo and Khoo, 2010; Seo et al., 2015). Under these assumptions the free-surface deformation is linked to the liquid pressure at the interface via a linearized Young-Laplace equation,

$$\Delta^2\eta \approx \frac{P_{liquid} - P_{gas}}{\sigma}, \tag{6.3}$$

where σ is the surface tension and, assuming P_{gas} to be uniform within all the lubricating gas layer, the plastron's mass conservation yields

$$\int\int \eta(x,z,t)\ dx\ dz = 0. \tag{6.4}$$

Doing so, we end up solving equations (6.1) over a time-dependent, deforming boundary, constituting a two-way coupled fluid structure interaction problem. It is important to underline that in this preliminary study we have neglected the motion of the gas, as well as considered it to maintain a constant pressure. Despite being strong simplifications (Lee and Kim, 2011), on one hand these assumptions allows the use of a simplified framework, as indicated in the following. On the other hand their influence on the behaviour of the overlying flow has still not been identified experimentally (Gose et al., 2018), precluding any eventual quantitative comparison for the validation of the numerical approach.

In the present study we make use of arbitrary-Lagrangian-Eulerian (ALE) description (Ramaswamy and Kawahara, 1987) to simulate the free-surface deformation, taking advantage of the implementation made by Lee-Wing and Patera (1990), natively coded and validated within Nek5000 (Ho, 1989). This approach provides an accurate and numerically efficient description of the free-surface dynamics while ensuring the kinematic condition

$$\boldsymbol{w} \cdot \hat{\boldsymbol{n}}|_{\eta} = \boldsymbol{U} \cdot \hat{\boldsymbol{n}}|_{\eta}, \tag{6.5}$$

where $\boldsymbol{w}$ is the mesh velocity and $\hat{\boldsymbol{n}}$ is the unit normal at the free surface $\eta(x,z,t)$. Provided that the mesh velocity at the wall is $\boldsymbol{w}|_{wall} = \dot{\eta}$, this MoVing Boundary (MVB)

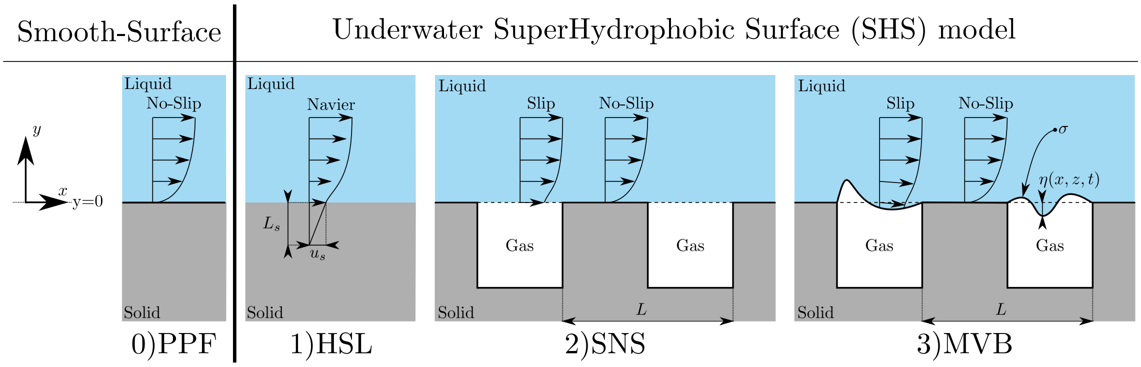

Figure 6.2 – Equivalent boundary conditions for modelling the influence of Underwater SuperHydrophobic surfaces.

model allows for non-zero wall normal velocity components over the free-surface interface. Although the resulting wall normal velocity at the boundary is negligible in fully turbulent flows over realistic SHS (Seo et al., 2017), we will show that it can strongly affect the processes occurring during the transitional phase. As a further remark we would like to hightlight that, owing to the small η compatible with wetting stable SHS, wall normal velocity induced by the interface deformation will assume the form:

$$\boldsymbol{V}(x, y = \eta, z, t) = \frac{D\eta}{Dt} = \frac{\partial \eta}{\partial t} + U\frac{\partial \eta}{\partial x} + W\frac{\partial \eta}{\partial z}, \tag{6.6}$$

as found by Seo et al. (2017) by linearizing the boundary condition for V at $y = \pm 1$. A summary of the three different SHS models is sketched in figure 6.2, as well as a reminder for the smooth-wall boundary condition providing the standard Plane Poiseuille Flow (PPF).

6.1.2 Simulation parameters

In this work we study how the fundamental K-type transition (Kachanov, 1994a) could be controlled in a periodic channel flow bounded by superhydrophobic surfaces. Simulations were performed in channels of size $2\pi\alpha \times 2H \times 2\pi\beta$. A constant flow rate corresponding to a laminar Reynolds number of $Re = 5000$ and $(\alpha, \beta) = (1.12, 2.10)$ have been set so that to match the transitional DNSs available in literature (Zang and Krist, 1989; Gilbert and Kleiser, 1990; Schlatter, 2005). The fully developed turbulent flow is characterised by the friction Reynolds number $Re_\tau = u_\tau \delta / \nu$, measuring the ratio between the external scales ($\delta \equiv H$ in a channel flow) and the viscous unit length $\delta_\nu = \nu / u_\tau$. The friction velocity is given as $u_\tau = \sqrt{\tau_w / \rho}$, using the wall shear stress $\tau_w = \nu\rho |\partial < U > / \partial y|_{wall}$, representing the mean skin friction averaged over the entire surface area. While the solid no-slip boundary is constantly located at $y = \pm 1$, the moving interface is free to deform and displace in the y direction. For this reason we will consider that a grid point belongs to the lower (upper) *wall* when it yields the lowest (highest) y value, for a given $x - z$ location. The use of SHS aiming at controlling transition requires an accurate design of the surface features. While highly slippery walls, resulting from large free-surface interfaces, have proven to be capable of delaying and eventually inhibiting the onset of turbulence (Min and Kim, 2005), it must be kept in mind that the texture size of SHS roughness shall not exceed the threshold for wetting stability to occur (Seo et al., 2017), limiting the maximum amount of slip these gas-impregnated surfaces could provide. Key dimensionless parameter is the size of the texture size in viscous units $L^+ = L/\delta_\nu$, where L is the SHS texture size, as indicated in figures 6.1 and 6.2. Experiments have demonstrated that SHS characterised by $L^+ \approx 0.5 - 10$ are capable of sustaining a fully developed turbulent flow (Daniello et al., 2009; Woolford et al., 2009; Park et al., 2014; Li et al., 2017; Gose et al., 2018), while larger surface texture would not be capable of withstanding wetting transition (Zhang et al., 2016). The use of a spatially Homogeneous Slip Length (HSL) boundary condition for the simulation of such flows presents no difficulties: an equivalent slip length can be dependably evaluated (Seo and Mani, 2016), ensuring for physically accurate simulations with no added computational cost when comparing to standard no-slip wall (Min and Kim, 2004; Fukagata et al., 2006). On the other hand employing spatially heterogeneous (SNS or MVB) models requires for extremely refined computational grids in order to accurately discretise the texture patterns, which have become affordable only in the last decade(Türk et al., 2014; Rastegari and Akhavan, 2015; Seo et al., 2015, 2017; Seo and Mani, 2018). Moreover, the treatment of the gas-liquid interface dynamics arising from MVB models imposes an additional limitation on our timestep, as indicated in equation (3.3) in the work of Seo et al. (2017).

Previous numerical investigations have made use of HSL models to simulate laminar-turbulent transition over superhydrophobic surfaces (Min and Kim, 2005), where the largest slip length considered is $L_s = 0.02$, that we consider as benchmark value. In order to compare the influence of surface modelling onto the transition process, we must determine the surface texture features required in SNS and MVB modelling to provide the same amount of slip using HSL boundaries. To do so we use the universal slip length representation for turbulent flows over SHS, (equation 15 in the work by Seo et al. (2015)):

$$L^+ = \frac{L_s^+}{C_b} + 0.328(L_s^+\sqrt{\phi_s})^3, \tag{6.7}$$

where the coefficient $C_b = (0.325/\sqrt{\phi_s}) - 0.44$, ϕ_s is the liquid-solid/liquid-gas area ratio of the texture pattern and L_s^+ is the slip length adimensionalised by its viscous counterpart. Based on previous studies of the transitional flow over SHS surfaces modelled with a single slip length, we know that setting a laminar $Re = 5000$ and keeping a constant flow rate, superhydrophobic substrates will decrease the friction Reynolds number defined in Section (5), resulting in $L_s = 0.02$ for a $Re_\tau \approx 190$. Setting $\phi_s = 0.25$ as first guess, equation (6.7) states that the surface texture size has to be $L+ \approx 19$, equivalent to $L \approx 0.1$. The value is close to the upper limit proposed by Seo and Mani (2016), who demonstrated the remarkable matching of DNS results obtained using both pattern-resolved (SNS) and equivalent homogeneous (HSL) boundary conditions for simulating a fully turbulent flow over SHS. It follows that accounting for superhydrophobic walls using spatially heterogeneous SNS and MVB models, there are $(2\pi/\alpha)/L \approx 53$ and $(2\pi/\beta)/L \approx 28$ posts in the streamwise and spanwise simulation, respectively. Each liquid-solid//liquid-gas interface has to be treated with a single spectral element owing to numerical constraints of the code we use, thus the imposed value of $\phi_s = 0.25$ implies that the domain will be discretized by 106 elements in the streamwise direction and 56 in the spanwise one in order to simulate isotropic square posts. Choosing a spectral order of 8, each texture element is discretised with 16 grid points per direction which, according to a recent study by Fairhall et al. (2018), allows for an accurate study of the turbulent state, therefore sufficient for the study of the transitional stage. The main interest of using the Navier model in equation (1.2) is that we do not need to discretize the surface texture iself, greatly reducing the computational cost of a single simulation. In table 6.1 we report the numerical discretisations employed during the present study, depending onto the surface model employed: the spatially homogeneous (PPF, HSL) as well as the spatially heterogeneous ones (SNS, MVB). The last dimensionless parameter we introduce is the Weber number $We^+ = \rho u_\tau^2 \delta_\nu / \sigma$, which relates the

Surface Model	$\mathbf{E_x \times E_z \times E_y}$	$\mathbf{N_x \times N_z \times N_y}$	$\langle \mathbf{\Delta x^+} \rangle \times \langle \mathbf{\Delta z^+} \rangle \times \mathbf{\Delta y^+_{y=\pm 1//0}}$
Homogeneous	$24 \times 24 \times 24$	$192 \times 192 \times 192$	$\approx 6.2 \times \approx 3.0 \times 0.04//4.1$
Heterogeneous	$106 \times 56 \times 24$	$848 \times 448 \times 192$	$\approx 1.2 \times \approx 1.2 \times 0.04//4.1$

Table 6.1 – Simulation parameters. Superhydrophobic surfaces capable of withstanding wetting transition while supporting a turbulent flow requires for $L^+ \approx 20$, therefore the spatial discretization arising from heterogeneous models (SNS, MVB) overwhelms the one needed to accurately compute the turbulent state over a smooth, spatially homogeneous (PPF, HSL) surfaces, as shown by Seo and Mani (2016).

surface tension σ of the gas-liquid interface to the momentum, and is required when using MVB modelling of SHS. In the present study we assume an air-lubricating water turbulent channel at a $20°C$, providing $\sigma = 0.072N/m$, $\rho \approx 10^3 N \cdot s^2/m^4$ and $\nu \approx 10^{-5} m^2/s$. For $Re_\tau = 190$ we will measure $u_\tau \approx 0.038m/s$. Considering that $u_\tau \delta_\nu = \nu$ we end up with $We^+ = \rho u_\tau \nu/\sigma \approx 5 \times 10^{-4}$ which, together with $L^+ \approx 19$ we discussed earlier, constitutes the key controlling parameters of our simulations. These L^+, We^+, comparable with the ones observed experimentally, have been considered suitable for the simulation of SHS capable of withstanding a turbulent flow without the occurrence of wetting transition (Seo et al., 2017).

6.2 Influence of Surface Modelling onto Linear Stability

In this section we study whether flow stability is modified by the use of different surface modellings of the SHS. To do so, we study the evolution of small-amplitude disturbances $\boldsymbol{q}(\boldsymbol{x}, t)$ around steady solutions of the Navier-Stokes equations (6.1) which constitute the base flow $\boldsymbol{Q}_b(\boldsymbol{x})$, so that $Q(\boldsymbol{x}, t) = \boldsymbol{Q}_b(\boldsymbol{x}) + \boldsymbol{q}(\boldsymbol{x}, t)$. The dynamics of such perturbations is governed by the linearised Navier-Stokes equations, which once projected onto a divergence-free vector space can be compactly written as

$$\frac{\partial \boldsymbol{u}}{\partial t} = \boldsymbol{J}\boldsymbol{u}. \tag{6.8}$$

Provided that equation (6.8) models the behaviour of a linear dynamical system autonomous in time, we can expand the perturbation $\boldsymbol{q}$ in normal modes, such that $\boldsymbol{u}(\boldsymbol{x}, t) = \sum_{k=1}^{\infty} \hat{\boldsymbol{u}}_k(\boldsymbol{x}) e^{\lambda_k t}$. Injecting this expansion into equation (6.8) yields the eigenvalue problem

$$\lambda \hat{\boldsymbol{u}} = \boldsymbol{J}\hat{\boldsymbol{u}}, \tag{6.9}$$

where $\lambda = \sigma + i\omega$ is the eigenvalue and $\hat{\boldsymbol{u}}$ its associated eigenvector, σ and ω representing the growth rate and the frequency of the eigenmode. When the critical Re number (Re_c) is overtaken, at least one eigenvalue of $\boldsymbol{J}$ will have $\sigma > 0$ and the whole system is said to be linearly unstable.

Min and Kim (2005) have been the first to investigate the influence of SHS on the stability of a pressure driven flow, modelled using an HSL model. Under this assumption the base flow is dependent only to the wall-normal direction (Philip, 1972) and on the slip length value, as

$$U_b(y) = \frac{2L_s + 1 - y^2}{3L_s + 1}. \tag{6.10}$$

Thus, in this particular case the perturbation can be further expanded as

$$\boldsymbol{u}(\boldsymbol{x},t) = \sum_{k=1}^{\infty} \tilde{\boldsymbol{u}}_k(y) e^{\lambda_k t} e^{i(\alpha x + \beta z)}, \tag{6.11}$$

where α and β represent the streamwise and spanwise wavenumbers, respectively. This expansion allows to carry out a computational inexpensive 1D local stability analysis (Orszag, 1971). Min and Kim (2005) have found that slippery surfaces stabilise the Tollmien-Schlichting waves (TS) by weakening the wall shear $\partial U / \partial y$, and that the critical Reynolds number Re_c increases with the slip length L_s.

In this work we investigate whether introducing the spatial heterogeneity of the SHS affects these results. In fact, depending on the chosen SHS pattern, the base flow will be homogeneous in only one or even zero directions, invalidating the assumption made in equation (6.11) and requiring an increasingly complex framework to tackle the linear stability problem. For instance, while the flow over streamwise ridges modeled using the SNS approach (Alinovi and Bottaro, 2018) can be treated with a 2D local stability analysis (Yu et al., 2016), the flow over isotropic posts will result in a base flow having no homogeneous directions, therefore requiring fully three-dimensional global stability analysis (Picella et al., 2018). Using the SNS/MVB models, we have run DNS of channel flow over SHS. The computations have been initialised using the base flow 1D solution reported in equation (6.10) and run until convergence have been reached, the residual having dropped to 10^{-8}. A fully three-dimensional, non-parallel base flow $\boldsymbol{U}_b(\boldsymbol{x}) = (U_b(\boldsymbol{x}), V_b(\boldsymbol{x}), W_b(\boldsymbol{x}))$ is obtained imposing a texture size L given by equation (6.7), with an averaged slip velocity at the wall equivalent to that obtained from equation (6.10), which reads $u_s = \langle u \rangle_{wall} = 2L_s/(3L_s + 1)$. For solving this eigenproblem, it appears clear that using direct methods (i.e. QZ or QR) is hardly possible at the moment due to the large number of degrees of freedom involved ($N_x \times N_y \times N_z \times 4 \rightarrow \mathcal{O}(10^8)$). Thus, we use a time-stepper formulation to find the leading eigenpairs of 6.8, based on the iterative Arnoldi algorithm (Arnoldi, 1951) as described by Loiseau et al. (2014). Using a Krylov subspace of dimension $K = 250$, we compute the most unstable mode developed over a spatially alternating slip–no-slip (SNS) boundary condition, which has the form of a modified TS wave.

Figure 6.3.a depicts the eigenspectra obtained using the HSL and SNS models. When the SHS is modeled by an HSL the eigenvalue problem is solved using a 1D local stability approach with $\alpha = 1.12, \beta = 0.00$ and $L_s = 0.02$. As predicted by Min and Kim (2005), we find that the most unstable mode is a 2D Tollmien-Schlichting (TS) modified wave, shown in figure 6.3.b. Using fully 3D, global stability analysis (Loiseau et al., 2014), we solve the eigenvalue problem for the SNS case, finding that the most unstable eigenvalue is superposed to that computed for the HSL case. Averaging the corresponding eigenvector along the $x - z$ planes we obtain an averaged 1D velocity profile, labeled as SNS_{avg} in figure 6.3.b, which slightly departs from that computed using the HSL model. The spatial heterogeneity arising from the surface pattern has a characteristic length L much smaller than the scale of the TS waves, affecting their shape only in the vicinity of the wall, as shown in figure 6.4.a. To quantitatively evaluate the influence of the heterogeneous SHS on the TS waves we define $U_d(\boldsymbol{x})$ as the deviation between the three-dimensional base flow obtained using the SNS approach and its HSL counterpart:

$$U_d(\boldsymbol{x}) = U_b^{SNS}(\boldsymbol{x}) - U_b(y)^{HSL}, \tag{6.12}$$

where the last term is the 1D velocity profile obtained using equation (6.10). U_d constitutes a measure of the spatial heterogeneity of the base flow, similarly as the streaks amplitude

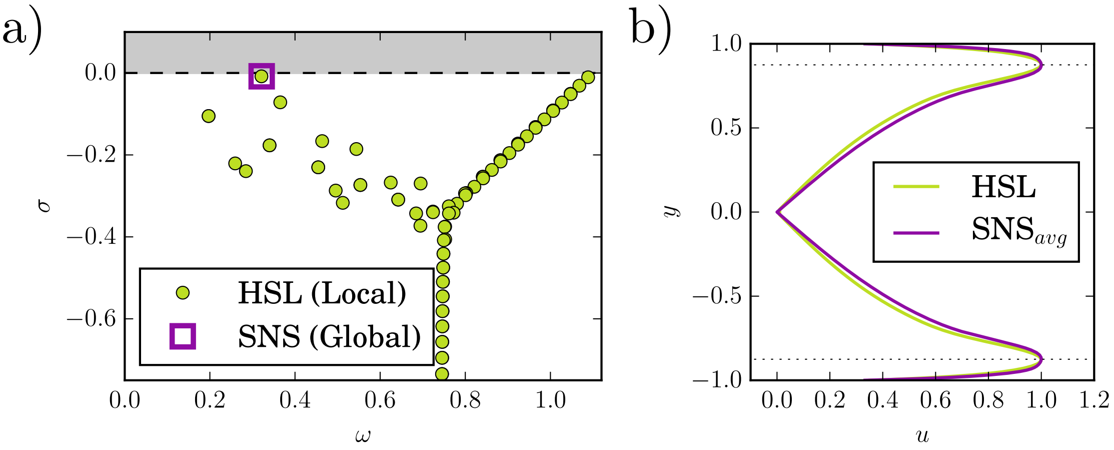

Figure 6.3 – (a) Eigenspectra of the linearized Navier-Stokes operator for a channel flow enclosed with superhydrophobic surfaces at $Re = 5000$. Using a spatially homogeneous slip length for modelling SHS allows for the use of a 1D local approach, where $\alpha = 1.0, \beta = 0.0$. Employing a spatially heterogeneous slip/no-slip one (SNS) requires for the use of a Global framework. (b) Norm of the streamwise component associated to the most unstable eigenvalue represented in (a). Despite the radically different framework employed and surface modelling employed, we recover in both case the same eigenmode, which represent the Tollmien-Schlichting wave equivalent for superhydrophobic surfaces. Mode obtained using SNS modelling has been averaged in wall-parallel directions so to make the comparison with the HSL case easier.

A_s defined by Brandt et al. (2003) to measure the intensity of streamwise vortices occurring during transition (Andersson et al., 1999). Averaging the leading eigenvector of the SNS case and U_d along the wall-parallel directions we get the 1D velocity profiles plotted in figure 6.4. The base flow deformation due to the spatially heterogeneous boundary reduces to 10% of its maximum value already at $y \pm 0.98$. Whereas, the wall-normal location of the peak amplitude of the TS wave is located at ≈ 0.875 (indicated with a black dashed line in figure 6.3.b and 6.4.b). These elements indicate that the heterogeneity of the surfaces slightly affect the TS waves frequency and shape since its effect is confined in the near-wall region.

We consider now the influence of air-water interfaces dynamics. The base flow obtained using the MVB approach starting from the SNS base flow (thus setting the initial deformation $\eta(x, z, t = 0)$ to zero and allowing it to evolve freely) is almost indistinguishable from that computed using SNS boundary condition. While in experiments the mass of the gas trapped withing the surface pattern does not change (unless wetting transition occurs) the MVB modelling assumes that the plastron volume remains constant (see equation (6.4)). This results into a maximum free-surface deformation $\eta_{max} \approx 5 \times 10^{-5}$, which is two orders of magnitude smaller than the surface texture length scale L, a posteriori confirming the viability of the linearised model of equation (6.3), as shown by Seo et al. (2017). Since including the interface dynamics into the time-stepping algorithm would complicate the eigenvalue problem solution from both computational and algorithmic point of views, we choose to use a continuation method (Theofilis and Colonius, 2003) to obtain the three-dimensional eigenfunctions starting from their respective local counterparts. We thus inject the eigenfunctions obtained using local stability analysis for the 1D base flow of the HSL case as initial condition for a DNS with a MVB modelled superhydrophobic surface. As

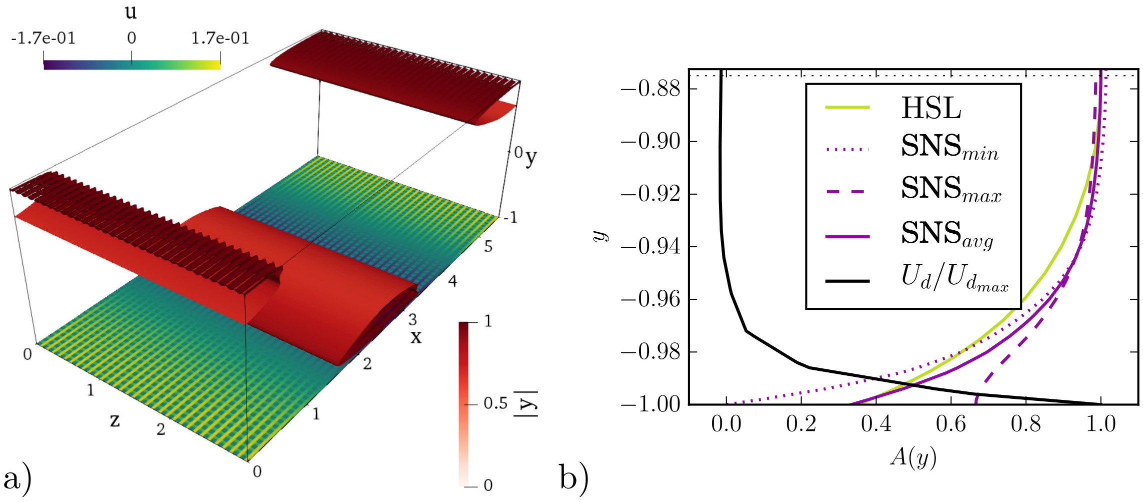

Figure 6.4 – (a) Streamwise velocity isocontours of the leading unstable mode computed for SNS superhydrophobic surfaces using the global stability analysis framework, on top of the streamwise velocity at the boundary. It appears clear that the lenghtscale associated to the spatial heterogeneity L is much smaller than the one of TS waves. Spatial heterogeneity does not interact with overlying structures, despite the closeness of TS waves to the wall. (b) Evolution of the leading unstable modes, computed for HSL and SNS modelled hydrophobic surfaces, together with the 3D base flow deformation U_d introduced in 6.12. Looking at the maximum and minimum mode amplitude at the wall for SNS we can immediately recognise the influence of the heterogeneous boundary condition slip (shear free, $\partial U/\partial y = 0$ and no slip $U = 0$). On the other hand spatial heterogeneity rapidly fades out further from the wall, as indicated by the U_d profile. 3D modes are coloured by their normalised distance from the wall $|y|$ in (a), while $A(y)$ represents the streamwise velocity component for each quantity plotted in (b).

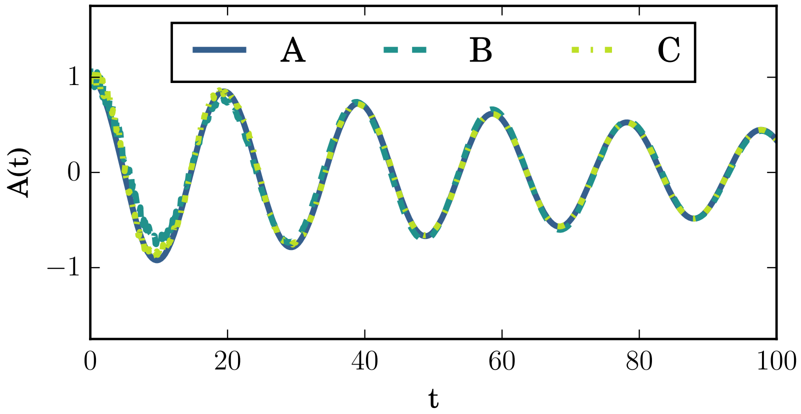

Figure 6.5 – Trace of the evolution of wall-normal velocity in a fixed point of the domain, measured during DNS. A, B, C lines represents computations performed for DNS onto HSL, SNS and MVB modelled surfaces respectively, but all of them initialized adding on top of their respective base flows the TS 2D wave computed from the 1D local framework using HSL approach. After a short initial transient, in all three cases we recover the dynamics predicted from the linear stability framework.

depicted in figure 6.5, after a short transient, the perturbation adapts to the heterogeneous boundary condition, but maintains both the frequency and the growth rate of the TS mode computed using the local stability analysis. This is probably due to the fact that the lengthscale of the spatial heterogeneity due to the SNS/MVB modelling L is small compared to the channel size H.

Thus, it appears that the eigenmodes of the linear stability problem are barely affected by the different methods used to model the SHS. However this result is strongly dependent on the fact that we have performed our analysis using small texture sizes, following the results shown by Seo and Mani (2016); Seo et al. (2017) for the SNS and MVB models in turbulent regimes.

6.3 K-type transition

We now focus on how different modelling of the SHS can affect the non-linear stages of the laminar-turbulent transition process. Amongst all the possible transition scenarios studied in literature (Schmid and Henningson, 2001), the K-type transition scenario (Klebanoff et al., 1962a; Sayadi et al., 2013a) has been chosen as a benchmark for the present study. Our choice is based onto the fact that this specific scenario is not only the most documented in both experimental (Nishioka et al., 1975; Kachanov, 1994a; Guo et al., 2010) and numerical (Gilbert and Kleiser, 1990; Kleiser and Zang, 1991; Sandham and Kleiser, 1992a; Rist and Fasel, 1995) studies, but most importantly because it has been recently shown to be the most sensitive to the use of slippery superhydrophobic surfaces as a mean of passive flow control (Chapter 5).

K-type transition can be triggered in a streamwise periodic (also called temporal (Schlatter, 2005)) channel flow, by setting as initial perturbation of the laminar base flow a linear combination of a 2D ($\boldsymbol{u}_{TS_{2D}}$) and two 3D $\boldsymbol{u}_{TS_{3D}}$ TS waves as

$$\boldsymbol{U}(t=0) = \boldsymbol{U}_b + A_{2D}\boldsymbol{u}_{TS_{2D}} + A_{3D}\boldsymbol{u}_{TS_{3D}} \tag{6.13}$$

. The amplitudes of the TS waves are set to $(A_{2D}, A_{3D}) = (0.03, 0.001)$ so that at subcritical Reynolds number $Re = 5000$, weakly non-linearities immediately develop (Sandham and Kleiser, 1992a; Sayadi et al., 2013a). The eigenmodes are shifted in x so that the maximum of their streamwise velocity component, which is normalised to one, is synchronised in space. These conditions allow to easily trigger transition in numerical experiments by originating from TS waves interaction a set of aligned Λ vortices which turn into hairpin ones up to their final breakdown to turbulence (Rist and Fasel, 1995). As shown in chapter 5, this scenario is radically modified by the introduction of SHS modelled as a spatially homogeneous boundary: slippery walls delay transition (Min and Kim, 2005), preventing the formation of Λ vortices by modifying the vortex stretching-tilting process usually occurring in the very first non-linear stages of transition and subsequently inhibiting the sweep-ejection process occurring during the onset of hairpin vortices. With this background we will show that while introducing spatial heterogeneity (with SNS modelling) does not change the previous findings, taking into account also the interface dynamics (MVB) leads to substantial modification of the physical mechanisms occurring during transition and, in a broader perspective, to the capacity of SHS of delaying the laminar-turbulent transition itself.

As we have shown in our previous work (chap. 5), we must increase the initial amplitude A_{2D}, A_{3D} in order to obtain transition over a SHS capable of providing an equivalent slip length $L_s = 0.02$. It turns out that all of the simulations shown in the present study have been triggered using as initial condition:

$$\boldsymbol{U}(t=0) = \boldsymbol{U}_b + 1.10 \cdot (A_{2D}\boldsymbol{u}_{TS_{2D}} + A_{3D}\boldsymbol{u}_{TS_{3D}}), \tag{6.14}$$

where the 2D and 3D global TS wave equivalents for spatially heterogeneous surface modellings SNS and MVB have been computed using the procedure presented in the previous section. In order to detect the onset of transition we follow the evolution of the friction Reynolds number, defined as:

$$Re_\tau = \sqrt{Re \left| \frac{\partial \langle U(\boldsymbol{x},t)\rangle}{\partial y} \right|_{y=\pm1}}, \tag{6.15}$$

where $\langle \bullet \rangle$ represents the spatial average computed onto wall-parallel planes $x-z$ at a given time t. Following the notation used in the present work, the Reynolds decomposition reads as:

$$U_i = \langle U_i \rangle + U_i' = \langle U_i(t) \rangle_{x,z} + U_i'. \tag{6.16}$$

When describing the statistically converged fully turbulent phases, the $\langle \bullet \rangle$ notation will be used to identify quantities averaged onto the wall-paralles planes x, z, as well as over time t.

As in the case of flows over compliant surfaces (Rosti and Brandt, 2017), when SHS are modelled with the MVB approach the quantity (6.15) must be modified in order to take into account the shear stresses which are non zero at the moving interface. Following the approach developed for porous walls (Breugem et al., 2006), the friction Reynolds number computed over a moving surface becomes:

$$Re_\tau = \sqrt{Re \left| \frac{\partial \langle U(\boldsymbol{x},t)\rangle}{\partial y} \right|_{y=\pm1} - \left|\langle U'V' \rangle\right|_{y=\pm1}}, \tag{6.17}$$

where $\langle U'V' \rangle$ is the off-diagonal component of the Reynolds stress tensor, evaluated on the spatially heterogeneous deformed SHS surface. Wall-normal velocity fluctuations V' are

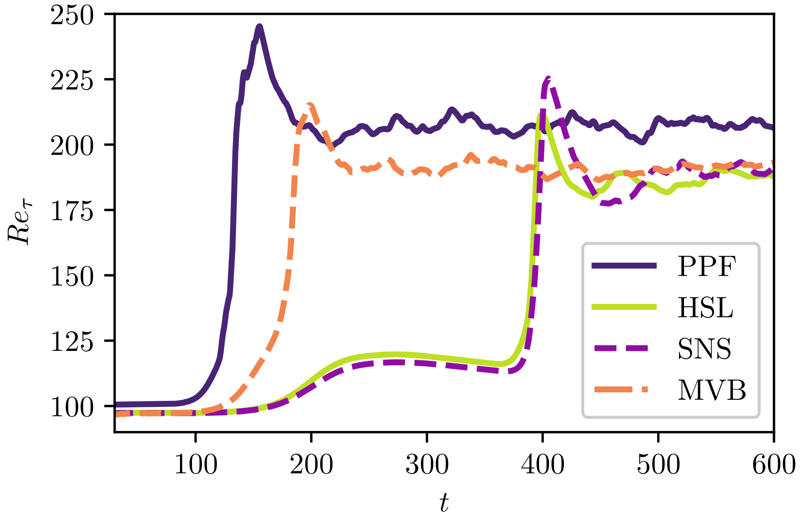

Figure 6.6 – Temporal evolution of the friction Reynolds number Re_τ, measured during laminar turbulent K-type triggered transition over no slip (PPF) walls, as well as onto spatially homogeneous (HSL), spatially heterogeneous (SNS) and deformable (MVB) modelled superhydrophobic surfaces. While Re_τ measured during the laminar and turbulent regimes is the same for the three models, the transition process is strongly affected by the different SHS modelling

zero on the solid-liquid interface. On the other hand, despite being small on the gas-liquid interfaces, their presence constitutes up to the 10% of Re_τ.

All simulations are computed for a constant flow rate and the laminar Reynolds number is set to $Re = 5000$. Figure 6.6 depicts the friction Reynolds measured during K-type simulations over differently modelled SHS, as well as the standard no-slip one for reference. What we immediately notice is that flat, spatially heterogeneous slip/no-slip boundaries (SNS) provide the same behaviour of spatially homogeneous slippery surfaces (HSL), delaying considerably transition with respect to the case of no-slip (PPF) walls. Thus, we can conclude that HSL and SNS models provide similar performances not only for laminar (Ybert et al., 2007) and turbulent flows (Seo et al., 2015) but also in the transitional regime, at least for the small value of the texture roughness size considered here. It is although possible that increasing L beyond a given threshold can affect this result, as it has been shown for turbulent flows (Seo et al., 2015). However, large superhydrophobic patterns would not guarantee to sustain wetting transition (Seo et al., 2017), making the MVB approach not viable anymore. On the other hand, taking into account the free-surface dynamics radically changes the dynamics of the flow as shown in figure 6.6, since the transition to the turbulent state is considerably advanced with respect to the SNS/HSL cases. In the remainder of this section we investigate the reason why the free-surface motion at the wall radically changes the dynamics of the flow with respect to a slippery flat surface.

6.3.1 Coherent structures and preliminary qualitative observations

Figure 6.7 provides a general overview of the structures occurring during K-type transition in a channel flow over no slip (PPF), homogeneous slippery (HSL) and flat Slip No-Slip boundaries (SNS), as well as taking into account for the interface dynamics with a moving boundary approach (MVB). The PPF case, depicted in figure 6.7.a, represents the benchmark K-type scenario as described in many other studies (Gilbert and Kleiser, 1990; Sandham and Kleiser, 1992a; Schlatter, 2005). The TS waves injected into the flow experience from the early phases weakly nonlinear interactions ($t < 80$), forming spanwise aligned TS-like vortices, that can be easily identified using λ_2 criterion. Secondary instabilities and vortex stretching promotes the three-dimensionalization of these spanwise vortices ($t = 85$), whose strong shear layers induce the formation of Λ shaped vortices, composed of two elongated legs ($t = 103$). Sweep-ejection events result into an increase of the spanwise vorticity on top of the λ legs forming the head of characteristic hairpin vortices ($t = 113$). During the late stages of transition ($t = 120$) we observe the rapid formation of multiple hairpin heads as a succession of sweep-ejection events (Rist and Fasel, 1995; Guo et al., 2010), up to the final breakdown to turbulence ($t > 130$). This process is radically modified by the introduction of a slippery boundary. While using HSL modelled superhydrophobic surfaces does not affect the very first weakly non-linear phase ($t < 85$), slippery boundaries inhibit the onset of λ vortices, which in turn prevents the formation of hairpin vortices. As discussed in detail in chapter 5, this is due to the reduction of the tilting of the spanwise TS-like vortices, due to the decreases shear at the wall. The transient bump in the Re_τ evolution depicted in figure 6.6 indicates the attenuation of vortical structures within the channel, as visualised for $t = 164, 190, 220$ in figure 6.7.b. Still, the flow receptivity to the residual velocity perturbations triggers a different transition scenario, characterised by the onset of linear streamwise-elongated velocity modulations (streaks) ($t = 325$). These structures saturate non-lineary and when they reach a certain amplitude the onset of sinuous instability is observed ($t = 365$), eventually leading to the fully turbulent regime.

Taking into account the spatial heterogeneity does not change the latter scenario. In fact, despite the different surface modelling, one can notice that HSL computation matches the SNS one, as shown in figure 6.7. Also the λ_2 isosurfaces as well as the averaged slip velocity at the wall depicted in 6.7.b appear to be qualitatively identical.

On the other hand, considering the deformability of the free-surface radically changes the transition scenario described above. The first stages of the transitional simulations over MVB modelled superhydrophobic surfaces, reported in figure 6.7, show that the onset of spanwise TS-like vortices is similar to that observed at the same time (< 90) for the cases with $\eta = 0$. However, although being constrained by the texture pattern, free surfaces experience a macroscopic deformation having the same streamwise periodicity as the overlying TS-like vortices. In fact, the streamwise velocity excess-defect resulting from these vortices produces an alternance of spanwise aligned pressure waves, deflecting the liquid-gas interface. High (low) streamwise velocities produce low (high) pressure waves, which in turn deflect the interface upwards (downwards). Similar behaviour has been first observed by Seo et al. (2017) and is quite common in the study of flows over compliant surfaces (Lucey and Carpenter, 1995; Zhang et al., 2017). As time advances spanwise vortices tilt downstream ($t = 123$), forming λ vortices similar to those observed in the PPF case, but in this case attenuated and stretched in the streamwise direction ($t = 135$). The interface deformation follows the overlying coherent structure, such as hairpin vortices whose onset is observed at $t \approx 150$. These vortical structures are characterised by larger heads and tinier stretched legs as compared to those observed in the PPF flow for $t = 113$. In this time range the maximum interface deformation is placed right below the large hairpin head ($t = 165$), and breakdown to turbulence takes place from > 175.

Thus, it appears that the interface deformation, directly linked to the pressure fluctuations at the wall, may contribute in enhancing the transition process. In fact, as shown in figure 6.8, free-surface dynamics taken into account by MVB modelling of SHS introduces

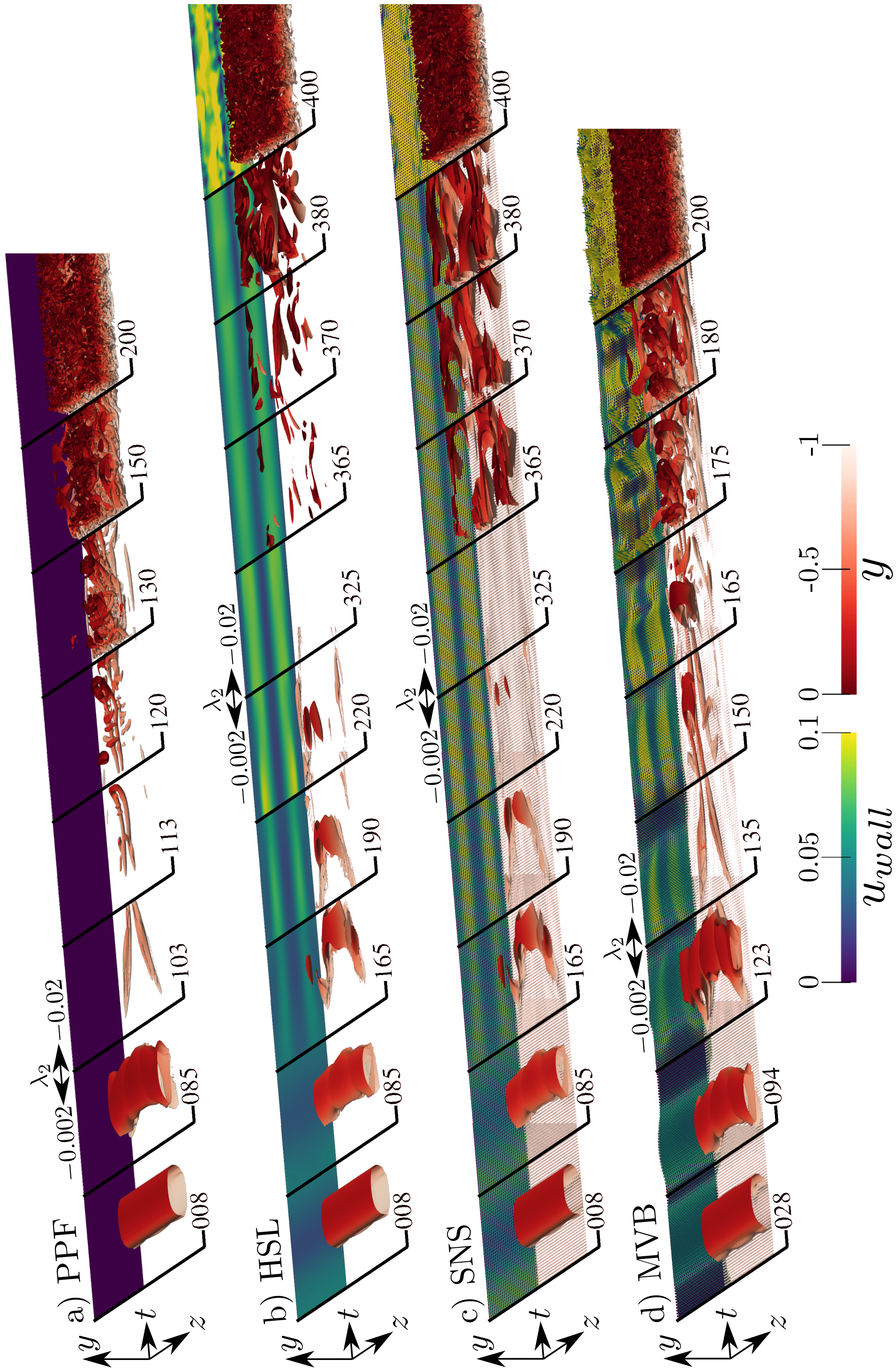
a) PPF
b) HSL
c) SNS
d) MVB
y
t
z
λ_2
−0.002
−0.02
008
085
103
113
120
130
150
200
008
085
165
190
220
325
365
370
380
400
008
085
165
190
220
325
365
370
380
400
028
094
123
135
150
165
175
180
200
u_{wall}
0
0.05
0.1
y
0
-0.5
-1

Figure 6.7 – Overview of K-type triggered laminar-turbulent transition over smooth, no slip wall (PPF), as well as variously modelled superhydrophobic surfaces (HSL, SNS, MVB). For each configuration, snapshots extracted at different times are placed one next to the other in order to provide an overall view of transition. The time values are reported on the black lines separating the snapshots. The iso-surfaces show the λ_2 criterion (Jeong and Hussain, 1995), coloured by its distance from the wall, and the iso-contours represent the streamwise velocity measured at the lower wall, shifted in the spanwise direction for visualisation issues. Only the lower channel half is showed for the sake of visualisation.

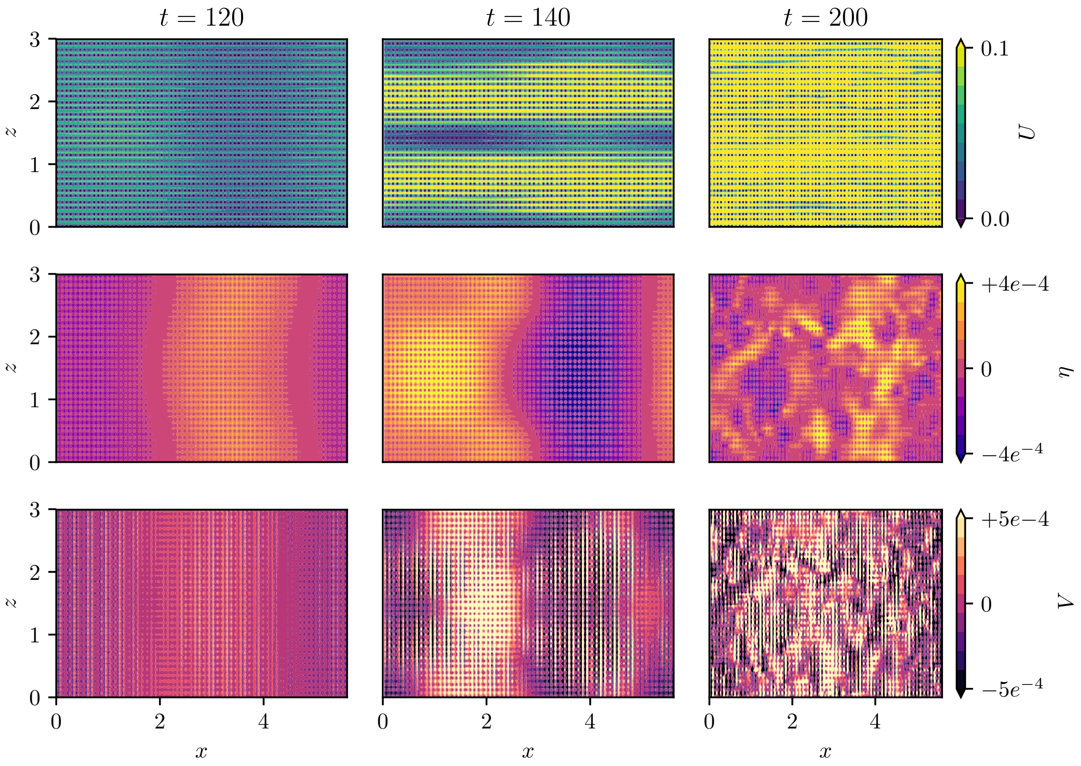

Figure 6.8 – Evolution of streamwise velocity U and wall-normal velocity V at the boundary, as well as interface deformation η, measured during K-type triggered transition over MVB modelled underwater superhydrophobic surfaces. The onset of coherent structures during transition leaves a characteristic footprint on the interface, producing wall-normal velocities at the wall that are synchronised with the overlying dynamics. This behaviour is kept until the late stages of transition ($t = 140$), while the interface dynamics during the turbulent regime qualitatively resembles the one found by Seo et al. (2017) for SHS having the same texture size. On top of textured microposts $U = V = 0$, leaving a characteristic pattern onto the presented slices.

a non zero velocity at the wall, induced by the gas-liquid interface deformation. The wall normal velocity at the wall is strictly linked to the interface deformation which, owing to the pressure coupling, is therefore dependent onto the streamwise velocity field. In the first non-linear stages ($t = 120$) the surface deformation follows the spanwise TS-like vortex, and the resulting wall normal velocity is in phase with η. After the onset of λ vortices ($t = 140$), the interface acts as an elastic potential energy reservoir, producing a highly localized mass injection, identified by the high values in wall normal velocities. In the following we will show that, while slippery surfaces damp Λ vortices, these localised mass injections amplify ejection events, leading to the rapid formation of vortices similar to hairpins head (cfr. figure 30 in the recent work by Zhang et al. (2017)) although devoid of their characteristic legs. When the flow is turbulent ($t > 190$) streamwise velocity obtained with MVB modelling matches that computed with HSL and SNS approaches, while interface deformation and wall normal velocity at the boundary are qualitatively identical to the ones found by Seo et al. (2017). Incidentally, we have verified a posteriori that the wall normal velocities at the deformable interface computed using equation (6.6) proposed by

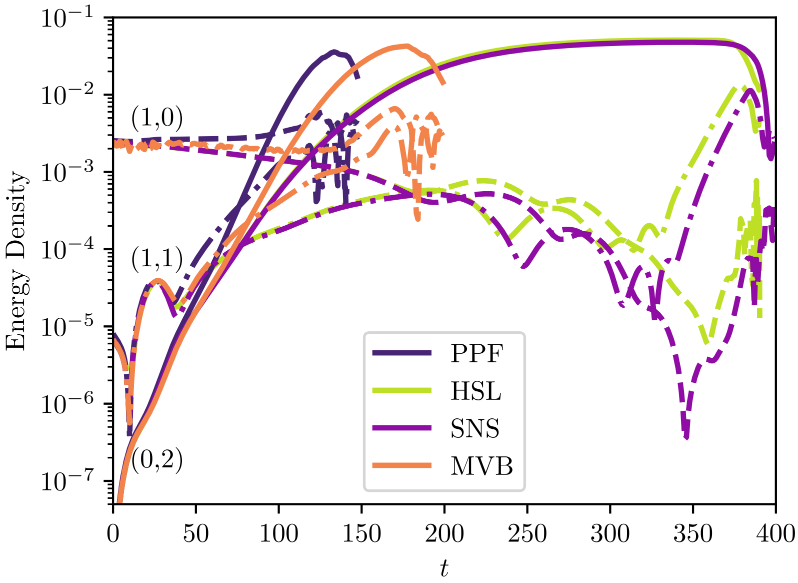

Figure 6.9 – Time evolution of the energy associated to (1,0), (1,1) and (0,2) Fourier modes during K-type transition over no-slip (PPF) and SHS surfaces (HSL, SNS, MVB). The initial linear and weakly non-linear stages of transition do not seem to be affected by the introduction of superhydrophobic surfaces. Besides a temporal shift, the late stages of transition appears to be qualitatively identical, suggesting that following the energy evolution mode by mode is not suitable to study the fully non-linear stages of the transition process.

Seo et al. (2017) are very close to those obtained using our ALE approach (MVB), since the root-mean-square of their normalized difference at time $t = 120, t = 140, t = 200$ is $2.6\%, 2.7\%, 3.5\%$, respectively. As a further remark regarding the MVB modelling, pressure fluctuations measured at the interface appear to be dominated by stagnation pressure and by the overlying transitional structures only. Pressure fluctuations due to capillary waves, characterised by their peculiar upstream-propagating dynamics, have not been detected throughout all the transitional phase nor in the turbulent regime. In fact, in this work we consider a SHS with texture of size $L^+ < 26$ in the fully turbulent regime, for which Seo et al. (2017) capillary effects are negligible and only downstream-propagating pressure perturbations have been measured. On the other hand, transitional structures enhance the spanwise-coherent interface deformations, which could affect the wetting stability of the SHS itself. However, studying this phenomenon would require the use of a multiphase approach, going beyond the scope of the present work.

6.3.2 Fourier harmonics

In order to study the initial stages of transition we track in time the amplitude of selected Fourier harmonics (Zang and Krist, 1989):

$$E_k(k_x, k_z) = \frac{1}{2E_0} \int_{-1}^{+1} |\hat{\boldsymbol{u}}_{k_x,k_z}(y,t)|^2 \, dy, \tag{6.18}$$

where $\hat{\boldsymbol{u}}_{k_x,k_z}(y,t)$ is a single component of the Fourier transform of the perturbation velocity field in the streamwise and spanwise direction with wavenumbers k_x, k_z, respectively, while E_0 is the kinetic energy of the laminar flow. In this framework the wavenumbers of the different Fourier modes are indicated as multiples (i_x, i_z) of the fundamental wavenumbers $(2\pi/L_x, 2\pi/L_z)$, in the streamwise and spanwise direction, respectively. In figure 6.9 we report the most energetic ones. Provided that K-type transition is triggered by adding on top of the base flow a linear combination of TS waves regardless of the surface modelling employed, the initial perturbation energy for all simulations is distributed onto the $(1, 0)$ and $(1, \pm 1)$ Fourier modes only, corresponding to the 2D and 3D fundamental TS waves, $u_{TS_{2D}}$ and $u_{TS_{3D}}$. In all simulations, the initial perturbation amplitude prescribed by the K-type scenario (see 6.14) is high enough so that weakly non-linear effects are immediately triggered, as indicated by the onset of the streamwise homogeneous subharmonic $(0, 2)$) mode. Transition takes place when the $(0, 2)$ modes attain a given threshold, and all four scenarios appear to be qualitatively similar despite shifted in time. While this analysis confirms that during the linear stages of transition ($t \approx 50$) K-type transition is not affected by the use of slippery, not deformable boundaries, it is also clear that studying the perturbation energy evolution of the Fourier harmonics cannot provide insightful information regarding the fully non-linear phases of this process.

On the other hand the interface deformation introduced by the MVB modelling of SHS appears to keep its spatial coherence, even during the highly non-linear stages of transition, as shown in figure 6.10. Figure 6.10.a displays λ vortices, with a bump formed between its legs at $t = 130$. Looking at the power spectral density (PSD) of the Fourier modes of the wall normal velocity at the boundary in figure 6.10.b we immediately notice the presence of quasi 2D waves (modes $(1, 0)$), as well as the footprint of the spatially heterogeneous discretization of the interface, indicated as a peak at $k_{x,z} \approx 28 = L_x/L = L_z/L$, corresponding to the surfaces roughness lengthscale. This behaviour is enhanced at $t = 145$, where the interface deflection further increases. The onset of quasi streamwise vortices over an interface dimple is observed together with the formation of a hairpin-like-head on top of a bump produced by an inward deformation of the free-surface, as shown in figure 6.10.c. At the same time we measure a strong increase in the wall normal velocity intensities, while their spatial distribution remains qualitatively the same (see figure6.10.d). These behaviours appear to be remarkably similar to those observed by Zhang et al. (2017) regarding the onset of coherent structures in a turbulent channel flow enclosed by compliant walls. As long as the flow becomes fully turbulent we recover the same dynamics found by Seo et al. (2017): the texture size L is small enough that the stagnation pressure and the oscillations due to the overlying turbulent behaviour dominate the pressure fluctuations at the wall. Again, the capillary pressure is negligible when compared to other components, resulting into a downstream-propagating deformation with wall-normal velocities at the interface characterised by a widespread $PSD(\boldsymbol{U})$ spectrum but still containing some influence of the characteristic texture size L (figure 6.10.f).

6.3.3 Vorticity dynamics

While the onset of spanwise TS-like vortices is substantially unmodified by the introduction of slippery neither compliant boundaries (see figure 6.7 for $t < 100$), SHS alter the standard K-type transition process starting from the fully non-linear phase, affecting the development of typical vortical structures, well identified by the isocontours of the λ_2 criterion. In order to quantitatitely identify the influence of SHS on these structures with the aim of providing a better understanding of the underlying physical mechanism involved, we track the time evolution of the vorticity $\boldsymbol{\omega}$. The streamwise component of vorticity $\omega_x = \partial W/\partial z - \partial V/\partial y$ indicates the onset of streamwise aligned vortices, such

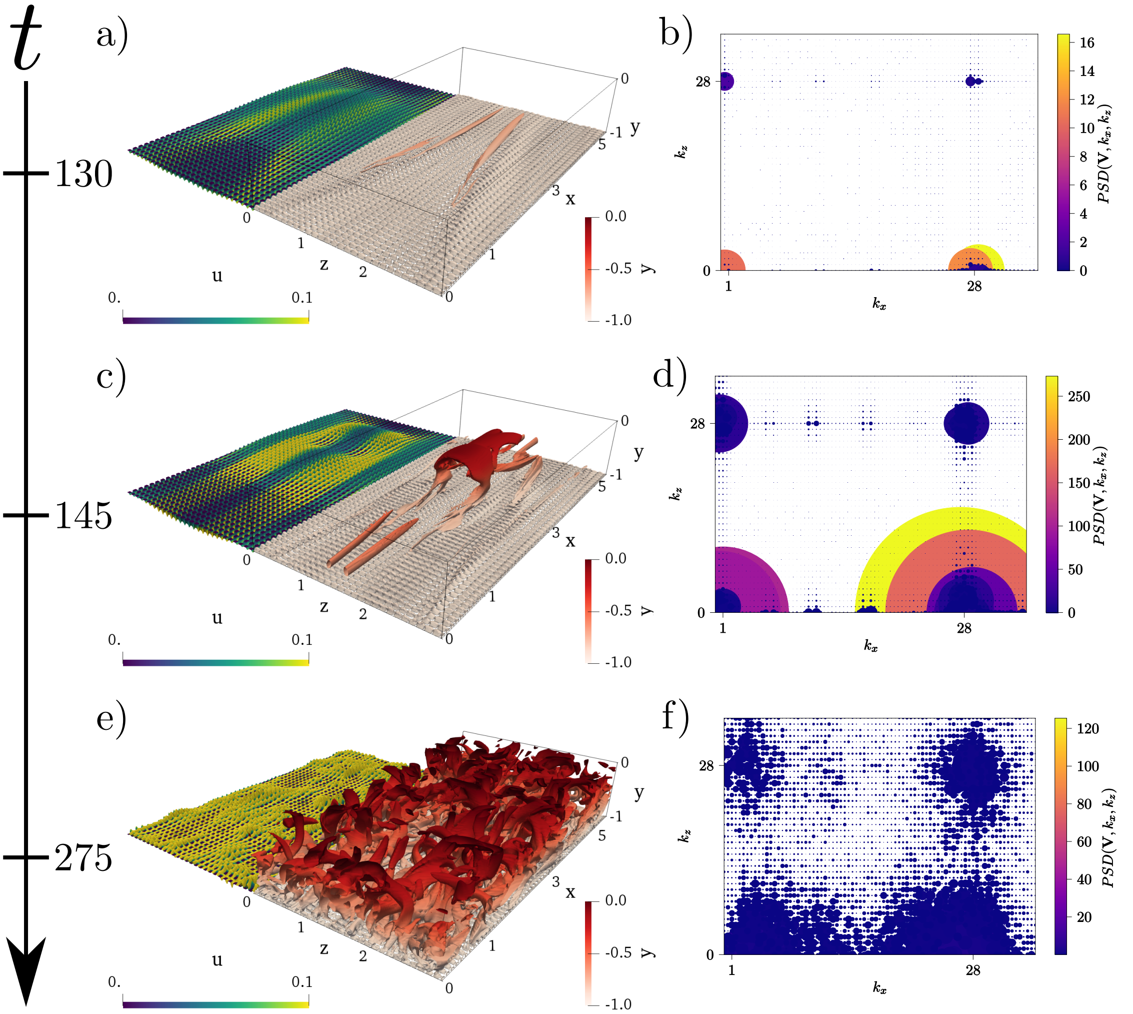

Figure 6.10 – (a,c,e) Selected Snapshots from figure 6.7 depicting the coherent structures and the underlying interface dynamics occurring onto MVB modelled surfaces during transition. (b,d,f) Power spectral density of the Fourier harmonics of the wall-normal velocity at the deformable interface. Long wavelengths $(k_x, k_z) = (1, 0)$ are associated to the deformation produced by the overlying coherent structures, while short ones $(k_x, k_z) = (28, 28)$ to the characteristic size of the textured superhydrophobic surface L. Their ratio is high enough so that they do not interfere with each other during transition ($t = 130, 145$). When fully developed turbulent state is achieved the PSD spectra becomes much noisier (f), but one can still recognise the wavelengths accounting for the highest intensities.

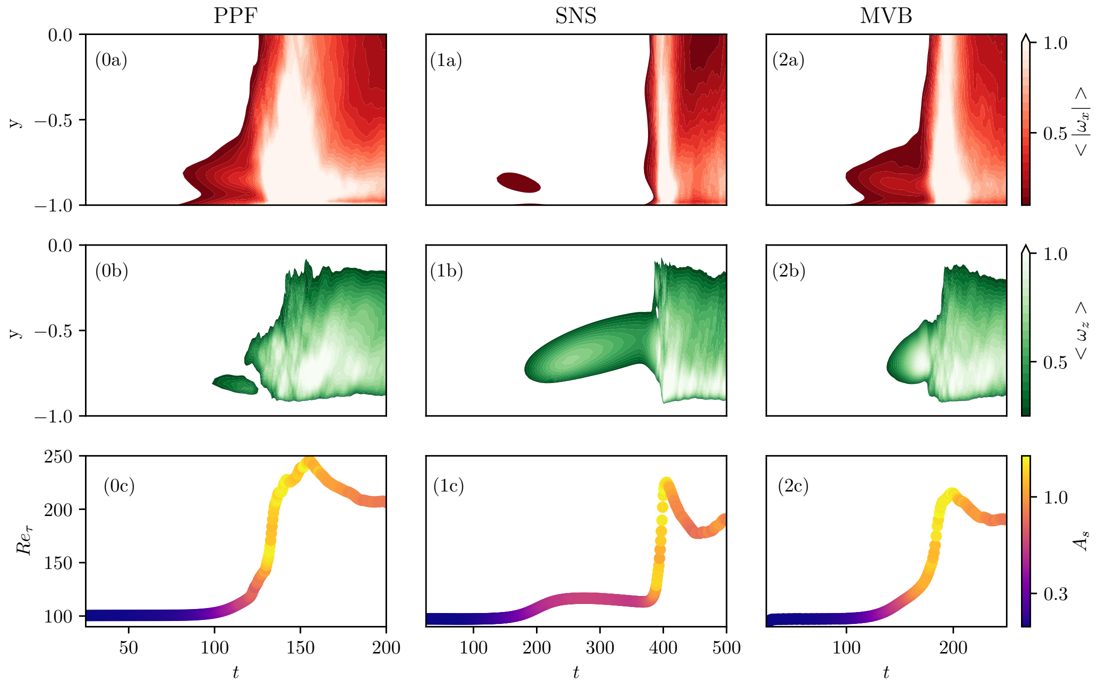

Figure 6.11 – Streamwise and spanwise vorticity averaged along the homogeneous directions $x-z$, $\langle\omega_x\rangle$, $\langle\omega_z\rangle$ in subplots x.a and x.b, respectively. Subplots x.c show the time evolution of the friction Reynolds number Re_τ, coloured by the spanwise deformation amplitude A_s. Plots are arranged in columns according to the surface modelling to which they belong. SNS results matches the observations made for HSL modelled superhydrophobic surfaces, and are reported in chapter 5.

as Λ vortices as well as the legs of hairpin structures, whereas the spanwise vorticity $\omega_z = \partial V/\partial x - \partial U/\partial y$ marks the presence of spanwise TS-like vortices as well as the appeareance of hairpin heads (Rist and Fasel, 1995; Zhou et al., 1999; Sayadi et al., 2013a). When the free-surface dynamics is neglected (HSL-SNS), we observe streamwise aligned vortices occurring prior to the final breakdown to turbulence (see figures 6.7.b and 6.7.c for $t = 325$), which seem to be linked to streaky structures. These elongated structures can be identified by tracking the evolution of the amplitude of spanwise modulation of $\boldsymbol{U}(\boldsymbol{x}, t)$ (Brandt et al., 2003), which is defined as:

$$A_s(t) = [max_{y,z}(\boldsymbol{U}(\boldsymbol{x}, t) - \boldsymbol{U}_b(\boldsymbol{x}) - min_{y,z}(\boldsymbol{U}(\boldsymbol{x}, t) - \boldsymbol{U}_b(\boldsymbol{x}))]. \tag{6.19}$$

In the first two rows of figure 6.11 we represent the evolution of streamwise and spanwise vorticity measured during K-type transitions over flat (SNS) or compliant (MVB) superhydrophobic surfaces, together with the no-slip case (PPF). Vorticities are averaged on the wall-parallel directions to better identify the onset of specific coherent structures (Zhou et al., 1999). During standard K-type transition, we first measure an increase of ω_x ($t \approx 90$ in figure 6.11.0a) close to the wall, indicating the onset of characteristic Λ vortices. Streamwise vorticity spreads in the wall-normal direction, and the isolated spot of ω_z appearing at $t = 113$ in figure 6.11.0b marks the formation of characteristic hairpin heads further from the wall. While the amplitude of spanwise deformation has homogeneously risen, the onset of hairpin heads marks a steep increase in friction Reynolds number (Fig. 6.11.0c), typical of the K-type transition scenario. After the late stages of transition have taken over (Sandham and Kleiser, 1992a), the fully turbulent state is characterised by a plateau in Re_τ, from $t \approx 200$. We have already shown how introducing a slippery boundary changes this scenario, damping the growth of the characteristic λ and hairpin vortices. When SNS modelled superhydrophobic surfaces are used we observe a transient behaviour for ω_x (see figure 6.11.1a). In fact, as we will demonstrate in the following, slip at the wall interferes with the vortex tilting and stretching that transform spanwise TS-like vortices into Λ structures. Therefore, it is clear that the transient growth of ω_x corresponds to the onset and decay of λ vortices (figure 6.7.b and 6.11.1a for $t \approx (165, 200)$). On the other hand, when λ vortices are damped by the wall slip, we observe the onset of high spanwise vorticity, moving from the wall towards the channel bulk (figure 6.11.1b, as well as a plateau value in the spanwise amplitude modulation (Fig. 6.11.1c)). This peculiar behaviour for ω_z indicates the onset of non-linear streamwise vortices (Mao et al., 2017), slowly saturating from $t \approx 200$ up to $t \approx 350$. We argue that these structures arise from the flow receptivity to the residual velocity perturbation left from the damped λ vortices 4, even if computations where designed so to trigger K-type transition, SHS surfaces are delaying this process undertaking a different route to turbulence. The process described above is qualitatively and quantitatively identical to the one observed over HSL modelled superhydrophobic surfaces (Chap. 5).

Taking into account the interface dynamics with MVB modelling provides a different scenario. The streamwise vorticity evolution (figure 6.11.2a) suggests that some kind of streamwise aligned structure is forming close to the wall such as in the PPF (figure 6.11.0a). At the same time strong spanwise vortices are forming far from the wall (figure 6.11.2b); the values and wall-normal location of the ω_z peak is similar to that found in the HSL case, but occurs much earlier (figure 6.11.1b) and not after saturation of the A_s value as previously observed. Looking at figure 6.7.d we can see that the streamwise vorticity marks the onset of vortices similar to the λ ones at $t > 130$, but stretched in the streamwise direction, whereas the ω_z peak is the signature of isolated, large hairpin-like vortex heads (see figure 6.7.d $t = 150, 165$).

It is clear that SHS can delay K-type transition by altering the processes occurring during the onset of characteristic Λ vortices, whose presence can be detected by measuring the intensity of the streamwise vorticity (Zhou et al., 1999). Figure 6.12 depicts the evolution of ω_z in time for K-type triggered transitions over differently modelled surfaces. For no-slip walls (PPF), Λ vortices result from the vortex tilting of the TS-like spanwise vortices used to trigger K-type transition, resulting into a constant ω_z intensity in the range $t = (20, 80)$ (Malm et al., 2011). In both the HSL and SNS cases, ω_z decreases in the same time range, suggesting that the vortex tilting process has been modified. However, taking into account the interface dynamics that introduces wall normal velocities at the compliant free-surface changes again the evolution of the spanwise vorticity in its initial stages, requiring a more accurate analysis of these findings. As previously done in chapter 5, we now focus on the evolution of the vorticyt transport equation, defined as 5.16. In figure 6.13 we show the volume integral of each term of equation (5.17) at time $t = 40$ but for different surface modellings. When no-slip boundaries (PPF) are employed, the terms of the equation vortex tilting T_{zy} and stretching S_{zz} are balanced, providing a characteristic ω_z plateau during the development of Λ-vortices. Introducing slippery boundaries decreases the intensity of normal gradients $\partial \bullet / \partial y$ (Min and Kim, 2004). All terms of equation 5.17 are affected, but with different rates, especially the ones explicitly containing the wall normal derivative, namely $T_{zy} = \partial u \partial z \cdot \partial w \partial y$ as well as $S_{zz} = (\partial v / \partial x - \partial u / \partial y) \partial w / \partial z$. This, similarly to the mechanism driving the linear transient growth (Schmid and Henningson, 2001), introduces an imbalance in equation 5.17, promoting the evolution of ω_z. The behaviour presented

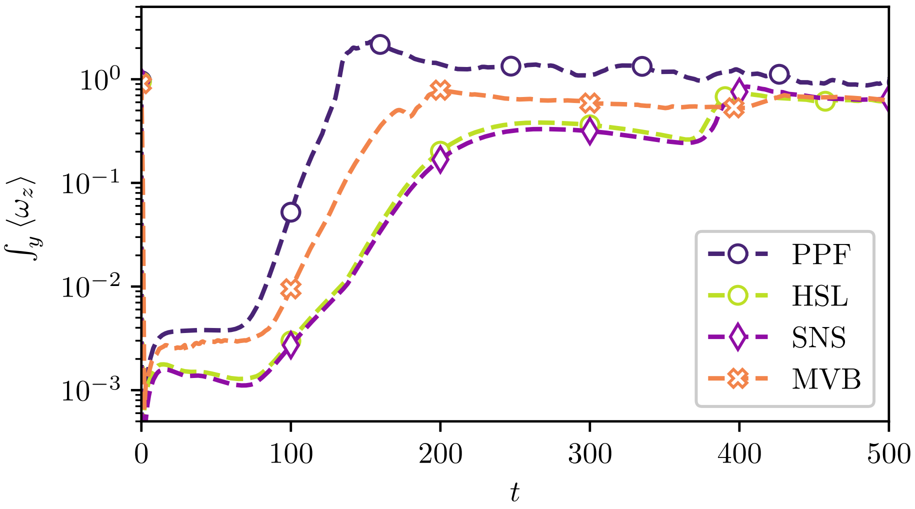

Figure 6.12 – Wall normal integral of the averaged spanwise component of vorticity. Notice the early plateau obtained in the benchmark PPF case, representing the saturation of TS-like spanwise vortices and their development into characteristic Λ vortices (Malm et al., 2011)
.

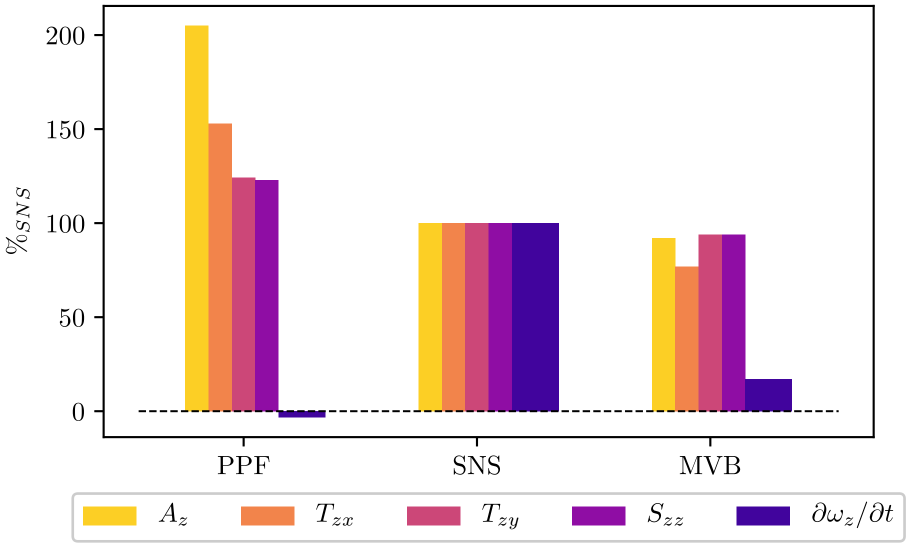

Figure 6.13 – Integrals of the spanwise vorticity equation (5.16) terms, for $t = 40$ and different surface modellings. Each term has been normalised with respect to the SNSs counterpart, so to enhance their variation.

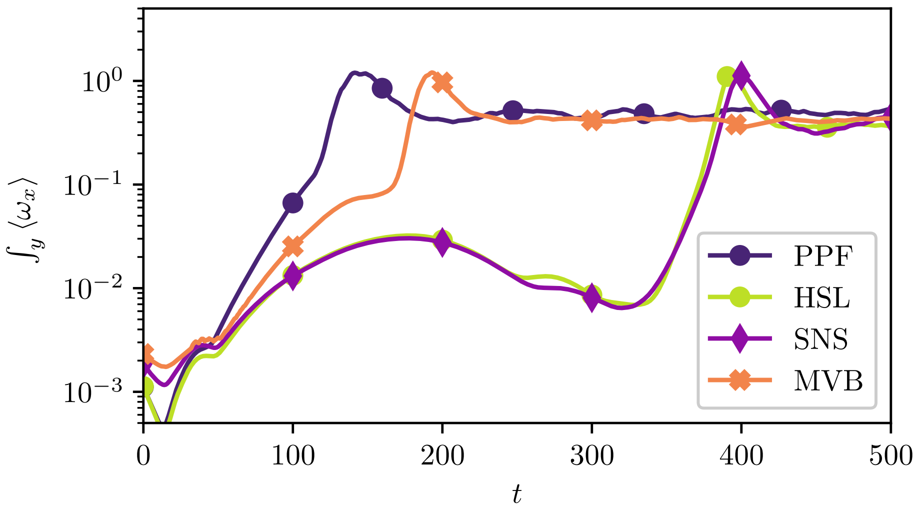

Figure 6.14 – Wall normal integral of the averaged streamwise component of vorticity. Notice the exponential growth obtained in the benchmark PPF case, marking the development of characteristic Λ vortices (Malm et al., 2011)
.

for SNS again matches the one found for SHS modelled with a flat, spatially homogeneous model (HSL, refeer to chapter 5), indicating that slippery surfaces delays K-type transition by inhibiting the onset of its characteristic Λ vortices altering the vortex tilting-stretching process. Taking into account the interface dynamics introduces wall normal velocities at the boundaries that change this picture, hindering the effect of wall slip and decreasing the $\partial\omega_z/\partial x$ amplitude by mostly acting on the T_{zx} term. Again we observe how different models for SHS produce opposite effects on the K-type transition process: on the one hand slip (HSL and SNS cases) delays transition by attenuating the vortex tilting process, which on the other hand is enhanced by the interface dynamics.

Studying the evolution of the streamwise vorticity in figure 6.14 provides some additional elements to understand how differently the surface modellings employed in this study behave. First we briefly describe the key feature of the ω_x evolution during the standard K-type transition over flat, no-slip surfaces (PPF). After an initial decrease, vortex tilting and stretching of the TS-like spanwise vortices leads to the onset of Λ-vortices. This phase produces a characteristic exponential growth in ω_x ($t \approx (70, 110)$), that can be explained as follows. Starting from equation (5.15) and following the approach proposed by Malm et al. (2011), the streamwise vorticity evolution can be reduced up to :

$$\frac{D\omega_x}{Dt} \approx \omega_x \frac{\partial u}{\partial x}, \tag{6.20}$$

where both the damping term $1/Re\Delta^2\boldsymbol{\omega}$ as well as the strain in other directions are neglected during this stage. Solving for ω_x provides

$$\omega_x \sim e^{(\partial u/\partial x)t}, \tag{6.21}$$

which therefore explains the exponential growth of streamwise vorticity along x, as found in our computation. Modelling SHS as a spatially homogeneous slippery boundary condition

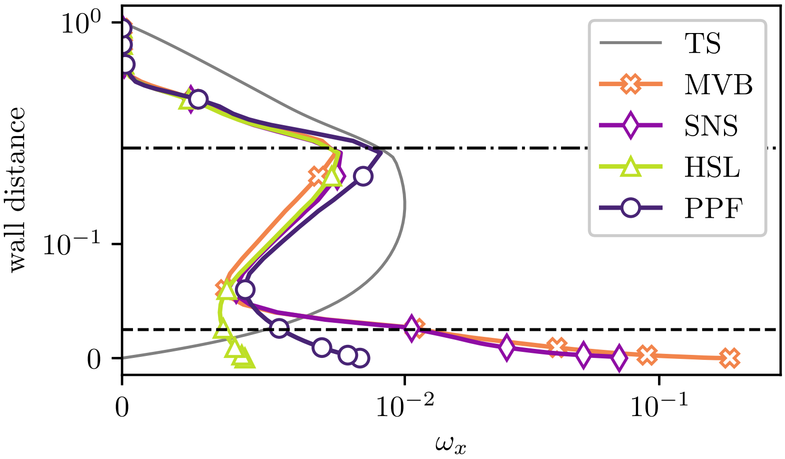

Figure 6.15 – Streamwise component of vorticity close to the wall for $t = 40$, averaged along the wall-parallel directions. High vorticity intensities measured for SNS and MVB cases are due to the presence of tiny vortices at the wall, generated by the slip/no-slip discontinuity used to spatially discretize the surface texture. These peaks rapidly fades out far from the wall, and do not affect the dynamics of the bulk flow. The streamwise velocity profile of a TS wave is reported as a reference of the typical wall-normal distance for the overlying structures occurring during transition. TS profile has been rescaled so that its maximum is 0.01, so to facilitate the comparison with ω_x profiles.

on a flat wall (HSL) this exponential growth phase disappears, indicating the absence of Λ vortices.

Instead, looking at figure 6.14 the influence of the spatial heterogeneity can be visualized in the initial phases, for $t < 50$. While ω_x strongly decreases for both PPF and HSL simulations, spatial heterogeneity (SNS and MVB cases) produce higher values of streamwise vorticity. This finding can appear counter intuitive provided that an increase of ω_x is usually linked to the onset of Λ vortices, which are almost absent in both HSL, SNS and MVB simulations. In order to better understand the source of such high streamwise intensities measured for spatially heterogeneous models, we plot ω_x averaged onto wall-parallel planes at time $t = 40$, as depicted in figure 6.15. While far from the wall, for $y \approx 0.3$, the peak measured for all simulations is associated to the vortex tilting process, eventually leading to the onset of Λ vortices, the near wall dynamics appears to be quite different. In fact, for $y \approx 0.02$, we can clearly see that while streamwise vorticity is reduced by homogeneous slip (HSL), it is strongly increased by spatially heterogeneity (SNS) and even more by wall-normal velocities at the deformable interface. Indeed, discretizing the SHS roughnesses results in the development of tiny vortices on top of the solid posts, associated to the slip-no-slip condition, which can be visualized observing the λ_2 isosurfaces close to the wall (see for example figures 6.10 a, c and e). On the other hand, provided that the characteristic size of these vortices is linked to the size of the microposts, L, this near wall behaviour does not affect the dynamics of the overlying transitional flow. In fact, starting from $t \approx 75$, the ω_x evolution for both HSL and SNS simulations matches again, further indicating the equivalence of these two modellings. In the MVB case we obtain a behaviour that is in between those observed for no-slip and flat slippery surfaces. During the very initial stages near wall vortices, stronger than those observed in the SNS

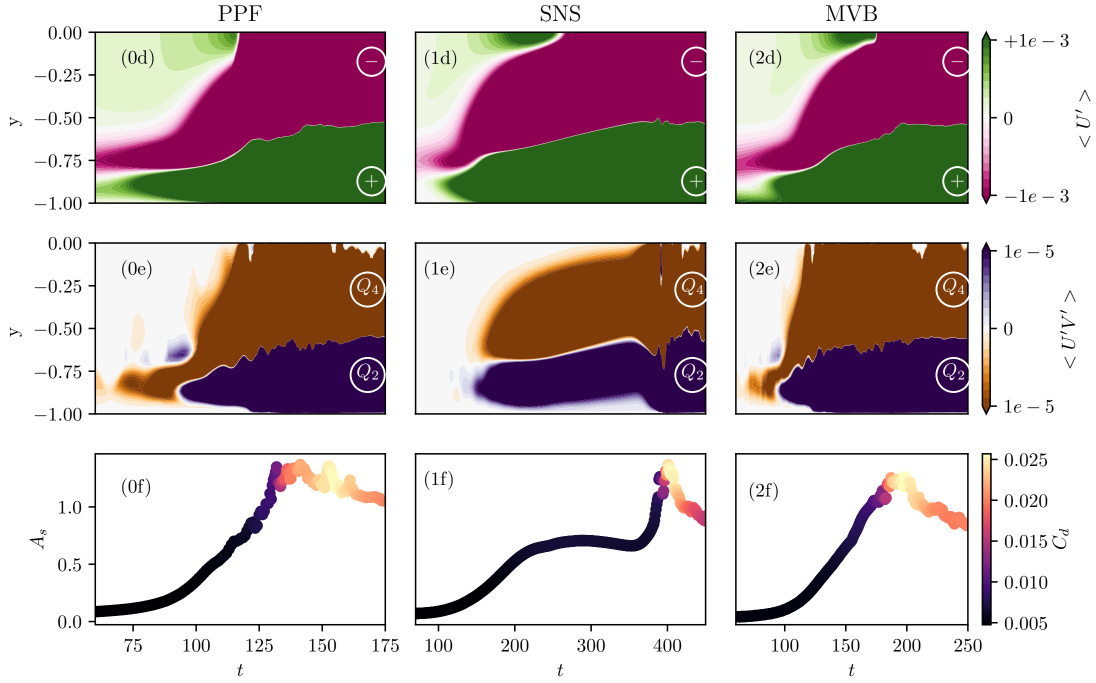

Figure 6.16 – First row: contours of the streamwise velocity disturbances averaged onto the x-z plane ($\langle U \rangle$). Second row: contours of the $U'V'$ product measuring Q2 and Q4 events averaged onto wall-parallel planes ($\langle U'V' \rangle$). Third row: time evolution of the spanwise amplitude deformation A_s, coloured by the friction coefficient C_f. Each column is associated to a given surface modelling. Results for SNS matches the ones for HSL, which are reported in chapter 5

simulations (see figure 6.15) result in high levels of ω_x as provided in figure 6.14. Then, we observe some oscillations followed by a monotonic growth of streamwise vorticity for $t \approx (90, 130)$. We argue that these oscillations are due to the interaction of the overlying TS-like spanwise vortices with the underlying compliant surface, producing coherent, large quasi 2D spanwise waves, such as those depicted in figure 6.7.d for $t = 94$ and characterised in figure 6.10.b. However, the monotonic increase of ω_x has a smaller growth rate than that measured during the onset of standard Λ-vortices on non-slippery surfaces (PPF), indicating that some key elements driving this process have been modified.

6.3.4 Generation of coherent structures

The contribution of SHS in delaying K-type transition has been attributed to their capacity to alter the standard development of characteristic coherent structures normally occurring during this process, namely Λ and hairpin vortices, by interfering with the vortex tilting-stretching process. This section aims at establishing how sweep and ejection events, strictly linked to the hairpin generation (Farano et al., 2015), are affected by SHS. According to Cohen et al. (2014), hairpin vortices are generated by the non-linear interaction of three ingredients, namely: a) shear in the wall normal direction, b) a pair of counter-rotating vortex and c) a 2D wavy vortex sheet. Wall-normal shear measured for PPF, SNS and MVB simulations is shown in figure 6.16.x.d. We can notice that wall shear is qualitatively the same in all cases, playing a small part in modifying the transition scenario. On

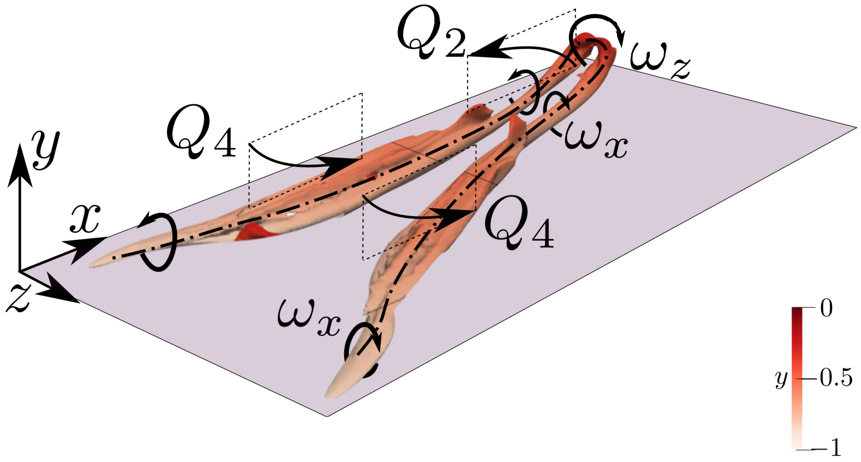

Figure 6.17 – Sketch based on data from PPF simulation at $t = 108$. -0.02 isosurfaces of the λ_2-criterion, depicting a Λ-vortex, characterised by ω_x vorticity, just after the formation of a primary hairpin arch, indicated with ω_z, and right before the development of a secondary arch. Dash-dotted line represent the rotation axis of the coherent structure, curved arrows its rotational sense, and $Q4, Q2$ annotations the key areas for sweep-ejection events. Notice how the hairpin legs, formerly Λ-vortices, produce an outward transport of mass

the other hand, we have already shown that SHS act on streamwise vortices, identified as ω_x (see figure 6.14). We have already shown that SHS modeled as a flat boundary do not alter much the 2D TS-waves, so HSL and SNS surfaces delay K-type transition by preventing the onset of hairpin vortices. Whereas, deformable interfaces enhance the development of small scale 2D wavy vortices, producing a wall-normal velocity at the boundary with the same spatial wavenumber of the fundamental 2D TS wave (see figure 6.10.a). Based onto these results we argue that MVB modelled SHS enhance the formation of hairpin-like vortices (and therefore advance transition comparing to HSL and SNS cases) owing to the interaction of coherent flow structures and interface deformation, similarly to what is found in turbulent flows over a compliant surface, where the surface deformation η is correlated with the velocity perturbations $\boldsymbol{U}'$ (Zhang et al., 2017). In this perspective we track the correlation between streamwise and wall normal velocity perturbations, and in particular their probability of occurring in the second (Q2) and fourth (Q4) quadrant of the $U' - V'$ plane (Adrian, 2007). Q2 events represent ejections, with negative U' lifted away from the wall by positive wall normal fluctuations, whereas Q4 events (sweeps) are characterised by positive streamwise velocity transported toward the wall by negative V', plotted in the second row of figure 6.16. For K-type transition on no-slip surfaces (PPF, figure 6.16.0e) we initially observe for $t \in (75, 100)$ the onset of Q4 events near the wall, indicating the sweeping action of Λ-vortices legs. For $t > 90$, Q2 events appear farther from the wall, marking the beginning of ejection events that result in the development of characteristic hairpin heads. This process is summarised in figure 6.17. Looking at figure 6.16.1e we notice how the onset of Q2 and Q4 events is modified by the introduction of slippery boundaries. The plot presented here for spatially heterogeneous surfaces matches that obtained for HSL modelled SHS (Chap. 5). In both cases the characteristic succession of sweep-ejection events is substantially attenuated, and the strong Q2-Q4 values occurring in correspondence with the plateau in A_s (figure 6.16.1f) identify the saturation of non-linear streaks, described in our previous investigation. MVB modelled superhydrophobic surfaces introduce a wall-normal velocity at the interface that modifies the scenario.

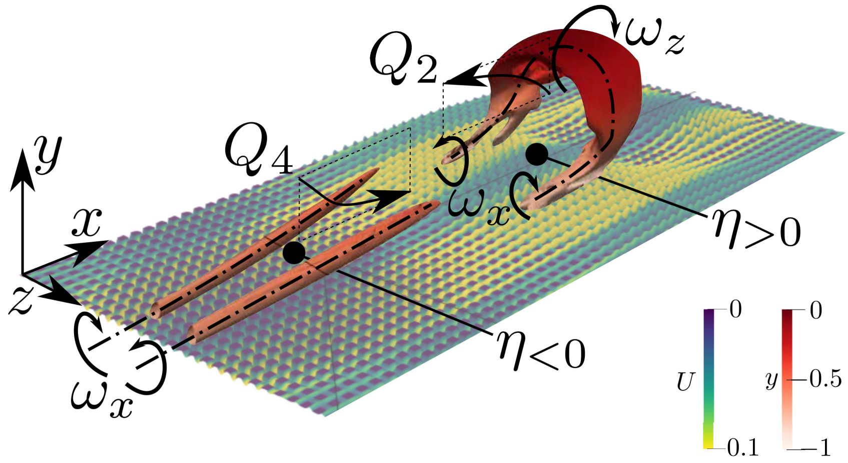

Figure 6.18 – Sketch based on data from MVB simulation at $t = 108$. -0.02 isosurfaces of the λ_2 criterion on top of the deformable U-SHS surface. Upward interface displacement is related to strong ejections (Q_2), producing ω_z vortices similar to the ones of hairpin-heads but without their typical legs. Streamwise vortices (not streaks) are measured on top of negative deformations of the MVB modelled surface. These latter, to which is associated most of the sweeping events (Q_4), have a rotation sense that is opposite to the one of the hairpin-like legs. Rotation axis are qualitatively indicated with a dash-dotted line.

As for the PPF case, we first observe the onset of sweeping events at the wall, followed by ejections in the bulk flow; but in contrast with what is found on rigid smooth walls, we observe rapid oscillations in the measured signal. In fact, analysing a single snapshot of MVB simulation for $t \approx 100$ we realize that the streamwise distribution of Q2-Q4 is far from being homogeneous. On the one hand, strong ejections occur on top of surface bumps, forming hairpin vortices characterised by large heads and small legs; on the other hand, counter rotating streamwise vortices, not streaks, occur on top of negative interface deformations, producing a sweeping event (see figure 6.18). These findings match those made by Zhang et al. (2017) regarding the development of coherent structures in a turbulent flow over compliant walls. Another remarkable feature is that at this stage we observe the coexistence of streamwise vortices and hairpin-like legs, characterised by an opposite sign in ω_x. This explains the oscillating behaviour observed in figure 6.16.2e, which passes undetected in figure 6.11.2.a showing the absolute value of ω_x. The deformable interface introduced by MVB modelling for SHS acts as an elastic energy reservoir, which advances transition by promoting the ejection process, forming hairpin like head without the need for Λ-vortices. After this phase, transition takes over in a way similar to that observed for standard K-type transition on PPF surfaces, with the development of secondary hairpin heads (Guo et al., 2010) up to the final breakdown to turbulence (Sandham and Kleiser, 1992a).

6.4 Summary and perspectives

The effects of underwater superhydrophobic surfaces on the K-type transition process has been investigated numerically, spanning through a series of different surface modellings, extending our previous work (Chap. 5). We have employed both global linear stability analysis and DNSs over flat as well as deformable boundaries to introduce the physical ingredients usually occurring for flows over gas lubricated surfaces. We have found that slippery surfaces are capable of delaying the transition process by inhibiting the onset of characteristic coherent structures arising during the process, namely Λ and hairpin vortices. Their influence begins from the very first non-linear stages, and has been attributed to a modification in the vortex stretching-tilting process occurring on saturated TS-like spanwise vortices, responsible for the onset of Λ aligned vortices in the case of standard K-type transition. In the limit of a flat interface we have found that K-type transition process is not dependent onto the spatial discretisation of the surface, as long as its characteristic size L is small enough so to match some physical requirements, namely if it is capable of withstanding wetting transition (Seo et al., 2017). In fact SHS modelled with a single spatially homogeneous slippery boundary as well as with a texture resolved alternating slip/no-slip boundary provides the same transition process, therefore extending the findings made for both laminar (Ybert et al., 2007) and turbulent (Seo and Mani, 2016) flows. Relaxing the flat-interface dynamics requires the resolution of a coupled fluid-structure like problem, where an arbitrary lagrangian eulerian approach is used to deform the computational mesh so to follow the interface evolution, which is taken into account via a linearised Young-Laplace equation (Seo et al., 2017). In this framework, the modelled air-water interface introduces a new physical ingredient to the process, namely wall-normal velocities at the moving boundaries. This additional element enhances the non-linear dynamics occurring during transition. Collective upwards moving interfaces enhance ejection events, leading to the development of hairpin-like structures, featuring large heads but with legs missing, while streamwise vortices are observed on top of the free-surface dimples.

Taking into account for interface deformation modifies the findings obtained for flat-modelled superhydrophobic surfaces, altering the time needed to transition as well as changing the underlying physical mechanism involved. Therefore, using SHS modellings including interface deformation in transitional flows does not provide the same results as the ones which assumes flat surfaces, in contrast with what has been found for fully turbulent flows (Seo et al., 2017).

A number of extensions and improvements to the present work can be envisioned.

- Run a series of parametric analysis in order to verify the robustness of our findings regarding the surface size L and the surface tension employed.
- Verify how different transition scenarios (Chap. 5), other than the K-type scenario, are affected by spatially heterogeneous SHS as well as moving interfaces.
- Extend our DNS to fully coupled two-phase flows, taking into account for the wetting stability process with appropriate contact line models so to study the eventual loss of gas lubricant.

Chapter 7

Conclusions

7.1 Overall Conclusions

The aim of this thesis has been to determine how transition processes in wall bounded shear flows are influenced by the use of slippery superhydrophobic surfaces. Whilst many recent studies have shown the effectiveness of such surfaces in reducing drag in both laminar and turbulent regimes, only the work by Min and Kim (2005) addresses the problem in transitional conditions. Therefore, the present thesis has aimed at determining which physical mechanisms occurring during transition are affected by the use of superhydrophobic surfaces as a mean of passive flow control, as well as predict their performance in real world applications. To tackle this problem we have used numerical simulations of transitional channel flows, enclosed with variously modelled superhydrophobic surfaces. The spectral element code NEK5000 has been employed together with a temporal simulation approach, enabling for an accurate resolution of the surface-linked dynamics.

We have shown that the effectiveness of gas lubricated surfaces in controlling transition strongly depends on the specific physical mechanism occurring during the process. When modelled with a spatially homogeneous and partially slippery boundary (Robin), superhydrophobic surfaces are capable of delaying K-type transition scenario by inhibiting the onset of Λ and hairpin vortices. In the cases tackled in this thesis, the slip length arising from the Robin boundary condition modelling the superhydrophobic surfaces is based onto a careful analysis of the available literature, ensuring that its gas-lubricated layer remains trapped within the surface roughnesses. Under these conditions we have found that wall slip modifies the typical vortex stretching-tilting process responsible for the development of these characteristic coherent structures, and transition can be delayed up to be completely avoided. A radically different behaviour has been found for the optimal and uncontrolled transition scenarios, which are barely affected by the presence of SHS. In particular, triggering uncontrolled transition in channel flows without any unphysical bias has required the construction and implementation of an ad-hoc theoretical and numerical framework. The method developed in this thesis consists of using a continuous synthetic forcing capable of inducing stochastic velocity perturbations with a prescribed energy level in wall-bounded parallel flows through receptivity mechanisms. Being built using concepts arising from the optimal forcing framework, unphysical transient effects such as those arising when using random perturbations are avoided, allowing the study of transition scenarios similar to the ones observed in poorly-controlled experiments. In this framework, it has been shown that *uncontrolled* transition is unaltered by the introduction of slippery surfaces. In fact this transition scenario is characterised by the onset of streamwise velocity perturbations far from the wall, called streaks, which we have also shown to be substantially unaffected by the use of superhydrophobic surfaces.

On the basis of these preliminary results, K-type transition has been selected as benchmark case to study the influence of more accurate substrate modellings, so to include other key physical features characteristic of superhydrophobic surfaces getting rid of some of the assumptions previously made. First, the influence of spatial heterogeneity has been studied. Global linear stability analysis of channel flows enclosed with SHS modelled by spatially discretizing each gas-liquid/liquid-solid interface as a slip/no-slip flat boundary condition provides virtually the same results obtained using a single, spatially homogeneous Robin one. This result relies onto the fact that typical wall roughness lengthscales of superhydrophobic surfaces capable of withstanding a fully turbulent flows are much smaller than those of characteristic transitional structures. As a matter of fact it is found that the whole transitional process appears to be unchanged by the two different modellings, complementing and extending the recent findings made for both laminar (Ybert et al., 2007) and turbulent regimes (Seo et al., 2015).

Taking into the account also the flat-interface dynamics has required the formulation and implementation of a fully coupled fluid-structure problem, where an Arbitrary Lagrangian Eulerian (ALE) approach is used to deform the computational mesh so to follow the interface evolution, which is taken into account via a linearised Young-Laplace equation (Seo et al., 2017). The whole has been accomplished using the same Spectral Element Method code NEK5000, taking inspiration from the ALE implementation introduced by Ho (1989). In this framework, the modelled air-water interface introduces a new physical ingredient to the process, namely wall-normal velocities at the moving boundaries. This additional element enhances the non-linear dynamics occurring during transition. Collective upwards moving interface enhance ejection events, leading to the development of hairpin-like structures, featuring large heads with small legs, while streamwise vortices are observed on top of the free-surface dimples.

Taking into account the interface deformation modifies the findings obtained for flat-modelled superhydrophobic surfaces, altering the time needed to reach transition as well as changing the underlying physical mechanism involved. Therefore, using SHS modellings including interface deformation in transitional flows does not provide the same results as those assuming flat surfaces, in contrast with what has been found for fully turbulent flows (Seo et al., 2017).

7.2 Perspectives

The work presented in this manuscript aims at determining the performances of gas-lubricated superhydrophobic surfaces as a mean of passive flow control. Extending the findings of previous works regarding the laminar and turbulent states, this thesis focuses on the transitional regime. K-type transition is the most affected by the introduction of such surfaces, balanced by two competing effects. On one hand slippery surfaces inhibits the development of hairpin vortices by reducing vortex stretching, while accounting for the free-surface dynamics produces wall-normal velocity oscillations that enhance the development of their characteristic heads. To the author's perspective, this work constitute a starting point for many future works. The non-exhaustive list of perspectives that follows arises from the current's author interest, the numerous discussions he had with his supervisors as well from the fruitful debates he had during conferences and non-official talks.

— Non-linear optimal perturbations in a channel flow are characterised by hairpin-like structures (Farano et al., 2015), similar to the ones occurring during K-type transition. On the other hand we have shown that slippery surfaces inhibit the onset of hairpin structures. Studying the non-linear optimal perturbation on SHS surfaces could allow to find a different preferential path for the laminar-turbulent transition process. A direct-adjoint optimization based on the conjugate gradient method is already available in NEK5000 (Farano et al., 2015). Performing such simulations on slippery surfaces would require nothing but the implementation of the equivalent Robin boundary condition for the adjoint solver.

- Global linear stability analysis has demonstrated the equivalency of spatially homogeneous and heterogeneous 'flat' modellings, provided that the surface's characteristic size to model is small enough. It would be interesting to find the threshold size beyond which 1D local and 3D global analysis diverges. This would suggest some important features for triggering transition in low Reynolds applications, where the roughness size (L) reaches lengths comparable to the one of the overlying flow (H)
- Implementing interface dynamics within the Arnoldi algorithm for the Global stability analysis would enable for the study of configurations where capillary lengths becomes predominant, such as in microchannels.
- Despite having a relatively slow amplitude, interface deformations strongly alters the transitional process, acting as an energy reservoir for the overlying flow in a similar way to the one observed for compliant surfaces (Zhang et al., 2017). Another interesting line of research would be to study the influence of compliant surfaces in transitions other than K-type.
- All the results presented in this thesis are based on the assumption that plastron layer are stably kept within the surface roughnesses, neglecting for an eventual wetting transition during the laminar-turbulent one. Numerical simulations of fully coupled two-phase fluids, accounting for both the interface movement as well as the triple point dynamics, would be crucial for an accurate study of the phenomena.
- Envisaging a collaboration with other researcher, notably with groups capable of performing experiments, is paramount in the author's opinion. On one hand the results presented in the present thesis would provide a starting point onto which to base the design of experimental essays; on the other the latter would provide fundamental data to validate the assumptions made in the modelling of superhydrophobic surfaces.

Figure 7.1 – The author posing with a Lotus Flower plant. Notice the water drop onto the large leaf. Silvery areas that can be seen in transparence are due to light reflection on the gas-water interface.

Appendix A

Derivation of Mean and Turbulent Kinetic Energy balance equations

We detail the derivation of Mean and Turbulent Kinetic Energy (MKE and TKE) balance equations in the framework of a temporal channel flow with F-type volume forcing. In the following we make use of the convention of summation over identical indices.

A.1 MKE derivation

Applying the time-averaging defined in equation (4.36) to equation (4.1) where the decomposition of the velocity field given in equations (4.34) and (4.35) has been used, one obtains:

$$\frac{\partial \widehat{U}_i}{\partial t} = -\frac{\partial \widehat{U_i U_j}}{\partial x_j} - \frac{\partial \widehat{u_i u_j}}{\partial x_j} - \frac{\partial \widehat{P}}{\partial x_i} + \frac{1}{Re}\frac{\partial^2 \widehat{U}_i}{\partial x_j^2} \tag{A.1}$$

In order to recover an equation for the mean kinetic energy we multiply equation (A.1) by U_i, giving:

$$\underbrace{\widehat{U}_i \frac{\partial \widehat{U}_i}{\partial t}}_{\text{a}} = -\underbrace{\widehat{U}_i \frac{\partial \widehat{U_i U_j}}{\partial x_j}}_{\text{b}} - \underbrace{\widehat{U}_i \frac{\partial \widehat{u_i u_j}}{\partial x_j}}_{\text{c}} - \underbrace{\widehat{U}_i \frac{\partial \widehat{P}}{\partial x_i}}_{\text{d}} + \underbrace{\widehat{U}_i \frac{1}{Re}\frac{\partial^2 \widehat{U}_i}{\partial x_j^2}}_{\text{e}} \tag{A.2}$$

Developing all the terms one by one one obtains:

$$(a) = \frac{\partial}{\partial t}\left(\frac{\widehat{U_i^2}}{2}\right) \tag{A.3}$$

$$(b) = \frac{\partial}{\partial x_j}\left(\frac{\widehat{U_i^2}\widehat{U_j}}{2}\right) \tag{A.4}$$

$$(c) = \underbrace{\widehat{u_i u_j}\frac{\partial \widehat{U}_i}{\partial x_j}}_{\text{c.1}} - \underbrace{\frac{\partial}{\partial x_j}\left(\widehat{u_i u_j}\widehat{U_j}\right)}_{\text{c.2}} \tag{A.5}$$

$$(d) = -\widehat{U}_i\frac{\partial \widehat{P}}{\partial x_i} \tag{A.6}$$

$$(e) = \underbrace{\frac{1}{Re}\frac{\partial}{\partial x_j}\left(\widehat{U}_i\frac{\partial \widehat{U}_i}{\partial x_j}\right)}_{\text{e.1}} - \underbrace{\frac{1}{Re}\left(\frac{\partial \widehat{U}_i}{\partial x_j}\right)^2}_{\text{e.2}} \tag{A.7}$$

which, rearranged into a single equation, provides the MKE balance equation for a generic incompressible newtonian flow. In the framework of a temporal channel flow, the MKE equation can be reduced as follows:

$$\underbrace{\frac{1}{2}\frac{\partial \widehat{U^2}}{\partial t}}_{\text{a}} + \underbrace{\widehat{U}\Pi}_{\text{d}} = +\underbrace{\widehat{uv}\frac{\partial \widehat{U}}{\partial y}}_{\text{c.1}} - \underbrace{\frac{\partial \widehat{uv}\widehat{U}}{\partial y}}_{\text{c.2}} + \underbrace{\frac{\partial}{\partial y}\left(\widehat{U}\frac{\partial \widehat{U}}{\partial y}\right)}_{\text{e.1}} - \underbrace{\left(\frac{\partial \widehat{U}}{\partial y}\right)^2}_{\text{e.2}}, \tag{A.8}$$

where the term (d) represents the power driving the flow, being Π the streamwise pressure gradient. Time averaging and using some physical arguments Ricco et al. (2012), one can obtain the global transport equation of the MKE:

$$U_b\tau_w = -\underbrace{\left[\widehat{uv}\frac{\partial \widehat{U}}{\partial y}\right]_g}_{P_{uv}} + \underbrace{\left[\left(\frac{\partial \widehat{U}}{\partial y}\right)^2\right]_g}_{D_u} \tag{A.9}$$

The first term on the left represents the global input power, given by the pressure gradient force times the bulk velocity. The first term on the right, P_{uv} (see (c.1)), is a *source* term for the MKE, allowing the energy to be transferred from the mean flow to the turbulent fluctuating field, thus providing the link between the MKE and the TKE. The last term on the right, D_u (see (e.2)), represents the viscous dissipation due to the gradient of the mean flow.

A.2 TKE derivation

We now derive the TKE balance equations under the same assumptions made in the previous section. Starting from equations (4.1), using the decomposition in equations (4.34) and (4.35), and then removing the equation for the mean state, we obtain the following equation for the perturbation evolution:

$$\frac{\partial u_i}{\partial t} = -\widehat{U_j}\frac{\partial u_i}{\partial x_j} - u_j\frac{\partial \widehat{U}_i}{\partial x_j} - \frac{\partial p}{\partial x_j} + \frac{1}{Re}\frac{\partial^2 u_i}{\partial x_j} - u_j\frac{\partial u_i}{\partial x_j} + u_i f_i \tag{A.10}$$

Similarly to Reynolds-Orr equation in the linear-stability framework (Schmid and Henningson, 2001), we derive an evolution equation for the TKE by scalar multiplication of u_i with the previous equation. By further rearranging equation (A.10), the following turbulent kinetic energy equation is obtained:

$$u_i\frac{\partial u_i}{\partial t} = \underbrace{-u_i u_j\frac{\partial \widehat{U}_i}{\partial x_j}}_{P_{ii}}\underbrace{-\frac{1}{Re}\left(\frac{\partial u_i}{\partial x_j}\right)^2}_{\epsilon_{ii}} \tag{A.11}$$

$$+ \frac{\partial}{\partial x_j}\left[\underbrace{-\frac{1}{2}u_i u_j\widehat{U_j}}_{A_{ii}}\underbrace{-\frac{1}{2}u_i u_i u_j}_{Q_{ii}}\underbrace{-u_i p\delta_{i,j}}_{\phi_{ii}}\underbrace{+\frac{1}{Re}u_i\frac{\partial u_i}{\partial x_j}}_{D_{ii}}\right] \tag{A.12}$$

$$+ \underbrace{u_i f_i}_{F_p}. \tag{A.13}$$

These terms are usually referred to as mean advection (A_{ii}), production (P_{ii}), transport by fluctuations Q_{ii}, pressure redistribution ϕ_{ii}, viscous diffusion D_t, and turbulent dissipation ϵ_{ii} terms. The presence of the F-type forcing appears in the last term of (A.11), which is called F_p.

As for the MKE, we now rewrite the TKE in a temporal channel flow framework, taking the average in the spatially homogeneous directions:

$$\frac{1}{2}\frac{\partial \widehat{q^2}}{\partial \tau} = \underbrace{-\frac{\partial\left(\widehat{vp}\right)}{\partial y}}_{\phi}\underbrace{-\frac{1}{2}\frac{\partial\left(\widehat{vq^2}\right)}{\partial y}}_{Q}\underbrace{-\widehat{uv}\frac{\partial \widehat{U}}{\partial y}}_{P_{uv}}\underbrace{+\frac{1}{2}\frac{\partial^2 \widehat{q^2}}{\partial y^2}}_{D}\underbrace{-\widehat{\frac{\partial u_i}{\partial x_j}\frac{\partial u_i}{\partial x_j}}}_{\epsilon}\underbrace{+u_i f_i}_{F_p} \tag{A.14}$$

where $q^2 = u_i u_i$. In the same way as for the MKE equations, time averaging and integration along y of equations (A.14) allows for further simplifications (Ricco et al., 2012), finally reading as:

$$-P_{uv} + F_p = \epsilon \tag{A.15}$$

Appendix B

Numerical validation of chapter 5

Direct Numerical Simulations have been validated comparing our results with those provided by Min and Kim (2004) on a fully developed turbulent flow over a superhydrophobic surface. Figure B.1.a depicts the statistics obtained with our code in the turbulent regime. To converge statistics the simulations have been run for $t \approx 1000$ time units after the onset of a turbulence state. Transition has been triggered following the K-type scenario. The mean velocity profiles U^+ slightly deviate from the reference ones when the slip length is increased. This behaviour is due the fact that our statistically converged states result from laminar-turbulent transition of a channel where we have imposed a constant flow rate for different values of the slip length, instead of a constant mean value of Re_τ in the turbulent regime as done by Min and Kim (2004). As a consequence, in our numerical configuration the mean friction Reynolds number in the fully developed turbulent regime reduces when the slip length L_s is increased, since the shear at the wall decreases. To allow a more direct comparison with Min and Kim (2004) results we make use of the shifted-turbulent boundary layer (S-TBL) model first proposed by Fukagata et al. (2006). Using equation (6) from Seo and Mani (2016) we obtain the profiles in figure B.1.b, which compare well with those obtained by DNS. As a further validation we present Reynolds stresses in figure B.2. Our results match the values computed by Schlatter (2005) for a no-slip boundary at $Re_\tau \approx 210$, while increasing the L_s we obtain the same behaviour prescribed by Min and Kim (2004) for a lower friction Reynolds number. This validates our approach, further confirming that the fully turbulent state is independent from the transition route.

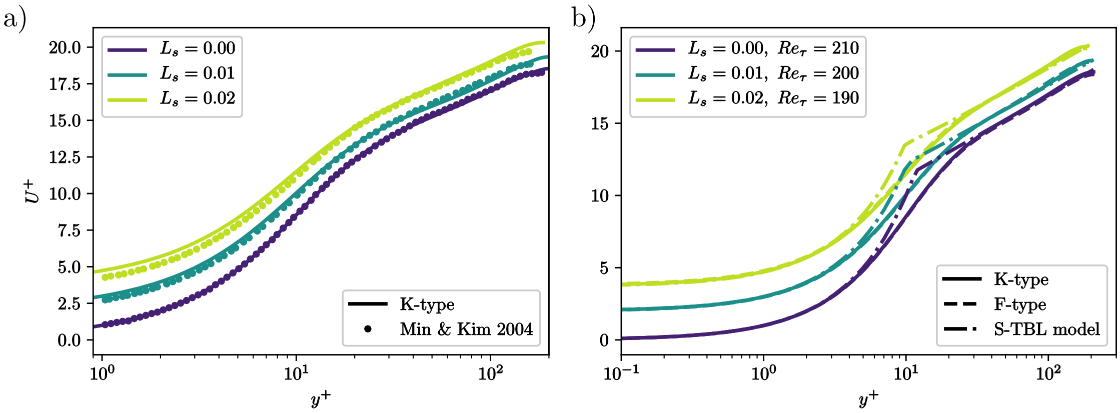

Figure B.1 – (a) Mean velocity profiles compared with the ones for $Re_\tau = 180$ (Min and Kim, 2004). The discrepancy derives from the fact that our turbulent states arise from transition made at a constant flow rate. (b) Same mean velocity profiles as in a), now compared with shifted-turbulent boundary layer model (Fukagata et al., 2006), for the different obtained Re_τ.

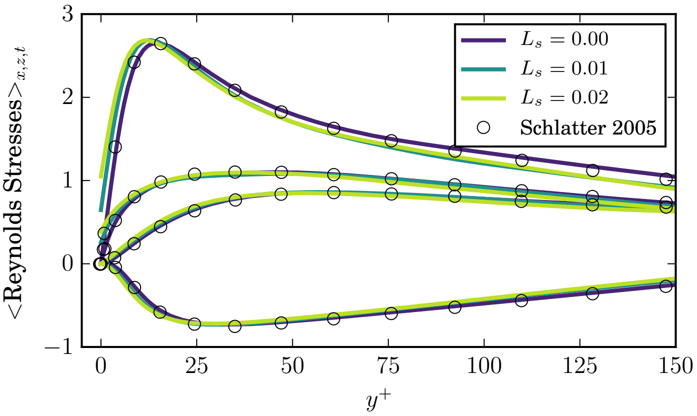

Figure B.2 – Reynolds stresses in wall scaling for different L_s. From top to bottom $\langle uu\rangle^{1/2}/u_\tau$, $\langle ww\rangle^{1/2}/u_\tau$, $\langle vv\rangle^{1/2}/u_\tau$, $\langle uv\rangle/u_\tau^2$. Open circles represents the values computed for $L_s = 0.0$ (no-slip wall) by Schlatter (2005) at $Re_\tau \approx 210$.

Appendix C

Fully turbulent channel flow over superhydrophobic substrates: influence of surface modellings

We report the averaged statistics of turbulent flows over SHS modelled using different approaches, obtained by extending the transitional DNS up to fully developed turbulent state. Statistical averaging is performed onto a $t = 400$ wide window, conventionally starting from 100 timesteps after the peak in friction Reynolds number. Regardless for the model employed, mean velocity profiles for turbulent flows over SHS provides the same result, matching the prediction made using the Shifted Turbulent Boundary Layer (S-TBL) model, as proposed by Fukagata et al. (2006):

$$U^{+} = \frac{1}{k} ln(Re_{\tau}) + B + {L_s}^{+}, \tag{C.1}$$

where in our case ${L_s}^{+} \approx 2$, whereas the constants (k, B) are set to $(0.41, 5.0)$. The footprint of spatially heterogeneous modelling of SHS can be recovered by looking at the Reynods stresses near the wall. The peculiar behaviour of $\langle U'U' \rangle$ and $\langle U'V' \rangle$ components near the wall is a typical feature of slip/no-slip modellings (Fairhall et al., 2018). Starting from $y^{+} > 15$ all SHS models provide the same results, constituting an a posteriori validation of the DNS computations described in the present work.

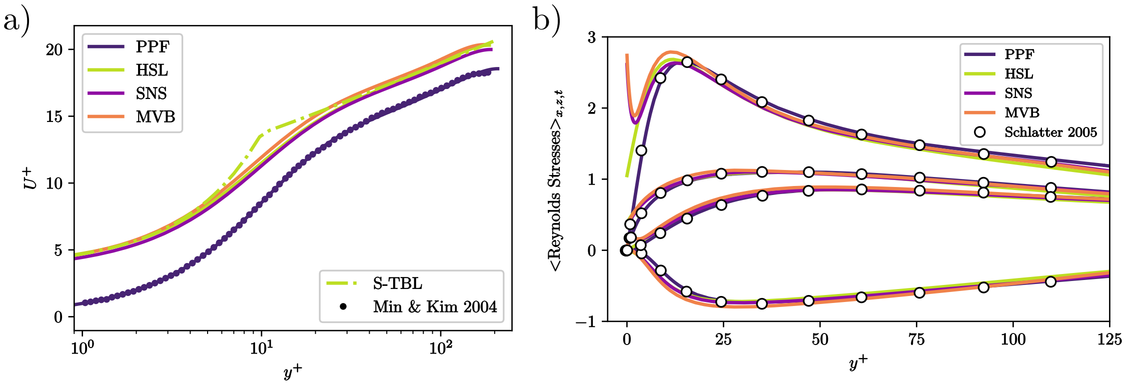

Figure C.1 – (a) Mean velocity profiles for statistically converged turbulen flows. Standard no-slip condition provides $Re_\tau = 210$, and is compared with Min and Kim (2004). Provided that flow is kept constant during all transitional simulations, slippery SHS provides a lower friction, resulting in $Re_\tau \approx 190$. For this reason we compare our profiles with the ones obtained using the S-TBL model C.1. (b) Reynolds stresses in wall scaling for different surfaces. From top to bottom $\langle U'U' \rangle$, $\langle W'W' \rangle$, $\langle V'V' \rangle$ and $\langle U'V' \rangle$.

Appendix D

Validation of DNS over deformable free-surfaces modelled with ALE approach

Solid lines represents the reference solution obtained using the 1D local framework as well as dashed lines represents the numerical results obtained for the DNS validation. The DNS code in which Free-surface dynamics implemented trough ALE approach (Ho, 1989) is verified against solutions found within the linear stability analysis framework. In particular, we select the water table flow (Olsson and Henningson, 1995) as benchmark case because it contains all the physical features of the liquid flow over a gas-infused superhydrophobic surface. Water table flow describes the flow of a liquid film down an inclined plane, driven by gravity and exposing a free-surface external environment. Following the procedure described in Schmid and Henningson (2001), the evolution of infinitesimal perturbations on top of the base flow $U_b(y) = 2y - y^2$v is governed by the classical Orr-Sommerfeld

$$(-i\omega + i\alpha U_b)(D^2 - k^2)\hat{v} - i\alpha U_b''\hat{v} = \frac{1}{Re}(D^2 - k^2)\hat{v} \tag{D.1}$$

and Squire equation

$$(-i\omega + i\alpha U_b)\hat{\zeta} + i\beta U_b' = \frac{1}{Re}(D^2 - k^2)\hat{\zeta}. \tag{D.2}$$

The above equations are derived from 6.8, where the the primitive formulation has been dropped in favour of the normal velocity-vorticity one, $\zeta = \partial u/\partial z - \partial w/\partial x$ and we have assumed disturbances of the form

$$v(x,y,z,t) = \hat{v}(y)e^{i(\alpha x + \beta z - \omega t)} \tag{D.3}$$

$$\zeta(x,y,z,t) = \hat{\zeta}(y)e^{i(\alpha x + \beta z - \omega t)} \tag{D.4}$$

where $k^2 = \alpha^2 + \beta^2$ and D and $'$ denote the normal derivative. Equations (D.1) and (D.2) are identical to the ones for any wall bounded flow, such as Poiseuille and Couette. Influence of the free-surface requires for a special care of the boundary condition, that will result an additional set of equations

$$k^2 S\hat{\eta} + \left[-i\omega + i\alpha - \frac{1}{Re}(D^3 - 3k^2)\right] D\hat{v} = 0 \tag{D.5}$$

$$-(D^2 + k^2)\hat{v} = 2i\alpha\hat{f} \tag{D.6}$$

$$(-i\omega + i\alpha)\hat{f} = \hat{v} \tag{D.7}$$

$$D\hat{\zeta} = 2i\beta\hat{f} \tag{D.8}$$

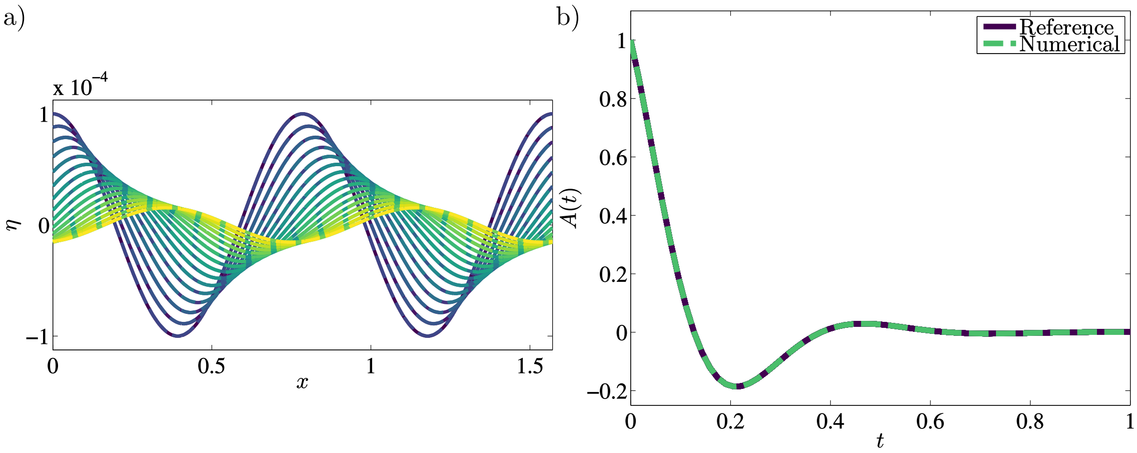

Figure D.1 – Evolution in time of the interface location, for a watertable flow configuration. Solid lines represents the reference solution obtained using the 1D local framework as well as dashed lines represents the numerical results obtained with the DNS having ALE modelled gas-liquid free interfaces. (a) Interface location in time in the range ($t = 0 - 0.2$), from blue to yellow. (b) Trace of the peak point of the wall-normal velocity, normalised by its initial intensity.

at at the gas-liquid interface for $y = 1$, while simple $\hat{v} = \partial\hat{v}/\partial y = \zeta = 0$ at the solid wall, for $y = 0$. Parameter S accounts for the influence of gravity and surface tension,

$$S = \frac{cos\phi}{Fr^2} + \frac{k^2}{We} \tag{D.9}$$

with the Froude (Fr) and Weber (We) number respectively, and ϕ the angle of the inclined plane. Setting $\phi = \pi/2$ neglect for the influence of gravity and, using a 1-D local stability analysis code, we are capable of retrieving the eigenvalues and its associate eigenvectors, as found by Olsson and Henningson (1995). We take the most unstable eigenvector, computed for $\alpha = 0.7, \beta = 1.3, Re = 1000$ and $S = 0.1$, and use it as initial condition for a DNS over ALE modelled free-surface interface. Our DNS solver provides the same interface motion prescribed by the 1-D linear stability analysis code, as depicted in figure D.1.

Appendix E

Nek5000 subroutines for Robin boundary condition

In the following section, comments to the code are indicated as

```
!ROBIN_BC
```

```
      SUBROUTINE PLAN3 (IGEOM)
C-----------------------------------------------------------------------
C
C     Compute pressure and velocity using consistent approximation spaces.
C     Operator splitting technique.
C
C-----------------------------------------------------------------------
      include 'SIZE'
      include 'INPUT'
      include 'EIGEN'
      include 'SOLN'
      include 'TSTEP'
      include 'GEOM'!ROBIN_BC
      include 'MASS'!ROBIN_BC
C
      COMMON /SCRNS/  RESV1 (LX1,LY1,LZ1,LELV)
     $ ,              RESV2 (LX1,LY1,LZ1,LELV)
     $ ,              RESV3 (LX1,LY1,LZ1,LELV)
     $ ,              DV1   (LX1,LY1,LZ1,LELV)
     $ ,              DV2   (LX1,LY1,LZ1,LELV)
     $ ,              DV3   (LX1,LY1,LZ1,LELV)
      COMMON /SCRVH/  H1    (LX1,LY1,LZ1,LELV)
     $ ,              H2    (LX1,LY1,LZ1,LELV)
      COMMON /MYROB/  H2_ROB(LX1,LY1,LZ1,LELV) !ROBIN_BC
      n=nx1*ny1*nz1*nelv !ROBIN_BC
C
      IF (IGEOM.EQ.1) THEN
C
C        Old geometry
C
         CALL MAKEF
C
      ELSE
C
C        New geometry, new b.c.
C
         INTYPE = -1
         CALL SETHLM  (H1,H2,INTYPE)
```

```
C-------------------------------------------------------------------!
C--------Create H2 that takes into account for Robin BC            !
         call rzero(H2_ROB,N) !ROBIN_BC                             !
         call bcneusc_mod(H2_ROB)!ROBIN_BC                          !
C--------Add contribution of Robin BC to standard Neumann condition!
         call add2(H2, H2_ROB,N) !ROBIN_BC                          !
C-------------------------------------------------------------------!
         CALL CRESVIF (RESV1,RESV2,RESV3,H1,H2)
         mstep = abs(param(94))
         if (param(94).ne.0. .and. istep.ge.mstep) then
          call ophinv_pr(dv1,dv2,dv3,resv1,resv2,resv3,h1,h2,tolhv,nmxh)
c         CALL OPHINV  (DV1,DV2,DV3,RESV1,RESV2,RESV3,H1,H2,TOLHV,NMXH)
         else
       CALL OPHINV  (DV1,DV2,DV3,RESV1,RESV2,RESV3,H1,H2,TOLHV,NMXH)
C            call ophinv_rob (DV1,DV2,DV3,RESV1,RESV2,RESV3,
C     &                        H1,H2,H2_ROB,TOLHV,NMXH)
         endif
         CALL OPADD2  (VX,VY,VZ,DV1,DV2,DV3)
c
c        Default Filtering
c
c        alpha_filt = 0.05
c        if (param(103).ne.0.) alpha_filt=param(103)
c        call q_filter(alpha_filt)
c
c        CALL SSNORMD (DV1,DV2,DV3)
c
         call incomprn(vx,vy,vz,pr)
C
      ENDIF
C
      RETURN
      END
C
C*********************************************************************
```

Listing E.1 – modified plan3 subroutine

```
C*********************************************************************
      SUBROUTINE BCNEUSC_MOD(S) !PICELLA
      include 'SIZE'
      include 'TOTAL'
      include 'CTIMER'
      include 'NEKUSE'
      DIMENSION S(LX1,LY1,LZ1,LELV)
      CHARACTER CB*3
      real NU
        slip_length=param(79)+1e-10! To be imposed within the .REA !
        NU = abs(param(02))
      if(nio.eq.0)write(6,*)'SLIP_LENGTH',SLIP_LENGTH,'NU',NU
      NFACES=2*NDIM
      NXYZ  =NX1*NY1*NZ1
      IFIELD=1 !flow variables
      NEL   =NELFLD(IFIELD)
      NTOT  =NXYZ*NEL
C      CALL RZERO(S,NTOT)
C      if(nio.eq.0)
C     $write(6,*)'SUBROUTINE␣BCNEUSC_MOD'
C     $         ,NFACES,NEL,NTOT,LELV
         DO 1000 IE=1,NEL
         DO 1000 IFACE=1,NFACES
```

```
            ieg=lglel(ie)
            CB =CBC(IFACE,IE,IFIELD)
            IF (CB.EQ.'SYM') THEN !Apply the condition to 'SYM' faces only...
               IA=0
C
C IA is areal counter, assumes advancing fastest index first. (IX...IY...IZ)
C
               CALL FACIND (KX1,KX2,KY1,KY2,KZ1,KZ2,NX1,NY1,NZ1,IFACE)
               DO 100 IZ=KZ1,KZ2
               DO 100 IY=KY1,KY2
               DO 100 IX=KX1,KX2
                  IA = IA + 1
!                 S(IX,IY,IZ,IE)=1/slip_length
                  S(IX,IY,IZ,IE) = S(IX,IY,IZ,IE) +
     $            NU/Slip_length*AREA(IA,1,IFACE,IE)/BM1(IX,IY,IZ,IE)
C                 if(nio.eq.0)write(6,*)IE,S(IX,IY,IZ,IE)
 100          CONTINUE
            endif
 1000    CONTINUE
      RETURN
      END
C
```

Listing E.2 – subroutine bcneusc_mod

As indicated within the subroutine, the slip length L_s value is prescribed within the *.REA file, using the blank variable PARAMETER(79).

```
[...]
            CALL HMHOLTZ ('VELX',OUT1,INP1,H1,H2,V1MASK,VMULT,
     $                                IMESH,TOLH,NMXI,1)
            CALL HMHOLTZ ('VELY',OUT2,INP2,H1,H2,V2MASK,VMULT,
     $                                IMESH,TOLH,NMXI,2)
            IF (NDIM.EQ.3)
     $      CALL HMHOLTZ ('VELZ',OUT3,INP3,H1,H2,V3MASK,VMULT,
     $                                IMESH,TOLH,NMXI,3)
[...]
```

Listing E.3 – standard ophinv subroutine

```
[...]
            CALL HMHOLTZ ('VELX',OUT1,INP1,H1,H2_X,V1MASK,VMULT,!ROBIN_BC
     $                                IMESH,TOLH,NMXI,1)
            CALL HMHOLTZ ('VELY',OUT2,INP2,H1,H2,V2MASK,VMULT,
     $                                IMESH,TOLH,NMXI,2)
            IF (NDIM.EQ.3)
     $      CALL HMHOLTZ ('VELZ',OUT3,INP3,H1,H2_Z,V3MASK,VMULT,!ROBIN_BC
     $                                IMESH,TOLH,NMXI,3)
[...]
```

Listing E.4 – ophinv_anisotropic subroutine

.

Scientific production

In the following are listed all the conferences to which the author has taken part during his period as a Ph.D. student, together with those where his work will be presented by others. Works related to the three-dimensional dynamics of an open cavity flow have began during the author's Master, and have been finalised during the first months of thesis.

International conferences

- **EFMC11**
  F. Picella, C. Douay, J.-C. Loiseau, J.-C. Robinet, S. Cherubini, L. Pastur and F. Lusseyran
  Stability analysis of three-dimensional open cavity.
  11th European Fluid Mechanics Conference
  2016, Sevilla, Spain
- **EDRFCM17**
  F. Picella, S. Cherubini, J.-C. Robinet
  SuperHydrophobic Channel flow, Transition an Passive Flow Control
  2017, Rome, Italy
- **Euromech591**
  SuperHydrophobic Channel Flow, Transition and Passive Flow Control
  F. Picella, S. Cherubini, J.-C. Robinet Euromech Colloquium 591
  2017, Bari, Italy
- **EFMC12**
  F. Picella, M.A. Bucci, S. Cherubini, J.-C. Robinet
  A novel technique for triggering bypass transition in internal flows based on the receptivity to forcing. 12th European Fluid Mechanics Conference
  2018, Wien, Austria
- **APS DFD 2018**
  F. Picella, J.-C. Robinet, S.Cherubini
  Influence of superhydrophobic surfaces on the laminar-to-turbulent transition in a channel flow
  American Physical Society, Division of Fluid Dynamics meeting
  `http://meetings.aps.org/Meeting/DFD18/Session/E27.6`
  2018, Atlanta, GA, USA
- **LIMSI2019**
  F. Picella, J.-C. Robinet, S.Cherubini
  Invited Talk: Influence of superhydrophobic surfaces on the laminar-to-turbulent transition in a channel flow
  LIMSI CNRS
  2019, Orsay, France

- **BIFD2019**
  F. Picella, J.-C. Robinet, S. Cherubini
  Influence of superhydrophobic surfaces on the laminar-to-turbulent transition in a channel flow
  Bifurcations in Fluid Dynamics
  2019, Limerick, Ireland
- **IUTAM Transition 2019**
  F. Picella, J.-C. Robinet, S. Cherubini
  Influence of superhydrophobic surfaces on the laminar-to-turbulent transition in a channel flow
  IUTAM Symposium on Laminar Turbulent Transition
  2019, London, UK.

Scientific papers

- F. Picella, J.-C. Loiseau, F. Lusseyran, J.-C. Robinet, S. Cherubini and L. Pastur
  Successive bifurcations in a fully three-dimensional open cavity flow
  Journal of Fluid Mechanics (Picella et al., 2018)
- F. Picella, M. A. Bucci, S. Cherubini, J.-C. Robinet
  A synthetic forcing to trigger laminar-turbulent transition in parallel wall bounded flows via receptivity
  Journal of Computational Physics (Picella et al., 2019)
- F. Picella, J.-C. Robinet, S. Cherubini
  Laminar-turbulent transition(s) over SuperHydrophobic Surfaces
  Submitted to Journal of Fluid Mechanics
- F. Picella, J.-C. Robinet, S. Cherubini
  K-type laminar-turbulent transition over SuperHydrophobic Surfaces: influence of free-surface dynamics
  Under preparation Journal of Fluid Mechanics

Pedagogy

As a Ph.D. student at Ecole Nationale Supérieure des Arts et Métiers, the author has joined the teaching staff of fluid mechanics department, providing courses to bachelor and master students of the school. Here are listed some of the courses he joined.

- **2017-2019** Simulation des systèmes fluides (Prof. V. Daru and Prof. X. Gloerfelt)
- **2018** Hydrodynamic Instabilities (Prof. J.C. Robinet)
- **2017-2018** Mathematique Informatique (Prof. X. Merle)

Bibliography

R. J. Adrian. Hairpin vortex organization in wall turbulence. *Physics of Fluids*, 19(4): 041301, apr 2007. doi: 10.1063/1.2717527. URL `https://doi.org/10.1063/1.2717527`.

S. K. Aghdam and P. Ricco. Laminar and turbulent flows over hydrophobic surfaces with shear-dependent slip length. *Physics of Fluids*, 28(3):035109, mar 2016. doi: 10.1063/1.4943671. URL `https://doi.org/10.1063/1.4943671`.

E. Alinovi. *Modelling the flow over superhydrophobic and liquid-impregnated surfaces*. PhD dissertation, DICCA, University of Genova, 2018.

E. Alinovi and A. Bottaro. Apparent slip and drag reduction for the flow over superhydrophobic and lubricant-impregnated surfaces. *Physical Review Fluids*, 3(12), dec 2018. doi: 10.1103/physrevfluids.3.124002. URL `https://doi.org/10.1103/physrevfluids.3.124002`.

P. Andersson, M. Berggren, and D. S. Henningson. Optimal disturbances and bypass transition in boundary layers. *Physics of Fluids*, 11(1):134–150, jan 1999. doi: 10.1063/1.869908. URL `https://doi.org/10.1063/1.869908`.

W. E. Arnoldi. The principle of minimized iterations in the solution of the matrix eigenvalue problem. *Quarterly of Applied Mathematics*, 9(1):17–29, apr 1951. doi: 10.1090/qam/42792. URL `https://doi.org/10.1090/qam/42792`.

F. Auteri, M. Carini, M. Fournié, D. Fratantonio, and F. Giannetti. Global linear stability analysis of the flow around a superhydrophobic circular cylinder. In *Springer Proceedings in Physics*, pages 165–170. Springer International Publishing, 2016. doi: 10.1007/978-3-319-30602-5_21. URL `https://doi.org/10.1007/978-3-319-30602-5_21`.

S. Bagheri, P. Schlatter, P. J. Schmid, and D. S. Henningson. Global stability of a jet in crossflow. *Journal of Fluid Mechanics*, 624:33, mar 2009. doi: 10.1017/s0022112009006053. URL `https://doi.org/10.1017/s0022112009006053`.

S. Bake, D. G. W. Meyer, and U. Rist. Turbulence mechanism in klebanoff transition: a quantitative comparison of experiment and direct numerical simulation. *Journal of Fluid Mechanics*, 459, may 2002. doi: 10.1017/s0022112002007954. URL `https://doi.org/10.1017/s0022112002007954`.

D. Barkley. Theoretical perspective on the route to turbulence in a pipe. *Journal of Fluid Mechanics*, 803, aug 2016. doi: 10.1017/jfm.2016.465. URL `https://doi.org/10.1017/jfm.2016.465`.

W. Barthlott and C. Neinhuis. Purity of the sacred lotus, or escape from contamination in biological surfaces. *Planta*, 202(1):1–8, apr 1997. doi: 10.1007/s004250050096. URL `https://doi.org/10.1007/s004250050096`.

W. Barthlott, M. Mail, B. Bhushan, and K. Koch. Plant surfaces: Structures and functions for biomimetic innovations. *Nano-Micro Letters*, 9(2), jan 2017. doi: 10.1007/s40820-016-0125-1. URL `https://doi.org/10.1007/s40820-016-0125-1`.

D. W. Bechert and M. Bartenwerfer. The viscous flow on surfaces with longitudinal ribs. *Journal of Fluid Mechanics*, 206(-1):105, sep 1989. doi: 10.1017/s0022112089002247. URL `https://doi.org/10.1017/s0022112089002247`.

S. Berlin, A. Lundbladh, and D. S. Henningson. Spatial simulations of oblique transition in a boundary layer. *Physics of Fluids*, 6(6):1949–1951, 1994. doi: 10.1063/1.868200. URL `https://doi.org/10.1063/1.868200`.

S. Berlin, M. Wiegel, and D. S. Henningson. Numerical and experimental investigations of oblique boundary layer transition. *Journal of Fluid Mechanics*, 393:23–57, 1999. doi: 10.1017/S002211209900511X.

D. Biau and A. Bottaro. An optimal path to transition in a duct. *Philosophical Transactions of the Royal Society A: Mathematical, Physical and Engineering Sciences*, 367(1888):529–544, feb 2009. doi: 10.1098/rsta.2008.0191. URL `https://doi.org/10.1098/rsta.2008.0191`.

R. A. Bidkar, L. Leblanc, A. J. Kulkarni, V. Bahadur, S. L. Ceccio, and M. Perlin. Skin-friction drag reduction in the turbulent regime using random-textured hydrophobic surfaces. *Physics of Fluids*, 26(8):085108, aug 2014. doi: 10.1063/1.4892902. URL `https://doi.org/10.1063/1.4892902`.

L. Brandt, C. Cossu, J.-M. Chomaz, P. Huerre, and D. S. Henningson. On the convectively unstable nature of optimal streaks in boundary layers. *Journal of Fluid Mechanics*, 485: 221–242, may 2003. doi: 10.1017/s0022112003004427. URL `https://doi.org/10.1017/s0022112003004427`.

L. Brandt, P. Schlatter, and D. S. Henningson. Transition in boundary layers subject to free-stream turbulence. *Journal of Fluid Mechanics*, 517:167–198, oct 2004a. doi: 10.1017/s0022112004000941. URL `https://doi.org/10.1017/s0022112004000941`.

L. Brandt, P. Schlatter, and D. S. Henningson. Transition in boundary layers subject to free-stream turbulence. *Journal of Fluid Mechanics*, 517:167âĂŞ198, 2004b. doi: 10.1017/S0022112004000941.

W. P. Breugem, B. J. Boersma, and R. E. Uittenbogaard. The influence of wall permeability on turbulent channel flow. *Journal of Fluid Mechanics*, 562:35, aug 2006. doi: 10.1017/s0022112006000887. URL `https://doi.org/10.1017/s0022112006000887`.

A. Busse and N. D. Sandham. Influence of an anisotropic slip-length boundary condition on turbulent channel flow. *Physics of Fluids*, 24(5):055111, may 2012. doi: 10.1063/1.4719780. URL `https://doi.org/10.1063/1.4719780`.

K. M. Butler and B. F. Farrell. Three-dimensional optimal perturbations in viscous shear flow. *Physics of Fluids A: Fluid Dynamics*, 4(8):1637–1650, 1992. doi: 10.1063/1.858386.

D. Byun, J. Kim, H. S. Ko, and H. C. Park. Direct measurement of slip flows in superhydrophobic microchannels with transverse grooves. *Physics of Fluids*, 20(11):113601, nov 2008. doi: 10.1063/1.3026609. URL `https://doi.org/10.1063/1.3026609`.

C. Canuto, M.Y Hussaini, A. Quarteroni, and Th.A. Zang. *Spectral Methods*. Springer Berlin Heidelberg, 2007. doi: 10.1007/978-3-540-30728-0. URL `https://doi.org/10.1007/978-3-540-30728-0`.

A. B. D. Cassie and S. Baxter. Wettability of porous surfaces. *Transactions of the Faraday Society*, 40:546, 1944. doi: 10.1039/tf9444000546. URL `https://doi.org/10.1039/tf9444000546`.

M. Castagna, N. Mazellier, and A. Kourta. Wake of super-hydrophobic falling spheres: influence of the air layer deformation. *Journal of Fluid Mechanics*, 850:646–673, jul 2018. doi: 10.1017/jfm.2018.480. URL `https://doi.org/10.1017/jfm.2018.480`.

S. L. Ceccio. Friction drag reduction of external flows with bubble and gas injection. *Annual Review of Fluid Mechanics*, 42(1):183–203, jan 2010. doi: 10.1146/annurev-fluid-121108-145504. URL `https://doi.org/10.1146/annurev-fluid-121108-145504`.

C.-H. Choi, K. Westin J. A., and K. S. Breuer. Apparent slip flows in hydrophilic and hydrophobic microchannels. *Physics of Fluids*, 15(10):2897, 2003. doi: 10.1063/1.1605425. URL `https://doi.org/10.1063/1.1605425`.

J. Cohen, M. Karp, and V. Mehta. A minimal flow-elements model for the generation of packets of hairpin vortices in shear flows. *Journal of Fluid Mechanics*, 747:30–43, apr 2014. doi: 10.1017/jfm.2014.140. URL `https://doi.org/10.1017/jfm.2014.140`.

R. J. Daniello, N. E. Waterhouse, and J. P. Rothstein. Drag reduction in turbulent flows over superhydrophobic surfaces. *Physics of Fluids*, 21(8):085103, aug 2009. doi: 10.1063/1.3207885. URL `https://doi.org/10.1063/1.3207885`.

J. Davies, D. Maynes, B. W. Webb, and B. Woolford. Laminar flow in a microchannel with superhydrophobic walls exhibiting transverse ribs. *Physics of Fluids*, 18(8):087110, aug 2006. doi: 10.1063/1.2336453. URL `https://doi.org/10.1063/1.2336453`.

A. M. J. Davis and E. Lauga. Hydrodynamic friction of fakir-like superhydrophobic surfaces. *Journal of Fluid Mechanics*, 661:402–411, aug 2010. doi: 10.1017/s0022112010003460. URL `https://doi.org/10.1017/s0022112010003460`.

A. de Cheveigné and H. Kawahara. Yin, a fundamental frequency estimator for speech and music. *The Journal of the Acoustical Society of America*, 2002.

M. O. Deville, P. F. Fischer, and E. H. Mund. *High-Order Methods for Incompressible Fluid Flow*. Cambridge University Press, 2002. doi: 10.1017/cbo9780511546792. URL `https://doi.org/10.1017/cbo9780511546792`.

E. De Donati. *Stability of the flow in a channel with grooved wall.* Master dissertation, AERO, Politecnico di Milano, 2015.

J. W. Elder. An experimental investigation of turbulent spots and breakdown to turbulence. *Journal of Fluid Mechanics*, 9(2):235–246, 1960. doi: 10.1017/S0022112060001079.

B. Emami, A. A. Hemeda, M. M. Amrei, A. Luzar, M. Gad el Hak, and H. Vahedi Tafreshi. Predicting longevity of submerged superhydrophobic surfaces with parallel grooves. *Physics of Fluids*, 25(6):062108, jun 2013. doi: 10.1063/1.4811830. URL `https://doi.org/10.1063/1.4811830`.

C. T. Fairhall and R. García-Mayoral. Spectral analysis of the slip-length model for turbulence over textured superhydrophobic surfaces. *Flow, Turbulence and Combustion*, 100 (4):961–978, may 2018. doi: 10.1007/s10494-018-9919-1. URL `https://doi.org/10.1007/s10494-018-9919-1`.

C. T. Fairhall, N. Abderrahaman-Elena, and R. García-Mayoral. The effect of slip and surface texture on turbulence over superhydrophobic surfaces. *Journal of Fluid Mechanics*, 861:88–118, dec 2018. doi: 10.1017/jfm.2018.909. URL `https://doi.org/10.1017/jfm.2018.909`.

M. Farano, S. Cherubini, J.-C. Robinet, and P. De Palma. Hairpin-like optimal perturbations in plane poiseuille flow. *Journal of Fluid Mechanics*, 775, jun 2015. doi: 10.1017/jfm.2015.320. URL `https://doi.org/10.1017/jfm.2015.320`.

B. F. Farrell. Optimal excitation of perturbations in viscous shear flow. *Physics of Fluids*, 31(8):2093, 1988. doi: 10.1063/1.866609. URL `https://doi.org/10.1063/1.866609`.

P. F. Fischer, J. W. Lottes, and S. G. Kerkemeier. nek5000 Web page, 2008. http://nek5000.mcs.anl.gov.

K. Fukagata, Kasagi N., and P. Koumoutsakos. A theoretical prediction of friction drag reduction in turbulent flow by superhydrophobic surfaces. *Physics of Fluids*, 18(5):051703, may 2006. doi: 10.1063/1.2205307. URL `https://doi.org/10.1063/1.2205307`.

M. Gad-El-Hak, R. F. Blackwelder, and J. J. Riley. On the interaction of compliant coatings with boundary-layer flows. *Journal of Fluid Mechanics*, 140(-1):257, mar 1984. doi: 10.1017/s0022112084000598. URL `https://doi.org/10.1017/s0022112084000598`.

N. Gilbert and L. Kleiser. Near-wall phenomena in transition to turbulence. *Near-Wall Turbulence*, pages 7–27, 1990.

S. Gogte, P. Vorobieff, R. Truesdell, A. Mammoli, F. van Swol, P. Shah, and C. J. Brinker. Effective slip on textured superhydrophobic surfaces. *Physics of Fluids*, 17(5):051701, may 2005. doi: 10.1063/1.1896405. URL `https://doi.org/10.1063/1.1896405`.

J. W. Gose, K. Golovin, M. Boban, J. M. Mabry, A. Tuteja, M. Perlin, and S. L. Ceccio. Characterization of superhydrophobic surfaces for drag reduction in turbulent flow. *Journal of Fluid Mechanics*, 845:560–580, apr 2018. doi: 10.1017/jfm.2018.210. URL `https://doi.org/10.1017/jfm.2018.210`.

H. Guo, V. I. Borodulin, Y. S. Kachanov, C. Pan, J. J. Wang, Q. X. Lian, and S. F. Wang. Nature of sweep and ejection events in transitional and turbulent boundary layers. *Journal of Turbulence*, 11:N34, jan 2010. doi: 10.1080/14685248.2010.498425. URL `https://doi.org/10.1080/14685248.2010.498425`.

A. S. Haase, J. A. Wood, R. G. H. Lammertink, and J. H. Snoeijer. Why bumpy is better: The role of the dissipation distribution in slip flow over a bubble mattress. *Physical Review Fluids*, 1(5), sep 2016. doi: 10.1103/physrevfluids.1.054101. URL `https://doi.org/10.1103/physrevfluids.1.054101`.

C. Henoch, T. Krupenkin, P. Kolodner, J. Taylor, M. Hodes, A. Lyons, C. Peguero, and K. Breuer. Turbulent drag reduction using superhydrophobic surfaces. In *3rd AIAA Flow Control Conference*. American Institute of Aeronautics and Astronautics, jun 2006. doi: 10.2514/6.2006-3192. URL `https://doi.org/10.2514/6.2006-3192`.

Lee Wing Ho. *A Legendre spectral element method for simulation of incompressible unsteady viscous free-surface flows.* PhD dissertation, Massachusetts Institute of Technology. Dept. of Mechanical Engineering, 1989.

J. Hoepffner, L. Brandt, and D. S. Henningson. Transient growth on boundary layer streaks. *Journal of Fluid Mechanics*, 537:91–100, 2005. doi: 10.1017/S0022112005005203.

J. Hoepffner, S. Popinet, P.-Y. Lagrée, G. Balestra, and G. Gallino. Basilisk, easystab. `http://basilisk.fr/sandbox/easystab/README`, 2019. Accessed: 2019 02 15.

C. C. Holt. Forecasting seasonals and trends by exponentially weighted moving averages. *International Journal of Forecasting*, 20(1):5–10, jan 2004. doi: 10.1016/j.ijforecast.2003.09.015. URL `https://doi.org/10.1016/j.ijforecast.2003.09.015`.

P Huerre and P A Monkewitz. Local and global instabilities in spatially developing flows. *Annual Review of Fluid Mechanics*, 22(1):473–537, jan 1990. doi: 10.1146/annurev.fl.22.010190.002353. URL `https://doi.org/10.1146/annurev.fl.22.010190.002353`.

O. Iida and Y. Nagano. The relaminarization mechanisms of turbulent channel flow at low reynolds numbers. *Flow, Turbulence and Combustion*, 60(2):193–213, 1998. doi: 10.1023/a:1009999606355. URL `https://doi.org/10.1023/a:1009999606355`.

R. G. Jacobs and P. A. Durbin. Simulations of bypass transition. *Journal of Fluid Mechanics*, 428:185–212, feb 2001a. doi: 10.1017/s0022112000002469. URL `https://doi.org/10.1017/s0022112000002469`.

R. G. Jacobs and P. A. Durbin. Simulations of bypass transition. *Journal of Fluid Mechanics*, 428:185–212, 2001b. doi: 10.1017/S0022112000002469.

N. Jarrin, S. Benhamadouche, D. Laurence, and R. Prosser. A synthetic-eddy-method for generating inflow conditions for large-eddy simulations. *International Journal of Heat and Fluid Flow*, 27(4):585 – 593, 2006. ISSN 0142-727X. doi: https://doi.org/10.1016/j.ijheatfluidflow.2006.02.006. URL `http://www.sciencedirect.com/science/article/pii/S0142727X06000282`. Special Issue of The Fourth International Symposium on Turbulence and Shear Flow Phenomena - 2005.

T. O. Jelly, S. Y. Jung, and T. A. Zaki. Turbulence and skin friction modification in channel flow with streamwise-aligned superhydrophobic surface texture. *Physics of Fluids*, 26(9):095102, sep 2014. doi: 10.1063/1.4894064. URL `https://doi.org/10.1063/1.4894064`.

J. Jeong and F. Hussain. On the identification of a vortex. *Journal of Fluid Mechanics*, 285(-1):69, feb 1995. doi: 10.1017/s0022112095000462. URL `https://doi.org/10.1017/s0022112095000462`.

A.J. Jerri. The shannon sampling theorem—its various extensions and applications: A tutorial review. *Proceedings of the IEEE*, 65(11):1565–1596, 1977. doi: 10.1109/proc.1977.10771. URL `https://doi.org/10.1109/proc.1977.10771`.

J. Jiménez. Near-wall turbulence. *Physics of Fluids*, 25(10):101302, oct 2013. doi: 10.1063/1.4824988. URL `https://doi.org/10.1063/1.4824988`.

J. Jiménez and P. Moin. The minimal flow unit in near-wall turbulence. *Journal of Fluid Mechanics*, 225:213–240, 1991. doi: 10.1017/S0022112091002033.

Y. C. Jung and B. Bhushan. Biomimetic structures for fluid drag reduction in laminar and turbulent flows. *Journal of Physics: Condensed Matter*, 22(3):035104, dec 2009. doi: 10.1088/0953-8984/22/3/035104. URL `https://doi.org/10.1088/0953-8984/22/3/035104`.

Y. S. Kachanov. Physical mechanisms of laminar-boundary-layer transition. *Annual Review of Fluid Mechanics*, 26(1):411–482, jan 1994a. doi: 10.1146/annurev.fl.26.010194.002211. URL `https://doi.org/10.1146/annurev.fl.26.010194.002211`.

Y. S. Kachanov. Physical mechanisms of laminar-boundary-layer transition. *Annual Review of Fluid Mechanics*, 26(1):411–482, 1994b. doi: 10.1146/annurev.fl.26.010194.002211. URL `https://doi.org/10.1146/annurev.fl.26.010194.002211`.

J. Kendall. Experiments on boundary-layer receptivity to freestream turbulence. In *36th AIAA Aerospace Sciences Meeting and Exhibit*. American Institute of Aeronautics and Astronautics, jan 1998. doi: 10.2514/6.1998-530. URL `https://doi.org/10.2514/6.1998-530`.

J. Kim, P. Moin, and R. Moser. Turbulence statistics in fully developed channel flow at low reynolds number. *Journal of Fluid Mechanics*, 177:133–166, 1987. doi: 10.1017/S0022112087000892.

P. S. Klebanoff. Characteristics of turbulence in boundary layer with zero pressure gradient. *NACA Technical Report 1247*, 1955.

P. S. Klebanoff, K. D. Tidstrom, and L. M. Sargent. The three-dimensional nature of boundary-layer instability. *Journal of Fluid Mechanics*, 12(01):1, jan 1962a. doi: 10.1017/s0022112062000014. URL `https://doi.org/10.1017/s0022112062000014`.

P. S. Klebanoff, K. D. Tidstrom, and L. M. Sargent. The three-dimensional nature of boundary-layer instability. *Journal of Fluid Mechanics*, 12(1):1âĂŞ34, 1962b. doi: 10.1017/S0022112062000014.

M. Klein, N. Chakraborty, and S. Ketterl. A comparison of strategies for direct numerical simulation of turbulence chemistry interaction in generic planar turbulent premixed flames. *Flow, Turbulence and Combustion*, 99(3-4):955–971, aug 2017. doi: 10.1007/s10494-017-9843-9. URL `https://doi.org/10.1007/s10494-017-9843-9`.

L Kleiser and T A Zang. Numerical simulation of transition in wall-bounded shear flows. *Annual Review of Fluid Mechanics*, 23(1):495–537, jan 1991. doi: 10.1146/annurev.fl.23.010191.002431. URL `https://doi.org/10.1146/annurev.fl.23.010191.002431`.

R. H. Kraichnan. Diffusion by a random velocity field. *The Physics of Fluids*, 13(1):22–31, 1970. doi: 10.1063/1.1692799. URL `https://aip.scitation.org/doi/abs/10.1063/1.1692799`.

C. Lee and C.-J. Kim. Maximizing the giant liquid slip on superhydrophobic microstructures by nanostructuring their sidewalls. *Langmuir*, 25(21):12812–12818, nov 2009. doi: 10.1021/la901824d. URL `https://doi.org/10.1021/la901824d`.

C. Lee and C.-J. Kim. Underwater restoration and retention of gases on superhydrophobic surfaces for drag reduction. *Physical Review Letters*, 106(1), jan 2011. doi: 10.1103/physrevlett.106.014502. URL `https://doi.org/10.1103/physrevlett.106.014502`.

C. Lee, C.-H. Choi, and C.-J. Kim. Superhydrophobic drag reduction in laminar flows: a critical review. *Experiments in Fluids*, 57(12), nov 2016. doi: 10.1007/s00348-016-2264-z. URL `https://doi.org/10.1007/s00348-016-2264-z`.

J. Lee and T. Zaki. Video: A computational laboratory for the study of transitional and turbulent boundary layers. In *68th Annual Meeting of the APS Division of Fluid Dynamics - Gallery of Fluid Motion*. American Physical Society, nov 2015. doi: 10.1103/aps.dfd.2015.gfm.v0056. URL `https://doi.org/10.1103/aps.dfd.2015.gfm.v0056`.

S. J. Lee and T. A. Zaki. Simulations of natural transition in viscoelastic channel flow. *Journal of Fluid Mechanics*, 820:232âĂŞ262, 2017. doi: 10.1017/jfm.2017.198.

H. Lee-Wing and A. T. Patera. A legendre spectral element method for simulation of unsteady incompressible viscous free-surface flows. *Computer Methods in Applied Mechanics and Engineering*, 80(1-3):355–366, jun 1990. doi: 10.1016/0045-7825(90)90040-s. URL `https://doi.org/10.1016/0045-7825(90)90040-s`.

G. Lemoult, L. Shi, K. Avila, S. V. Jalikop, M. Avila, and B. Hof. Directed percolation phase transition to sustained turbulence in couette flow. *Nature Physics*, 12(3):254–258, feb 2016. doi: 10.1038/nphys3675. URL `https://doi.org/10.1038/nphys3675`.

Y. Li, K. Alame, and K. Mahesh. Feature-resolved computational and analytical study of laminar drag reduction by superhydrophobic surfaces. *Physical Review Fluids*, 2 (5), may 2017. doi: 10.1103/physrevfluids.2.054002. URL `https://doi.org/10.1103/physrevfluids.2.054002`.

H. Ling, S. Srinivasan, K. Golovin, G. H. McKinley, A. Tuteja, and J. Katz. High-resolution velocity measurement in the inner part of turbulent boundary layers over super-hydrophobic surfaces. *Journal of Fluid Mechanics*, 801:670–703, jul 2016. doi: 10.1017/jfm.2016.450. URL `https://doi.org/10.1017/jfm.2016.450`.

E. Lisi, M. Amabili, S. Meloni, A. Giacomello, and C. M. Casciola. Self-recovery superhydrophobic surfaces: Modular design. *ACS Nano*, 12(1):359–367, dec 2017. doi: 10.1021/acsnano.7b06438. URL `https://doi.org/10.1021/acsnano.7b06438`.

Y. Liu, J. S. Wexler, C. Schönecker, and H. A. Stone. Effect of viscosity ratio on the shear-driven failure of liquid-infused surfaces. *Physical Review Fluids*, 1(7), nov 2016. doi: 10.1103/physrevfluids.1.074003. URL `https://doi.org/10.1103/physrevfluids.1.074003`.

J.-C. Loiseau, J.-C. Robinet, S. Cherubini, and E. Leriche. Investigation of the roughness-induced transition: global stability analyses and direct numerical simulations. *Journal of Fluid Mechanics*, 760:175–211, nov 2014. doi: 10.1017/jfm.2014.589. URL `https://doi.org/10.1017/jfm.2014.589`.

A. D. Lucey and P. W. Carpenter. Boundary layer instability over compliant walls: Comparison between theory and experiment. *Physics of Fluids*, 7(10):2355–2363, oct 1995. doi: 10.1063/1.868748. URL `https://doi.org/10.1063/1.868748`.

P. Luchini. Reynolds-number-independent instability of the boundary layer over a flat surface: optimal perturbations. *Journal of Fluid Mechanics*, 404:289âĂŞ309, 2000. doi: 10.1017/S0022112099007259.

P. Luchini, F. Manzo, and A. Pozzi. Resistance of a grooved surface to parallel flow and cross-flow. *Journal of Fluid Mechanics Digital Archive*, 228:87, jul 1991. doi: 10.1017/s0022112091002641. URL `https://doi.org/10.1017/s0022112091002641`.

M. Luhar, A. S. Sharma, and B. J. McKeon. A framework for studying the effect of compliant surfaces on wall turbulence. *Journal of Fluid Mechanics*, 768:415–441, mar 2015. doi: 10.1017/jfm.2015.85. URL `https://doi.org/10.1017/jfm.2015.85`.

T. S. Lund, X. Wu, and K. D. Squires. Generation of turbulent inflow data for spatially-developing boundary layer simulations. *Journal of Computational Physics*, 140(2):233 – 258, 1998. ISSN 0021-9991. doi: https://doi.org/10.1006/jcph.1998.5882. URL `http://www.sciencedirect.com/science/article/pii/S002199919895882X`.

A. Lundbladh and A. V. Johansson. Direct simulation of turbulent spots in plane couette flow. *Journal of Fluid Mechanics*, 229(-1):499, aug 1991. doi: 10.1017/s0022112091003130. URL `https://doi.org/10.1017/s0022112091003130`.

J. Malm, P. Schlatter, and N. D. Sandham. A vorticity stretching diagnostic for turbulent and transitional flows. *Theoretical and Computational Fluid Dynamics*, 26(6): 485–499, nov 2011. doi: 10.1007/s00162-011-0245-7. URL `https://doi.org/10.1007/s00162-011-0245-7`.

P. Manneville. On the transition to turbulence of wall-bounded flows in general, and plane couette flow in particular. *European Journal of Mechanics - B/Fluids*, 49:345–362, jan 2015. doi: 10.1016/j.euromechflu.2014.03.017. URL `https://doi.org/10.1016/j.euromechflu.2014.03.017`.

X. Mao, T. A. Zaki, S. J. Sherwin, and H. M. Blackburn. Transition induced by linear and nonlinear perturbation growth in flow past a compressor blade. *Journal of Fluid Mechanics*, 820:604–632, may 2017. doi: 10.1017/jfm.2017.240. URL `https://doi.org/10.1017/jfm.2017.240`.

M. B. Martell, J. B. Perot, and J. P. Rothstein. Direct numerical simulations of turbulent flows over superhydrophobic surfaces. *Journal of Fluid Mechanics*, 620:31–41, 2009. doi: 10.1017/S002211208004916.

M. B. Martell, J. P. Rothstein, and J. B. Perot. An analysis of superhydrophobic turbulent drag reduction mechanisms using direct numerical simulation. *Physics of Fluids*, 22(6): 065102, jun 2010. doi: 10.1063/1.3432514. URL `https://doi.org/10.1063/1.3432514`.

M. Matsubara and P. H. Alfredsson. Disturbance growth in boundary layers subjected to free-stream turbulence. *Journal of Fluid Mechanics*, 430:149–168, mar 2001. doi: 10.1017/s0022112000002810. URL `https://doi.org/10.1017/s0022112000002810`.

T. Min and J. Kim. Effects of hydrophobic surface on skin-friction drag. *Physics of Fluids*, 16(7):L55–L58, jul 2004. doi: 10.1063/1.1755723. URL `https://doi.org/10.1063/1.1755723`.

T. Min and J. Kim. Effects of hydrophobic surface on stability and transition. *Physics of Fluids*, 17(10):108106, 2005. doi: 10.1063/1.2126569. URL `https://doi.org/10.1063/1.2126569`.

R. Moarref, M. R. Jovanovic, J. A. Tropp, B. J. McKeon, and N. Sharma. A low-order decomposition of turbulent channel flow via resolvent analysis and convex optimization. *Physics of Fluids*, 26(51701):1–7, 2014. URL `https://eprints.soton.ac.uk/364749/`.

M. V. Morkovin. Transition in open flow systems-a reassessment. *Bull. Am. Phys. Soc.*, 39:1882, 1994.

R. D. Moser, J. Kim, and N. N. Mansour. Direct numerical simulation of turbulent channel flow up to retau=590. *Physics of Fluids*, 11(4):943–945, apr 1999. doi: 10.1063/1.869966. URL `https://doi.org/10.1063/1.869966`.

N. J. Mullenix, D. V. Gaitonde, and M. R. Visbal. Spatially developing supersonic turbulent boundary layer with a body-force-based method. *AIAA Journal*, 51(8):1805–1819, aug 2013. doi: 10.2514/1.j051861. URL `https://doi.org/10.2514/1.j051861`.

C. L. M. H. Navier. Mémoire sur les lois du mouvement des fluides. *Mémoires de l'Académie Royale des Sciences de l'Institut de France*, 1823.

M. Nishioka, S. Iid A, and Y. Ichikawa. An experimental investigation of the stability of plane poiseuille flow. *Journal of Fluid Mechanics*, 72(04):731, dec 1975. doi: 10.1017/s0022112075003254. URL `https://doi.org/10.1017/s0022112075003254`.

P. J. Olsson and D. S. Henningson. Optimal disturbance growth in watertable flow. *Studies in Applied Mathematics*, 94(2):183–210, feb 1995. doi: 10.1002/sapm1995942183. URL `https://doi.org/10.1002/sapm1995942183`.

S. A. Orszag. Accurate solution of the Orr–Sommerfeld stability equation. *Journal of Fluid Mechanics*, 50(04):689, dec 1971. doi: 10.1017/s0022112071002842. URL `https://doi.org/10.1017/s0022112071002842`.

J. Ou, B. Perot, and J. P. Rothstein. Laminar drag reduction in microchannels using ultrahydrophobic surfaces. *Physics of Fluids*, 16(12):4635–4643, dec 2004. doi: 10.1063/1.1812011. URL `https://doi.org/10.1063/1.1812011`.

H. Park, H. Park, and J. Kim. A numerical study of the effects of superhydrophobic surface on skin-friction drag in turbulent channel flow. *Physics of Fluids*, 25(11):110815, nov 2013. doi: 10.1063/1.4819144. URL `https://doi.org/10.1063/1.4819144`.

H. Park, G. Sun, and C.-H. Chang-Jin Kim. Superhydrophobic turbulent drag reduction as a function of surface grating parameters. *Journal of Fluid Mechanics*, 747:722–734, apr 2014. doi: 10.1017/jfm.2014.151. URL `https://doi.org/10.1017/jfm.2014.151`.

N. A. Patankar. Thermodynamics of trapping gases for underwater superhydrophobicity. *Langmuir*, 32(27):7023–7028, jun 2016. doi: 10.1021/acs.langmuir.6b01651. URL `https://doi.org/10.1021/acs.langmuir.6b01651`.

A. T. Patera. A spectral element method for fluid dynamics: Laminar flow in a channel expansion. *Journal of Computational Physics*, 54(3):468–488, jun 1984. doi: 10.1016/0021-9991(84)90128-1. URL `https://doi.org/10.1016/0021-9991(84)90128-1`.

J. R. Philip. Flows satisfying mixed no-slip and no-shear conditions. *Zeitschrift für angewandte Mathematik und Physik ZAMP*, 23(3):353–372, may 1972. doi: 10.1007/bf01595477. URL `https://doi.org/10.1007/bf01595477`.

F. Picella, J.-Ch. Loiseau, F. Lusseyran, J.-Ch. Robinet, S. Cherubini, and L. Pastur. Successive bifurcations in a fully three-dimensional open cavity flow. *Journal of Fluid Mechanics*, 844:855–877, apr 2018. doi: 10.1017/jfm.2018.169. URL `https://doi.org/10.1017/jfm.2018.169`.

Francesco Picella, Michele Alessandro Bucci, Stefania Cherubini, and Jean-Christophe Robinet. A synthetic forcing to trigger laminar-turbulent transition in parallel wall bounded flows via receptivity. *Journal of Computational Physics*, 393:92–116, September 2019. doi: 10.1016/j.jcp.2019.04.011. URL `https://doi.org/10.1016/j.jcp.2019.04.011`.

Stephen B. Pope. *Turbulent Flows.* Cambridge University Press, 2000. doi: 10.1017/CBO9780511840531.

J. O. Pralits, E. Alinovi, and A. Bottaro. Stability of the flow in a plane microchannel with one or two superhydrophobic walls. *Physical Review Fluids*, 2(1), jan 2017. doi: 10.1103/physrevfluids.2.013901. URL `https://doi.org/10.1103/physrevfluids.2.013901`.

B. Ramaswamy and M. Kawahara. Arbitrary lagrangian-eulerianc finite element method for unsteady, convective, incompressible viscous free surface fluid flow. *International Journal for Numerical Methods in Fluids*, 7(10):1053–1075, oct 1987. doi: 10.1002/fld.1650071005. URL `https://doi.org/10.1002/fld.1650071005`.

A. Rastegari and R. Akhavan. On the mechanism of turbulent drag reduction with superhydrophobic surfaces. *Journal of Fluid Mechanics*, 773, may 2015. doi: 10.1017/jfm.2015.266. URL `https://doi.org/10.1017/jfm.2015.266`.

S. C. Reddy and D. S. Henningson. Energy growth in viscous channel flows. *Journal of Fluid Mechanics*, 252(-1):209, jul 1993. doi: 10.1017/s0022112093003738. URL `https://doi.org/10.1017/s0022112093003738`.

S. C. Reddy, P. J. Schmid, J. S. Baggett, and D. S. Henningson. On stability of streamwise streaks and transition thresholds in plane channel flows. *Journal of Fluid Mechanics*, 365:269–303, 1998. doi: 10.1017/S0022112098001323.

E. Reshotko. Transient growth: A factor in bypass transition. *Physics of Fluids*, 13(5):1067–1075, may 2001. doi: 10.1063/1.1358308. URL `https://doi.org/10.1063/1.1358308`.

P. Ricco, C. Ottonelli, Y. Hasegawa, and M. Quadrio. Changes in turbulent dissipation in a channel flow with oscillating walls. *Journal of Fluid Mechanics*, 700:77–104, apr 2012. doi: 10.1017/jfm.2012.97. URL `https://doi.org/10.1017/jfm.2012.97`.

U. Rist and H. Fasel. Direct numerical simulation of controlled transition in a flat-plate boundary layer. *Journal of Fluid Mechanics*, 298(-1):211, sep 1995. doi: 10.1017/s0022112095003284. URL `https://doi.org/10.1017/s0022112095003284`.

V. A. Romanov. Stability of plane-parallel couette flow. *Functional Analysis and Its Applications*, 7(2):137–146, 1973. doi: 10.1007/bf01078886. URL `https://doi.org/10.1007/bf01078886`.

B. J. Rosenberg, T. Van Buren, M. K. Fu, and A. J. Smits. Turbulent drag reduction over air- and liquid- impregnated surfaces. *Physics of Fluids*, 28(1):015103, jan 2016. doi: 10.1063/1.4939272. URL `https://doi.org/10.1063/1.4939272`.

M. E. Rosti and L. Brandt. Numerical simulation of turbulent channel flow over a viscous hyper-elastic wall. *Journal of Fluid Mechanics*, 830:708–735, oct 2017. doi: 10.1017/jfm.2017.617. URL `https://doi.org/10.1017/jfm.2017.617`.

J. P. Rothstein. Slip on superhydrophobic surfaces. *Annual Review of Fluid Mechanics*, 42(1):89–109, jan 2010. doi: 10.1146/annurev-fluid-121108-145558. URL `https://doi.org/10.1146/annurev-fluid-121108-145558`.

W. A. Rowin, J. Hou, and S. Ghaemi. Inner and outer layer turbulence over a superhydrophobic surface with low roughness level at low reynolds number. *Physics of Fluids*, 29(9):095106, sep 2017. doi: 10.1063/1.5004398. URL `https://doi.org/10.1063/1.5004398`.

W. A. Rowin, J. Hou, and S. Ghaemi. Turbulent channel flow over riblets with superhydrophobic coating. *Experimental Thermal and Fluid Science*, 94:192–204, jun 2018. doi: 10.1016/j.expthermflusci.2018.02.001. URL `https://doi.org/10.1016/j.expthermflusci.2018.02.001`.

N. D. Sandham and L. Kleiser. The late stages of transition to turbulence in channel flow. *Journal of Fluid Mechanics*, 245(-1):319, dec 1992a. doi: 10.1017/s002211209200048x. URL `https://doi.org/10.1017/s002211209200048x`.

N. D. Sandham and L. Kleiser. The late stages of transition to turbulence in channel flow. *Journal of Fluid Mechanics*, 245:319âĂŞ348, 1992b. doi: 10.1017/S002211209200048X.

M. Sano and K. Tamai. A universal transition to turbulence in channel flow. *Nature Physics*, 12(3):249–253, feb 2016. doi: 10.1038/nphys3659. URL `https://doi.org/10.1038/nphys3659`.

W. S. Saric, H. L. Reed, and E. J. Kerschen. Boundary-Layer Receptivity to Freestream Disturbances. *Annual Review of Fluid Mechanics*, 34(1):291–319, jan 2002. doi: 10.1146/annurev.fluid.34.082701.161921. URL `https://doi.org/10.1146/annurev.fluid.34.082701.161921`.

T. Sayadi, C. W. Hamman, and P. Moin. Direct numerical simulation of complete h-type and k-type transitions with implications for the dynamics of turbulent boundary layers. *Journal of Fluid Mechanics*, 724:480–509, apr 2013a. doi: 10.1017/jfm.2013.142. URL `https://doi.org/10.1017/jfm.2013.142`.

T. Sayadi, C. W. Hamman, and P. Moin. Direct numerical simulation of complete h-type and k-type transitions with implications for the dynamics of turbulent boundary layers. *Journal of Fluid Mechanics*, 724:480âĂŞ509, 2013b. doi: 10.1017/jfm.2013.142.

D. Schäffel, K. Koynov, D. Vollmer, H.-J. Butt, and C. Schönecker. Local flow field and slip length of superhydrophobic surfaces. *Physical Review Letters*, 116(13), mar 2016. doi: 10.1103/physrevlett.116.134501. URL `https://doi.org/10.1103/physrevlett.116.134501`.

F. Schellenberger, N. Encinas, D. Vollmer, and H.-J. Butt. How water advances on superhydrophobic surfaces. *Physical Review Letters*, 116(9), feb 2016. doi: 10.1103/physrevlett.116.096101. URL `https://doi.org/10.1103/physrevlett.116.096101`.

P. Schlatter, S. Stolz, and L. Kleiser. LES of transitional flows using the approximate deconvolution model. *International Journal of Heat and Fluid Flow*, 25(3):549–558, jun 2004. doi: 10.1016/j.ijheatfluidflow.2004.02.020. URL `https://doi.org/10.1016/j.ijheatfluidflow.2004.02.020`.

P. Schlatter, S. Stolz, and L. Kleiser. Large-eddy simulation of spatial transition in plane channel flow. *Journal of Turbulence*, 7:N33, jan 2006. doi: 10.1080/14685240600602929. URL `https://doi.org/10.1080/14685240600602929`.

P. Schlatter, R. Örlü, Q. Li, G. Brethouwer, J. H. M. Fransson, A. V. Johansson, P. H. Alfredsson, and D. S. Henningson. Turbulent boundary layers up to reÎÿ=2500 studied through simulation and experiment. *Physics of Fluids*, 21(5):051702, 2009. doi: 10.1063/1.3139294. URL `https://doi.org/10.1063/1.3139294`.

P. C. Schlatter. *Large-eddy simulation of transition and turbulence in wall-bounded shear flow.* PhD thesis, ETH Zurich, 2005. URL `http://hdl.handle.net/20.500.11850/38300`.

H. Schlichting and K. Gersten. *Boundary-Layer Theory.* Springer Berlin Heidelberg, 2017. doi: 10.1007/978-3-662-52919-5. URL `https://doi.org/10.1007/978-3-662-52919-5`.

P. J. Schmid. Nonmodal stability theory. *Annual Review of Fluid Mechanics*, 39(1):129–162, 2007. doi: 10.1146/annurev.fluid.38.050304.092139. URL `https://doi.org/10.1146/annurev.fluid.38.050304.092139`.

P. J. Schmid and L. Brandt. Analysis of fluid systems: Stability, receptivity, SensitivityLecture notes from the FLOW-NORDITA summer school on advanced instability methods for complex flows, stockholm, sweden, 2013. *Applied Mechanics Reviews*, 66(2):024803, mar 2014. doi: 10.1115/1.4026375. URL `https://doi.org/10.1115/1.4026375`.

P. J. Schmid and D. S. Henningson. *Stability and Transition in Shear Flows.* Springer New York, 2001. doi: 10.1007/978-1-4613-0185-1. URL `https://doi.org/10.1007/978-1-4613-0185-1`.

S. Schmidt and M. Breuer. Source term based synthetic turbulence inflow generator for eddy-resolving predictions of an airfoil flow including a laminar separation bubble. *Computers & Fluids*, 146:1–22, mar 2017. doi: 10.1016/j.compfluid.2016.12.023. URL `https://doi.org/10.1016/j.compfluid.2016.12.023`.

C. Schönecker, T. Baier, and S. Hardt. Influence of the enclosed fluid on the flow over a microstructured surface in the cassie state. *Journal of Fluid Mechanics*, 740:168–195, feb 2014. doi: 10.1017/jfm.2013.647. URL `https://doi.org/10.1017/jfm.2013.647`.

J. Seo and A. Mani. On the scaling of the slip velocity in turbulent flows over superhydrophobic surfaces. *Physics of Fluids*, 28(2):025110, feb 2016. doi: 10.1063/1.4941769. URL `https://doi.org/10.1063/1.4941769`.

J. Seo and A. Mani. Effect of texture randomization on the slip and interfacial robustness in turbulent flows over superhydrophobic surfaces. *Physical Review Fluids*, 3(4), apr 2018. doi: 10.1103/physrevfluids.3.044601. URL `https://doi.org/10.1103/physrevfluids.3.044601`.

J. Seo, R. García-Mayoral, and A. Mani. Pressure fluctuations and interfacial robustness in turbulent flows over superhydrophobic surfaces. *Journal of Fluid Mechanics*, 783:448–473, oct 2015. doi: 10.1017/jfm.2015.573. URL `https://doi.org/10.1017/jfm.2015.573`.

J. Seo, R. García-Mayoral, and A. Mani. Turbulent flows over superhydrophobic surfaces: flow-induced capillary waves, and robustness of air–water interfaces. *Journal of Fluid Mechanics*, 835:45–85, nov 2017. doi: 10.1017/jfm.2017.733. URL `https://doi.org/10.1017/jfm.2017.733`.

A.S. Sharma, R. Moarref, and B.J. Mckeon. Scaling and interaction of self-similar modes in models of high-reynolds number wall turbulence. *Philosophical Transactions of The Royal Society A*, 375(2089):1–14, 2017. URL `https://eprints.soton.ac.uk/402214/`.

B. Song, D. Barkley, B. Hof, and M. Avila. Speed and structure of turbulent fronts in pipe flow. *Journal of Fluid Mechanics*, 813:1045–1059, jan 2017. doi: 10.1017/jfm.2017.14. URL `https://doi.org/10.1017/jfm.2017.14`.

H. B. Squire. On the stability for three-dimensional disturbances of viscous fluid flow between parallel walls. *Proceedings of the Royal Society A: Mathematical, Physical and Engineering Sciences*, 142(847):621–628, nov 1933. doi: 10.1098/rspa.1933.0193. URL `https://doi.org/10.1098/rspa.1933.0193`.

S. Srinivasan, J. A. Kleingartner, J. B. Gilbert, R. E. Cohen, A. J. B. Milne, and G. H. McKinley. Sustainable drag reduction in turbulent taylor-couette flows by depositing sprayable superhydrophobic surfaces. *Physical Review Letters*, 114(1), jan 2015. doi: 10.1103/physrevlett.114.014501. URL `https://doi.org/10.1103/physrevlett.114.014501`.

A. Steinberger, C. Cottin-Bizonne, P. Kleimann, and E. Charlaix. High friction on a bubble mattress. *Nature Materials*, 6(9):665–668, jul 2007. doi: 10.1038/nmat1962. URL `https://doi.org/10.1038/nmat1962`.

T. Tatsumi and T. Yoshimura. Stability of the laminar flow in a rectangular duct. *Journal of Fluid Mechanics*, 212(-1):437, mar 1990. doi: 10.1017/s002211209000204x. URL `https://doi.org/10.1017/s002211209000204x`.

C. J. Teo and B. C. Khoo. Flow past superhydrophobic surfaces containing longitudinal grooves: effects of interface curvature. *Microfluidics and Nanofluidics*, 9(2-3): 499–511, jan 2010. doi: 10.1007/s10404-010-0566-7. URL `https://doi.org/10.1007/s10404-010-0566-7`.

V. Theofilis and T. Colonius. An algorithm for the recovery of 2- and 3d BiGlobal instabilities of compressible flow over 2d open cavities. In *33rd AIAA Fluid Dynamics Conference and Exhibit*. American Institute of Aeronautics and Astronautics, jun 2003. doi: 10.2514/6.2003-4143. URL `https://doi.org/10.2514/6.2003-4143`.

D. C. Tretheway and C. D. Meinhart. Apparent fluid slip at hydrophobic microchannel walls. *Physics of Fluids*, 14(3):L9–L12, mar 2002. doi: 10.1063/1.1432696. URL `https://doi.org/10.1063/1.1432696`.

R. Truesdell, A. Mammoli, P. Vorobieff, F. van Swol, and C. J. Brinker. Drag reduction on a patterned superhydrophobic surface. *Physical Review Letters*, 97(4), jul 2006.

doi: 10.1103/physrevlett.97.044504. URL `https://doi.org/10.1103/physrevlett.97.044504`.

Peichun Tsai, Alisia M. Peters, Christophe Pirat, Matthias Wessling, Rob G. H. Lammertink, and Detlef Lohse. Quantifying effective slip length over micropatterned hydrophobic surfaces. *Physics of Fluids*, 21(11):112002, nov 2009. doi: 10.1063/1.3266505. URL `https://doi.org/10.1063/1.3266505`.

T. Tsukahara, Y. Seki, H. Kawamura, and D. Tochio. Dns of turbulent channel flow at very low reynolds numbers, 2014.

S. Türk, G. Daschiel, A. Stroh, Y. Hasegawa, and B. Frohnapfel. Turbulent flow over superhydrophobic surfaces with streamwise grooves. *Journal of Fluid Mechanics*, 747: 186–217, apr 2014. doi: 10.1017/jfm.2014.137. URL `https://doi.org/10.1017/jfm.2014.137`.

J. van Ingen. The eN method for transition prediction. historical review of work at TU delft. In *38th Fluid Dynamics Conference and Exhibit*. American Institute of Aeronautics and Astronautics, jun 2008. doi: 10.2514/6.2008-3830. URL `https://doi.org/10.2514/6.2008-3830`.

R. N. Wenzel. Resistance of solid surfaces to wetting by water. *Industrial & Engineering Chemistry*, 28(8):988–994, aug 1936. doi: 10.1021/ie50320a024. URL `https://doi.org/10.1021/ie50320a024`.

J. S. Wexler, I. Jacobi, and H. A. Stone. Shear-driven failure of liquid-infused surfaces. *Physical Review Letters*, 114(16), apr 2015. doi: 10.1103/physrevlett.114.168301. URL `https://doi.org/10.1103/physrevlett.114.168301`.

B. Woolford, J. Prince, D. Maynes, and B. W. Webb. Particle image velocimetry characterization of turbulent channel flow with rib patterned superhydrophobic walls. *Physics of Fluids*, 21(8):085106, aug 2009. doi: 10.1063/1.3213607. URL `https://doi.org/10.1063/1.3213607`.

X. Wu. Inflow turbulence generation methods. *Annual Review of Fluid Mechanics*, 49(1): 23–49, 2017. doi: 10.1146/annurev-fluid-010816-060322. URL `https://doi.org/10.1146/annurev-fluid-010816-060322`.

X. Wu, P. Moin, and J.-P. Hickey. Boundary layer bypass transition. *Physics of Fluids*, 26 (9):091104, 2014. doi: 10.1063/1.4893454. URL `https://doi.org/10.1063/1.4893454`.

Y. Xiang, S. Huang, P. Lv, Y. Xue, Q. Su, and H. Duan. Ultimate stable underwater superhydrophobic state. *Physical Review Letters*, 119(13), sep 2017. doi: 10.1103/physrevlett.119.134501. URL `https://doi.org/10.1103/physrevlett.119.134501`.

M. Xu, G. Sun, and C.-J. Kim. Infinite lifetime of underwater superhydrophobic states. *Physical Review Letters*, 113(13), sep 2014. doi: 10.1103/physrevlett.113.136103. URL `https://doi.org/10.1103/physrevlett.113.136103`.

C. Ybert, C. Barentin, C. Cottin-Bizonne, P. Joseph, and L. Bocquet. Achieving large slip with superhydrophobic surfaces: Scaling laws for generic geometries. *Physics of Fluids*, 19(12):123601, dec 2007. doi: 10.1063/1.2815730. URL `https://doi.org/10.1063/1.2815730`.

Q. Ye, F. F. J. Schrijer, and F. Scarano. On reynolds number dependence of micro-ramp-induced transition. *Journal of Fluid Mechanics*, 837:597–626, jan 2018. doi: 10.1017/jfm.2017.840. URL `https://doi.org/10.1017/jfm.2017.840`.

K. H. Yu, C. J. Teo, and B. C. Khoo. Linear stability of pressure-driven flow over longitudinal superhydrophobic grooves. *Physics of Fluids*, 28(2):022001, feb 2016. doi: 10.1063/1.4940336. URL `https://doi.org/10.1063/1.4940336`.

G. A. Zampogna, J. Magnaudet, and A. Bottaro. Generalized slip condition over rough surfaces. *Journal of Fluid Mechanics*, 858:407–436, nov 2019. doi: 10.1017/jfm.2018.780. URL `https://doi.org/10.1017/jfm.2018.780`.

T. A. Zang and S. E. Krist. Numerical experiments on stability and transition in plane channel flow. *Theoretical and Computational Fluid Dynamics*, 1(1):41–64, Jan 1989. ISSN 1432-2250. doi: 10.1007/BF00271421. URL `https://doi.org/10.1007/BF00271421`.

C. Zhang, J. Wang, W. Blake, and J. Katz. Deformation of a compliant wall in a turbulent channel flow. *Journal of Fluid Mechanics*, 823:345–390, jun 2017. doi: 10.1017/jfm.2017.299. URL `https://doi.org/10.1017/jfm.2017.299`.

J. Zhang, H. Tian, Z. Yao, P. Hao, and N. Jiang. Mechanisms of drag reduction of superhydrophobic surfaces in a turbulent boundary layer flow. *Experiments in Fluids*, 56(9), sep 2015. doi: 10.1007/s00348-015-2047-y. URL `https://doi.org/10.1007/s00348-015-2047-y`.

J. Zhang, Z. Yao, and P. Hao. Drag reductions and the air-water interface stability of superhydrophobic surfaces in rectangular channel flow. *Physical Review E*, 94(5), nov 2016. doi: 10.1103/physreve.94.053117. URL `https://doi.org/10.1103/physreve.94.053117`.

Y. Zhao, Z. Xia, Y. Shi, Z. Xiao, and S. Chen. Constrained large-eddy simulation of laminar-turbulent transition in channel flow. *Physics of Fluids*, 26(9):095103, sep 2014. doi: 10.1063/1.4895589. URL `https://doi.org/10.1063/1.4895589`.

Y. Zhao, Y. Yang, and S. Chen. Evolution of material surfaces in the temporal transition in channel flow. *Journal of Fluid Mechanics*, 793:840–876, mar 2016. doi: 10.1017/jfm.2016.152. URL `https://doi.org/10.1017/jfm.2016.152`.

J. Zhou, R. J. Adrian, S. Balachandar, and T. M. Kendall. Mechanisms for generating coherent packets of hairpin vortices in channel flow. *Journal of Fluid Mechanics*, 387:353–396, 1999. doi: 10.1017/S002211209900467X.

Retarder la transition vers la turbulence en imitant les feuilles de lotus

Résumé : Nombreuses stratégies de contrôle ont été récemment proposées par la communauté scientifique afin de pouvoir réduire la traînée dans les écoulements pariétaux. Entre autres, les Surfaces Superhydrophobes (SHS) ont montré leurs capacités de pouvoir réduire considérablement le frottement pariétal d'un écoulement liquide grâce à la présence de microbulles de gaz piégées dans les nano-rugosités de la surface. Dans des conditions géométrique et thermodynamique données pour lesquelles la transition de mouillage est évitée (condition pour laquelle normalement la taille des rugosités qui caractérise la SHS est de plusieurs ordres de grandeur plus petite que l'échelle caractéristique de l'écoulement principal), on peut atteindre ce qu'on appelle 'l'effet Lotus', pour lequel l'écoulement glisse à la paroi, avec une vitesse différente de zéro.. Dans ce cadre, nous nous sommes proposés d'étudier, à l'aide de simulations numériques l'influence des SHS sur la transition laminaire-turbulent dans un écoulement de canal. Pour cela, nous avons réalisé une série de simulations numériques directes (DNS), allant de l'état laminaire au cas turbulent pleinement développé, en traitant la plupart de scénarios de transition connu en littérature. Des analyses de stabilité locale et globale ont aussi été réalisées afin de déterminer l'influence de ces surfaces sur la première phase du processus de transition. Bien que la procédure de déclenchement de la transition contrôlée (type K, H, C,...) soit bien décrite dans la littérature, cela n'est pas le cas pour les transitions naturelles. À cette fin, une nouvelle méthode a été développée pour déclencher puis étudier la transition naturelle dans des écoulements de type canal. Cette méthode est basée sur des mécanismes de réceptivité de l'écoulement (resolvent global) permettant de construire un forçage volumique spécifique. Plusieurs approches pour modéliser les SHS ont été utilisées, de complexités croissantes, tout en tenant en compte des caractéristiques physiques de ces surfaces. Dans un premier temps, une condition de glissement homogène a été utilisée et son influence analysée. Chaque rugosité a été ensuite discrétisée spatialement, d'abord avec une alternance de condition limite sur une surface plate, ensuite en tenant compte de la dynamique de l'interface gaz-liquide par une méthode Lagrangienne-Eulerienne Arbitraire (ALE). Nous avons montré que les SHS permettent d'efficacement retarder les transitions contrôlées mais qu'en revanche elles ont peu d'influence sur les transitions naturelles (développant des stries de vitesse). En effet, ce comportement dérive de l'équilibre entre deux effets contradictoires. D'un côté, le glissement pariétal nuit au développement des structures cohérentes de type *hairpin*, en altérant le processus de *vortex stretching-tilting*. D'autre part, le mouvement de l'interface gaz-liquide interagit avec les structures cohérentes de l'écoulement, en produisant des vitesses normales à la paroi favorisant davantage le processus de *sweep-ejection* et entraînant le développement de structures en forme d'arche. Nous avons montré que les interfaces gaz-liquide statiques retardent la transition de façon analogue à une condition aux limites homogène (si l'hétérogénéité pariétale est petite). En revanche la prise en compte de leur dynamique limite le retard de la transition, montrant l'importance du modèle de SHS dans les écoulements transitionnels.

Mots clés : transition laminaire-turbulent, surfaces superhydrophobes, interaction fluide-structure, contrôle passif, réduction de traînée, analyse de stabilité globale.

Delay transition to turbulence with Lotus leaves bio-mimetic superhydrophobic surfaces

Abstract: Many passive control strategies have been recently proposed for reducing drag in wall-bounded shear flows. Among them, underwater SuperHydrophobic Surfaces (SHS) have proven to be capable of dramatically reducing the skin friction of a liquid flowing on top of them, due to the presence of gas bubbles trapped within the surface nano-sculptures. In specific geometrical and thermodynamical conditions for which wetting transition is avoided (in particular, when the roughness elements characterizing the SHS are several orders of magnitude smaller than the overlying flow), the so-called 'Lotus effect' is achieved, for which the flow appears to slip on the surface with a non zero velocity. In this framework, we propose to study, by means of numerical simulations, the influence of SHS on laminar-turbulent transition in a channel flow. To do so we have performed a series of direct numerical simulations (DNS), from the laminar to the fully turbulent state, covering the majority of transition scenarios known in the literature, as well as local and global stability analysis so to determine the influence of SHS onto the initial stages of the process. While the conditions for observing controlled K-type transition in a temporal channel flow are well defined, this is not the case for uncontrolled ones. To this end, a novel theoretical numerical framework has been developed so to enable the observation of natural transition in wall-bounded flows. This method, similarly to the Free-Stream-Turbulence framework available for the boundary layer flow, is capable of triggering uncontrolled transition through flow receptivity to a purpose-built forcing. Different surface modellings for the superhydrophobic surfaces are tested. First, homogeneous slip conditions are used. Then, the spatial heterogeneity of the SHS has been considered by modelling it as a flat surface with alternating slip no-slip boundary conditions. Finally, the dynamics of each microscopic liquid-gas free-surface has been taken into account by means of a fully coupled fluid-structure solver, using an Arbitrary Lagrangian Eulerian formulation. We show that while SHS are ineffective in controlling transition in noisy environment, they can strongly delay transition to turbulence for the K-type scenario. This behaviour results from the balance of two opposing effects. On one hand slippery surfaces inhibit the development of characteristic hairpin vortices by altering the vortex stretching-tilting process. On the other hand, the movement of the gas-liquid free-surfaces interacts with the overlying coherent structures, producing wall-normal velocities that enhance the sweep-ejection process, leading to a rapid formation of hairpin-like head vortices. Thus, when considering flat interfaces transition time is strongly increased, while taking into account the interface dynamics induces smaller changes with respect to the no-slip case, indicating the need for an appropriate modelling of SHS for transition delay purposes.

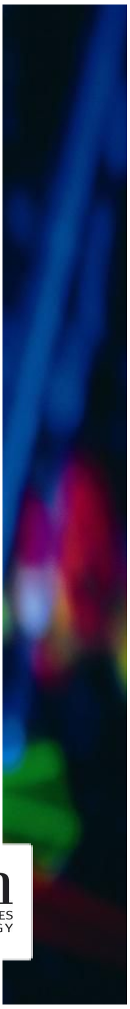Keywords: laminar-turbulent transition, superhydrophobic surfaces, fluid-structure interaction, passive flow control, drag reduction, global stability analysis.